

Copyright

By

Nick Andrew Moreno

2016

**U-Pb and $^{40}\text{Ar}/^{39}\text{Ar}$ geochronology of rhyolitic tuffs and
lavas of the Sierra Madre Occidental silicic large igneous
province: Insights into Eocene-Oligocene silicic volcanism
from a new sample transect, Chihuahua and Durango
border region, northern Mexico**

By

Nick Andrew Moreno

A Thesis Submitted to the Department of Geological Sciences
California State University, Bakersfield
In Partial Fulfillment for the Degree of
Masters of Science in Geology

Spring 2016

U-Pb and $^{40}\text{Ar}/^{39}\text{Ar}$ geochronology of rhyolitic tuffs and lavas of the Sierra Madre Occidental silicic large igneous province: Insights into Eocene-Oligocene silicic volcanism from a new sample transect, Chihuahua and Durango border region, northern Mexico

By Nick Andrew Moreno

This thesis or project has been accepted on behalf of the Department of Geological Sciences by their supervisory committee:



Dr. Graham D.M. Andrews
Committee Chair



Dr. Sarah R. Brown



Dr. William C. Krugh

For my mother Jeannette—

■ *The light of my life.*

Acknowledgements

I would first like to thank **Dr. Graham Andrews** for inviting me on to this project -- I never anticipated a simple rock-cutting gig would ultimately evolve into the focus of my graduate career. I would also like to thank him for his excellent mentorship and support in the laboratory, classroom, and field -- our time in Mexico was magical, when I was not dying of illness. His insightful input improved this thesis by many orders of magnitude, and also made me a better geoscientist. I do not think I could thank him enough for the impact he has had on my academic pursuits.

I extend my appreciation to **Dr. Sarah Brown** for her assistance with sample preparation, tutelage on the various analytical instruments, data analysis, and for her thesis feedback. I would also like to acknowledge **Dr. William Krugh** for his valuable input on this thesis -- how some typos and omissions made it through all the drafts I will never know. To **Dr. Pablo Davila-Harris**: thank you for assisting with the field work in Mexico and for the creation of the beautiful composite stratigraphic column used in this thesis. The hospitality you and your department extended to us in Mexico was as divine as the bottle of Mezcal you suggested I buy.

To **Linda Anderson**, for her meticulous point counting work, I am eternally grateful. The data proved to be crucial for the sample correlations. For their assistance with puck imaging, I thank **Alana Crown**, **Alyssa Kaess**, and **Dr. Sarah Brown**. Their help came at a time when the SEM was required to run nearly 24 hours per day in order to meet a strict deadline. I also express my appreciation to the folks at the UCLA SIMS Lab, **Matt Wielicki** and **Ming-Chang Liu**: they ensured the ims 1270 was up and running smoothly, even after it died several times. To fellow Bruin **Brenda Pack**: thank you for your help with mount polishing and gold coating, and for being my travel buddy during our geochronology trip to Alabama.

Dr. Bill Hames of the Auburn Noble Isotope Mass Analysis Laboratory (ANIMAL) at Auburn University, Alabama: thank you for assistance with the argon data processing and for welcoming me and Brenda into your wonderful lab.

I would also like to thank the **CREST program** (NSF award HRD1137774) for fully supporting me financially, and making it possible for me to attend school and conduct this research. Likewise, thank you to the **Student Research Scholars** program for also providing much-appreciated funding. **Andrea Medina** -- I honestly can't fathom what the current state of the CREST program would be without your tireless efforts to ensure the ship was always running smoothly.

To **Elizabeth Powers**: I should have kept a notepad around so I could document all the ways in which you helped me during my time at CSUB. You opened locked doors, dealt with the IT department to get much-needed software packages installed, took time out of your day to assist me in locating documents and samples. You taught me how to service the SEM, how to earn my defensive drivers training certificate, even how to turn in this thesis. The geological sciences department would collapse without you. Likewise, thank you **Sue Holt** for assisting with class enrollment, door access, and for your absolutely refreshing positive attitude.

To **Michelle (Casterline) Anderson**: thank you for your support and understanding nature during my time as an intern at the Kern County Water Agency. My time there was my first exposure to the science of hydrogeology.

I would also like to give very special thanks to **Alana Crown**, with whom I have worked closely throughout my time as a graduate student at CSUB. She was always there for me when I needed to vent, work through a problem, crush rocks, analyze data, build a map, whine about class, nearly anything and everything. Alana is insightful, witty, and a wonderful human being. Once she even gave me a dollar for knowing a Strange Brew reference. I am truly a better individual for having her in my life.

To all my friends in the geology department: thank you for the laughs, Lengthwise brews, and late nights that truly made my time at CSUB special.

Finally, I thank **my mother Jeannette and stepfather John** for encouraging me to return to school to pursue a master's degree in the geosciences. This choice has irrevocably altered my life in so many positive ways I could never do it justice by describing it here.

ABSTRACT

I present seventeen new U-Pb and eight $^{40}\text{Ar}/^{39}\text{Ar}$ ages from a previously unstudied geological traverse across the central Sierra Madre Occidental silicic large igneous province along the Chihuahua-Durango state border in Mexico. These data indicate progressive younging of volcanism to the southwest, with a succession of exclusively Eocene rhyolites in the northeast (c. 40 – 37 Ma), Eocene rhyolites overlain by Oligocene rhyolites in the center (c. 39 – 33 Ma), and primarily Oligocene rhyolites in the southwest (c. 34 – 30 Ma). A 39.6 Ma ignimbrite overlies Mesozoic metasedimentary basement at the northeastern end of the transect, approximately 20 km west of Hidalgo del Parral. A 29.5 Ma ignimbrite overlies a Cretaceous ignimbrite (67.0 Ma) at the western end of the transect at Guadalupe y Calvo. Southwestward younging of the volcanic stratigraphy agrees with data from elsewhere in the SMO, and all are inferred to record southwestward slab-rollback of the Farallon slab and arc migration during the waning stages of Sierra Madre Occidental volcanism. The non-uniform rate of Farallon slab retreat was approximated using available age and spatial data. These rates were 15.1 km/Ma through the northern sector, 11.7 km/Ma through the central sector, and 13.7 km/Ma through the southern sector. These values are in close agreement with reported rates of arc-trench retreat in modern arcs. In addition, I used these geochronological data to constrain the longevity of these silicic magmas to ≤ 2.2 Myrs and to attempt to correlate between ignimbrites. One correlation between three deposits is observed: the informally-identified 38.5 Ma, ≥ 26 km³ Ojito tuff.

Contents

List of Tables	4
List of Figures	5
Highlights.....	10
1. Introduction.....	11
1.1 Geological history of the Sierra Madre Occidental and adjacent areas	11
1.1.1 The Proterozoic basement and accreted terranes.....	11
1.1.2 The Laramide magmatic belt and the Lower Volcanic Complex (LVC).....	13
1.1.3 The Upper Volcanic Supergroup (UVS) and Southern Cordillera Basaltic Andesite (SCORBA).....	17
1.1.4 Cenozoic extensional domains in northern Mexico	19
1.2 Project Motivation.....	19
2. Methods.....	23
2.1 Sample Collection and Preparation	23
2.2 Zircon and U-Pb Geochronology	23
2.2.1 Sample Preparation.....	31
2.2.2 Analytical Methods.....	31
2.2.3 Statistical Methodology	35
2.3 ⁴⁰ Ar/ ³⁹ Ar Geochronology	37
2.3.1 Sample Preparation.....	37
2.3.2 Analytical Methods.....	39
3. Results.....	42
3.1 U-Pb and ⁴⁰ Ar/ ³⁹ Ar Age Data.....	42
3.1.1 SMO13_02 — ‘Guadalupe tuff’ — quartz-biotite rhyolitic tuff — (26°04'43.0"N, 106°56'54.2"W)	42
3.1.2 SMO13_04 — ‘Cerro El Ahorado tuff’ — rhyodacitic lapilli tuff — (26°03'48.8"N, 106°55'37.5"W)	42
3.1.3 SMO13_08 — unnamed crystal and lithics-poor, non-welded tuff — (26°04'57.9"N, 106°45'32.4"W)	46
3.1.4 SMO13_12 — ‘Turuachi tuff’ — crystal and lithic-rich welded ignimbrite — (26°07'49.4"N, 106°43'18.5"W)	46
3.1.5 SMO13_13 — unnamed plagioclase-rich, welded ignimbrite — (26°07'54.4"N, 106°41'11.3"W)	46

3.1.6 SMO13_16 — unnamed biotite-rich welded lapilli-tuff — (26°08'05.9"N, 106°40'03.8"W)	50
3.1.7 SMO13_19 — unnamed biotite-phyric, non-welded tuff — (26°16'45.3"N, 106°29'52.1"W)	50
3.1.8 SMO13_22 — ‘Rio Verde Tuff’ — rhyodacite lapilli tuff — (26°17'02.1"N, 106°29'10.4"W)	53
3.1.9 SMO13_28 — unnamed lithic-rich, welded lapilli tuff — (26°34'02.8"N, 106°17'43.5"W)	53
3.1.10 SMO13_33 — unnamed quartz and biotite-rich tuff — (26°36'58.3"N 106°16'17.0"W)	53
3.1.11 SMO13_35 — unnamed plagioclase-phyric, flow-banded, dacite lava — (26°39'12.0"N 106°13'44.0"W)	59
3.1.12 SMO13_37 — unnamed weakly welded, quartz-rich tuff — (26°40'55.4"N, 106°11'58.2"W)	59
3.1.13 SMO13_42 — ‘Navarro tuff’ — quartz and plagioclase-phyric lapilli-tuff — (26°41'00.4"N, 106°11'18.4"W)	59
3.1.14 SMO13_43 — unnamed weakly welded, pumice lapilli-tuff — (26°42'13.5"N, 106°07'13.9"W)	64
3.1.15 SMO13_46 — unnamed quartz-biotite, lapilli-tuff — (26°42'20.1"N 106°07'05.3"W)	64
3.1.16 SMO13_48 — ‘Ballezas Junction tuff’ — sanidine-phyric lapilli-tuff — (26°48'52.2"N, 106°00'50.0"W)	72
3.1.17 SMO13_53 — unnamed non-welded tuff — (26°52'25.1"N, 105°58'35.1"W)	72
4. Discussion	76
4.1 Comparison of ²⁰⁶ Pb/ ²³⁸ U and ⁴⁰ Ar/ ³⁹ Ar data from double-dated samples	76
4.2 Age relationships in stratigraphic sections	77
4.3 Testing of possible correlations between SMO ignimbrites	77
4.3.1 Methodology and scoring rubric	78
4.3.2 Geochronologic comparison, methodology and scoring	78
4.3.3 Point count data comparison, methodology and scoring	78
4.3.4 Geochemical comparison--incompatible trace elements, methodology and scoring ...	81
4.3.5 Correlation results	83
4.3.6 The Ojito tuff	84
4.4 The Guadalupe tuff (SMO13_02) and the edge of the UVS	84
4.5 SMO zircons as probes of the basement and magma chamber processes	85
4.5.1 Xenocrystic zircons	85
4.5.2 Antecrystic zircons	87

4.6 Patterns and rates of arc migration during roll-back of the Farallon slab.....	90
5. Conclusions.....	98
References.....	101
Appendix A –U-Pb Data.....	108
Appendix B – ⁴⁰ Ar/ ³⁹ Ar Data.....	115
Appendix C – Point Count Correlation Data	116
Appendix D – Geochemistry Correlation Data.....	121

List of Tables

Table 1	24
Rock descriptions of the seventeen samples in this study	
Table 2	36
Summary of U-Pb and ⁴⁰ Ar/ ³⁹ Ar age data	
Table 3	79
Results of correlation tests	

List of Figures

Figure 1	12
Extent of the Sierra Madre Occidental silicic large igneous province (SMO SLIP)	
Figure 2	14
Underlying terranes of Mexico	
Figure 3	15
Distribution of Lower Volcanic Complex (LVC) units in Mexico	
Figure 4	20
Cenozoic extensional provinces in the SMO	
Figure 5	21
Summary of age data locations for the northern, central, and southern SMO transects	
Figure 6	25
The sample transect in this study and relevant tectonic domains	
Figure 7	27
Composite graphic log of the volcanic stratigraphy inferred in the eastern flank of the Rio Turuachi valley.	
Figure 8	29
Schematic representation of alpha and beta decay.	
Figure 9	30
The Wetherill concordia diagram	
Figure 10	32
The Tera-Wasserburg diagram	
Figure 11	38
Decay scheme for ⁴⁰ K	

Figure 12	40
Example of a probability density plot	
Figure 13	41
Example of a step-heating diagram	
Figure 14	43
U-Pb summary for sample SMO13_02	
Figure 15	44
⁴⁰ Ar/ ³⁹ Ar summary (step heating and single-crystal total fusion) for sample SMO13_02	
Figure 16	45
U-Pb summary for sample SMO13_04	
Figure 17	47
U-Pb summary for sample SMO13_08	
Figure 18	48
U-Pb summary for sample SMO13_12	
Figure 19	49
U-Pb summary for sample SMO13_13	
Figure 20	51
U-Pb summary for sample SMO13_16	
Figure 21	52
U-Pb summary for sample SMO13_19	
Figure 22	54
U-Pb summary for sample SMO13_22	
Figure 23	55
Probability density plot for sample SMO13_22	

Figure 24	56
⁴⁰ Ar/ ³⁹ Ar summary (single-crystal total fusion) for sample SMO13_22	
Figure 25	57
U-Pb summary for sample SMO13_28	
Figure 26	58
U-Pb summary for sample SMO13_33	
Figure 27	60
U-Pb summary for sample SMO13_35	
Figure 28	61
⁴⁰ Ar/ ³⁹ Ar summary (single-crystal total fusion) for sample SMO13_35	
Figure 29	62
U-Pb summary for sample SMO13_37	
Figure 30	63
⁴⁰ Ar/ ³⁹ Ar summary (single-crystal total fusion) for sample SMO13_37	
Figure 31	65
U-Pb summary for sample SMO13_42	
Figure 32	66
⁴⁰ Ar/ ³⁹ Ar summary (step heating and single-crystal total fusion) for sample SMO13_42	
Figure 33	67
U-Pb summary for sample SMO13_43	
Figure 34	68
⁴⁰ Ar/ ³⁹ Ar summary (step heating and single-crystal total fusion) for sample SMO13_43	
Figure 35	70
U-Pb summary for sample SMO13_46	

Figure 36	71
⁴⁰ Ar/ ³⁹ Ar summary (step heating and single-crystal total fusion) for sample SMO13_46	
Figure 37	73
U-Pb summary for sample SMO13_48	
Figure 38	74
⁴⁰ Ar/ ³⁹ Ar summary (step heating and single-crystal total fusion) for sample SMO13_48	
Figure 39	75
U-Pb summary for sample SMO13_53	
Figure 40	80
Explanation for how the geochronological data were used in the pair selection process	
Figure 41	82
Graphical explanation for the comparison of trace element data	
Figure 42	88
Relative percentages of zircon phenocrysts, antecrysts, and xenocrysts within each sample	
Figure 43	91
Combined probability density plots of the northern, central, and southern SMO transects	
Figure 44	92
Probability density plots for the northern and central sectors of the SMO	
Figure 45	93
Probability density plot for the southern sector of the SMO	
Figure 46	94
Age and location data for previous geochronological studies in the SMO	
Figure 47	95

Ages from Figure 5 plotted as a function of distance from the Gulf of California coastal plain

Figure 48.....97

The rate of arc-trench migration in terms of km/Myr

Figure 49.....98

Illustration of slab rollback and trench migration

Figure 50.....99

Illustration of migration-induced extension

Highlights

- U-Pb zircon geochronology reveals the absolute ages of a suite of seventeen rhyolitic ignimbrites and lavas in a new traverse across the Eocene-Oligocene Sierra Madre Occidental silicic large igneous province, Mexico.
- Double-dating with $^{40}\text{Ar}/^{39}\text{Ar}$ ages constrains the longevity of rhyolitic magmas to ≤ 2.2 Myrs.
- Three ignimbrites up to 40 km apart are inferred to be the deposits of the same eruption based on common ages, and geochemical and petrological characteristics.
- Geochronology data supports previous interpretations of westward arc migration through the Eocene and Oligocene. Rates were broadly similar in the north, center, and south of the Sierra Madre Occidental, and are in close agreement with present-day arc-retreat rates.

1. Introduction

Large igneous provinces (LIPs) are magmatic provinces characterized by igneous volumes $>0.1 \text{ Mkm}^3$, areal extents $>0.1 \text{ Mkm}^2$, and maximum life spans of 50 m.y. emplaced in short “pulses” lasting 1-5 Myrs (Bryan and Ferrari, 2013). *Silicic large igneous provinces* (SLIPs) are LIPs with dominantly silicic ($>65 \text{ wt\% SiO}_2$) composition (Bryan, 2007). The Eocene-Miocene Sierra Madre Occidental (SMO) is a SLIP that forms a wide plateau dominated by rhyolitic ignimbrites and lavas covering $300,000 \text{ km}^2$ of northern Mexico (Wark, 1991; Bryan and Ferrari, 2013). It extends from the US-Mexico border south to the Trans-Mexican Volcanic Belt (central Mexico), west into Baja California, and east into central Chihuahua and Durango (Figure 1; Swanson et al., 1978). The estimated volume of its Oligocene-Early Miocene silicic volcanic components, termed the *Upper Volcanic Supergroup* (UVS) by McDowell and Keizer (1977), exceeds $3.9 * 10^5 \text{ km}^3$, with ignimbrite successions $>1 \text{ km}$ thick (Bryan et al., 2008; Bryan and Ferrari, 2013). This makes the SMO one of the largest continuous rhyolitic ignimbrite provinces in the world, and the largest in North America (Swanson et al., 1978).

Nearly four hundred years of silver and gold exploration and exploitation has confined most geologic interest to the Cretaceous-Eocene ore-bearing rocks underlying the UVS, known collectively as the *Lower Volcanic Complex* (LVC) (McDowell and Keizer, 1977; McDowell and Clabaugh, 1979; Swanson and McDowell, 1984). It is only comparatively recently that focus has shifted to understanding the cover of massive ignimbrites and their relationship with the tectonic evolution of North America.

1.1 Geological history of the Sierra Madre Occidental and adjacent areas

1.1.1 The Proterozoic basement and accreted terranes

Outcrops of Precambrian crystalline rocks in the SMO are restricted to northeastern Sonora (Anderson and Silver, 2005). These rocks are primarily para- and orthogneisses, siliciclastic rocks, and sparse schistose units aged 1.7-1.6 Ga, intruded by younger equigranular quartz diorite to quartz monzonite plutons aged 1.5-1.1 Ga (Anderson and Silver, 1981). These Proterozoic rocks are remnants of the North American craton (“Caborca block”) displaced from California and the Mojave block by the mid-Jurassic left-lateral “Mojave-Sonora megashear” (Anderson and Silver, 2005). The southern extent of the North American basement is inferred

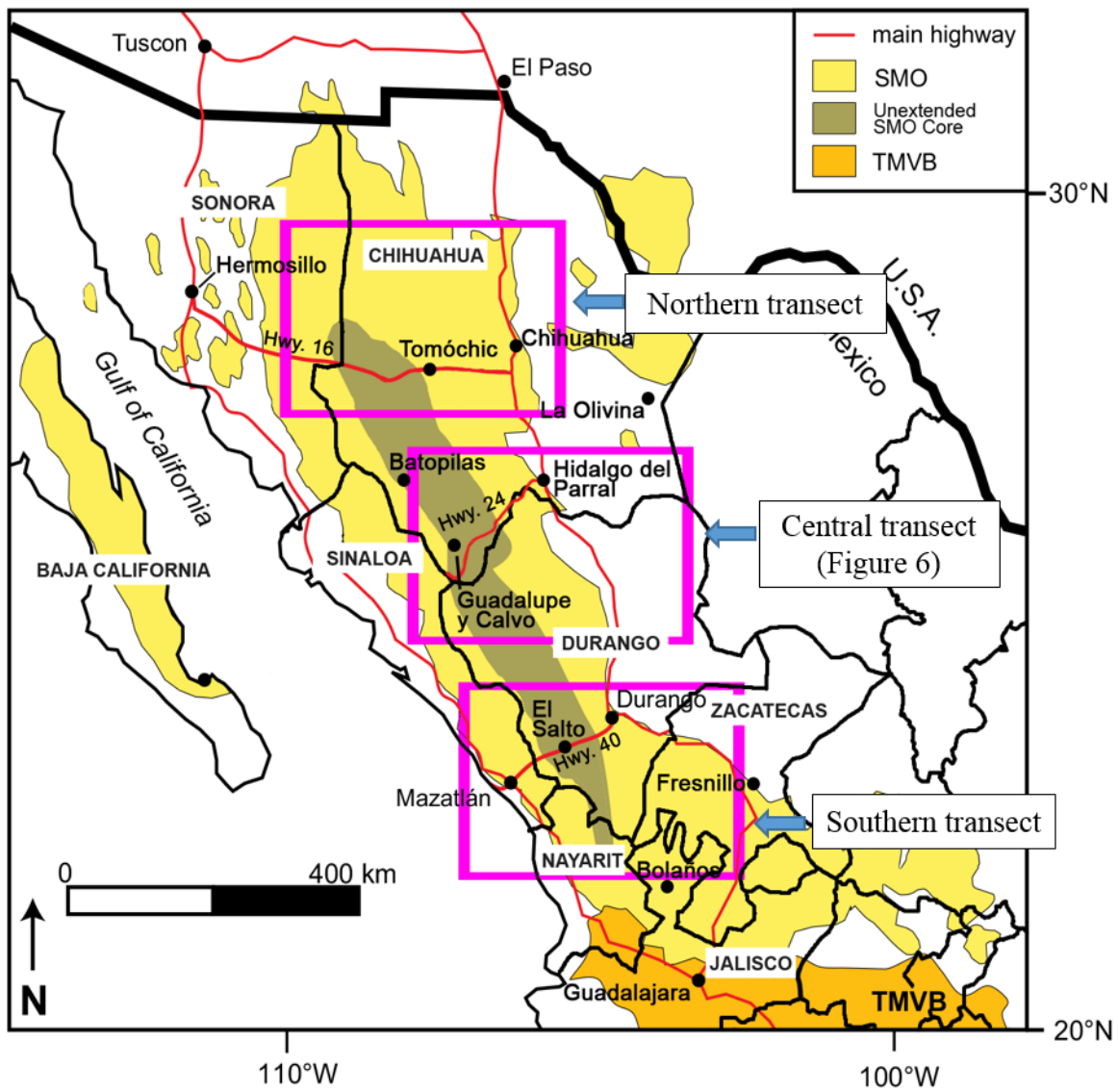


Figure 1. Approximate extent of the Sierra Madre Occidental volcanic province (yellow) and other locations mentioned in the text. SMO = Sierra Madre Occidental, TMVB = Trans-Mexican Volcanic Belt. Modified from Murray et al. (2013).

from isotopic and geochemical studies to be located in Sonora more than 200 km south of Hermosillo (Figure 2; Valencia-Moreno et al., 2001). Geochemical studies on deep crustal xenoliths imply the presence of Proterozoic North American basement beneath northern Mexico at least as far south as La Olivina in southernmost Chihuahua (Figure 3; Cameron et al., 1992) suggesting North American Craton may underlie significant portions of northern Mexico.

The majority of the Precambrian basement beneath the SMO is obscured by overlying, accreted continental and oceanic terranes, and continental arcs (Figure 2; Campa and Coney, 1983; Centeno-García et al., 2008, 2011). The largest accreted terrane is the Late Jurassic to middle Cretaceous Guerrero Composite Terrane (Centeno-García et al., 2008) that is comprised of five distinct sub-terrane: Tahue, Zihuatanejo, Guanajuato, Arcelia, and Teloloapan. These are usually interpreted as oceanic arc-related volcanics, and associated sedimentary sequences, that docked with North America in the Late Cretaceous (Valencia-Moreno et al., 2001; Centeno-García et al., 2008; 2011).

1.1.2 The Laramide magmatic belt and the Lower Volcanic Complex (LVC)

Through the end of the Mesozoic and beginning of the Cenozoic, a NNW striking magmatic arc swept northeastward across Mexico, contemporaneous with the Laramide orogenic episode of the western US and Sierra Madre Oriental (Coney and Reynolds, 1977; McDowell and Keizer, 1977; Valencia-Moreno et al., 2001; Ferrari et al., 2007; Pérez-Segura et al., 2009). The Cordilleran arc resulted from subduction of the Farallon Plate beneath North America, emplacing mafic to felsic volcanics and plutonic rocks, including composite batholiths like the Sinaloa batholith throughout northern and northwestern Mexico between 100 and 40 Ma (McDowell and Clabaugh, 1979; Damon et al., 1981; Ferrari et al., 2007). U-Pb ages show decreasing age trends away from the suspected paleotrench (e.g., Pérez-Segura et al., 2009), while decreasing convergence rates and shallowing subduction angle suggest the arc's eastward sweep ceased almost entirely by 40 Ma (Coney and Reynolds, 1977).

The Cretaceous-Eocene plutonic complexes and coeval extrusive igneous sequences form the LVC. Though voluminous, much of the LVC is unconformably buried by the flat-lying ignimbrite carpet of the SMO, limiting exposure to the SMO's extended flanks, especially the western margin where rivers and Cenozoic uplift associated with the opening of the Gulf of California have incised canyons comparable to the Grand Canyon (Figure 3; McDowell and

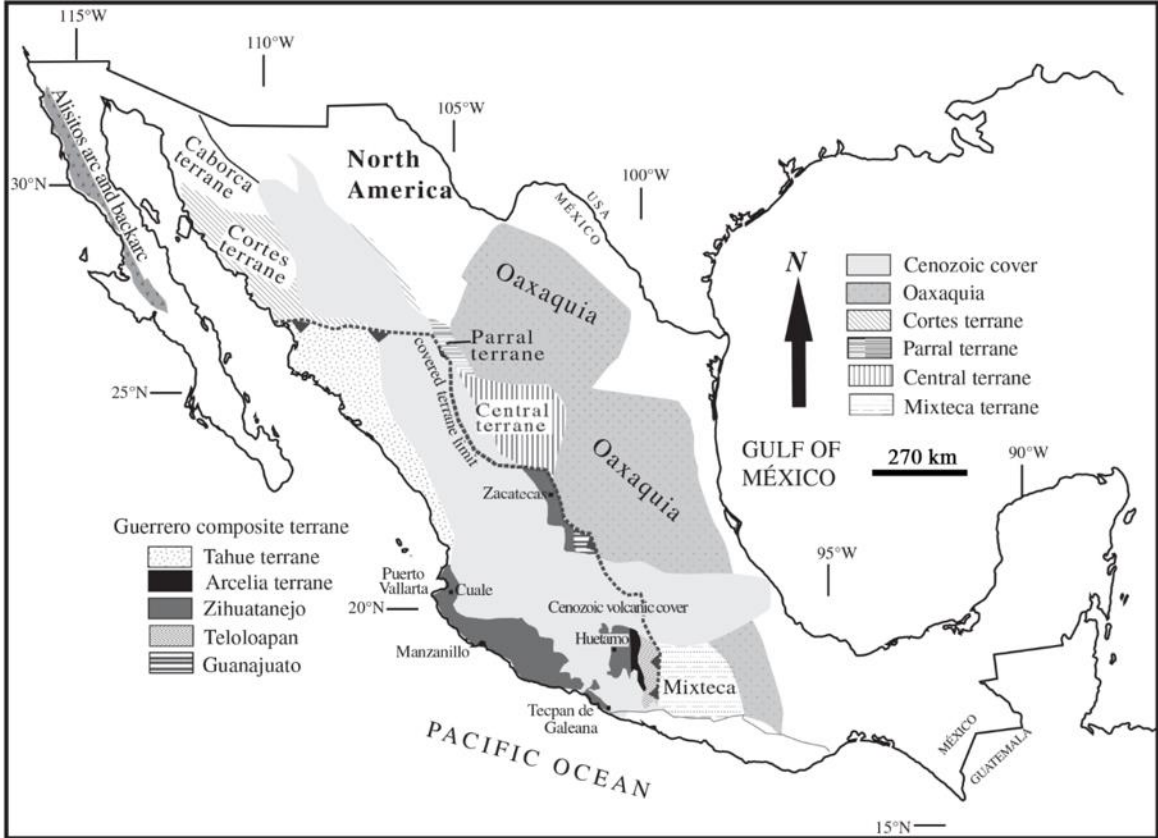


Figure 2. Basement terranes of Mexico. Modified from Centeno-García et al. (2011).

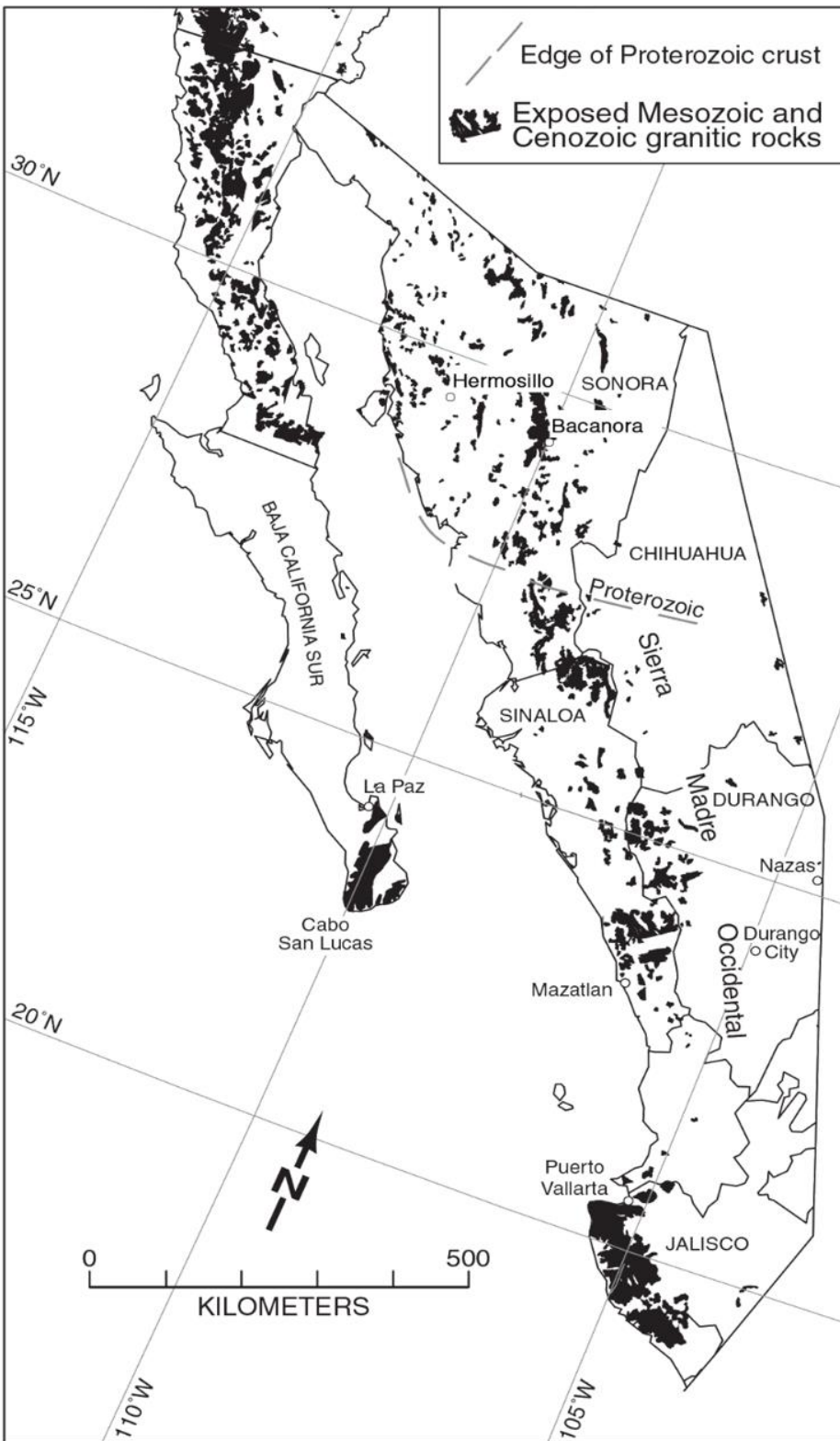


Figure 3. LVC plutonic rocks exposed in and adjacent to the Sierra Madre Occidental. Modified from Henry et al. (2003).

Keizer, 1977; Aguirre-Díaz and McDowell, 1991; McDowell and Mauger, 1994; Ferrari et al., 2007; Busby, 2008). Deformation, alteration, and mineralization have made dating of the LVC volcanics difficult but have also made the SMO host to the largest silver province in the world (Swanson and McDowell, 1984; Busby, 2008), and important porphyry copper and W and Fe skarn deposits (Damon et al., 1981; Roldán-Quintana, 1991).

The LVC is well-exposed in northwestern Mexico where González León et al. (2000) described four packages of Laramide-aged rocks in north-central Sonora. These were highly altered, Late Cretaceous andesitic lavas and volcanoclastic rocks, Paleocene andesites and dacite lavas, and granodiorite and quartz monzonite plutons dated by $^{40}\text{Ar}/^{39}\text{Ar}$ of biotite at ca. 68 Ma and ca. 57 Ma, respectively. All these rocks displayed high-K, calc-alkalic, and metaluminous compositions, common for the LVC (McDowell et al., 2001; Ferrari et al., 2007) and typical of continental arcs. Approximately 100 km northeast of Hermosillo, in east-central Sonora, Roldán-Quintana (1991) interpreted two, comingled granitic batholiths (the Sororan batholith) as the extension of the North American batholithic belt that includes the Peninsular Ranges and Sierra Nevada batholiths (Bateman, 1992) into Mexico. The oldest batholith was dated ca. 60-52 Ma by K/Ar and the second batholith was dated to ca. 36 Ma, also by K/Ar (the only age obtained for this second batholith). However, U-Pb zircon ages of ca. 90 Ma and ca. 71 Ma obtained elsewhere in the Sonoran batholith suggest that the emplacement of the LVC may not have followed a simple eastward-migration as predicted by the Farallon slab-flattening model (McDowell et al., 2001; Ferrari et al., 2007; Pérez-Segura et al., 2009).

On the eastern flank of the SMO in central Chihuahua, McDowell and Mauger (1994) reported U-Pb zircon ages between ca. 70 and 30 Ma of dominantly intermediate lavas, small intrusions, and felsic tuffs. They interpreted the younger date as the age at which Laramide compression ceased in northern Mexico. In east-central Durango, near Nazas (Figure 3), Aguirre-Díaz and McDowell (1991) reported K/Ar ages for crystal-rich, partly welded, felsic ash flow tuffs and andesitic lavas of ca. 52 Ma (Abasolo tuff, K-spar) and ca. 41 Ma (Pedriceñas andesite, plagioclase), respectively. In southwestern Durango, LVC rocks have been mapped by Henry et al. (2003) near the silver-gold mines of Tayoltita and Panuco as well as west into Sinaloa. There the mining sites contain nearly 2,000 m of rhyolitic tuffs and andesite lavas, though at Panuco rhyolitic tuffs and lavas are more abundant than andesite lavas. Henry et al. (2003) reported U-Pb zircon ages for two granodiorite plutons and one tonalite pluton of ca. 48

Ma, ca. 67 Ma and ca. 101 Ma. South of Durango, Ferrari et al. (2007) reported sparse K/Ar ages of rhyolitic domes and andesitic lavas of ca. 38-50 Ma and 74 Ma, near the city of Zacatecas.

1.1.3 The Upper Volcanic Supergroup (UVS) and Southern Cordillera Basaltic Andesite (SCORBA)

By the middle Eocene, the Farallon Plate had ceased migrating eastward and began rolling back toward the trench (Coney and Reynolds, 1977; Humphreys, 1995; Ferrari et al., 2002; 2007; McDowell and McIntosh, 2012). As the plate foundered, hot upwelling of basaltic magma induced partial melting through mafic underplating, triggering pulses of the “ignimbrite flare-up” of southwestern North America (Ferrari et al., 2002; 2007; Bryan et al., 2008). Geochronology data suggest the bulk of ignimbrite generation occurred between ca. 46-40, ca. 36-28 Ma, and ca. 24-20 Ma (Wark et al., 1990; Bryan et al., 2008; McDowell and McIntosh, 2012), of which the 36-28 Ma pulse was most voluminous (Bryan and Ferrari, 2013). Volcanism occurred in broad, NNW-oriented belts which become younger to the southwest, toward the Gulf of California (McDowell and McIntosh, 2012).

Emplacement mechanisms vary by region. In the relatively unextended central “core” of the SMO, ignimbrite emplacement is believed to be caldera-derived, though the vast majority of calderas in this region remain to be discovered (McDowell and Clabaugh, 1979; Swanson and McDowell, 1984; Wark et al., 1990). In the SMO’s extended flanks, Aguirre-Díaz and Labarthe-Hernández (2003) have proposed the concept of *fissure ignimbrites*, in which rapidly decompressing magmas erupt from dikes intruded along graben-bounding normal faults.

Regardless of eruptive mechanism, significant portions of northwestern and northern Mexico were buried by rhyolitic ignimbrites throughout the Eocene and Miocene (Figure 1). In central Chihuahua, McDowell and Mauger (1994) identified concentrations of coarsely porphyritic, felsic, high-K calc-alkaline ignimbrites emplaced between ca. 36-29 Ma within 25 km of Chihuahua City. To the west, approximately 150 km from Chihuahua City, Wark et al. (1990) reported K/Ar ages of 31.8 Ma and 31.4 Ma for the Rio Verde Tuff that was erupted from the nearby Tomochic-Varas caldera. Lanphere et al. (1980), in a geochemical study of the calc-alkalic rhyolitic ignimbrites in the Batopilas region of southwest Chihuahua, reported a K/Ar age for ignimbrites of ca. 30 Ma. In southern Sonora approximately 200 km southeast of Hermosillo,

near Santa Rosa, Gans (1997) reported an $^{40}\text{Ar}/^{39}\text{Ar}$ sanidine age of ca. 33 Ma for a crystal-rich, rhyolitic ignimbrite.

McDowell and Keizer (1977) described the stratigraphy of the SMO with accompanying K/Ar age data along a 200 km transect of Highway 40 west of Durango City to El Salto. They identified two major sequences: (1) an older rhyolitic sequence called the Durango Volcanic Sequence with a mean K/Ar feldspar age of ca. 30 Ma, and (2) a younger, overlying, rhyolitic sequence, the Espinazo-El Salto Volcanic Sequence, with a mean K/Ar feldspar age of ca. 23 Ma. Aguirre-Díaz and McDowell (1993) identified two ignimbrite units almost 500 m thick in east-central Durango at Nazas. The lower, Cerro Prieto tuff was erupted at 29.9 Ma (K/Ar sanidine) while the overlying Santa Clara tuff erupted at 29.5 Ma (K/Ar sanidine). Nearby at Rodeo Luhr et al. (2001) reported an $^{40}\text{Ar}/^{39}\text{Ar}$ sanidine age of 30.6 Ma for an unnamed rhyolitic ignimbrite, possibly correlative with the Santa Clara tuff.

Lang et al. (1988) reported a K/Ar age of ca. 38 Ma for a basal, tilted red-brown welded lithic tuff at Sierra de Valdecañas near Fresnillo, Zacatecas; one of the oldest and most easterly ages reported in the southern SMO. Up section, two porphyritic, rhyolitic tuffs yielded K/Ar ages of 27.7 Ma and 27.5 Ma, respectively. Approximately 50 km northwest of Guadalajara, at the southernmost extent of the SMO, Ferrari et al. (2002) reported a K/Ar (biotite) age of 30.1 Ma for a welded ignimbrite. In east-central Nayarit, Ferrari et al. (2002) reported $^{40}\text{Ar}/^{39}\text{Ar}$ ages for a ~300 m thick succession of rhyolitic ignimbrites and domes, including an age for an unnamed, 31.5 Ma quartz and plagioclase-rich, ignimbrite from Sierra de Valparaiso, and a pair of 31 Ma and 28.6 Ma ignimbrites in Huejuquilla. In the Bolaños Graben (Nayarit and Jalisco) Scheubel et al. (1988) reported a K/Ar (plagioclase) age of 23.7 Ma from the basal andesite and a K/Ar (biotite) age of 21.3 Ma from a 100 m ignimbrite succession. Ferrari et al. (2010) reported an $^{40}\text{Ar}/^{39}\text{Ar}$ age of 18.4 Ma for the uppermost unit, the Chimal Tuff.

Mafic lavas of the Southern Cordillera Basaltic Andesites (SCORBA; Cameron et al. 1989) are interstratified within the tuffs and commonly cap the volcanic succession. These are inferred to have been mafic melts cogenetic with the SMO rhyolites that became penetrated through the crust when extension began (e.g., Ferrari et al., 2007; Bryan and Ferrari, 2013). SCORBAs were initially believed to be confined to the northernmost SMO and southwestern US (e.g., Sedlock et al., 1993) but samples collected in this study (Andrews et al., 2014) indicate the

presence of SCORBAs as far south as the Chihuahua-Durango border. This supports Ferrari et al. (2007) who reported SCORBAs as far south as Zacatecas.

1.1.4 Cenozoic extensional domains in northern Mexico

The SMO is flanked by extensional provinces to the east and west (Figure 4). The eastern flank is the ~23-12 Ma southern continuation of the Basin and Range province into northern Mexico (Stewart, 1978; Henry and Aranda-Gomez, 1992; 2000). The western flank is the ~12-6 Ma Gulf of California Extensional Province (GEP; Henry and Aranda-Gomez, 2000). These provinces converge at the SMO's northern and southern ends and are interpreted to be the same province divided by the intervening and unextended thick central SMO core (Stewart, 1978; Henry and Aranda-Gomez, 2000; Ferrari et al., 2007). The NNW-trending faults characteristic of these domains developed at least in the early Oligocene (Henry and Aranda-Gomez, 1992) suggesting that SMO volcanism was coeval with extension, although numerous studies have found evidence for volcanism having occurred before and after extension (Murray et al., 2013 and references therein).

The distribution of the extensional domains is a function of crustal thickness. In the unextended SMO core the crust is at least 50 km thick (Bonner and Herrin, 1999) due to the inferred presence of a Cretaceous batholith (Henry and Aranda-Gomez, 2000) but thins to ~ 20 km beneath the GEP (Bryan and Ferrari, 2013). Consequently, extensional domains are mostly restricted to these thin crustal zones on the eastern and western SMO flanks (Figure 4).

1.2 Project Motivation

Though numerous studies are cited here, the SMO nevertheless maintains a paucity of geochronological data and a comprehensive, unified stratigraphy is absent (e.g., Centeno-García et al., 2011). A recent and thorough $^{40}\text{Ar}/^{39}\text{Ar}$, K/Ar and U-Pb age data compilation by McDowell and McIntosh (2012), summarizes the current extent of known age trends in the SMO. These data, collected from field and geochronological studies from as far back as the late 1970s, are from two east-west transects across central Chihuahua and Durango, respectively (Figure 5). Together, these transects provide key insights into arc migration rates that tracked the foundering of the Farallon Plate.

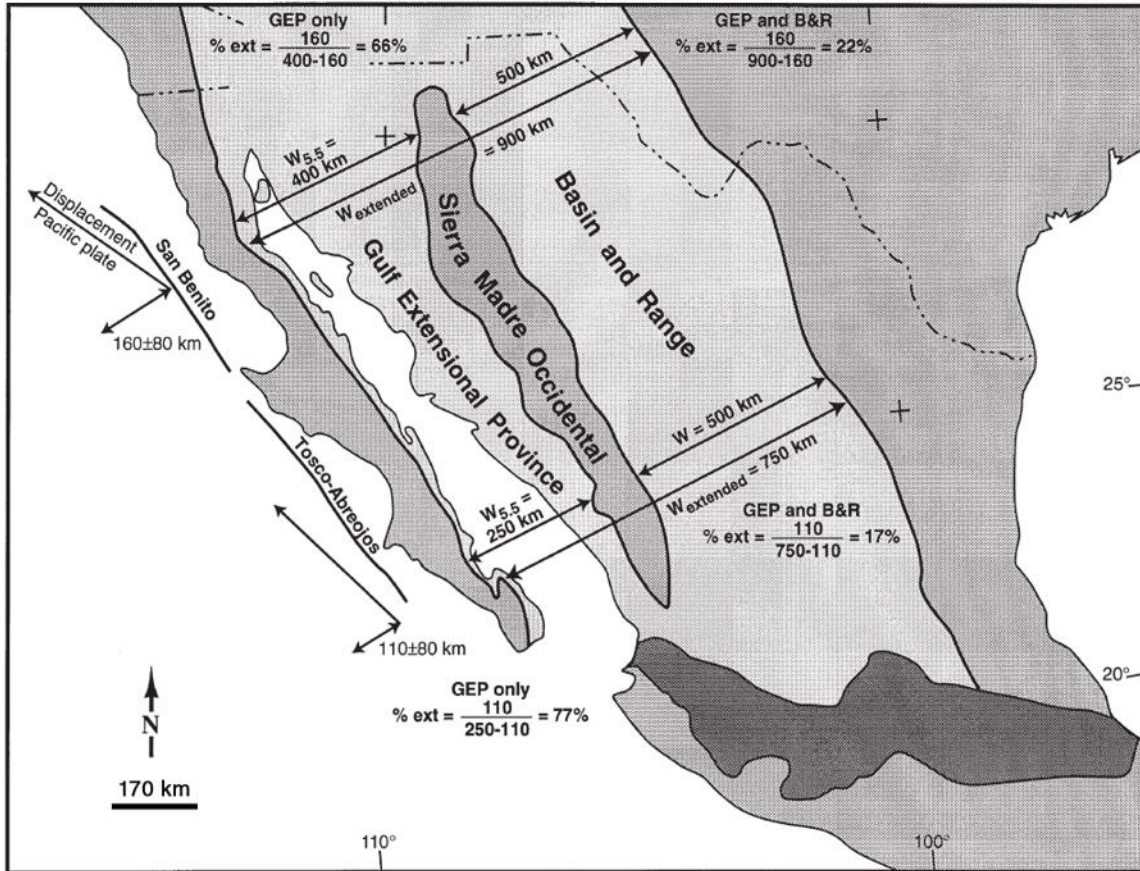


Figure 4. The extensional provinces flanking the SMO and its unextended core (Henry and Aranda-Gomez, 2000).

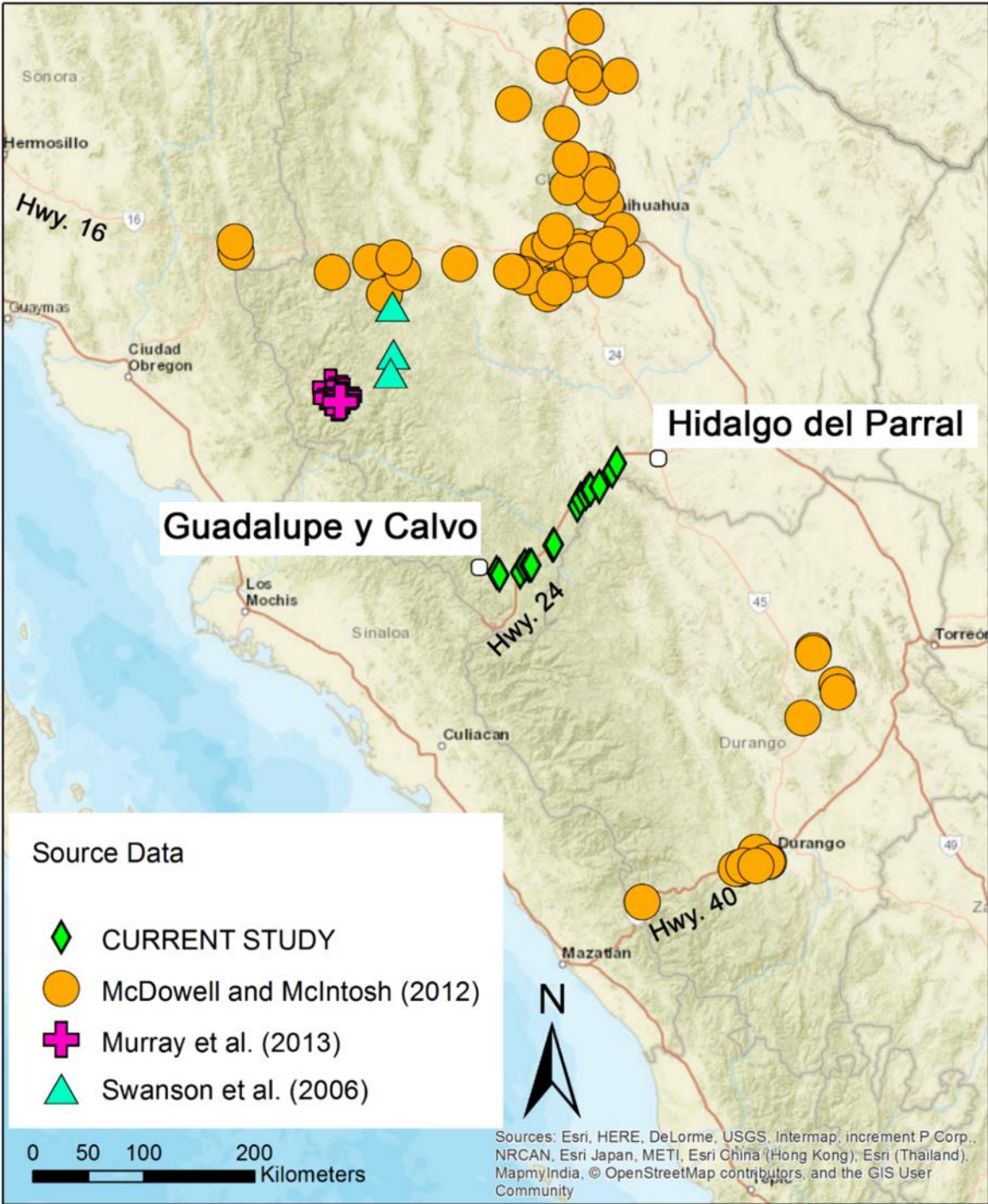


Figure 5. A summary of SMO geochronology data locations from transects in the north, center, and south.

This study builds upon the work of McDowell and McIntosh (2012) by dating samples of rhyolitic ignimbrites and lavas collected along the Chihuahua-Durango border, a region entirely absent from their compilation (Figure 5), and with the addition of other published data from southern Chihuahua (Swanson et al., 2006; Murray et al., 2013). This will also be the first study to apply U-Pb geochronology to a single transect across the SMO, significantly improving the currently sparse geochronological database. These and other published age data will provide significant insights into the temporal and spatial patterns of SMO volcanism.

2. Methods

2.1 Sample Collection and Preparation

Fifty-four ~7-12 kg samples of rhyolitic ignimbrites and lavas (Table 1) were collected over three days along Mexican Federal Highway 24 between the towns of Hidalgo del Parral and Guadalupe y Calvo, along the Chihuahua-Durango state border (Figure 6). This traverse, previously unstudied, was chosen because it crosses the boundaries between the Gulf of California and southern Basin and Range extensional provinces, and the intervening non-extended central core of the Sierra Madre Occidental (Ferrari et al., 2002). Based on known SMO age distributions to the north and south of Highway 24 (e.g., McDowell and McIntosh, 2012), samples were expected to young southwestwards, i.e. toward the Gulf of California extensional province.

Samples were collected from road-cuts along the highway and include units exposed singly and from several units exposed in stratigraphic order (e.g., Rio Turuachi valley; Figure 7). Where possible, samples were collected from the inferred bottom and top of stratigraphic sections defined in the field, although exposure is rarely continuous and stratigraphic breaks are probably present and significant. To attempt to constrain the stratigraphy established in the field, 17 of 54 samples were chosen for geochronology, emphasizing samples collected at the bases and tops of stratigraphic sections. In so doing, the ages obtained will bracket those of non-dated units in between. Of the 17 selected for U-Pb analysis a subset of eight samples were chosen for $^{40}\text{Ar}/^{39}\text{Ar}$ analysis. Double-dating of the units will provide insight into magma residence times because U-Pb dates are interpreted as crystallization ages while the $^{40}\text{Ar}/^{39}\text{Ar}$ dates are interpreted as eruption ages.

2.2 Zircon and U-Pb Geochronology

Zircon (ZrSiO_4) is a useful mineral for U-Pb geochronology due to its ubiquity in felsic igneous rocks, relatively high concentrations of U, resistance to alteration and low- and medium-grade metamorphism, strong tendency to reject “common” non-radiogenic Pb during crystallization, strong retention of radiogenic Pb, and the ease with which it can be extracted from rock samples (Ireland and Williams, 2003).

Sample	Name	Description
SMO13_02	Guadalupe tuff	Weakly welded, quartz-biotite-rich tuff, with a few lithic lapilli.
SMO13_04	Cerro El Ahorado tuff	Plagioclase-sanidine-rich, rhyodacite lapilli-tuff, with abundant lithics and few fiamme.
SMO13_08	unnamed non-welded tuff	Distinctively white crystal and lithic-poor, non-welded tuff.
SMO13_12	Turuachi tuff	Fiamme and crystal and lithic-rich, welded, rhyolitic ignimbrite.
SMO13_13	unnamed welded ignimbrite	Plagioclase-rich, quartz-poor, welded ignimbrite.
SMO13_16	unnamed lapilli-tuff	Pumice and lithic-rich, welded ignimbrite with abundant biotite and little plagioclase.
SMO13_19	unnamed non-welded tuff	Biotite-phyric non-welded tuff.
SMO13_22	Rio Verde Tuff	Plagioclase-rich rhyodacite with abundant large fiamme and oxidized biotite.
SMO13_28	unnamed welded lapilli-tuff	Strongly devitrified, lithic-rich, welded lapilli-tuff.
SMO13_33	Ojito Tuff	Quartz and biotite-rich tuff with abundant plagioclase-phyric lapilli.
SMO13_35	unnamed dacite lava	Strongly devitrified, plagioclase-phyric, flow-banded, dacite lava.
SMO13_37	unnamed tuff	Weakly welded tuff with occasional fiamme and abundant ~1 mm quartz and biotite.
SMO13_42	Navarro tuff	Welded, quartz and plagioclase-phyric lapilli-tuff with occasional lithic lapilli.
SMO13_43	unnamed lapilli-tuff	Weakly-welded, fiamme-rich, pumice lapilli tuff with small quartz crystals and abundant ~3 mm biotite.
SMO13_46	Ojito Tuff	Pink, columnar-jointed quartz and biotite-rich, fiamme-rich, lapilli-tuff with few lithics.
SMO13_48	Ballezas Junction tuff	Sanidine-phyric lapilli-tuff with abundant small pumice, and lithic lapilli.
SMO13_53	Ojito Tuff	Non-welded tuff with small red lithics and sparse biotite and orthoclase entirely lacking in fiamme.

Table 1. Rock descriptions for the 17 samples analyzed in this study. All are rhyolitic ignimbrites with the exception of SMO13_35, a dacite lava. Samples SMO13_33, SMO13_46, and SMO13_53 have been tentatively correlated and provisionally named the Ojito Tuff based on correlation tests in this study.

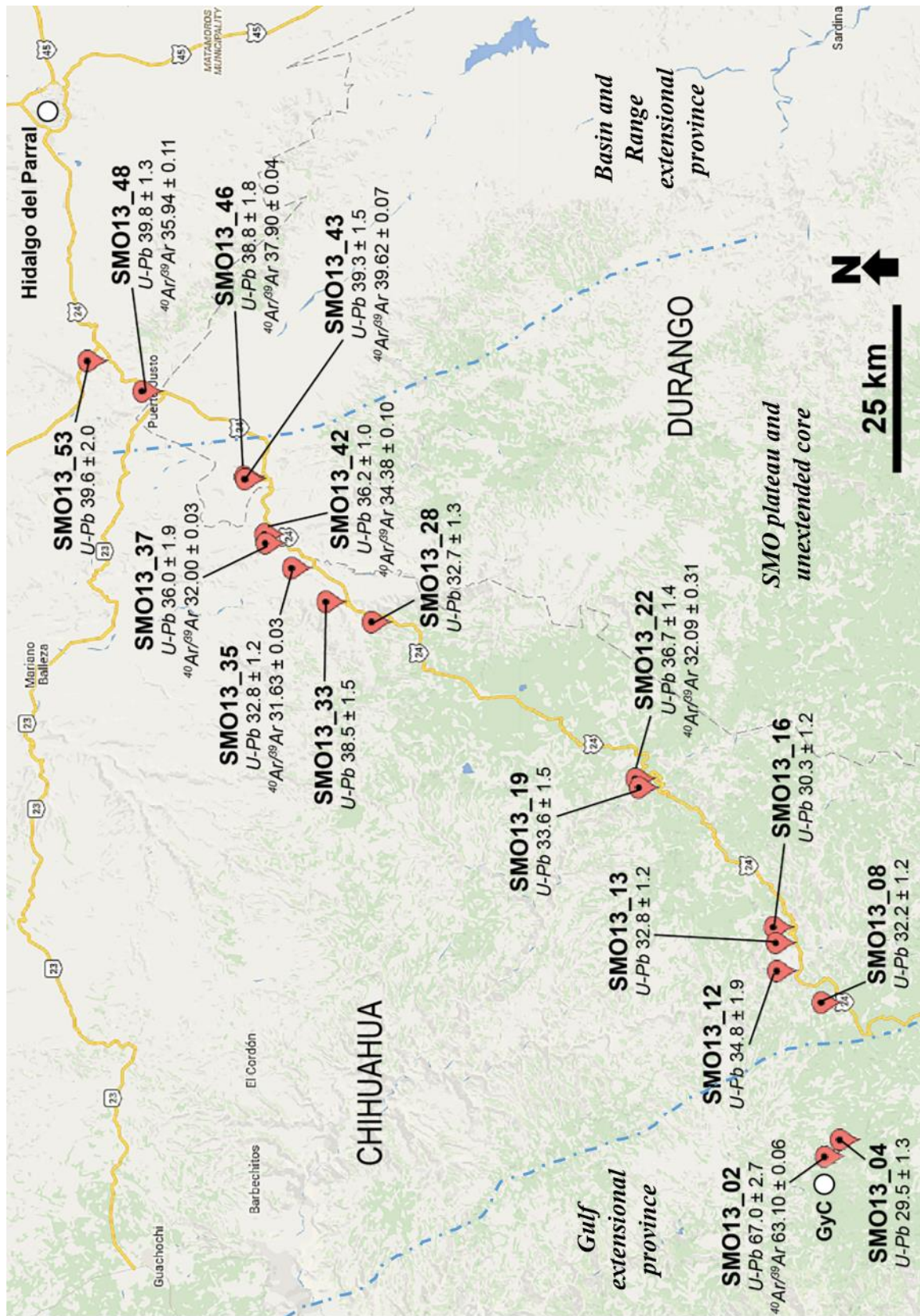


Figure 6. The SMO13 sample transect along Mexican Federal Highway 24 on the Durango-Chihuahua state border. Samples were collected from west (GyC = Guadalupe y Calvo) to east (Hidalgo del Parral). Note that the traverse crosses extended and non-extended regions of the SMO. Available age data (U-Pb and $^{40}\text{Ar}/^{39}\text{Ar}$ obtained in this study are listed under each sample name. All ages (Ma) are reported at $\pm 2\sigma$.

Log section Turuachi - El Vergel

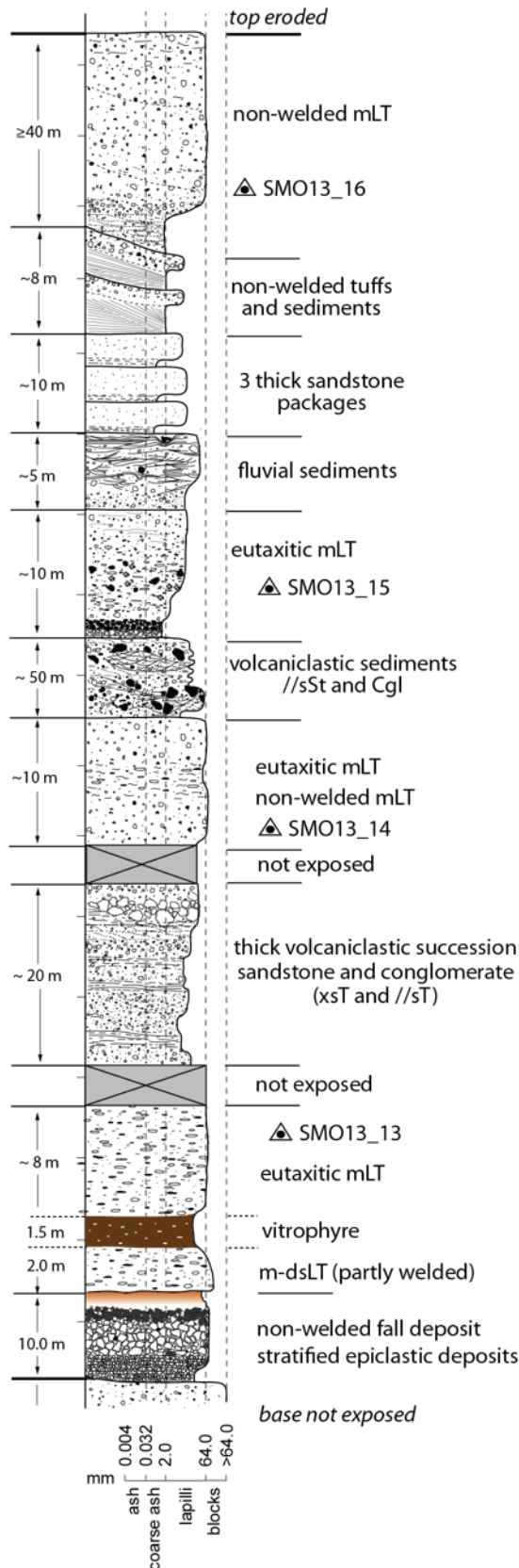


Figure 7. Composite graphic log of the volcanic stratigraphy inferred in the eastern flank of the Rio Turuachi valley, including the units samples as SMO13_13 to SMO13_16 (Andrews et al., 2014). Note that unit thicknesses are approximate and that this is a composite section established over ~3.5 km of the road (~1.9 km as the crow flies) and ~300 m of elevation. Graphic log drafted by Dr. Pablo Davila-Harris. Abbreviations: Cgl - conglomerate, m-dsLT - massive, density-stratified lapilli-tuff, mLT - massive lapilli-tuff, //sSt - parallel-stratified sandstone, //sT - parallel-stratified tuff, xsT - cross-stratified tuff.

U-Pb geochronology makes use of the slow radioactive decay of uranium to lead. *Radioactive decay* includes the ejection of alpha and beta particles from the nucleus of unstable atomic isotopes. Through a series of these decays, radioactive *parent* isotopes ultimately decay to stable *daughter* isotopes (Figure 8). Within the U-Pb system, at least two decay series are known: the uranium series, which describes the decay of ^{238}U to ^{206}Pb , and the actinium series, which describes the decay of ^{235}U to ^{207}Pb . These parent-daughter decay sequences are tied to time via *half-lives* ($t_{1/2}$), which are the times required for one half of the parent product to decay to the daughter product. The *decay constant* (λ) is the proportion of the size of a population of atoms to the rate at which that population decays, and is derived from the half-life of the parent isotope:

$$\lambda = \frac{\ln(2)}{t_{1/2}}$$

where λ = decay constant and $t_{1/2}$ = half-life. For ^{238}U , $\lambda_{238} = 1.55125 * 10^{-10} \text{ yr}^{-1}$ and for ^{235}U , $\lambda_{235} = 9.8485 * 10^{-10} \text{ yr}^{-1}$ (Steiger and Jäger, 1977). To calculate a date for a tested sample, standard “age equations” utilize these decay constants in conjunction with measurements of daughter-parent ratios:

$$\left(\frac{^{206}\text{Pb}^*}{^{238}\text{U}} \right) = (e^{\lambda_{238}t} - 1)$$

$$\left(\frac{^{207}\text{Pb}^*}{^{235}\text{U}} \right) = (e^{\lambda_{235}t} - 1)$$

where t = the time since crystallization and $^{206}\text{Pb}^*/^{238}\text{U}$ and $^{207}\text{Pb}^*/^{235}\text{U}$ are the ratios of radiogenic lead to uranium. Assuming the U-Pb system has not been disturbed post-crystallization, the two equations should yield the same age; thus the U-Pb system provides two age clocks against which the accuracy of a date can be evaluated. If the ratio of $^{207}\text{Pb}^*/^{235}\text{U}$ is plotted against the ratio $^{206}\text{Pb}^*/^{238}\text{U}$, the solutions for which the age equations are equal form a curved line called *concordia* (Figure 9). Dates which plot on the curve are called *concordant* (i.e. they are equal within assigned error) and dates that do not plot on the curve are called *discordant*. The most common causes of discordancy are post-crystallization open-system behavior (e.g., Pb loss or U gain, Figure 9) and mixing of age domains during analysis (Schoene,

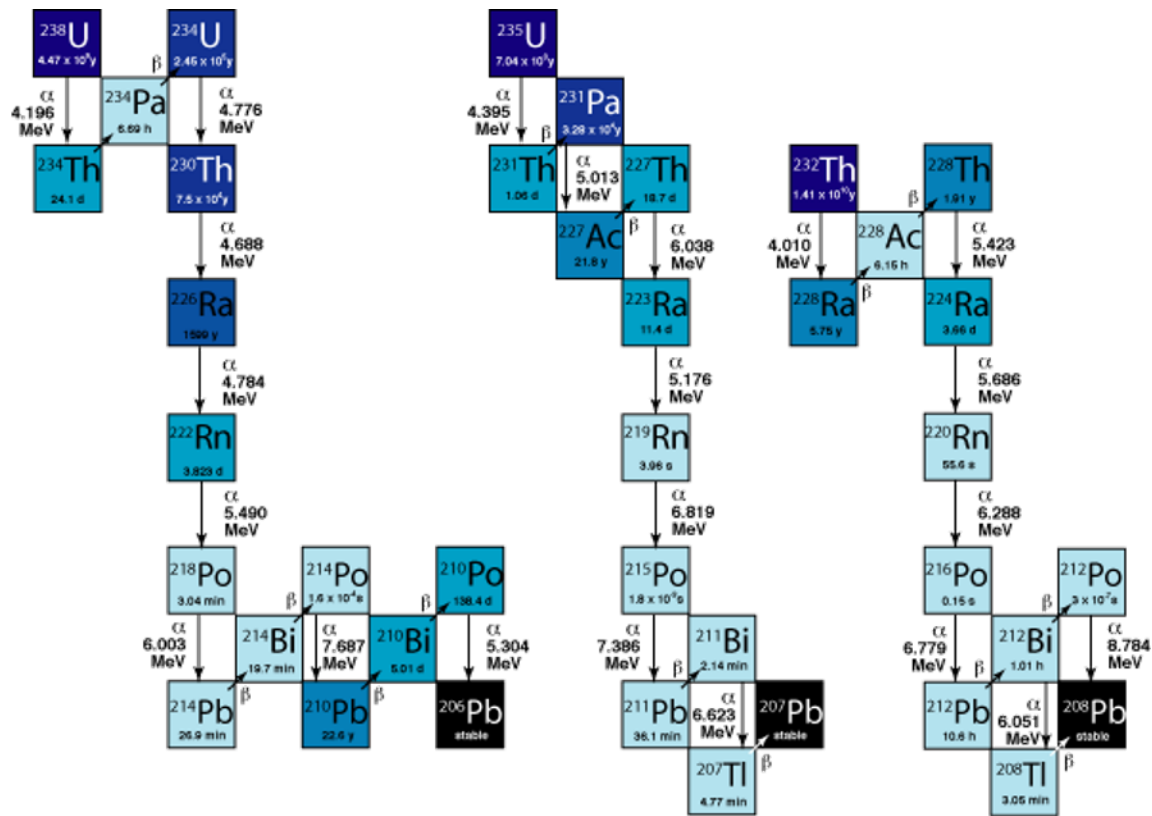


Figure 8. Schematic representation of alpha (α) and beta decay (β). A parent nucleus transforms into a daughter nucleus of another element as radiation is spontaneously ejected from the parent. These decays occur in discrete paths which ultimately end at a stable isotope of Pb. Vertical arrows signify alpha decay; diagonal arrows signify beta decay. From USRG (2008).

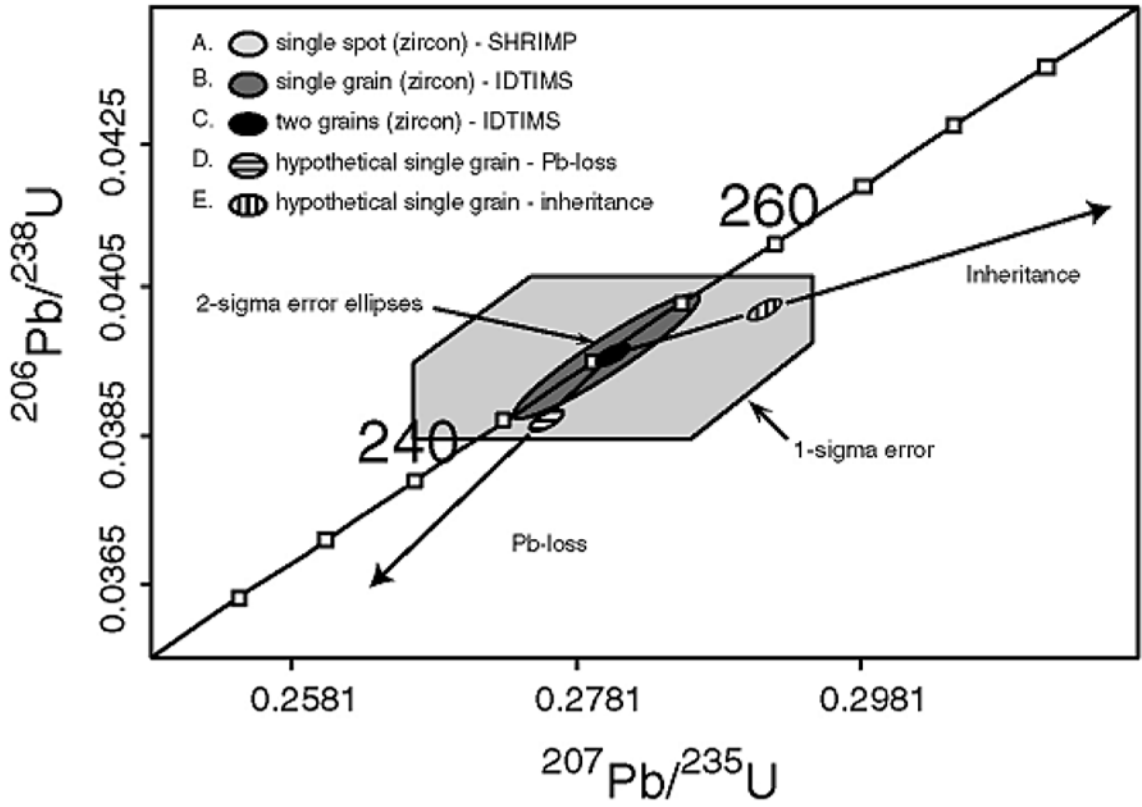


Figure 9. Wetherill concordia diagram. The relevant isotopic ratios are plotted along the x and y axes, generating an isochron (diagonal black line through figure). Points and their corresponding error ellipses are then plotted on the diagram. Ellipses which intersect concordia are called *concordant*. The effects of Pb loss are shown. From Bowring and Schmitz (2003).

2013). Samples which have undergone Pb loss will show underestimates of a “true” age and the point will plot off concordia.

Two graphical methods exist for assessing data discordancy. The Wetherill concordia diagram (Wetherill, 1956; Schoene, 2013) plots $^{207}\text{Pb}^*/^{235}\text{U}$ along the x -axis and $^{206}\text{Pb}^*/^{238}\text{U}$ along the y -axis, where the asterisks denote radiogenic ^{207}Pb and ^{206}Pb (Figure 9). The location on concordia in this space indicates the age of the sample, where older samples correspond to higher values of $^{207}\text{Pb}^*/^{235}\text{U}$ and $^{206}\text{Pb}^*/^{238}\text{U}$ (i.e. the top right of the curve). The other graphical method is the Tera-Wasserburg diagram, which plots $^{238}\text{U}/^{206}\text{Pb}^*$ along the x -axis and $^{207}\text{Pb}/^{206}\text{Pb}^*$ along the y -axis (Schoene, 2013; Figure 10a). The Tera-Wasserburg concordia is especially suited for younger rocks because younger rocks tend to have smaller $^{207}\text{Pb}/^{206}\text{Pb}$ ratios and larger $^{238}\text{U}/^{206}\text{Pb}$ ratios by nature of the timing of radioactive decay. Therefore, unlike the Wetherill plot, younger samples plot further on the right of the curve. In both diagrams, error ellipses encompass the plotted points and are proportional to the standard error of the sample (Figure 9). If the error ellipses do not touch concordia, the analysis can be considered discordant (Schoene, 2013). However, a regression line drawn through discordant error ellipses should intersect concordia at the “true” age of the sample, denoted the *intercept age* (Figure 10b).

2.2.1 Sample Preparation

Zircons were extracted from 17 rock samples using standard crushing, pulverizing, gravity, density and magnetic separation techniques at California State University, Bakersfield (CSUB). About 15 to 25 hand-picked grains from each sample were mounted, along with numerous AS3 zircon standards (age 1099.1 Ma; Paces and Miller, 1993), in two 1-inch epoxy mounts at CSUB that were polished and ultrasonically cleaned in dilute HCL before Au sputter coating at UCLA. The coated mounts were then imaged on a scanning electron microscope at CSUB in secondary electron and cathodoluminescence modes to generate maps to aid in mount navigation, identify zoning, and to minimize the interference of cracks and inclusions during SIMS analysis at UCLA.

2.2.2 Analytical Methods

Geochronologists utilize three major analytical techniques to measure the relative ratios of parent-daughter products: isotope dilution thermal ionization mass spectrometry (ID-TIMS),

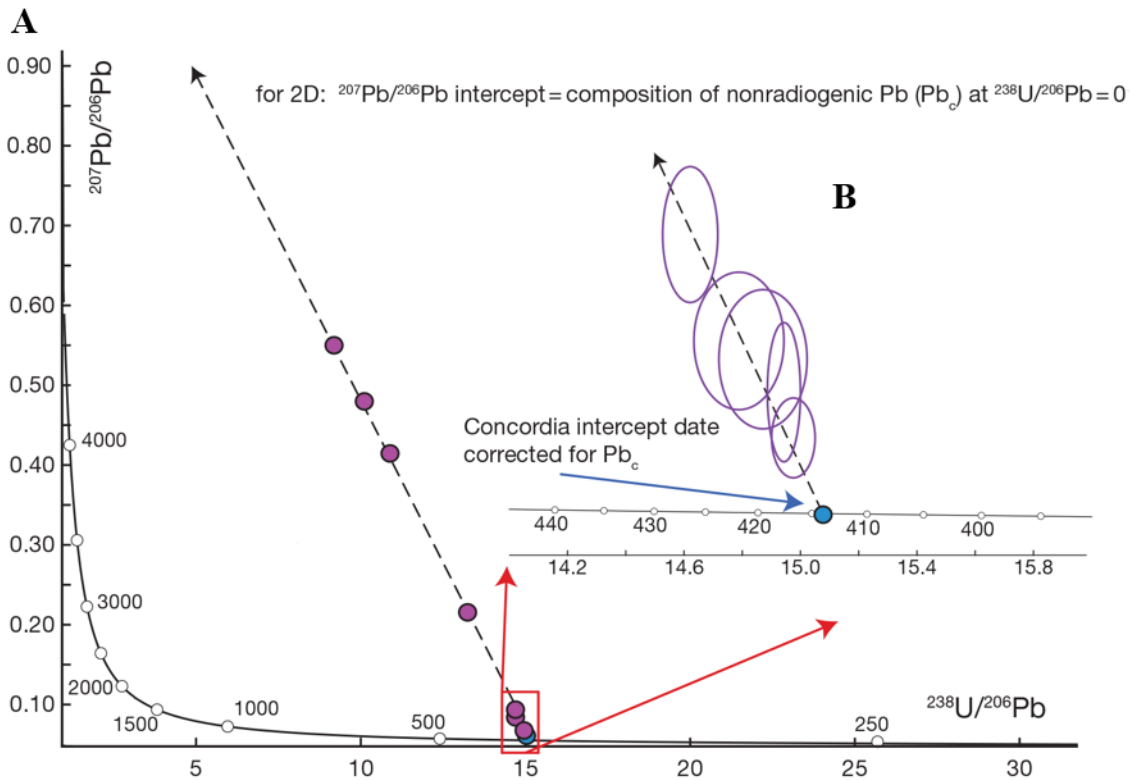


Figure 10. A) A Tera-Wasserburg diagram. The relevant parent-daughter ratios are plotted along each axis and an isochron (curved black line) is generated. Samples which plot on the isochron, or whose error ellipses intersect the isochron, are concordant. **B)** When samples plot off concordia, a regression line (dashed line) can be drawn through the ellipses. The point at which the line intersects the concordia is the *intercept age*. From Schoene (2013).

secondary ion mass spectrometry (SIMS), and laser ablation inductively coupled plasma mass spectrometry (LA-ICPMS) (Schoene, 2013). With ID-TIMS, zircon concentrates are chemically abraded and dissolved before undergoing thermal ionization mass spectrometry procedures (Schaltegger et al., 2015). On the other hand, SIMS and LA-ICPMS utilize *in-situ* microprobe analysis wherein zircon crystals, mounted in circular epoxy resin “pucks,” are bombarded with an ion beam or laser focused to an elliptical or circular spot 20-40 μm in diameter. This process, called ablation or “sputtering,” liberates ions from the crystal which are sorted by mass and charge and then counted by the mass spectrometer (Schaltegger et al, 2015); with these measurements, or “counts,” the ratios of relevant parent-daughter products (e.g., $^{206}\text{Pb}^*/^{238}\text{U}$) can be determined, allowing for the derivation of an age.

For this project I applied *in-situ* SIMS analysis to mounted zircon separates for several reasons. First, the use of concentrates in TIMS sacrifices its ability to date zircon cores and rims separately. TIMS also destroys entire crystals and requires only three to five grains per analysis, so it is unable to adequately address polymodal age populations. Second, while both LA-ICPMS and SIMS can date zircon zones seen from cathodoluminescence (CL) imaging, the reduced precision of LA-ICPMS is likely to mix zones and destroy small crystals. SIMS, on the other hand, is a minimally-destructive dating technique applied to small but precisely-measured zircon crystal populations. The minimally-destructive nature also allows the zircons to be “double-dipped” for additional chemical information such as $\delta^{18}\text{O}$ and ϵHf in future studies. Finally, SIMS is more useful in hydrothermally altered rocks where other dating technique (e.g., Ar/Ar) may not be applicable. The SIMS analyses were conducted over two sessions at the University of California, Los Angeles (UCLA).

Seventeen samples were analyzed on a CAMECA ims 1270 secondary ion mass spectrometer over two sessions at UCLA using an $^{16}\text{O}^-$ primary ion beam focused to an elliptical spot $\sim 35\text{-}40$ μm in diameter. Mass readings of uranium and lead were calibrated using AS3 zircon standards set in the same mounts as the zircon separates. Sample readings were bracketed such that every 10 to 15 sample spots were followed by one to three readings of the AS3 standard. Fifteen to 25 different grains per sample were analyzed producing 15-25 core and rim ages per sample. The SIMS data were reduced with Zips 3.0.4 (UCLA’s in-house SIMS data

software) and processed further in Microsoft Excel 2003 using the Isoplot 3.75 add-in (Ludwig, 2012).

2.2.3 Statistical Methodology

Single dates of the same sample often vary due to natural variations in zircon chemistry, grain mount topography, or analytical conditions. However, if one assumes these ages are evenly distributed around a single value, a weighted mean can be reasonably assumed to represent the “true” age of the sample, especially for large data sets (Schoene, 2013). The mean square of weighted deviations (MSWD) is the goodness-of-fit statistic used to evaluate the degree to which the sample mean represents a single age population (e.g., Colón et al., 2015). When the MSWD is approximately 1, the observed scatter of data is solely the result of analytical uncertainties. When the MSWD is significantly greater than 1, the data scatter too much given the assigned analytical uncertainties (multiple age populations may exist). When the MSWD is significantly less than 1, the data do not scatter enough given the assigned analytical uncertainties, indicating an overestimation of analytical error. Therefore, if one accounts for miscalculated analytical errors or artificial age scatter prior to calculation of the weighted mean, the resulting age should adequately represent the age of the sample when the MSWD is approximately 1.

In this project, $^{206}\text{Pb}/^{238}\text{U}$ ages were used in all calculations because Cenozoic rocks contain little radiogenic ^{207}Pb (Steiger and Jäger, 1977; Coenraads et al., 1990; Schoene, 2013). Individual analyses were quality controlled on the basis of percent-error and age prior to formulation of the weighted mean. Analyses yielding errors significantly greater than 10% were automatically excluded from calculations due to their unreliability. Mean and standard deviation were also used to identify potentially aberrant ages. The standard deviation, which is the square root of the variance, measures dispersion of data around the mean. Statistically, one standard deviation above and below the mean represents 68% of the sample data. Therefore, it is a good approximation of where most of the ages in the sample should reside. Ages exceeding ± 1 standard deviation (1σ) beyond the mean were further scrutinized for Pb loss (showing abnormally young age) and inheritance (ages exceeding 45 Ma). Pb loss was identified graphically using Tera-Wasserburg concordia plots (Figure 10a). Abnormally old ages were also excluded because their presence would artificially inflate the sample mean. Exclusions were made in this manner until the MSWD satisfactorily represented a single age population. Overall, most age pools exhibited 2σ errors within 3-5% of the weighted mean, n -values greater than 3, and MSWD values around 1 (Table 2).

Sample	U-Pb				⁴⁰ Ar/ ³⁹ Ar					
	Weighted Mean ²⁰⁶ Pb/ ²³⁸ U Age (Ma)	Error (±2σ)	MSWD ¹	n ²	Age (Ma)	Error (±2σ)	Phase	Method	MSWD	% in Plateau
SMO13_02	67.0	2.7	1.5	14 / 19	63.10	0.06	Sanidine	SCTF ³	1.3	-
	-	-	-	- / -	63.29	0.24	Biotite	SCIH ⁴	0.6	100
SMO13_04	29.5	1.3	1.1	16 / 18	-	-	-	-	-	-
SMO13_08	32.2	1.2	1.8	10 / 18	-	-	-	-	-	-
SMO13_12	34.8	1.9	1.3	10 / 17	-	-	-	-	-	-
SMO13_13	32.8	1.2	1.0	11 / 20	-	-	-	-	-	-
SMO13_16	30.3	1.2	1.6	12 / 20	-	-	-	-	-	-
SMO13_19	33.6	1.5	1.1	12 / 19	-	-	-	-	-	-
SMO13_22	36.7	1.4	1.3	9 / 14	32.09	0.31	Sanidine	SCTF	3.3	-
SMO13_28	32.7	1.3	2.0	8 / 17	-	-	-	-	-	-
SMO13_33	38.5	1.5	0.7	15 / 15	-	-	-	-	-	-
SMO13_35	32.8	1.2	0.3	15 / 16	31.63	0.03	Sanidine	SCTF	1.6	-
SMO13_37	36.0	1.9	0.4	9 / 18	32.00	0.03	Sanidine	SCTF	1.4	-
SMO13_42	36.2	1.0	1.3	19 / 23	34.38	0.10	Sanidine	SCTF	1.8	-
	-	-	-	- / -	34.59	0.17	Biotite	SCIH	0.9	73.8
SMO13_43	39.3	1.5	1.8	9 / 21	39.62	0.13	Biotite	SCIH	1.1	100
	-	-	-	- -	40-35	-	-	-	-	-
SMO13_46	38.8	1.8	0.4	11 / 15	37.90	0.04	Sanidine	SCTF	1.30	-
	-	-	-	- / -	38.79	0.17	Biotite	SCIH	1.1	80.7
SMO13_48	39.8	1.3	0.6	14 / 21	35.94	0.11	Sanidine	SCTF	1.00	-
	-	-	-	- / -	40.50	0.21	Biotite	SCIH	1.0	93.5
SMO13_53	39.6	2.0	0.3	13 / 15	-	-	-	-	-	-

Table 2. Summary of U-Pb and ⁴⁰Ar/³⁹Ar age data. ¹Mean Square of Weighted Deviations.

²Analyses used in calculation of weighted mean / total analyses available in sample. ³Single-crystal total fusion analyses.

⁴Single-crystal incremental heating analyses.

2.3 $^{40}\text{Ar}/^{39}\text{Ar}$ Geochronology

As with U-Pb analysis, ages calculated by the $^{40}\text{Ar}/^{39}\text{Ar}$ method record time passed since the crystal cooled to its *blocking temperature*, which is the temperature at which daughter products no longer diffuse out of the crystal lattice (Dodson, 1973; Braun et al., 2006). The estimated blocking temperatures for biotite and sanidine are $\sim 360^\circ\text{C}$ and $\sim 235^\circ\text{C}$, respectively; for zircon, the estimated blocking temperature is 960°C (Hodges, 2013). Because the cooling temperatures for biotite and sanidine are much lower than for zircon, $^{40}\text{Ar}/^{39}\text{Ar}$ ages better reflect the cooling age of the unit, which is typically interpreted to be the eruption age (Hora et al., 2010; Crowley et al., 2007).

$^{40}\text{Ar}/^{39}\text{Ar}$ geochronology utilizes the decay of ^{40}K to ^{40}Ar (Kelley, 2002; Figure 11). High-potassium minerals such as sanidine, biotite, and hornblende are irradiated along with standards of known age. Neutron bombardment within the reactor generates ^{39}Ar from stable ^{39}K and also allows for the calculation of a unitless “J-value,” which is a measure of the effect of the neutron bombardment on the known standard. After the irradiated sample has cooled, it is fused with a laser which liberates argon gas. As with U-Pb analysis, isotope counts of the relevant argon isotopes are measured in a mass spectrometer and ages are calculated with a modified age equation:

$$t = \frac{1}{\lambda} \ln(R \times J + 1)$$

where t = time at which the mineral reached its closing temperature, λ = the decay constant of ^{40}K , R = the ratio of radiogenic ^{40}Ar to ^{39}Ar ($^{40}\text{Ar}^*/^{39}\text{Ar}$), and J = a constant determined by the irradiation process.

2.3.1 Sample Preparation

Polished thin sections of eight $^{40}\text{Ar}/^{39}\text{Ar}$ candidate samples were screened for potassium-bearing minerals (sanidine, biotite, hornblende) on a scanning electron microscope in Energy Dispersive X-ray Spectroscopy (EDS) mode. All eight samples were found to be sufficiently potassium-mineral-rich and powdered versions of these samples were picked for $^{40}\text{Ar}/^{39}\text{Ar}$ analysis at the Auburn Noble Isotope Mass Analysis Laboratory (ANIMAL) at Auburn University. Samples were hand-crushed and single grains were picked using a binocular

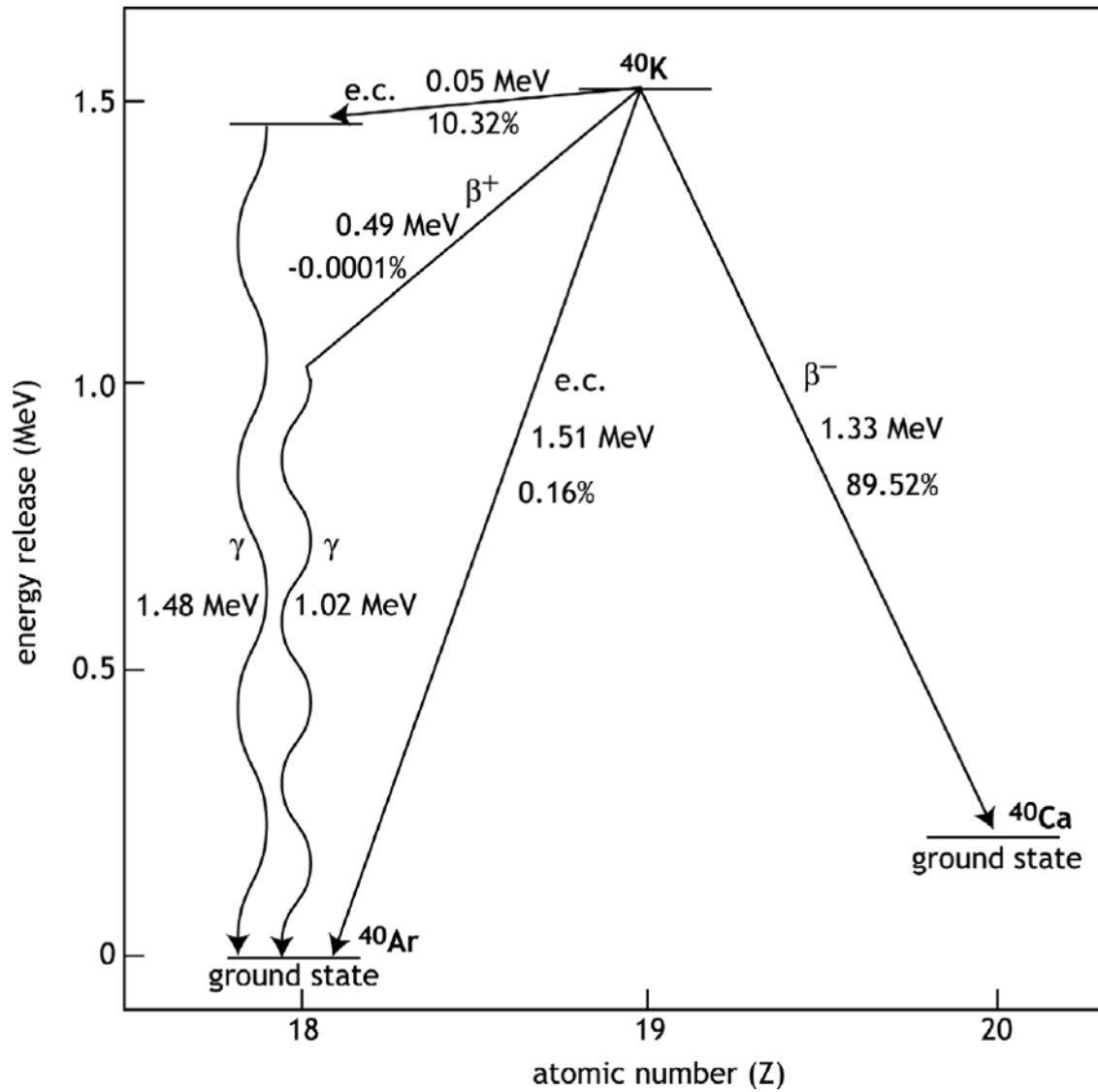


Figure 11. The branching decay scheme for ^{40}K . The majority (~90%) of ^{40}K decays to ^{40}Ca , but a measurable fraction (~0.2%) decays to ^{40}Ar . From Kelley (2002).

microscope. The grains were then loaded into an aluminum canister with the flux monitors GA1550-Biotite and Fish Canyon sanidine, and irradiated for 16 hours at the US Geological Survey's TRIGA nuclear reactor facility in Denver, Colorado. Following irradiation, the flux monitors and samples were loaded into copper planchets and placed in an ultrahigh vacuum extraction system for heating and fusion with a CO₂ laser.

2.3.2 Analytical Methods

All eight samples were analyzed on an ultra-high vacuum 10-cm, 90° sector mass spectrometer with second-order focusing and single electron multiplier detector at ANIMAL and were reduced against sanidine standards of the Fish Canyon Tuff (age ~28.0 Ma; Bachmann et al., 2007). Air blanks were tested every five to ten analyses to calibrate the mass spectrometer. ANIMAL applied single-crystal total fusion and single-crystal incremental heating analyses to biotite and sanidine (Table 2). In single-crystal total fusion analysis individual sanidine grains are completely fused by laser to liberate argon gas (Lee, 2015). The argon isotopes are measured in the mass spectrometer. This method produces one age per fused grain, and therefore, requires multiple grains to produce an age spectrum that is typically represented in probability density plots generated in Isoplot. These plots bin ages into age range histograms along the *x*-axis and display probability curves (Figure 12). The taller the peak of the probability curve for an age range, the higher the probability the next sampled grain will be within that range ('probability' is a unitless number, in this case). The peak is usually inferred to be the age of the rock, though a weighted mean of the different single-crystal fusion ages can also be generated in Isoplot.

In single-crystal incremental-heating analysis, individual biotite grains are fused completely with a defocused laser that gradually increases in power (Lee, 2015). The argon isotopes released from each "step" are measured in the mass spectrometer producing a spectrum of ages for a single grain. This technique is useful because it can detect alteration or other diffusion effects, indicated by abnormally young ages at the beginning and ends of each test (WiscAr, 2016). The goal of the technique is to gradually pass through altered portions of the grain in "steps" until the ages reach a plateau in which they are indistinguishable within error (Figure 13). The plateau ages are used by Isoplot to calculate the mean age of the sample.

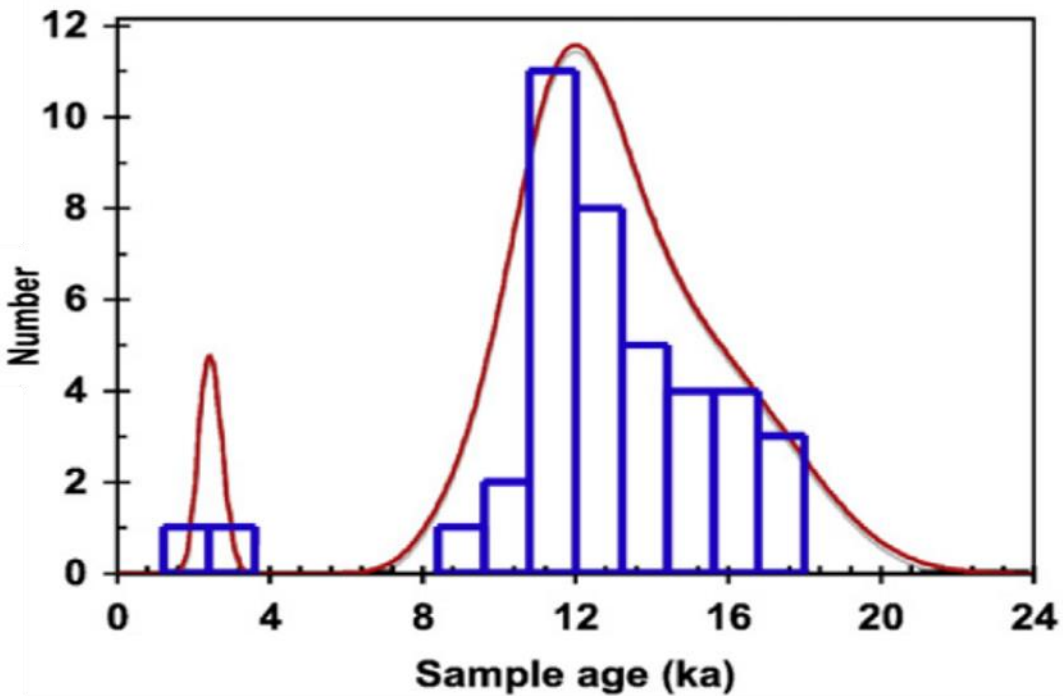


Figure 12. Probability density plot. Ages are binned into groups (e.g. 12-13, 16-17 ka). The heights of the histogram bins correspond to how many items are in the bin. The red curve is a probability density function and signifies where the next sampled grain is most likely to fall. Peak width corresponds to the precision of the data (the greater the precision, the narrower the curve). In this case, the strong peak at ~12 ka suggests the sample may be this age. From Matmon et al. (2010).

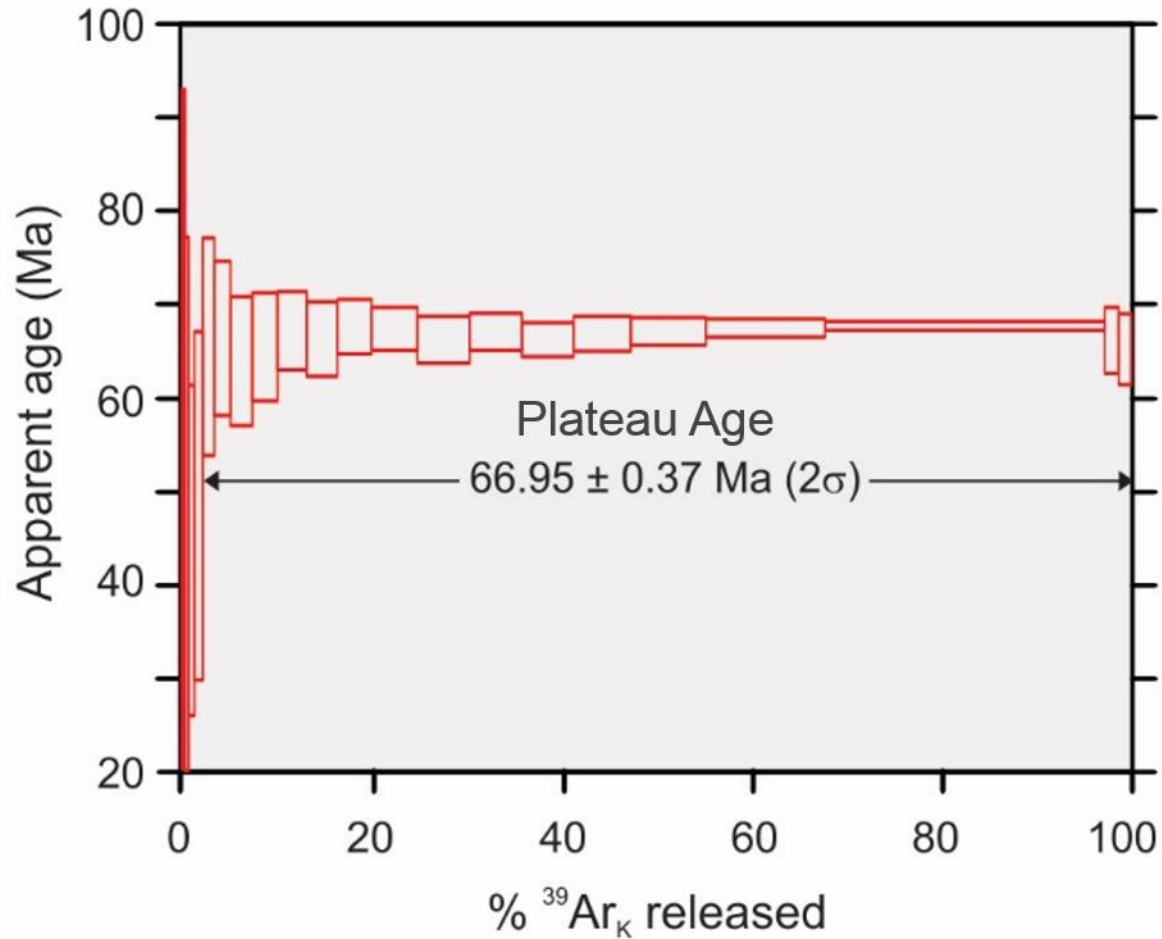


Figure 13. An example of a step-heating diagram produced by single-crystal $^{40}\text{Ar}/^{39}\text{Ar}$ incremental heating analysis. A defocused laser fuses the sample in steps of increasing-power. The gas released at each step is used to calculate an age, generating an age spectrum. The technique is useful for detecting alteration or diffusion effects. Note the large spike yielding an abnormal age at the beginning of the test, likely due to excess argon or boundary effects. When ages become indistinguishable within error, the grain has reached its ‘plateau age’ and is taken as the age of the crystal. From WiscAr Geochronology Lab (2016).

3. Results

3.1 U-Pb and $^{40}\text{Ar}/^{39}\text{Ar}$ Age Data

Table 2 contains a summary of weighted mean $^{206}\text{Pb}/^{238}\text{U}$ and $^{40}\text{Ar}/^{39}\text{Ar}$ ages; all U-Pb and $^{40}\text{Ar}/^{39}\text{Ar}$ age errors are reported at 2σ uncertainty. The U-Pb and $^{40}\text{Ar}/^{39}\text{Ar}$ age data used in weighted mean calculations can be found in Appendices A and B, respectively.

3.1.1 SMO13_02 — ‘Guadalupe tuff’ — quartz-biotite rhyolitic tuff — (26°04'43.0"N 106°56'54.2"W)

SMO13_02 (Figure 6) is a weakly welded, quartz-biotite-rich tuff, with a few lithic lapilli. It is one of two samples (along with SMO13_01) of the Guadalupe tuff at the base of a composite stratigraphic section east of Guadalupe y Calvo. Zircons exhibited clear oscillatory zoning with prismatic and euhedral crystal forms 280–350 μm in length (Figure 14a). The sample's weighted mean $^{206}\text{Pb}/^{238}\text{U}$ crystallization age is **67.0 \pm 2.7 Ma** ($n = 14/19$, MSWD = 1.5, 2σ ; Figure 14b). Single-crystal incremental heating analyses of biotite yielded a cooling age of age **63.29 \pm 0.24 Ma** (2σ , MSWD = 0.6; Figure 15a) while single-crystal total fusion analyses of sanidine yielded a cooling age of **63.10 \pm 0.06 Ma** (2σ , MSWD = 1.3; Figure 15b). Sanidine ages ranged from 64 to 55 Ma, but the probability density peak (Figure 15b) spiked strongly at ca. 63 Ma, concordant with step-heating data. The sample's age suggests this rock is associated with Laramide-aged, felsic volcanics thought to underlie much of the SMO (McDowell et al., 2001; Aguirre-Díaz and McDowell, 1991).

3.1.2 SMO13_04 — ‘Cerro El Ahorado tuff’ — rhyodacitic lapilli tuff — (26°03'48.8"N, 106°55'37.5"W)

Sample SMO13_04 (Figure 6) is a plagioclase-sanidine-rich, rhyodacite lapilli-tuff, with abundant lithics and few fiamme. It forms the topographic top of a composite stratigraphic section east of Guadalupe y Calvo, and conformably overlies non-dated rhyolite lava SMO13_03. Zircons exhibited vague or absent zonation and occasional bright outer rims with stubby crystal forms 250–380 μm in length (Figure 16a). The sample's weighted mean $^{206}\text{Pb}/^{238}\text{U}$ crystallization age is **29.5 \pm 1.3 Ma** ($n = 16/18$, MSWD = 1.1, 2σ ; Figure 16b).

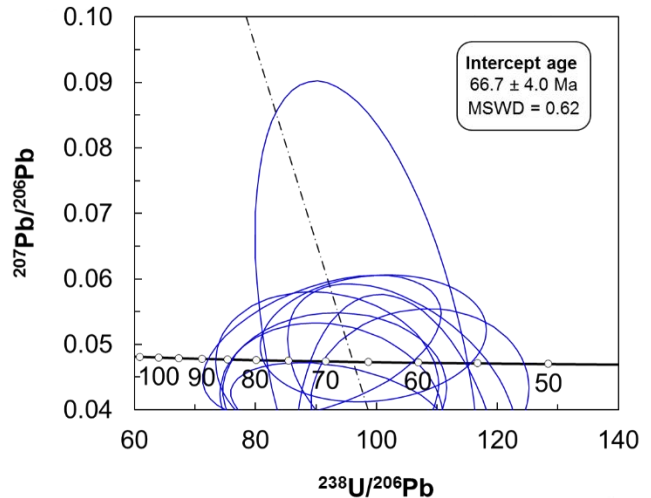
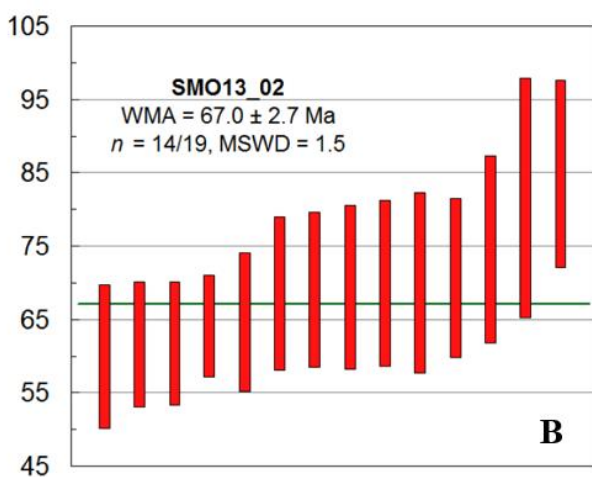
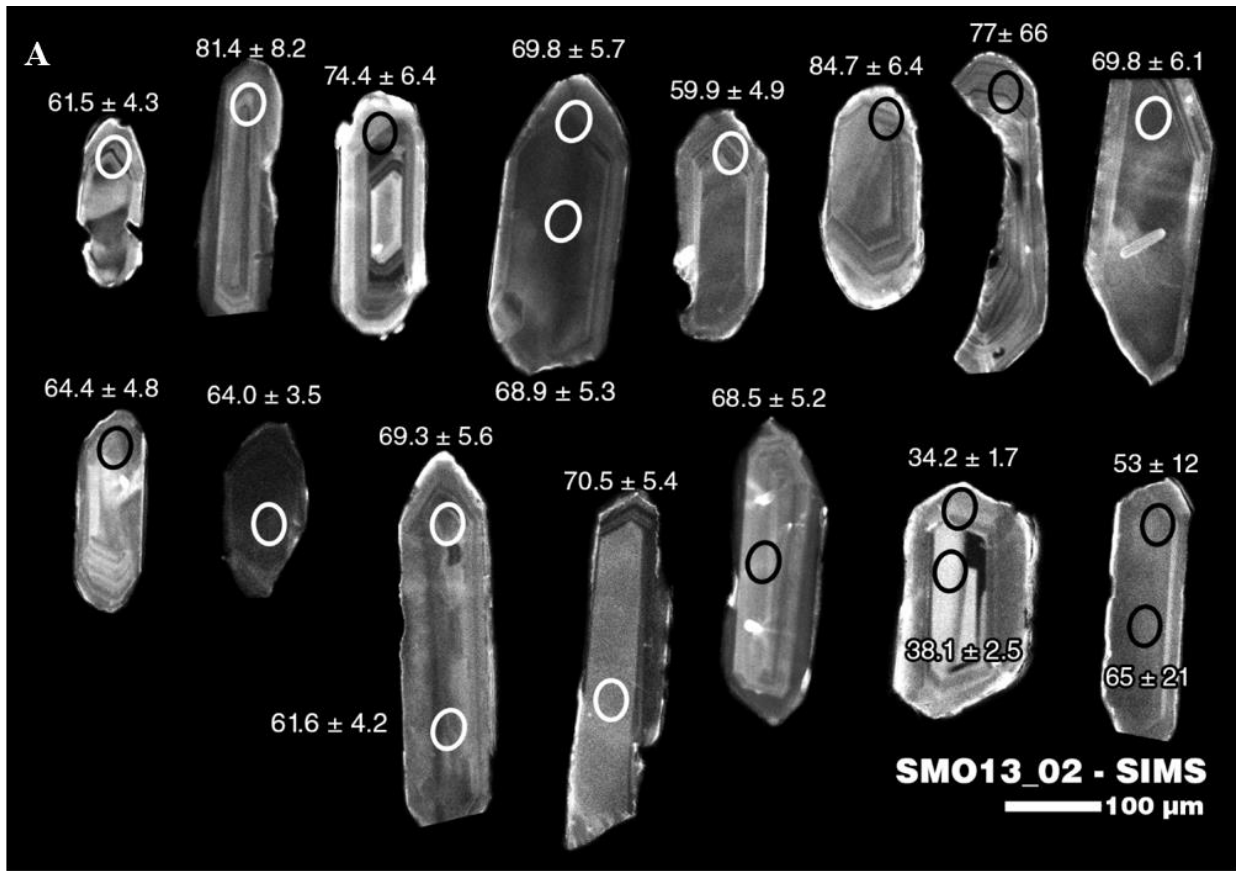


Figure 14. Sample SMO13_02. **A)** Zircons exhibited clear oscillatory zoning with prismatic and euhedral crystal forms 280-350 μm in length. SIMS U-Pb dates ($\pm 1\sigma$) for individual sample spots are listed next to each grain. **B)** The sample's weighted mean $^{206}\text{Pb}/^{238}\text{U}$ crystallization age is 67.0 ± 2.7 Ma ($n = 14/19$, MSWD = 1.5, 2σ). Bar heights at 2σ . **C)** Tera-Wasserburg diagram for sample SMO13_02. Error ellipses are at 2σ .

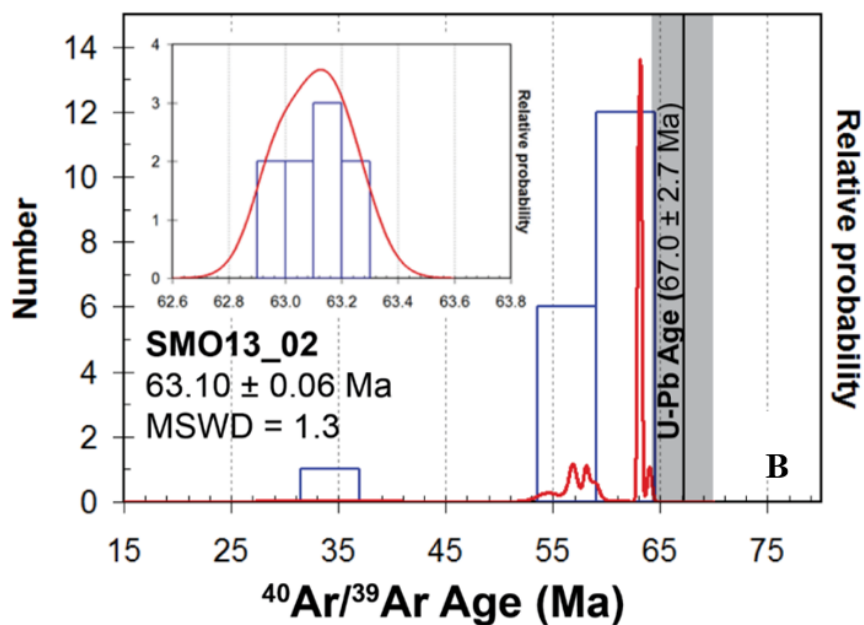
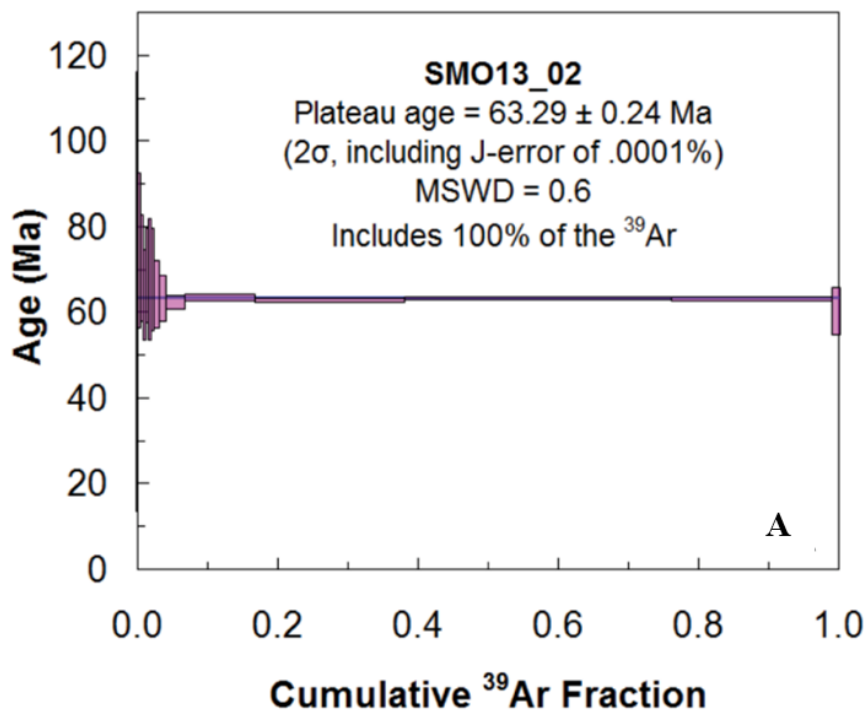


Figure 15. $^{40}\text{Ar}/^{39}\text{Ar}$ data for sample SMO13_02. **A)** Step-heating age spectra of biotite. Box heights are 2σ . **B)** Probability density function illustrating the age spectra for the single-crystal total fusion analyses of sanidine. The sanidine age spectrum ranged to as low as 55 Ma, but the curve suggests a much stronger peak at ~63. The inset shows a zoomed in version of the curve.

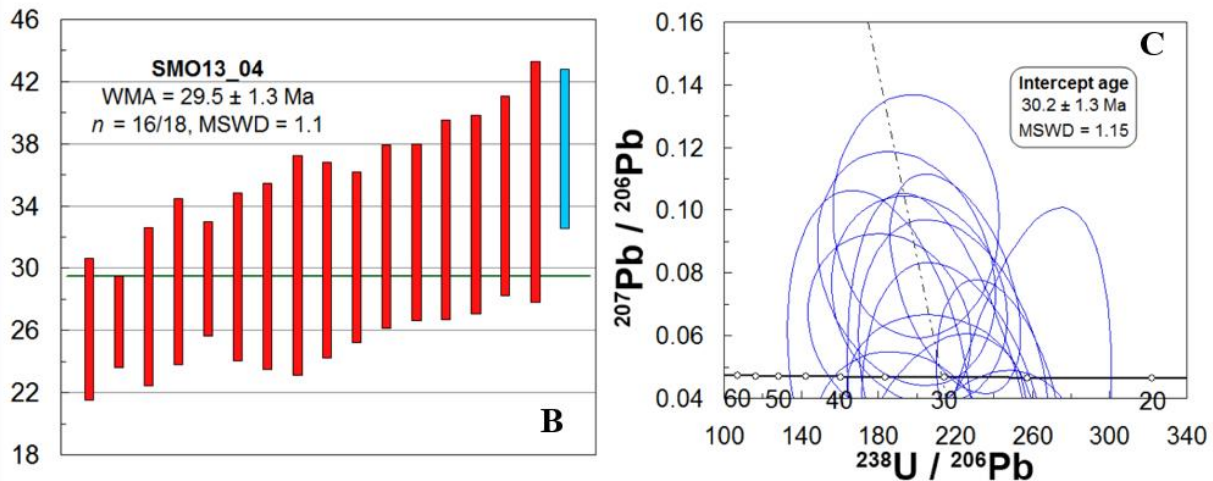


Figure 16. Sample SMO13_04. **A)** Zircons exhibited vague or absent zonation and occasional bright outer rims with stubby crystal forms 250-380 μm in length. SIMS U-Pb dates ($\pm 1\sigma$) for individual sample spots are listed next to each grain. **B)** The sample's weighted mean $^{206}\text{Pb}/^{238}\text{U}$ crystallization age is **29.5 ± 1.3 Ma** ($n = 16/18$, MSWD = 1.1, 2σ). Bar heights at 2σ . One old outlier (blue box) was automatically dropped from calculations by Isoplot. **C)** Tera-Wasserburg diagram for sample SMO13_04. Error ellipses are at 2σ .

3.1.3 SMO13_08 — *unnamed crystal and lithics-poor, non-welded tuff* — (26°04'57.9"N, 106°45'32.4"W)

Sample SMO13_08 (Figure 6) is a distinctively white crystal and lithic-poor, non-welded tuff. It forms the topographic top of a composite stratigraphic section west of the Rio Turuachi valley; its base is not seen. Zircons were faintly zoned with subhedral to anhedral crystal forms that were stubby to round (Figure 17a). The selected zircon population was bimodal in size and exhibited lengths between 50 and 300 μm . The sample's weighted mean $^{206}\text{Pb}/^{238}\text{U}$ crystallization age is **32.2 \pm 1.2 Ma** ($n = 10/18$, MSWD = 1.8, 2 σ ; Figure 17b). Sample SMO13_08 had numerous weighted mean exclusions due to high individual errors, lead loss, and xenocrystic behavior (Figure 17c). I interpret the oldest grain ($^{207}\text{Pb}/^{206}\text{Pb}$ age = 1560 \pm 42 Ma, 1 σ) to be a xenocryst of old North American Proterozoic basement thought to underlie significant portions of the SMO (e.g., Ferrari et al., 2007).

3.1.4 SMO13_12 — *'Turuachi tuff'* — *crystal and lithic-rich welded ignimbrite* — (26°07'49.4"N, 106°43'18.5"W)

Sample SMO13_12 (Figure 6) is a fiamme and crystal and lithic-rich, welded, rhyolitic ignimbrite. It forms the base of a composite stratigraphic section west of the Rio Turuachi valley; its base is not seen and it is conformably overlain by non-dated ignimbrite SMO13_11. Zircons were stubby or football-shaped and about 125 to 325 μm in length. Several of the crystals had distinct 'gash marks' and vague to patchy core-rim distinction (Figure 18a). The sample exhibited the highest average percent-error of the transect (~9%). All seven zircons excluded possessed errors larger than ~12%, more than one standard deviation above the mean error. The sample's final weighted mean crystallization $^{206}\text{Pb}/^{238}\text{U}$ age is **34.8 \pm 1.9 Ma** ($n = 10/17$, MSWD = 1.3, 2 σ ; Figure 18b).

3.1.5 SMO13_13 — *unnamed plagioclase-rich, welded ignimbrite* — (26°07'54.4"N, 106°41'11.3"W)

Sample SMO13_13 (Figure 6) is plagioclase-rich, quartz-poor, welded ignimbrite. It forms the base of a composite stratigraphic section east of the Rio Turuachi valley; its base is not seen and it is conformably overlain by non-dated ignimbrite SMO13_14 (Figure 7). Zircons were subhedral to anhedral and clearly zoned (sector and oscillatory) with both football-shaped and elongate crystals between 100 and 300 μm in length (Figure 19a). The sample's weighted mean

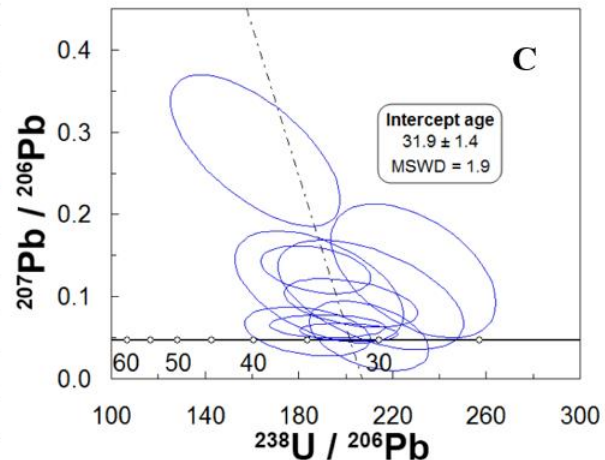
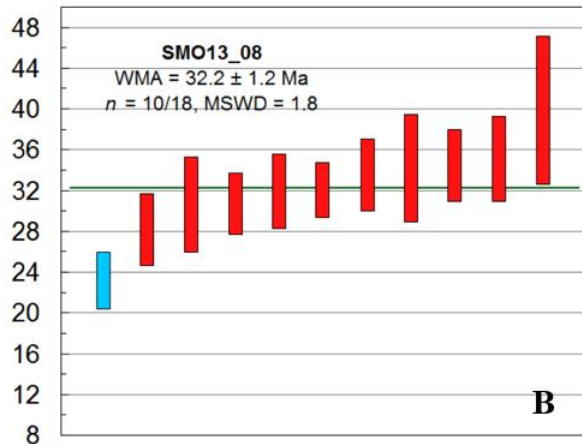
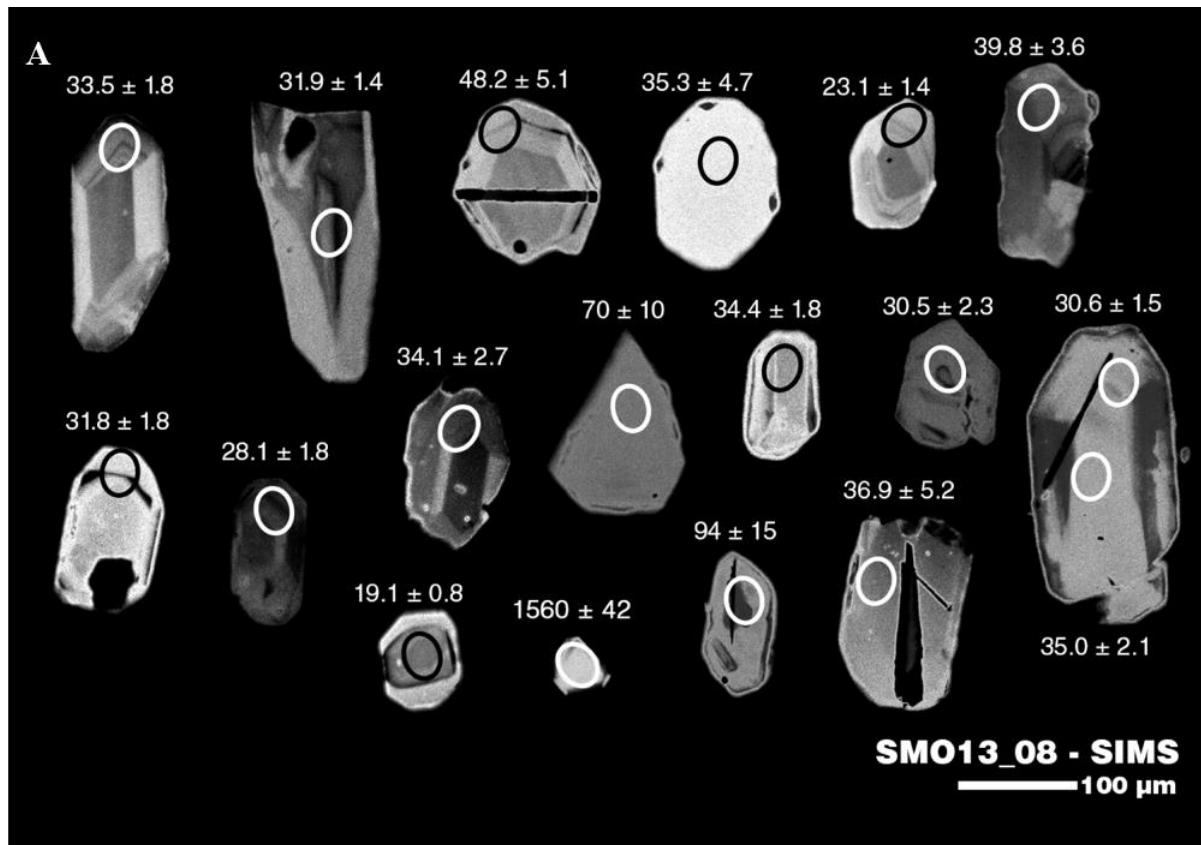


Figure 17. Sample SMO13_08. **A)** Zircons were only vaguely zoned with subhedral to anhedral crystal forms that were stubby to round. The selected zircon population was bimodal in size and exhibited lengths between 50 and 300 μm. SIMS U-Pb dates ($\pm 1\sigma$) for individual sample spots are listed next to each grain. **B)** The sample's weighted mean $^{206}\text{Pb}/^{238}\text{U}$ crystallization age is **32.2 ± 1.2 Ma** ($n = 10/18$, MSWD = 1.8, 2σ). Bar heights at 2σ . One young outlier (blue box) was automatically dropped from calculations by Isoplot. **C)** Tera-Wasserburg diagram for sample SMO13_08. Error ellipses are at 2σ .

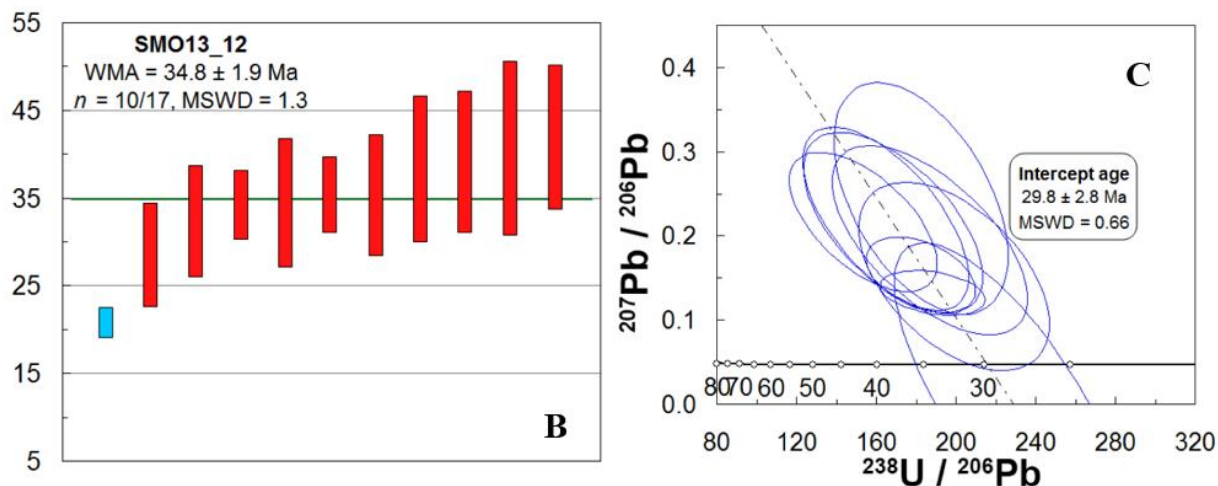
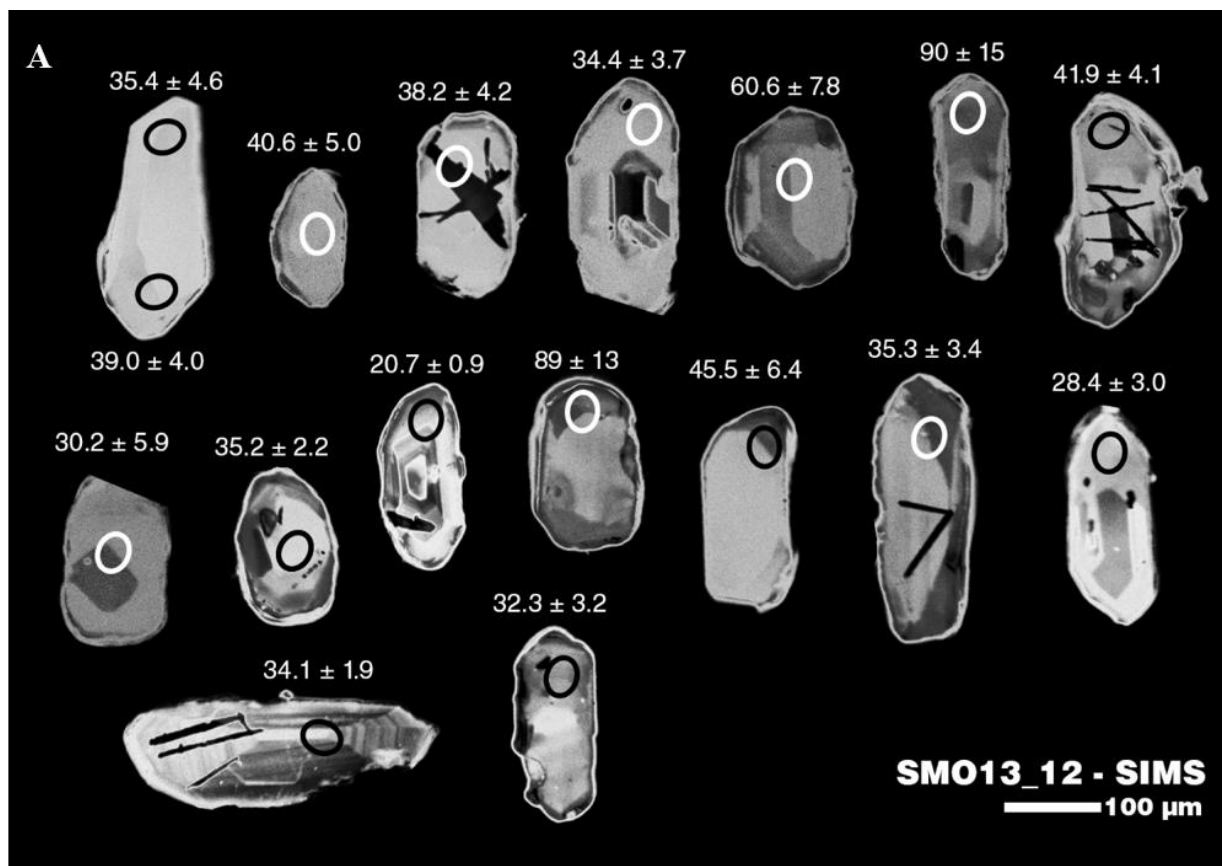


Figure 18. Sample SMO13_12. **A)** Zircons were stubby or football-shaped and about 125 to 325 μm in length. Several of the crystals had distinct ‘gash marks’ and vague to patchy core-rim distinction. SIMS U-Pb dates ($\pm 1\sigma$) for individual sample spots are listed next to each grain. **B)** The sample’s final weighted mean crystallization $^{206}\text{Pb}/^{238}\text{U}$ age is **34.8 ± 1.9 Ma** (n = 10/17, MSWD = 1.3, 2σ). Bar heights at 2σ . One young outlier (blue box) was automatically dropped by Isoplot. **C)** Tera-Wasserburg concordia diagram for sample SMO13_12. Error ellipses are at 2σ .

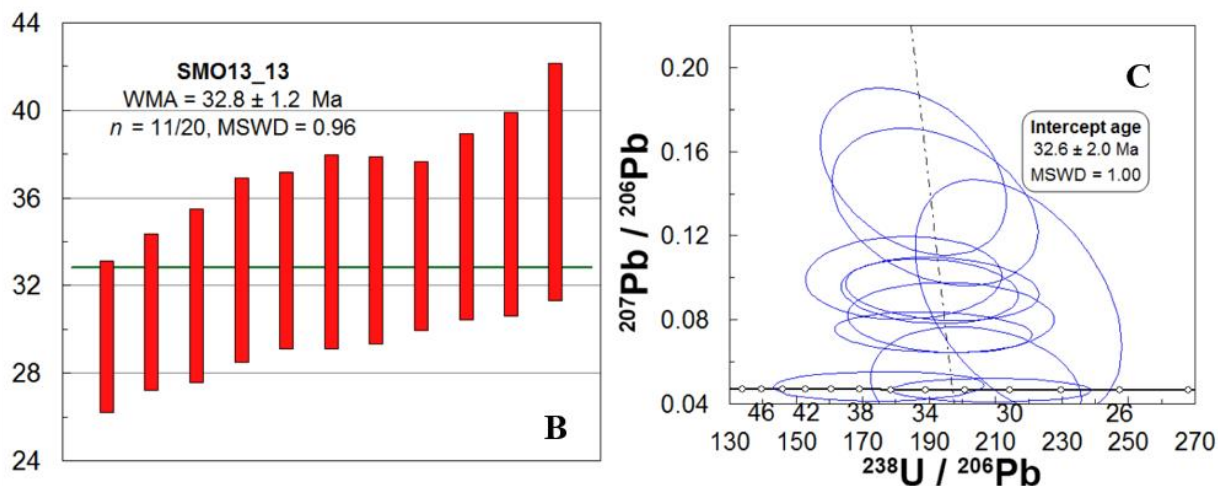
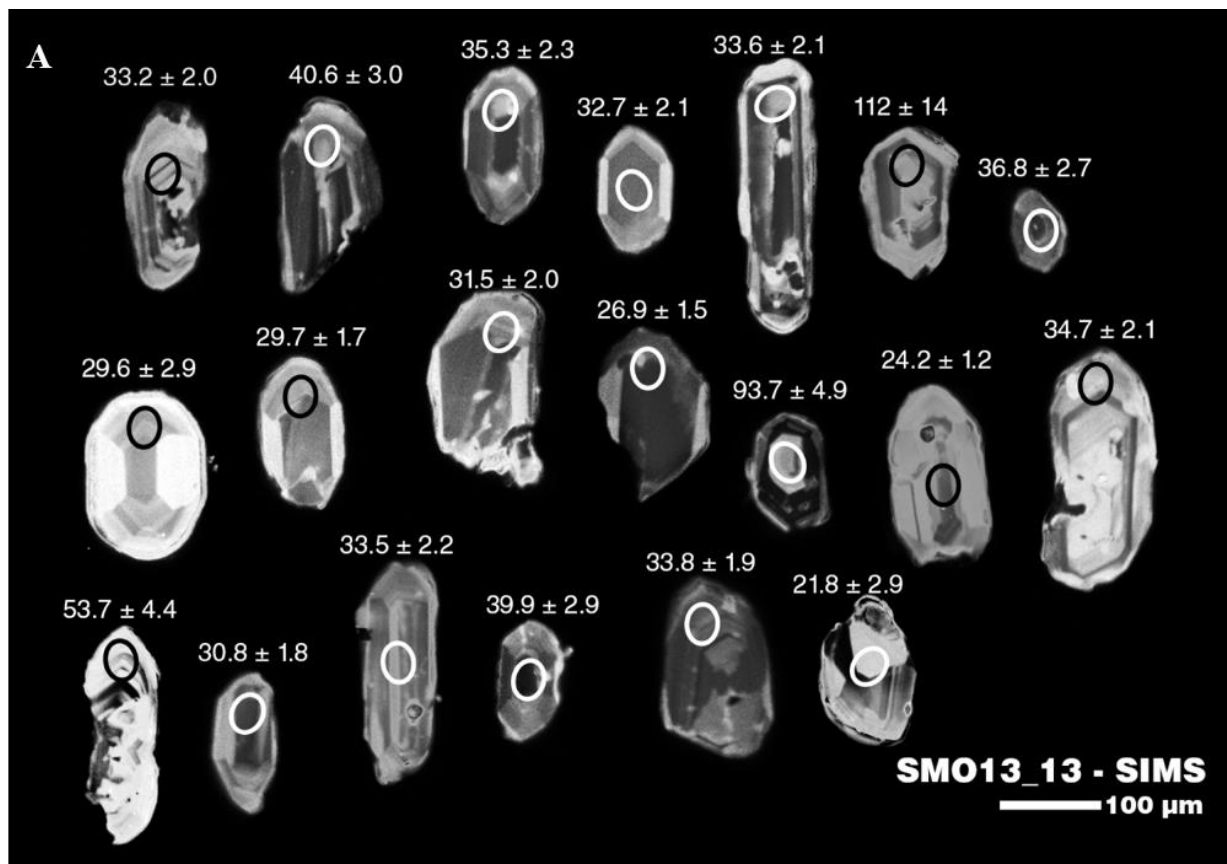


Figure 19. Sample SMO13_13. **A)** Zircons were subhedral to anhedral and clearly zoned (sector and oscillatory) with both football-shaped and elongate crystals between 100 and 300 μm in length. SIMS U-Pb dates ($\pm 1\sigma$) for individual sample spots are listed next to each grain. **B)** The sample's weighted mean $^{206}\text{Pb}/^{238}\text{U}$ crystallization age is **32.8 ± 1.2 Ma** ($n = 11/20$, MSWD = 1.0, 2σ). Bar heights at 2σ . **C)** Tera-Wasserburg concordia diagram for sample SMO13_13. Error ellipses are at 2σ .

$^{206}\text{Pb}/^{238}\text{U}$ crystallization age is **32.8 ± 1.2 Ma** ($n = 11/20$, MSWD = 1.0, 2σ ; Figure 19b). Three grains with errors ~10% or greater were excluded from the mean. Four suspected antecrysts (39.9, 40.6, 93.7, and 53.7 Ma) were excluded also. Two grains younger than 30 Ma (24.2 and 26.9 Ma) were excluded to ensure the remaining crystals satisfactorily represented a single age population.

3.1.6 SMO13_16 — unnamed biotite-rich welded lapilli-tuff — (26°08'05.9"N, 106°40'03.8"W)

Sample SMO13_16 (Figure 6) is a pumice and lithic-rich, welded ignimbrite with abundant biotite and little plagioclase. It forms the topographic top of a composite stratigraphic section east of the Rio Turuachi valley; it conformably overlies the non-dated ignimbrite SMO13_15 (Figure 7). Zircons are euhedral to subhedral and sector zoned. A significant portion of the zircons are stubby and rounded while another significant portion of the zircons are elongate and thin, ranging in length from 100-250 μm (Figure 20a). The sample's weighted mean $^{206}\text{Pb}/^{238}\text{U}$ crystallization age is **30.3 ± 1.2 Ma** ($n = 12/20$, MSWD = 1.6, 2σ ; Figure 20b). The oldest excluded grains are Jurassic (157 and 176 Ma) and are interpreted to be xenocrystic inheritance from underlying basement terranes (Centeno-García et al., 2008; 2011). Four additional grains with errors greater than 10% were excluded from the weighted mean age calculation. In addition, three suspected antecrysts (36.7, 42.5, and 44.8 Ma) and two anomalously young zircons were excluded from the weighted mean calculations.

3.1.7 SMO13_19 — unnamed biotite-phyric, non-welded tuff — (26°16'45.3"N, 106°29'52.1"W)

Sample SMO13_19 (Figure 6) is a biotite-phyric non-welded tuff. It forms the topographic top of a simple stratigraphic section either side of the Rio Verde gorge; it conformably overlies the non-dated ignimbrite SMO13_20. Zircons are anhedral to subhedral, stubby and elongate crystals measuring 125-325 μm and show core-rim and sector and oscillatory zoning (Figure 21a). The sample's weighted mean $^{206}\text{Pb}/^{238}\text{U}$ crystallization age is **33.6 ± 1.5 Ma** ($n = 12/19$, MSWD = 1.1, 2σ ; Figure 21b). Several (~36%) of the crystals are suspected to be inherited (58.9, 63.6, 87.3, 98.3, 99.2, 150, and 371 Ma). The Late Devonian grain (371 Ma) is interpreted to be xenocrystic inheritance from underlying basement terranes (Centeno-García et al., 2008). The Cretaceous grains are interpreted as Laramide-aged, felsic volcanics thought to underlie much of the SMO (McDowell et al., 2001; Aguirre-Díaz and McDowell, 1991). Three additional exclusions were made due to high error.

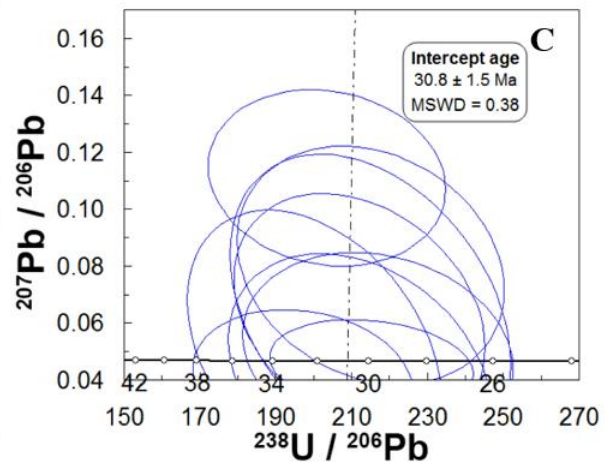
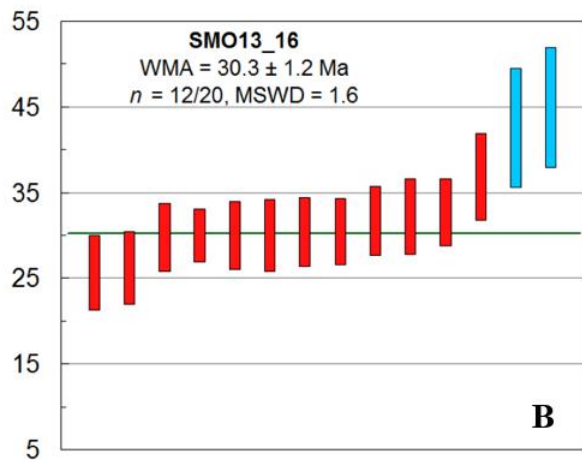
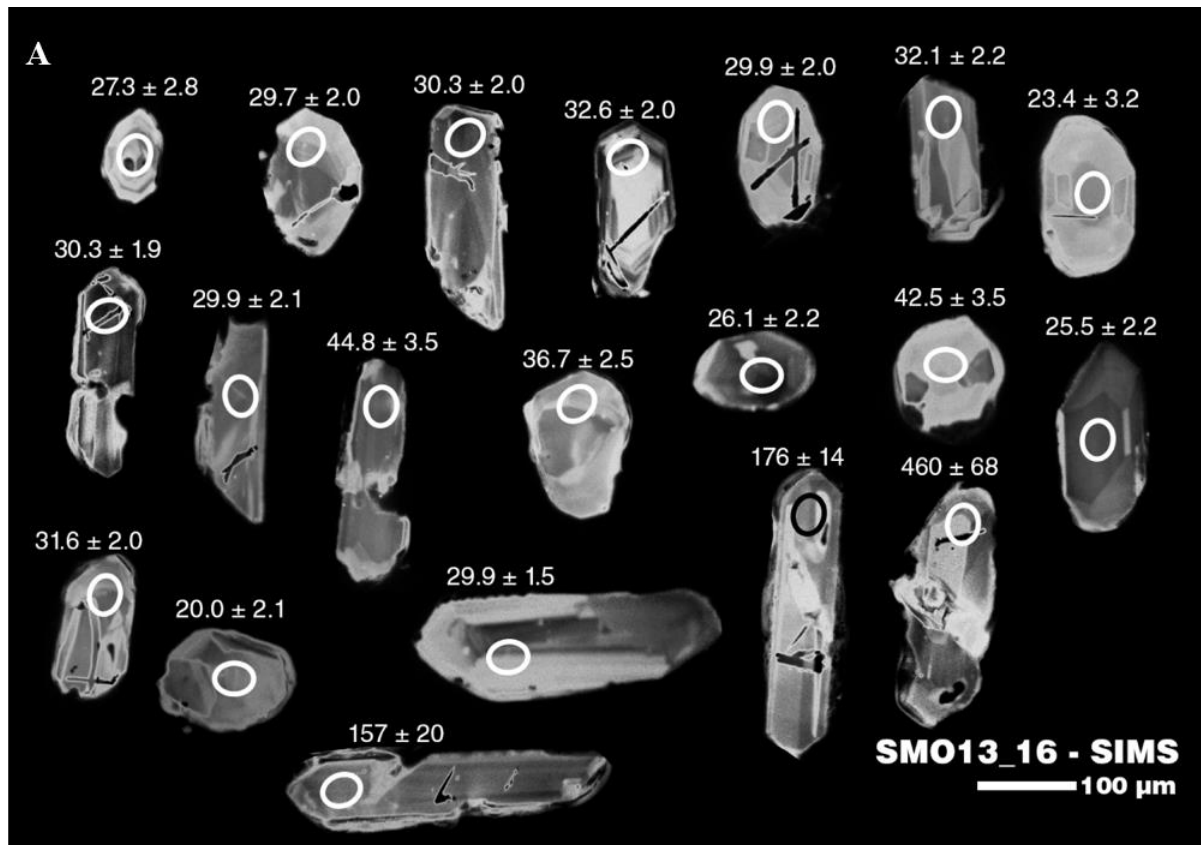


Figure 20. Sample SMO13_16. A) Zircons are euhedral to subhedral and sector zoned. A significant portion of the zircons are stubby and rounded while another significant portion of the zircons are elongate and thin, ranging in length from 100-250 μm. SIMS U-Pb dates ($\pm 1\sigma$) for individual sample spots are listed next to each grain. B) The sample's weighted mean $^{206}\text{Pb}/^{238}\text{U}$ crystallization age is 30.3 ± 1.2 Ma ($n = 12/20$, $\text{MSWD} = 1.6$, 2σ). Bar heights at 2σ . Two older analyses (blue bars) were dropped from calculations by Isoplot. C) Tera-Wasserburg concordia diagram for sample SMO13_16. Error ellipses are at 2σ .

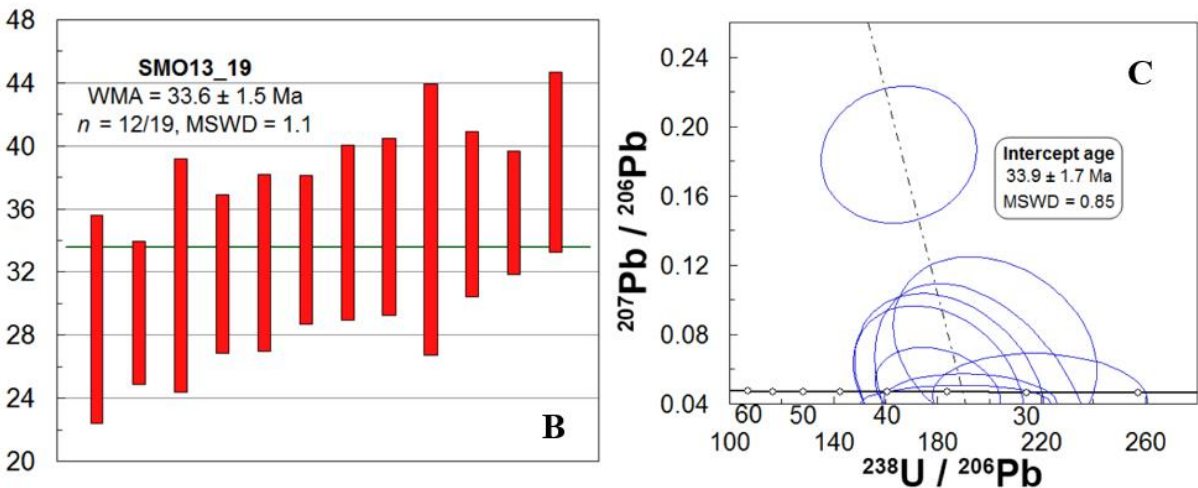
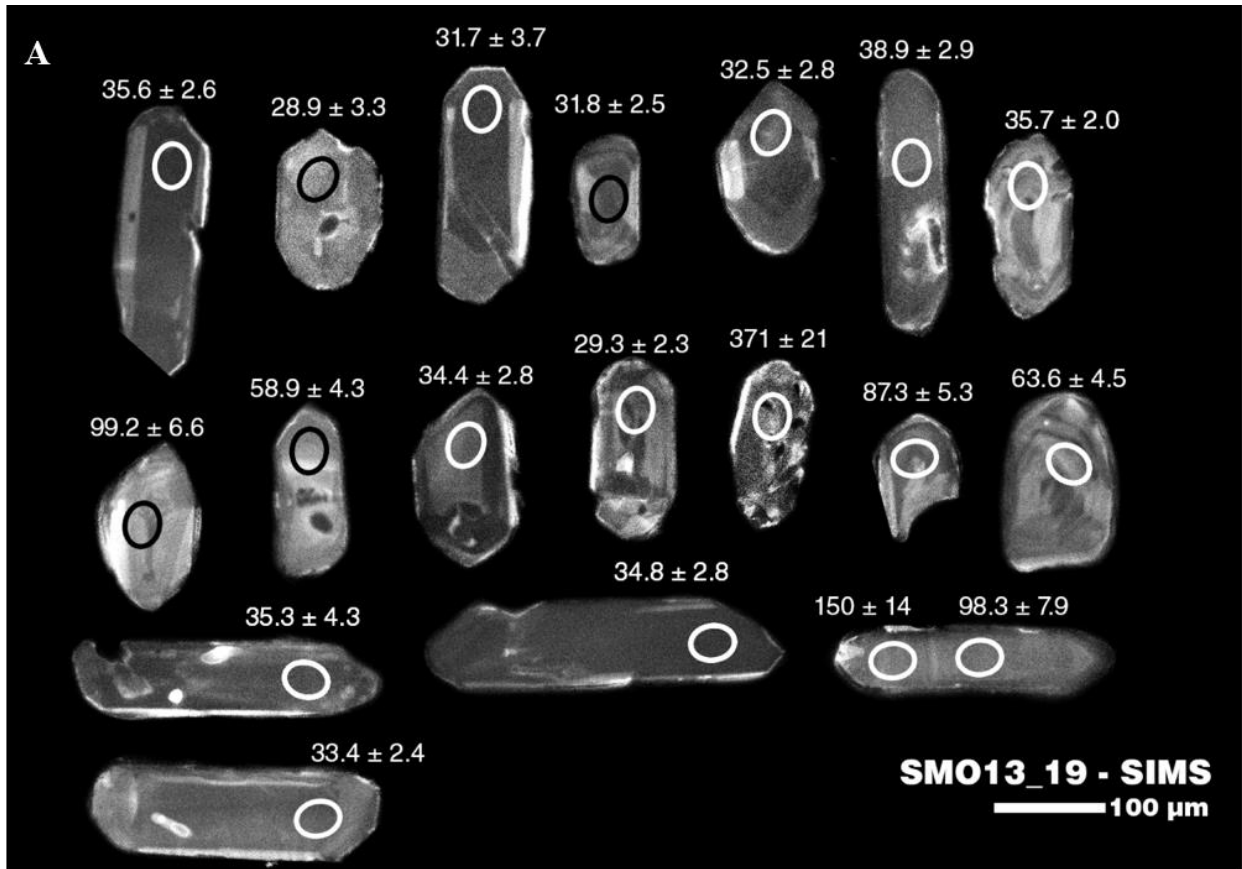


Figure 21. Sample SMO13_19. **A)** Zircons are anhedral to subhedral, stubby and elongate crystals measuring 125-325 μm and show core-rim and sector and oscillatory zoning. SIMS U-Pb dates ($\pm 1\sigma$) for individual sample spots are listed next to each grain. **B)** The sample's weighted mean $^{206}\text{Pb}/^{238}\text{U}$ crystallization age is 33.6 ± 1.5 Ma ($n = 12/19$, MSWD = 1.1, 2σ). Bar heights at 2σ . **C)** Tera-Wasserburg concordia diagram for sample SMO13_19. Error ellipses are at 2σ .

3.1.8 SMO13_22 — *'Rio Verde Tuff' — rhyodacite lapilli tuff — (26°17'02.1"N, 106°29'10.4"W)*

Sample SMO13_22 (Figure 6) is a plagioclase-rich rhyodacite with abundant large fiamme and oxidized biotite. It forms the base of a simple stratigraphic section either side of the Rio Verde gorge; its base is not seen and it is conformably overlain by the non-dated ignimbrite SMO13_21. Zircons are subhedral to anhedral, have oscillatory zoning with generally stubby forms, and range in length from 150 to 200 μm . The sample exhibited unusual dark and light patterns under cathodoluminescence, with several crystals rendering almost invisible (Figure 22a). The sample's weighted mean $^{206}\text{Pb}/^{238}\text{U}$ crystallization age is **36.7 \pm 1.4 Ma** ($n = 9/14$, MSWD = 1.3, 2σ ; Figure 22b). Three crystals are suspected to be inherited (46.2, 46.4, and 47.4 Ma) while three younger crystals were also excluded from the mean because the probability density plot (Figure 23) indicated a strong peak at ~ 36 Ma. Single-crystal total fusion analyses of sanidine yielded a cooling age of **32.09 \pm 0.31 Ma** (MSWD = 3.3, 2σ ; Figure 24).

3.1.9 SMO13_28 — *unnamed lithic-rich, welded lapilli tuff — (26°34'02.8"N, 106°17'43.5"W)*

Sample SMO13_28 (Figure 6) is a strongly devitrified, lithic-rich, welded lapilli-tuff. It forms the topographic cap of an extensive plateau between the town of El Vergel and the Rio Balleza graben. It conformably overlies a pair of older ignimbrites (in stratigraphic order, SMO13_30 and SMO13_29), and it is unconformably overlain by a basaltic andesite lava (SMO13_27). Zircons (length 200-350 μm) are elongate and euhedral to subhedral with oscillatory zoning, and clear to patchy core-rim distinctions (Figure 25a). The sample's weighted mean $^{206}\text{Pb}/^{238}\text{U}$ crystallization age is **32.7 \pm 1.3 Ma** ($n = 8/17$, MSWD = 2.0, 2σ ; Figure 25b). One grain was excluded due to high error. Six grains are suspected to be inherited (50-39 Ma). Two young grains were excluded so that the remaining analyses represented a single age population.

3.1.10 SMO13_33 — *unnamed quartz and biotite-rich tuff — (26°36'58.3"N 106°16'17.0"W)*

Sample SMO13_33 (Figure 6) is a quartz and biotite-rich tuff with abundant plagioclase-phyric lapilli. It forms the base of a composite stratigraphic section west of the Rio Balleza graben; its base is not seen and it is conformably overlain by non-dated ignimbrite SMO13_32. Zircons (150-350 μm in length) are euhedral and generally prismatic with vague or patchy core-rim distinctions as well as occasional oscillatory zoning (Figure 26a). The sample's weighted mean $^{206}\text{Pb}/^{238}\text{U}$ crystallization age is **38.5 \pm 1.5 Ma** ($n = 15/15$, MSWD = 0.7, 2σ ; Figure 26b).

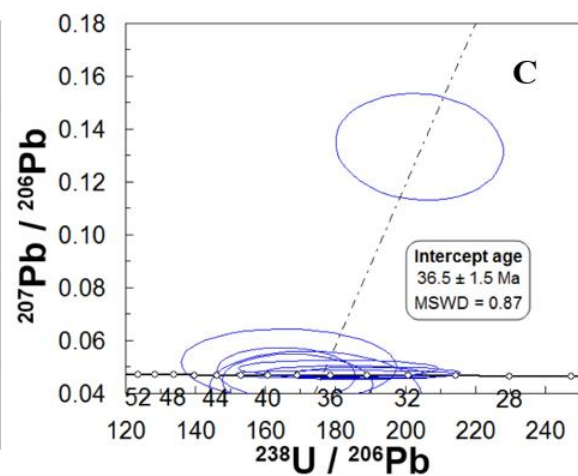
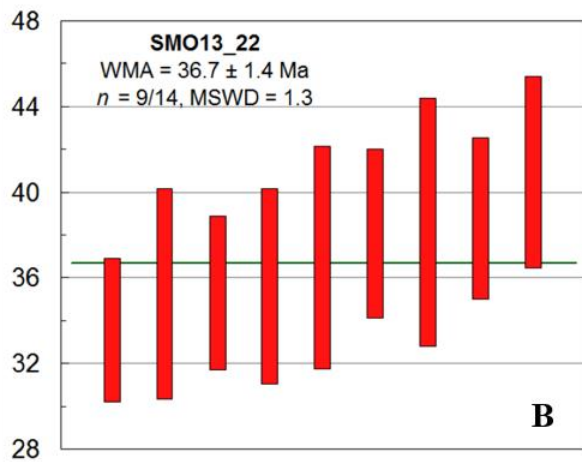
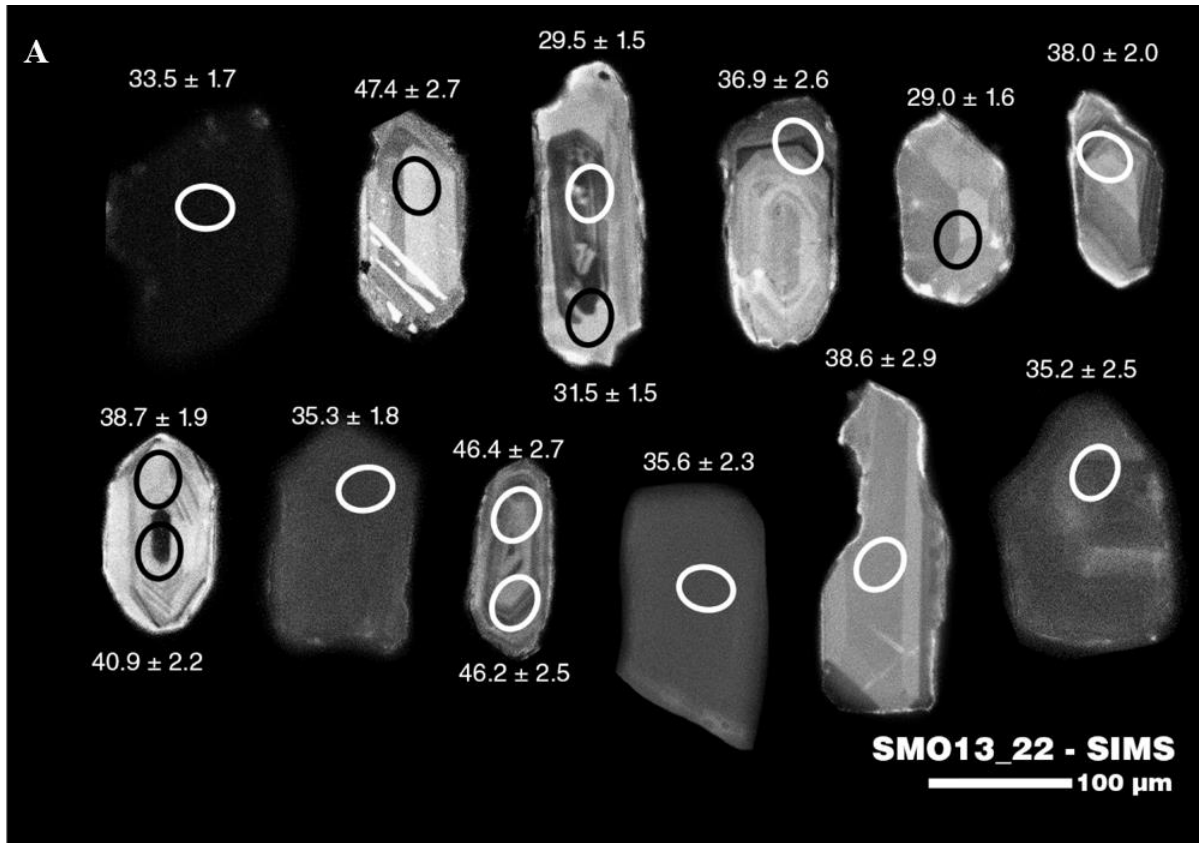


Figure 22. Sample SMO13_22. **A)** Zircons are subhedral to anhedral, have oscillatory zoning with generally stubby forms, and range in length from 150 to 200 μm . The sample exhibited unusual dark and light patterns under cathodoluminescence, with several crystals rendering almost invisible (e.g. top left of image). SIMS U-Pb dates ($\pm 1\sigma$) for individual sample spots are listed next to each grain. **B)** The sample's weighted mean $^{206}\text{Pb}/^{238}\text{U}$ crystallization age is **36.7 ± 1.4 Ma** ($n = 9/14$, MSWD = 1.3, 2σ). Bar heights at 2σ . **C)** Tera-Wasserburg concordia diagram for sample SMO13_22. Error ellipses are at 2σ .

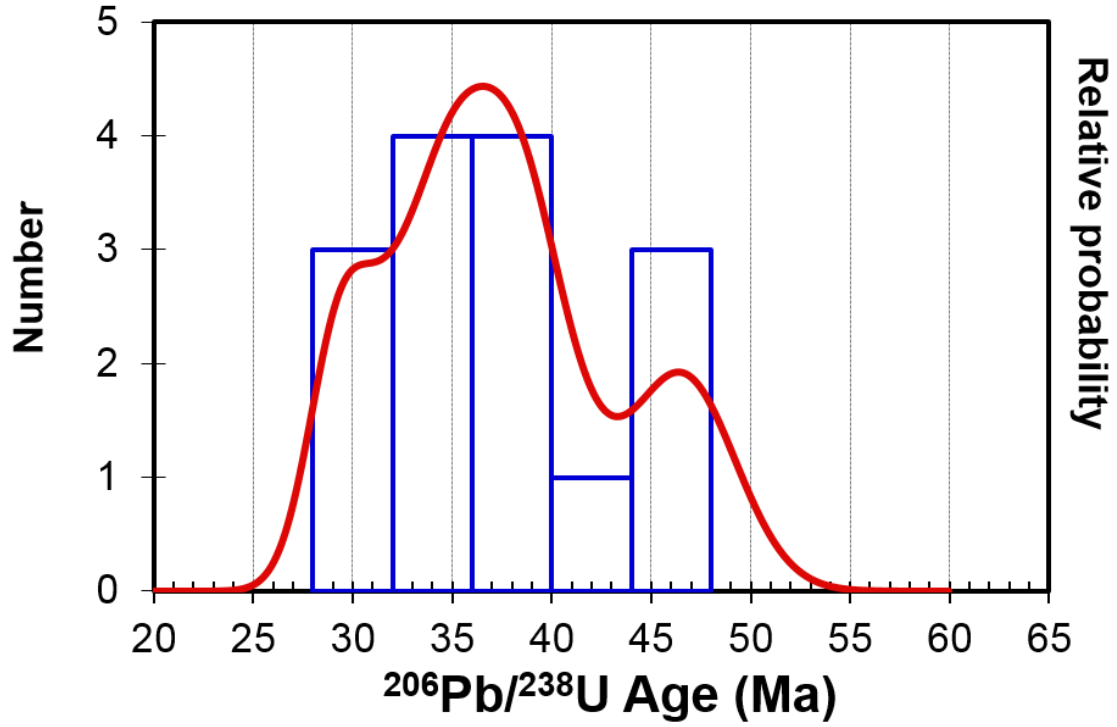


Figure 23. U-Pb probability density plot for SMO13_22. A strong peak at ~36 Ma suggests the sample may be this age, but the skewed right side indicates older, inherited grains are also in the sample.

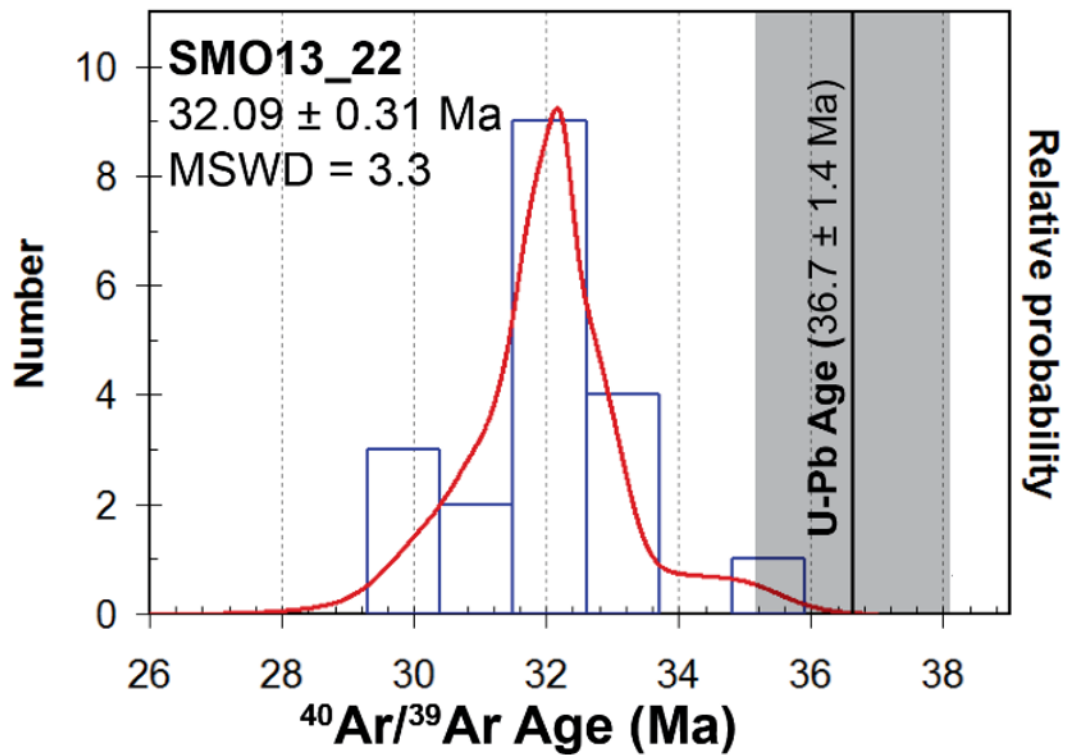


Figure 24. Probability density function for sample SMO13_22 illustrating the age spectra for the single-crystal total fusion analyses of sanidine. The corresponding U-Pb zircon age and associated error (shaded box) have been plotted as well.

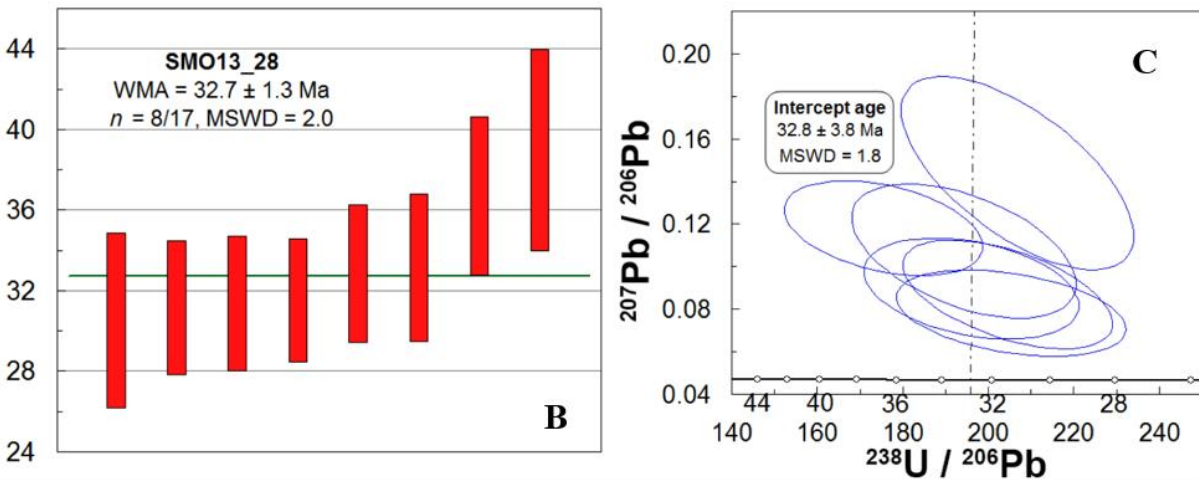


Figure 25. Sample SMO13_28. **A)** Zircons (length 200-350 μm) are elongate and euhedral to subhedral with oscillatory zoning, and clear to patchy core-rim distinctions. SIMS U-Pb dates ($\pm 1\sigma$) for individual sample spots are listed next to each grain. **B)** The sample's weighted mean $^{206}\text{Pb}/^{238}\text{U}$ crystallization age is 32.7 ± 1.3 Ma ($n = 8/17$, MSWD = 2.0, 2σ). Bar heights at 2σ . **C)** Tera-Wasserburg concordia diagram for sample SMO13_28. Error ellipses are at 2σ .

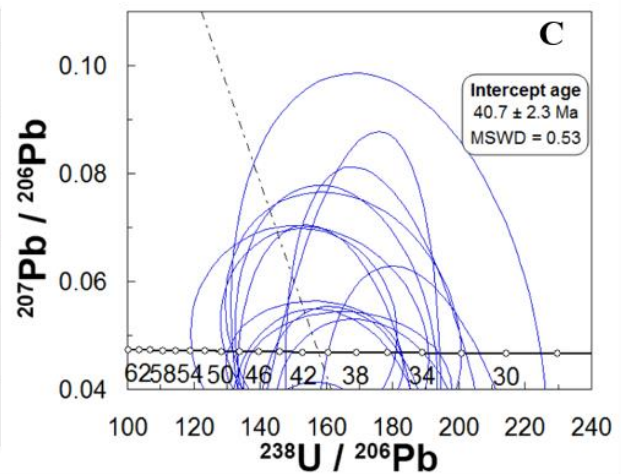
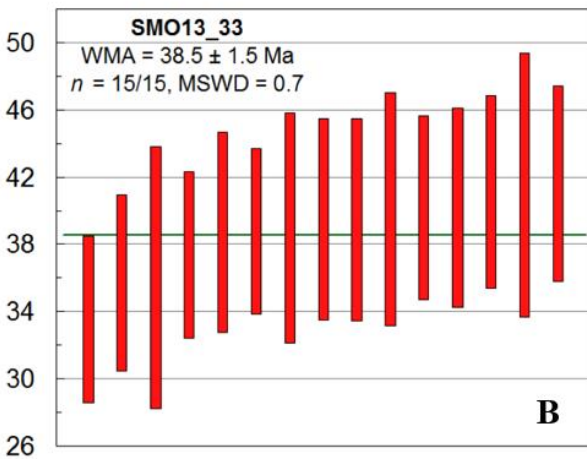
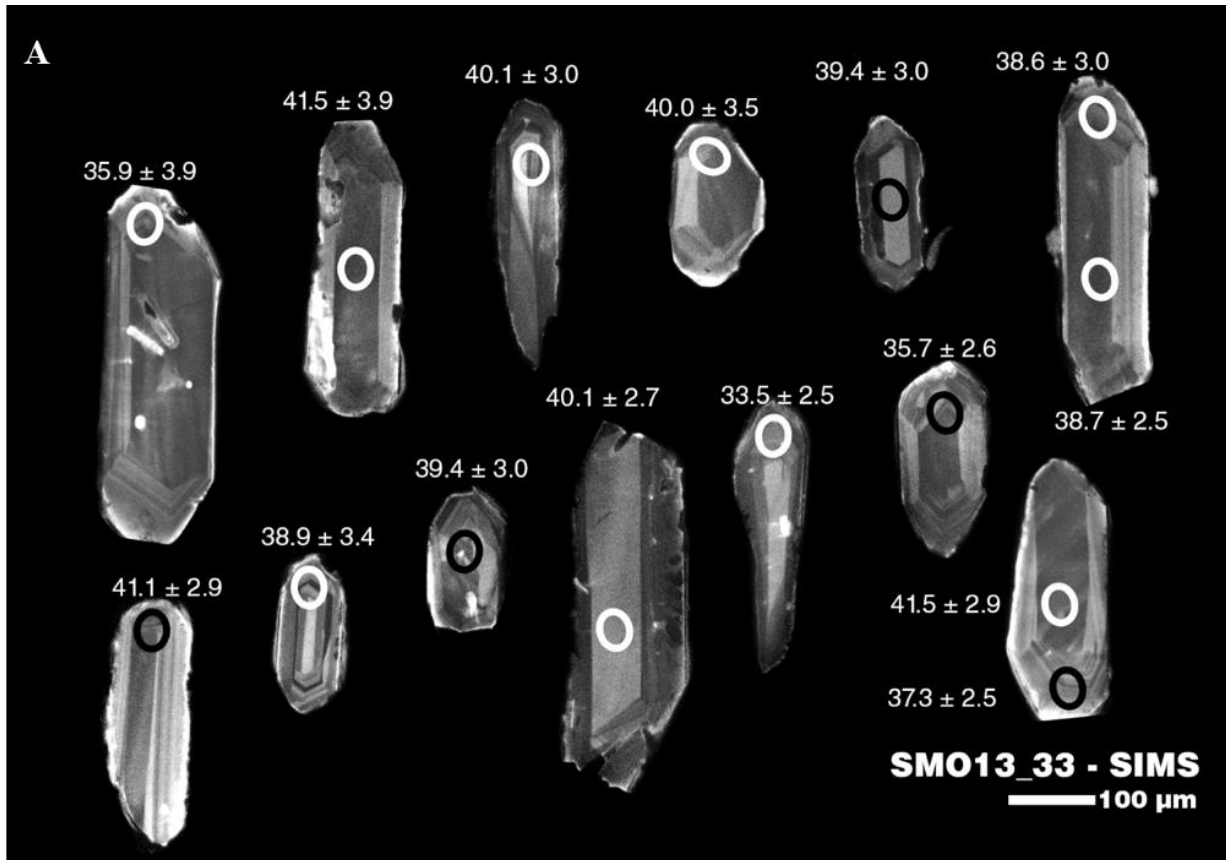


Figure 26. Sample SMO13_33. **A)** Zircons (150-350 μm in length) are euhedral and generally prismatic with vague or patchy core-rim distinctions as well as occasional oscillatory zoning. SIMS U-Pb dates ($\pm 1\sigma$) for individual sample spots are listed next to each grain. **B)** The sample's weighted mean $^{206}\text{Pb}/^{238}\text{U}$ crystallization age is 38.5 ± 1.5 Ma ($n = 15/15$, MSWD = 0.7, 2σ). Bar heights at 2σ . **C)** Tera-Wasserburg concordia diagram for sample SMO13_33. Error ellipses are at 2σ .

3.1.11 SMO13_35 — *unnamed plagioclase-phyric, flow-banded, dacite lava* — (26°39'12.0"N 106°13'44.0"W)

Sample SMO13_35 (Figure 6) is a strongly devitrified, plagioclase-phyric, flow-banded, dacite lava. It is located within the Rio Balleza graben and is conformably overlain by fluvial gravels capped by basaltic andesite lava (SMO13_34); its base is not seen. Zircons (125-300 μm in length) are subhedral to anhedral with stubby elongate crystals (aspect ratio ~ 2.5) and patchy core-rim zonation (Figure 27a). The sample's weighted mean $^{206}\text{Pb}/^{238}\text{U}$ crystallization age is **32.8 \pm 1.2 Ma** ($n = 15/16$, MSWD = 0.30, 2σ ; Figure 27b). Single-crystal total fusion analyses of sanidine yielded a cooling age of **31.63 \pm 0.03 Ma** ($n = 20$, MSWD = 1.6, 2σ ; Figure 28). One suspected xenocryst ($^{207}\text{Pb}/^{206}\text{Pb}$ age = 1057 \pm 20 Ma, 1σ) was excluded and is likely sourced from underlying basement rock (Ferrari et al., 2007).

3.1.12 SMO13_37 — *unnamed weakly welded, quartz-rich tuff* — (26°40'55.4"N, 106°11'58.2"W)

Sample SMO13_37 (Figure 6) is a weakly welded tuff with occasional fiamme and abundant ~ 1 mm quartz and biotite. It is the thickest of two ignimbrites at the top of a composite stratigraphic section east of the Rio Balleza graben in the Sierra Mesa Brincadero; it conformably overlies the non-dated ignimbrite SMO13_40 and is conformably overlain by non-dated ignimbrite SMO13_36. Zircons (125-250 μm in length) are euhedral to anhedral with both stubby and sharp terminations as well as oscillatory and patchy core-rim zoning (Figure 29a). The sample's weighted mean $^{206}\text{Pb}/^{238}\text{U}$ crystallization age is **36.0 \pm 1.9 Ma** ($n = 9/18$, MSWD = 1.9, 2σ ; Figure 29b). Single-crystal total fusion analyses of sanidine yielded a cooling age of **32.00 \pm 0.03 Ma** (MSWD = 1.4; Figure 30). Three $^{206}\text{Pb}/^{238}\text{U}$ dates with errors exceeding 15% were excluded from the weighted mean.

3.1.13 SMO13_42 — *'Navarro tuff'* — *quartz and plagioclase-phyric lapilli-tuff* — (26°41'00.4"N, 106°11'18.4"W)

Sample SMO13_42 (Figure 6) is a welded, quartz and plagioclase-phyric lapilli-tuff with occasional lithic lapilli. It forms the base of a composite stratigraphic section in the eastern flank of the Sierra Mesa Brincadero; its base is not seen and it is conformably overlain by the non-dated ignimbrite SMO13_41. Zircons (100-315 μm in length) are euhedral with an average aspect ratio of ~ 2 and show clear oscillatory zoning and distinct core-rim boundaries (Figure

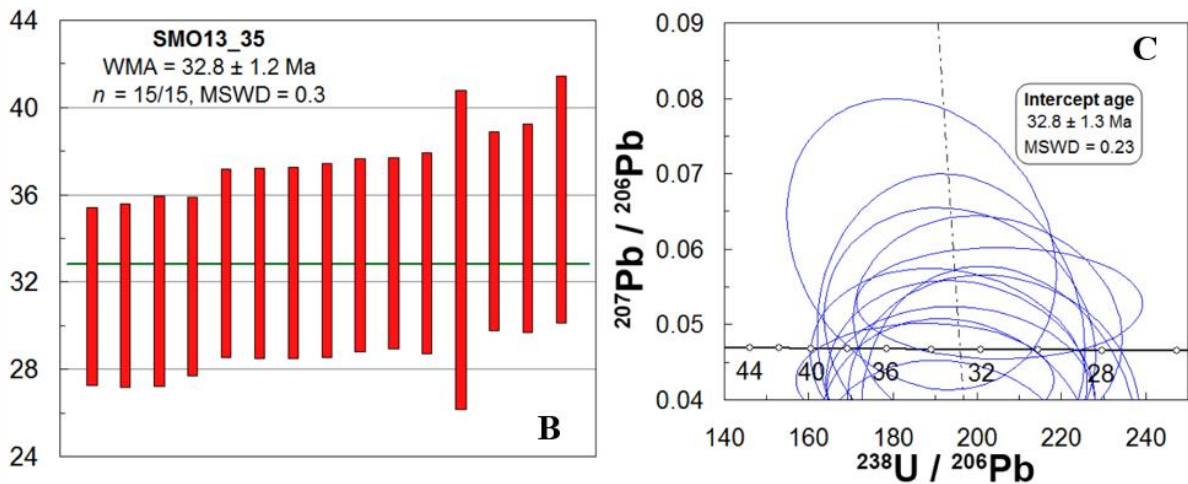
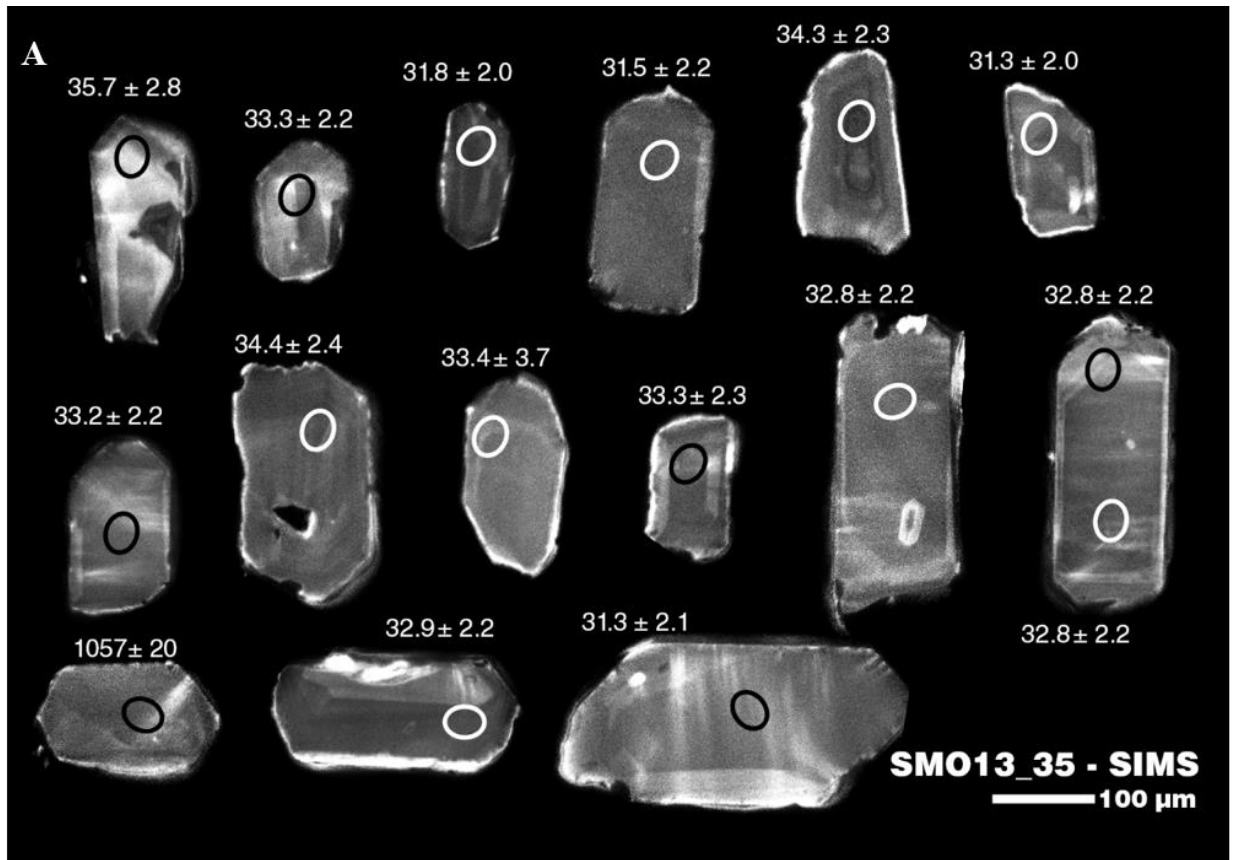


Figure 27. Sample SMO13_35. **A)** Zircons (125-300 μm in length) are subhedral to anhedral with stubby elongate crystals (aspect ratio ~2.5) and patchy core-rim zonation. SIMS U-Pb dates ($\pm 1\sigma$) for individual sample spots are listed next to each grain. **B)** The sample's weighted mean $^{206}\text{Pb}/^{238}\text{U}$ crystallization age is **32.8 ± 1.2 Ma** ($n = 15/16$, MSWD = 0.30, 2σ). Bar heights at 2σ . **C)** Tera-Wasserburg concordia diagram for sample SMO13_35. Error ellipses are at 2σ .

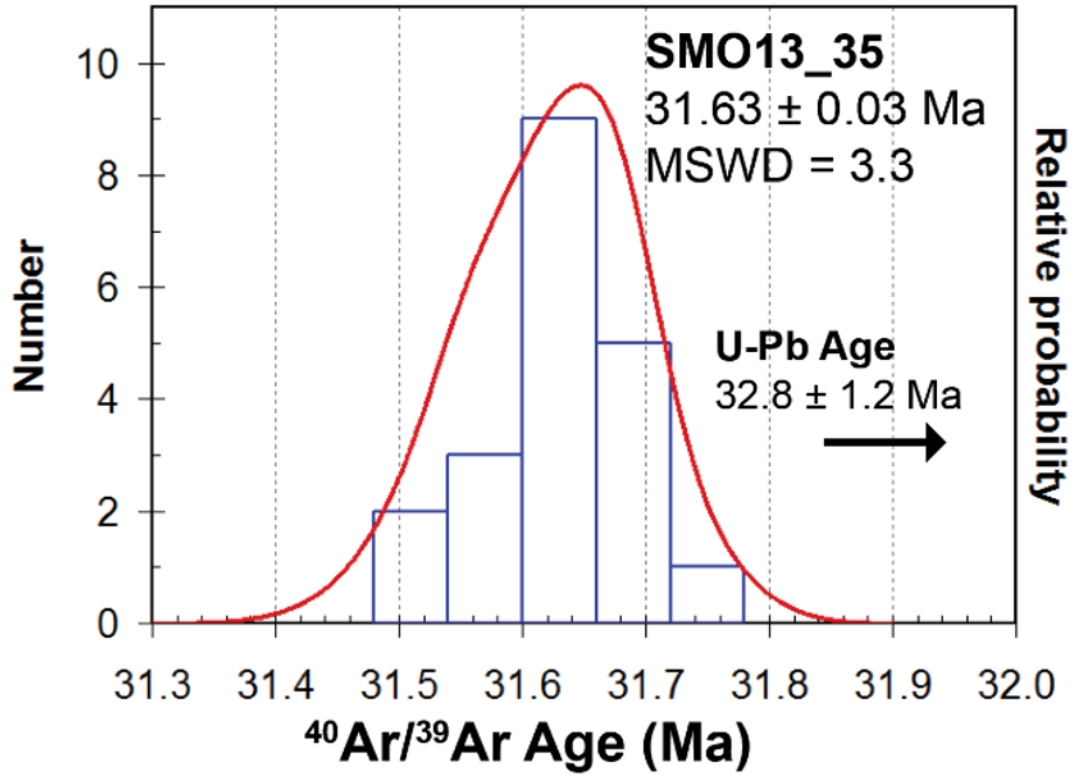


Figure 28. Probability density function for sample SMO13_35 illustrating the age spectra for the single-crystal total fusion analyses of sanidine. The corresponding U-Pb zircon age is too old to plot on the same graph, indicated by the arrow.

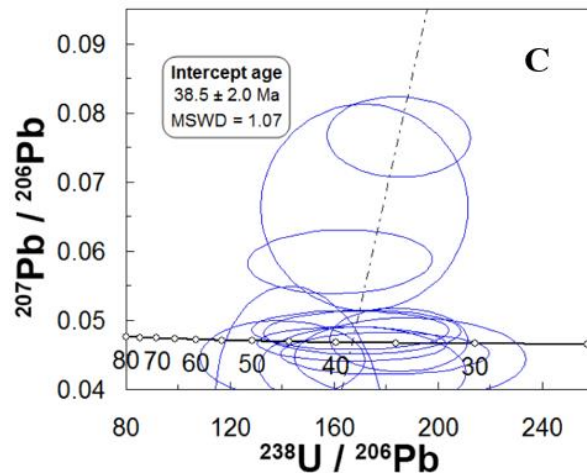
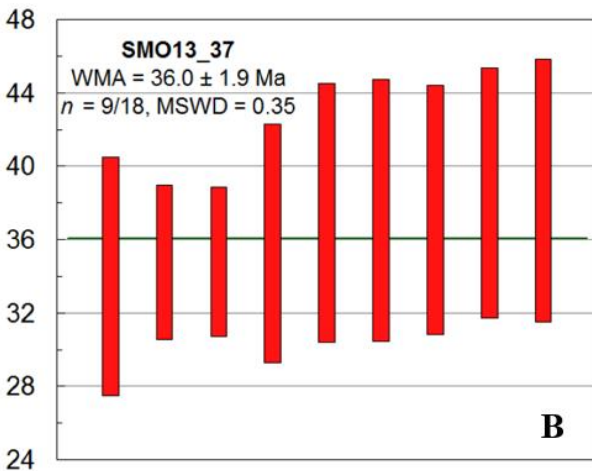
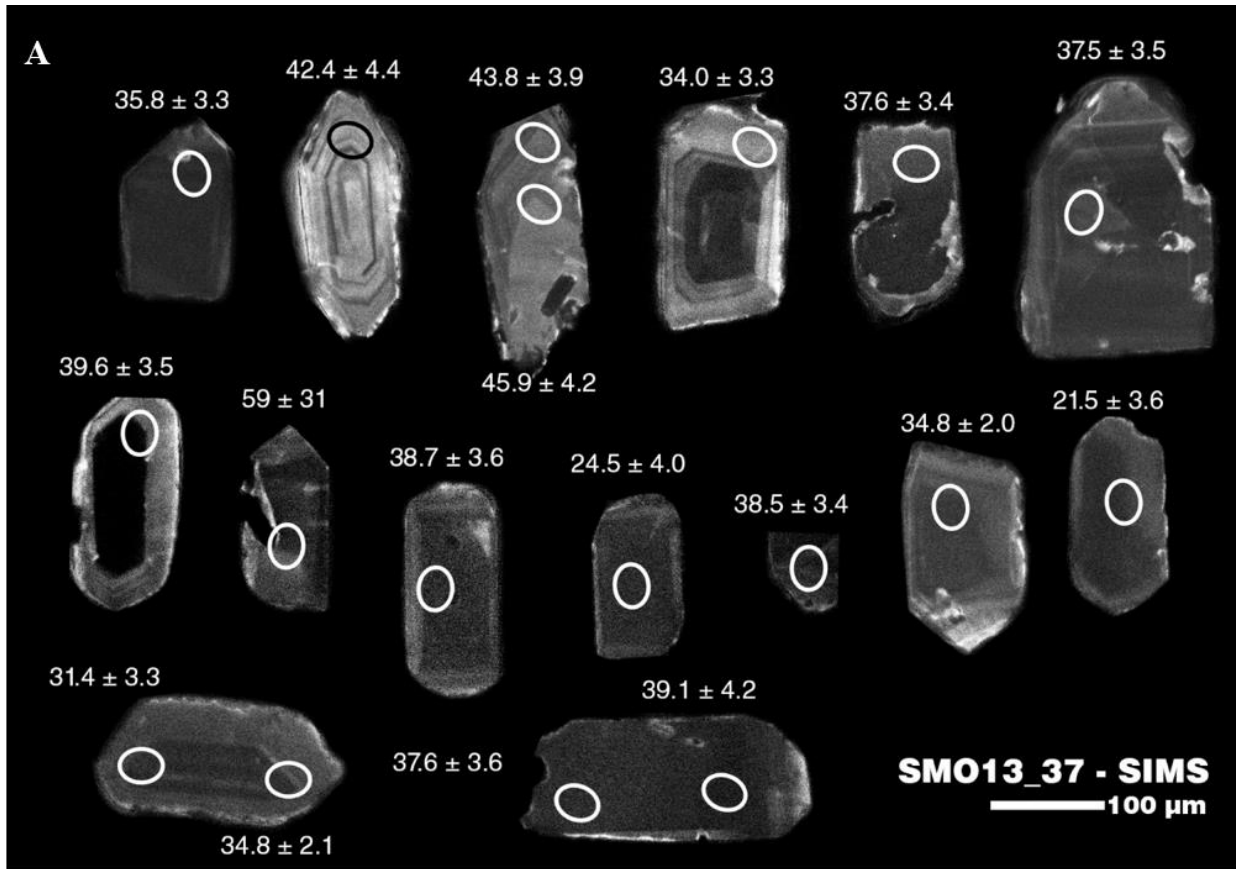


Figure 29. Sample SMO13_37. **A)** Zircons (125-250 μm in length) are euhedral to anhedral with both stubby and sharp terminations as well as oscillatory and patchy core-rim zoning. SIMS U-Pb dates ($\pm 1\sigma$) for individual sample spots are listed next to each grain. **B)** The sample's weighted mean $^{206}\text{Pb}/^{238}\text{U}$ crystallization age is 36.0 ± 1.9 Ma ($n = 9/18$, MSWD = 1.9, 2σ). Bar heights at 2σ . **C)** Tera-Wasserburg concordia diagram for sample SMO13_37. Error ellipses are at 2σ .

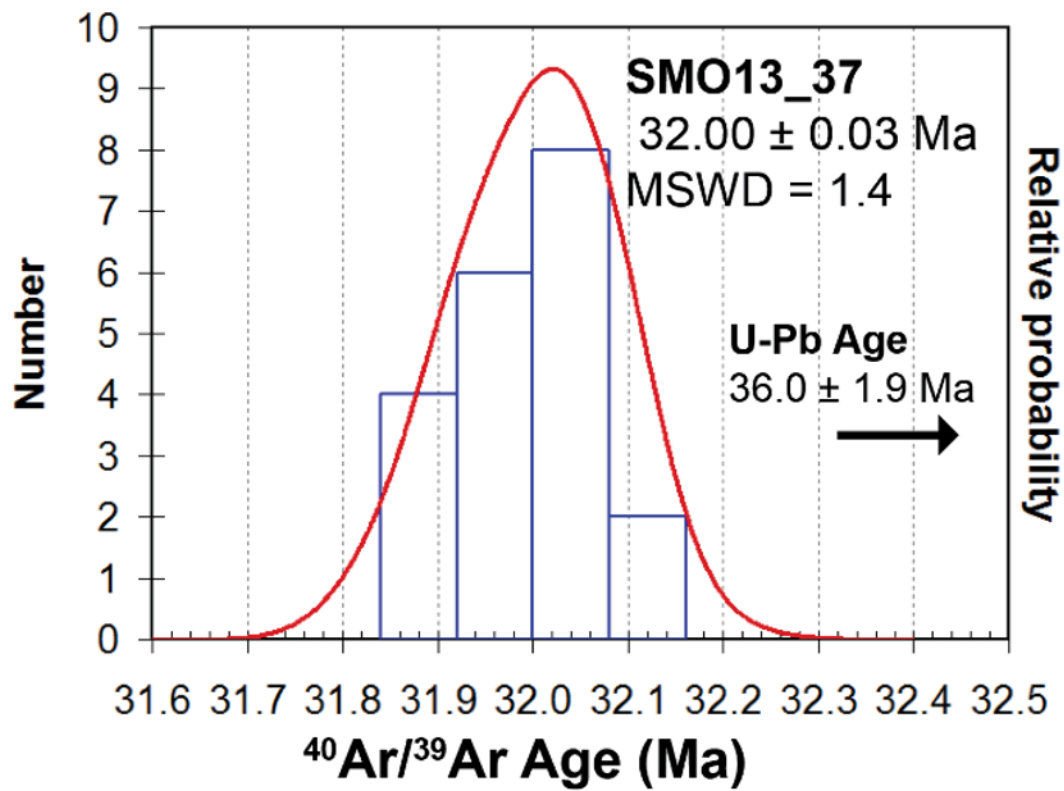


Figure 30. Probability density plot for sample SMO13_37 illustrating the age spectra for the single-crystal total fusion analyses of sanidine. The corresponding U-Pb zircon age is too old to plot on the same graph, indicated by the arrow.

31a). The sample's weighted mean $^{206}\text{Pb}/^{238}\text{U}$ crystallization age is **36.2 ± 1.0 Ma** ($n = 19/23$, MSWD = 1.3, 2σ ; Figure 31b). Single-crystal incremental heating analyses of biotite yielded a cooling age of **34.59 ± 0.17 Ma** (MSWD = 0.9, 73.8% in plateau, 2σ ; Figure 32a). Single-crystal total fusion analyses of sanidine yielded a cooling age of **34.38 ± 0.10 Ma** (MSWD = 1.8; Figure 32b).

3.1.14 SMO13_43 — unnamed weakly welded, pumice lapilli-tuff — (26°42'13.5"N, 106°07'13.9"W)

Sample SMO13_43 (Figure 6) is a weakly-welded, fiamme-rich, pumice lapilli tuff with small quartz crystals and abundant ~3 mm biotite. It forms the base of a composite stratigraphic section between Jarillas and El Ojito; its base is not seen and it is conformably overlain by the non-dated ignimbrite SMO13_44. Zircons (150-420 μm in length) are distinctly elongate and prismatic with clear oscillatory zoning and core-rim distinctions (Figure 33a). The sample's weighted mean $^{206}\text{Pb}/^{238}\text{U}$ crystallization age is **39.3 ± 1.5 Ma** ($n = 9/19$, MSWD = 1.8, 2σ ; Figure 33b). Single-crystal incremental heating analyses of biotite yielded a cooling age of **39.62 ± 0.13 Ma** (MSWD = 1.1, 100% in plateau, 2σ ; Figure 34a). Single-crystal total fusion of sanidine yielded a $\pm 1\sigma$ age range of 40-35 Ma (highest probability ~39 Ma; Figure 34b).

3.1.15 SMO13_46 — unnamed quartz-biotite, lapilli-tuff — (26°42'20.1"N 106°07'05.3"W)

Sample SMO13_46 (Figure 6) is a pink, columnar-jointed quartz and biotite-rich, fiamme-rich, lapilli-tuff with few lithics. It forms the top of a composite stratigraphic section between Jarillas and El Ojito; it conformably overlies the non-dated ignimbrite SMO13_45, and is unconformably overlain by basaltic andesite lava SMO13_47. Zircons (150-290 μm in length) are euhedral to subhedral and have oscillatory zoning and clear core-rim distinction (Figure 35a). The sample's weighted mean $^{206}\text{Pb}/^{238}\text{U}$ crystallization age is **38.8 ± 1.8 Ma** ($n = 11/15$, MSWD = 0.42, 2σ ; Figure 35b). There were four exclusions due to high error. Single-crystal incremental heating analyses of biotite yielded a cooling age of **38.79 ± 0.17 Ma** (MSWD = 1.1, 80.7% in plateau; Figure 36a). Single-crystal total fusion analyses of sanidine yielded a cooling age of **37.90 ± 0.04 Ma** (MSWD = 1.3; Figure 36b).

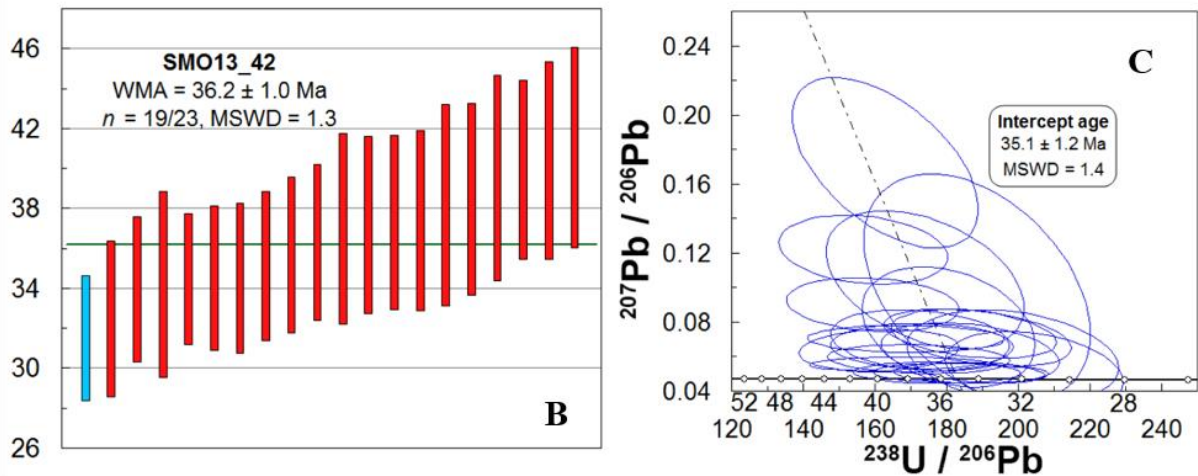


Figure 31. Sample SMO13_42. **A)** Zircons (100-315 μm in length) are euhedral with an average aspect ratio of ~2 and show clear oscillatory zoning and distinct core-rim boundaries. SIMS U-Pb dates ($\pm 1\sigma$) for individual sample spots are listed next to each grain. **B)** The sample's weighted mean $^{206}\text{Pb}/^{238}\text{U}$ crystallization age is **36.2 ± 1.0 Ma** ($n = 19/23$, MSWD = 1.3, 2σ). Bar heights at 2σ . One young outlier (blue box) was dropped from calculations by Isoplot. **C)** Tera-Wasserburg concordia diagram for sample SMO13_42. Error ellipses are at 2σ .

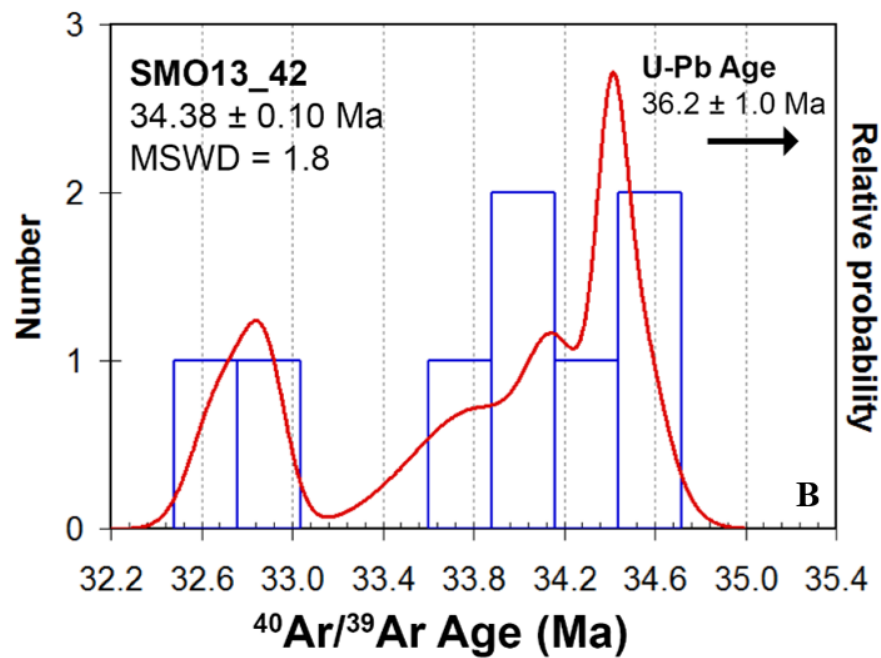
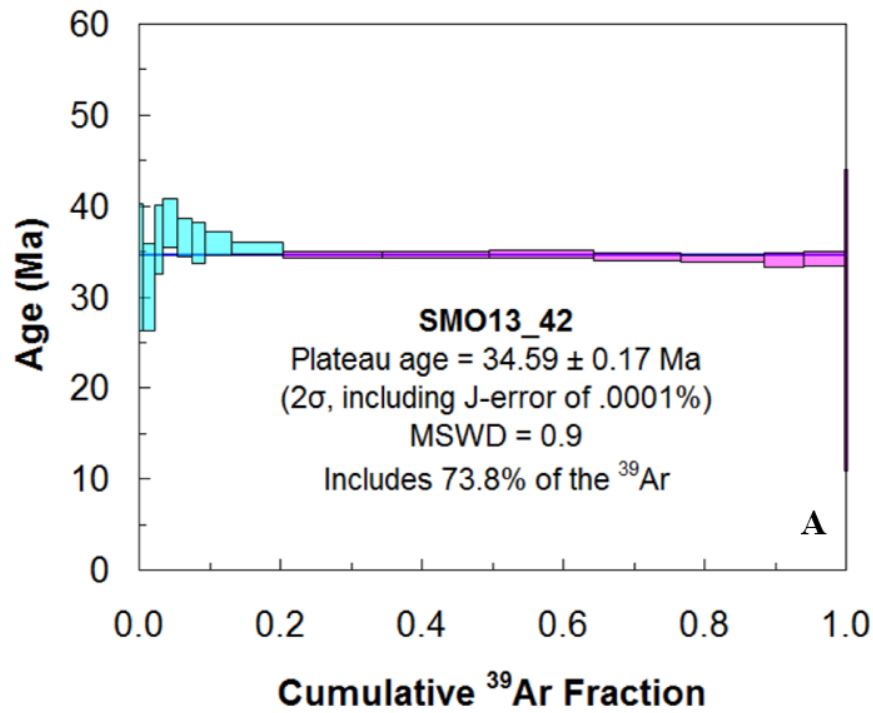


Figure 32. $^{40}\text{Ar}/^{39}\text{Ar}$ data for sample SMO13_42. **A)** Step-heating age spectra of biotite. Box heights are 2σ . **B)** Probability density function illustrating the age spectra for the single-crystal total fusion analyses of sanidine. The corresponding U-Pb zircon age is too old to plot on the same graph, indicated by the arrow.

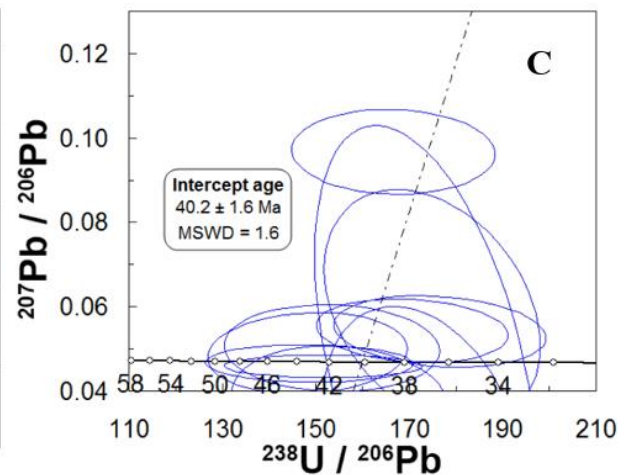
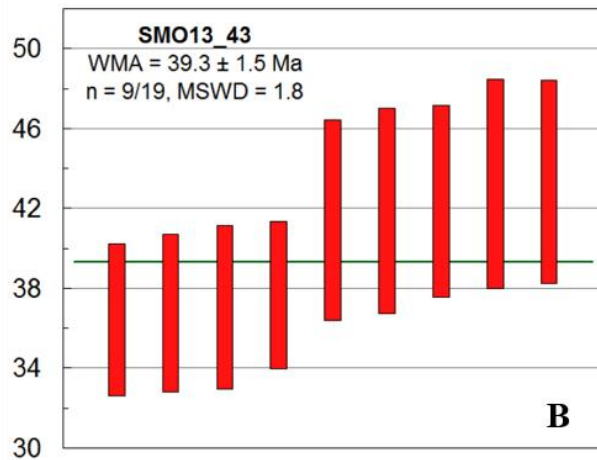
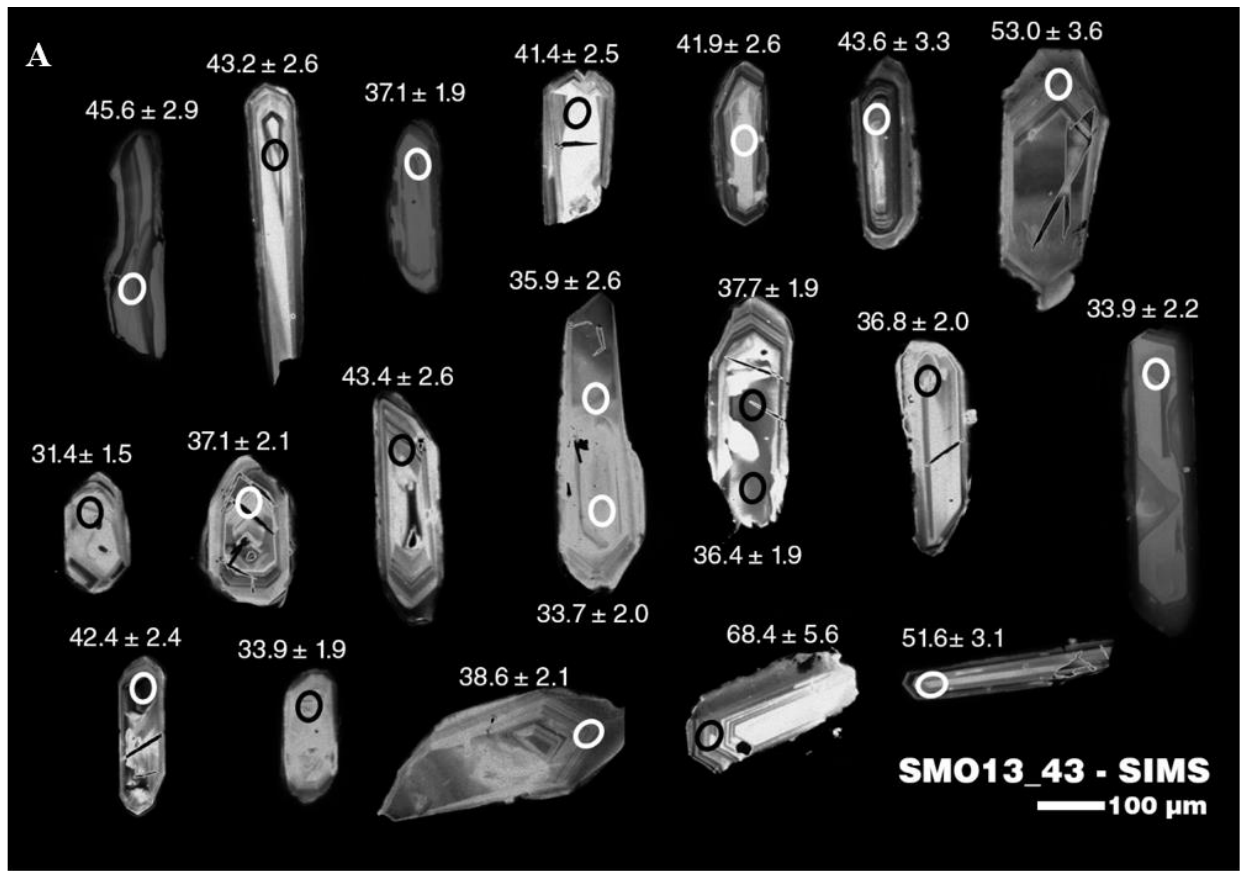


Figure 33. Sample SMO13_43. **A)** Zircons (150-420 μm in length) are distinctly elongate and prismatic with clear oscillatory zoning and core-rim distinctions. SIMS U-Pb dates ($\pm 1\sigma$) for individual sample spots are listed next to each grain. **B)** The sample's weighted mean $^{206}\text{Pb}/^{238}\text{U}$ crystallization age is 39.3 ± 1.5 Ma ($n = 9/19$, MSWD = 1.8, 2σ). Bar heights at 2σ . **C)** Tera-Wasserburg concordia diagram for sample SMO13_43. Error ellipses are at 2σ .

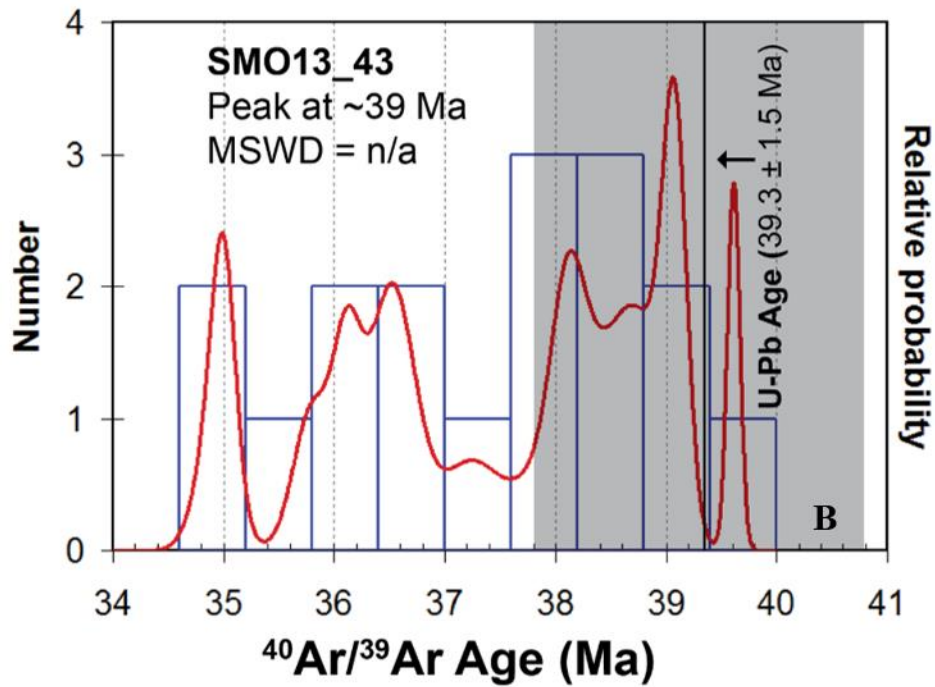
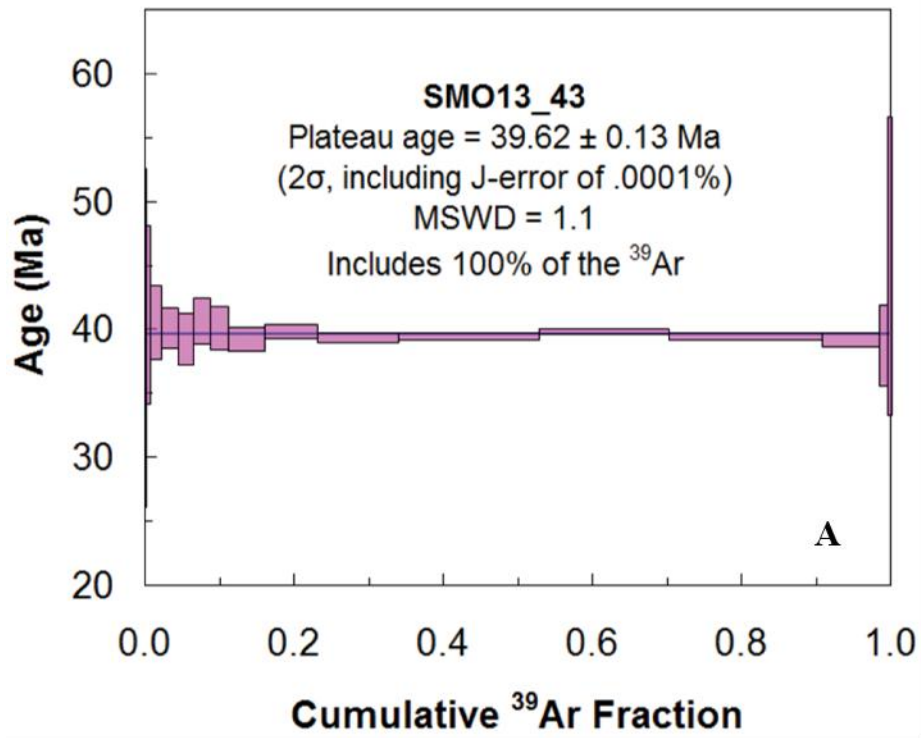


Figure 34. $^{40}\text{Ar}/^{39}\text{Ar}$ data for sample SMO13_43. **A)** Step-heating age spectra of biotite. Box heights are 2σ . **B)** Probability density function illustrating the age spectra for the single-crystal total fusion analyses of sanidine. The corresponding U-Pb zircon age and associated error (shaded box) have been plotted as well. The non-Gaussian distribution of the probability density curve suggests a complex cooling history, but the step-heating, U-Pb, and highest peak are all roughly concordant, suggesting the true age may be ~ 39 Ma.

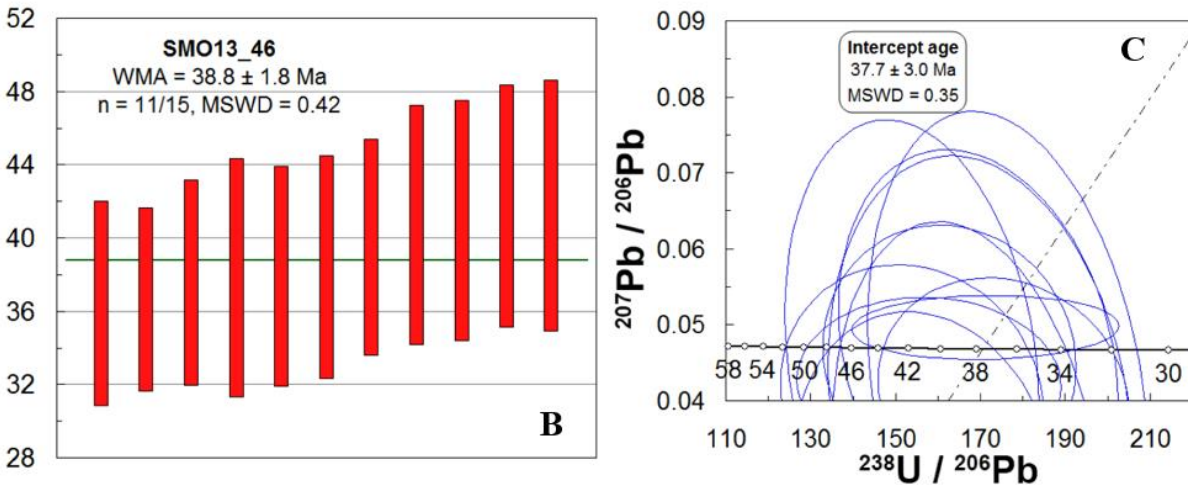
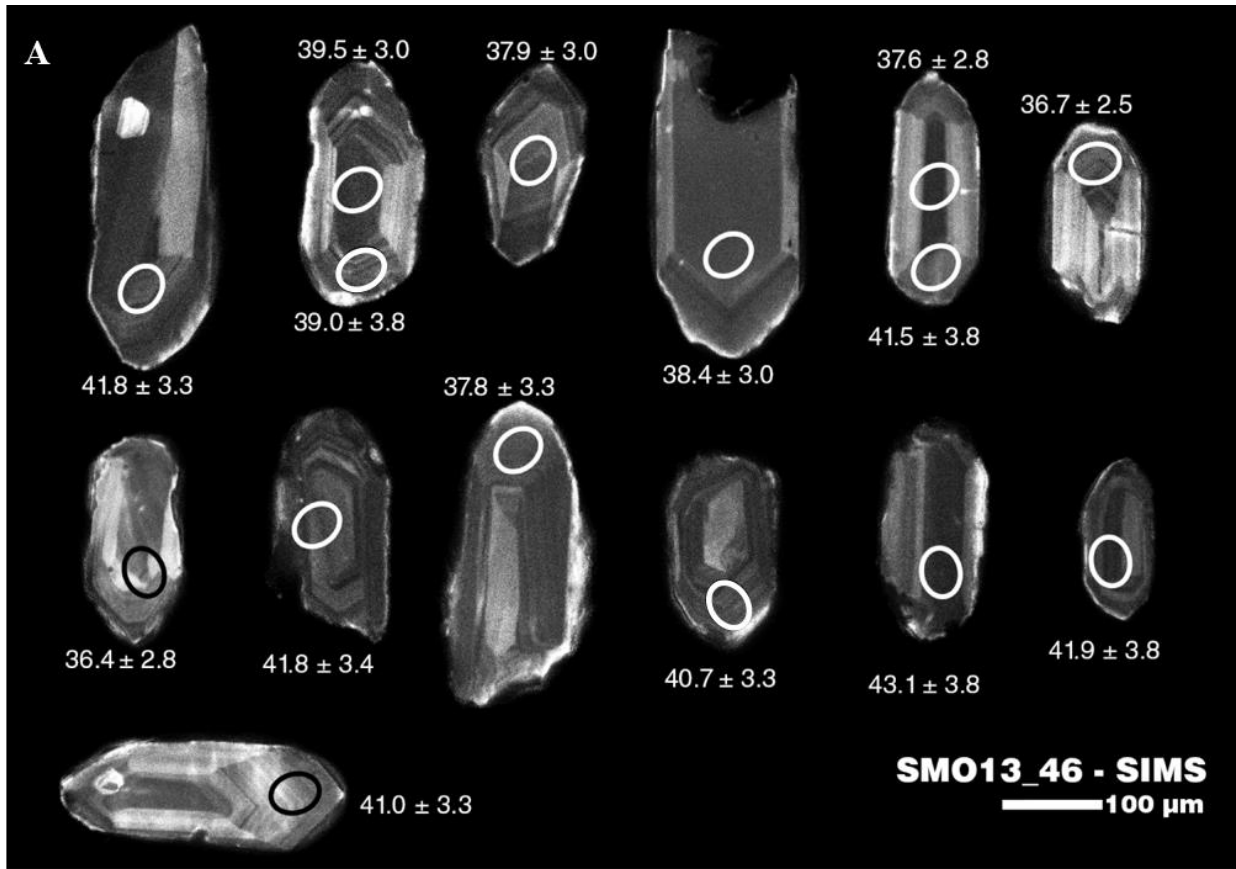


Figure 35. Sample SMO13_46. **A)** Zircons (150-290 μm in length) are euhedral to subhedral and have oscillatory zoning and clear core-rim distinction. SIMS U-Pb dates ($\pm 1\sigma$) for individual sample spots are listed next to each grain. **B)** The sample's weighted mean $^{206}\text{Pb}/^{238}\text{U}$ crystallization age is 38.8 ± 1.8 Ma ($n = 11/15$, MSWD = 0.42, 2σ). Bar heights at 2σ . **C)** Tera-Wasserburg concordia diagram for sample SMO13_46. Error ellipses are at 2σ .

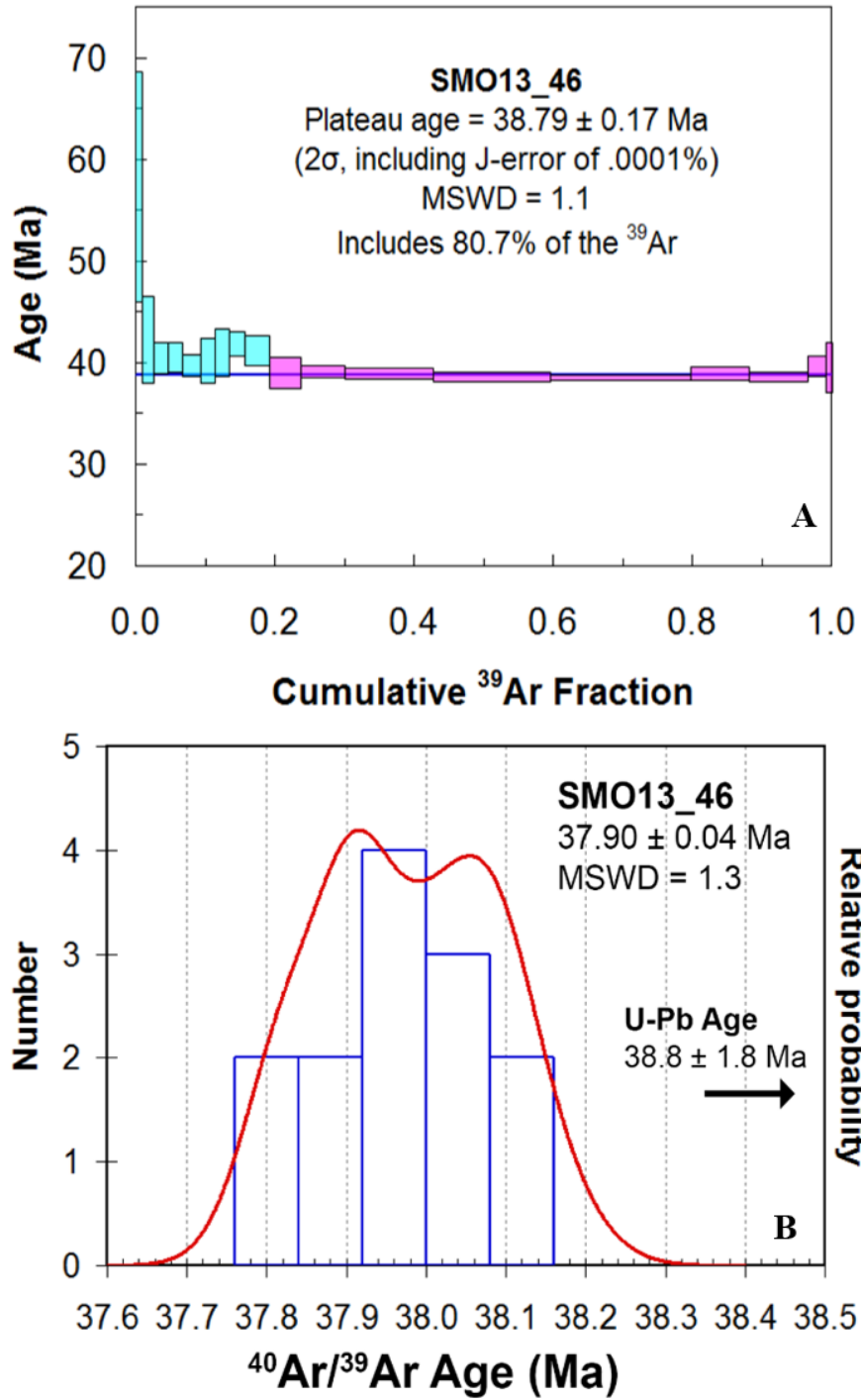


Figure 36. $^{40}\text{Ar}/^{39}\text{Ar}$ data for sample SMO13_46. **A)** Step-heating age spectra of biotite. Box heights are 2σ . **B)** Probability density function illustrating the age spectra for the single-crystal total fusion analyses of sanidine. The corresponding U-Pb zircon age is too old to plot on the same graph, indicated by the arrow.

3.1.16 SMO13_48 — ‘Ballezas Junction tuff’ — sanidine-phyric lapilli-tuff — (26°48'52.2"N, 106°00'50.0"W)

Sample SMO13_48 (Figure 6) is a sanidine-phyric lapilli-tuff with abundant small pumice, and lithic lapilli. It forms the base of a composite stratigraphic section immediately east of Puerto Justo; its base is not seen and it is conformably overlain by the non-dated ignimbrite SMO13_52. Zircons (100-470 μm in length) show clear oscillatory zoning, distinct cores and rims, and generally elongate crystal form (aspect ratio ~ 3 ; Figure 37a). The sample's weighted mean $^{206}\text{Pb}/^{238}\text{U}$ crystallization age is **39.8 \pm 1.3 Ma** ($n = 14/21$, MSWD = 0.6, 2σ ; Figure 37b). One suspected xenocryst ($^{207}\text{Pb}/^{206}\text{Pb}$ age = 1237 ± 20 Ma, 1σ) was excluded and is likely sourced from underlying basement rock (Ferrari et al., 2007). Single-crystal incremental heating analyses of biotite yielded a cooling age of **40.50 \pm 0.21 Ma** (MSWD = 1.0, 93.5% in plateau, 2σ ; Figure 38a). Single-crystal total fusion analyses of sanidine yielded a cooling age of **35.94 \pm 0.11 Ma** (MSWD = 1.0, 2σ ; Figure 38b).

3.1.17 SMO13_53 — unnamed non-welded tuff — (26°52'25.1"N, 105°58'35.1"W)

Sample SMO13_53 (Figure 6) is a non-welded tuff with small red lithics and sparse biotite and orthoclase entirely lacking in fiamme. It forms the base of a stratigraphic section at Rancho Blanco; it unconformably overlies the Mesozoic basement and is conformably overlain by non-dated ignimbrite SMO13_54. Zircons (200-450 μm in length) are distinctly prismatic with good oscillatory zoning and clear cores and rims (Figure 39a). The sample's weighted mean $^{206}\text{Pb}/^{238}\text{U}$ crystallization age is **39.6 \pm 2.0 Ma** ($n = 13/15$, MSWD = 0.29, 2σ , Figure 39b). One analysis was excluded from the weighted mean due to high individual error ($>11\%$).

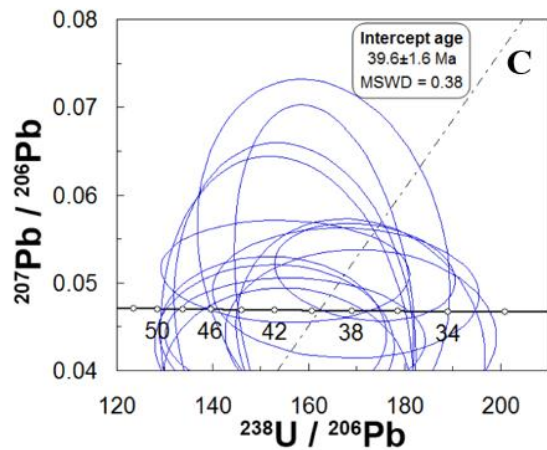
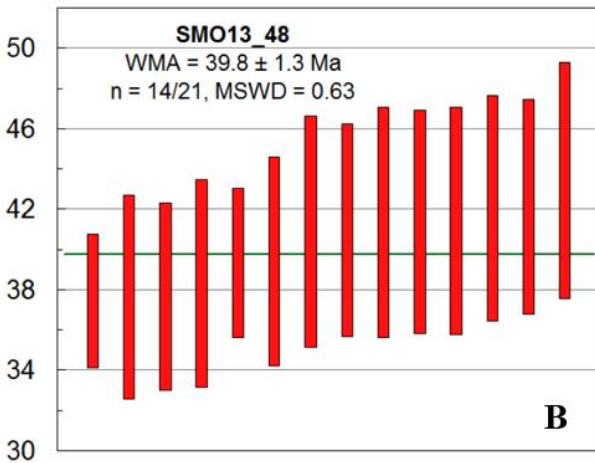
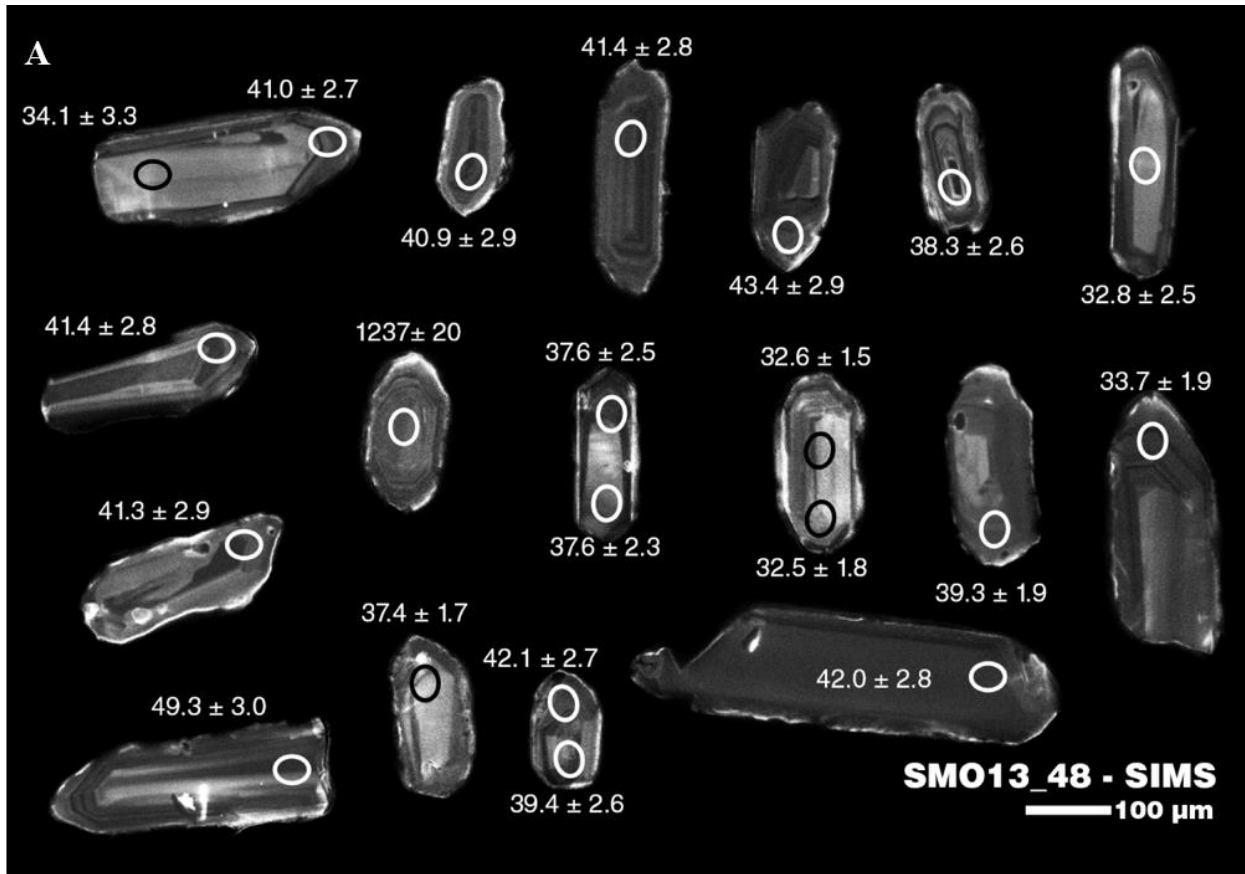


Figure 37. Sample SMO13_48. **A)** Zircons (100-470 μm in length) show clear oscillatory zoning, distinct cores and rims, and generally elongate crystal form (aspect ratio ~3). SIMS U-Pb dates ($\pm 1\sigma$) for individual sample spots are listed next to each grain. **B)** The sample's weighted mean $^{206}\text{Pb}/^{238}\text{U}$ crystallization age is 39.8 ± 1.3 Ma ($n = 14/21$, MSWD = 0.6, 2σ). Bar heights at 2σ . **C)** Tera-Wasserburg concordia diagram for sample SMO13_48. Error ellipses are at 2σ .

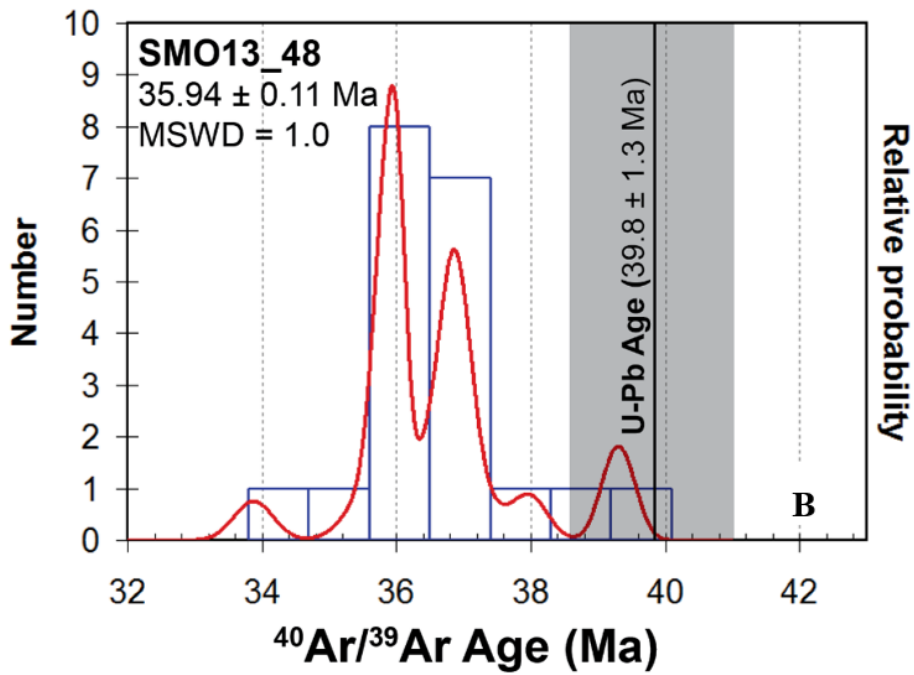
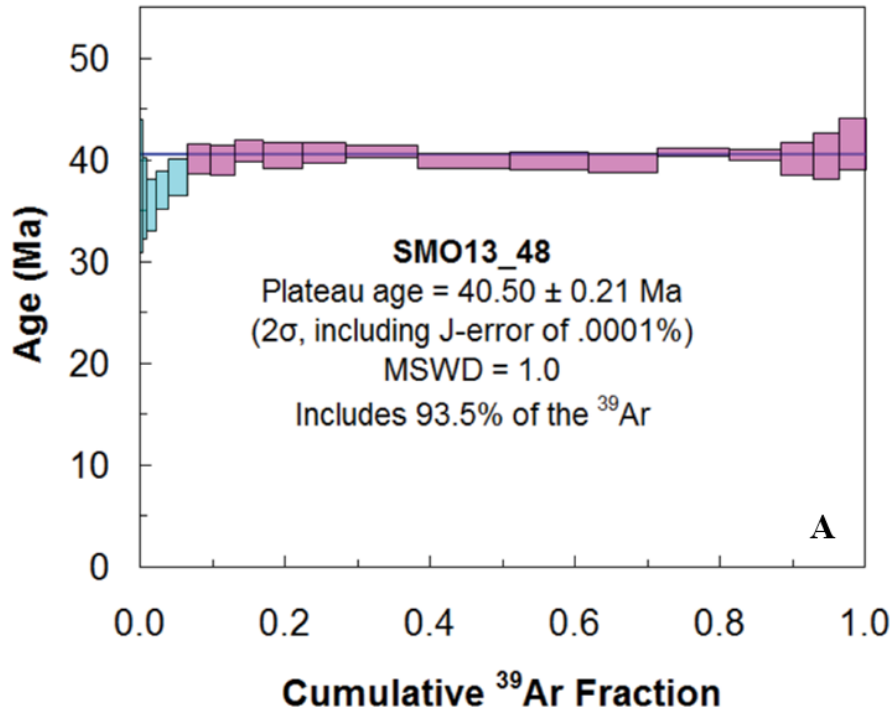


Figure 38. $^{40}\text{Ar}/^{39}\text{Ar}$ data for sample SMO13_48. **A)** Step-heating age spectra of biotite. Box heights are 2σ . **B)** Probability density function illustrating the age spectra for the single-crystal total fusion analyses of sanidine. The corresponding U-Pb zircon age and associated error (shaded box) have been plotted as well.

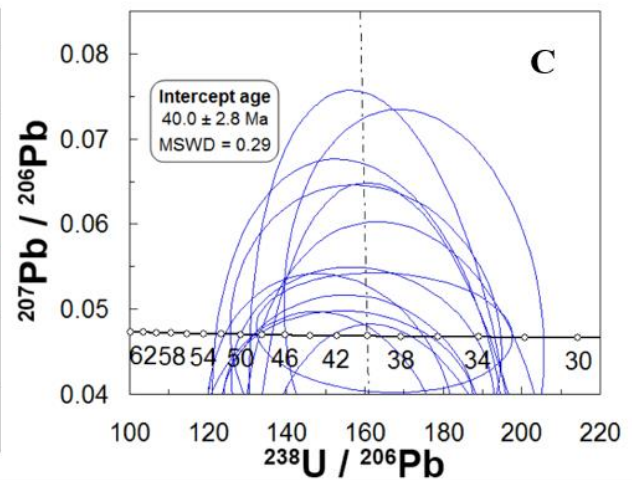
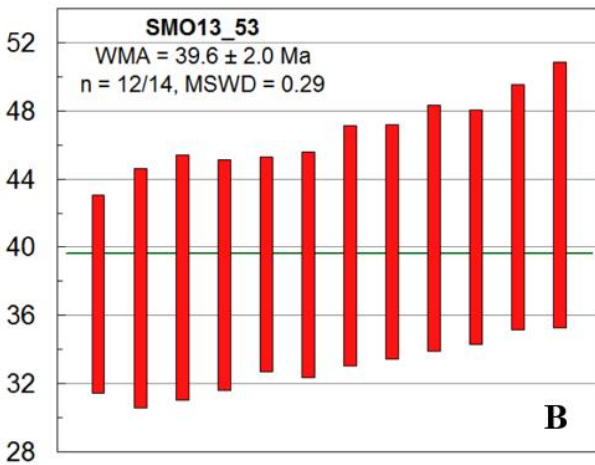
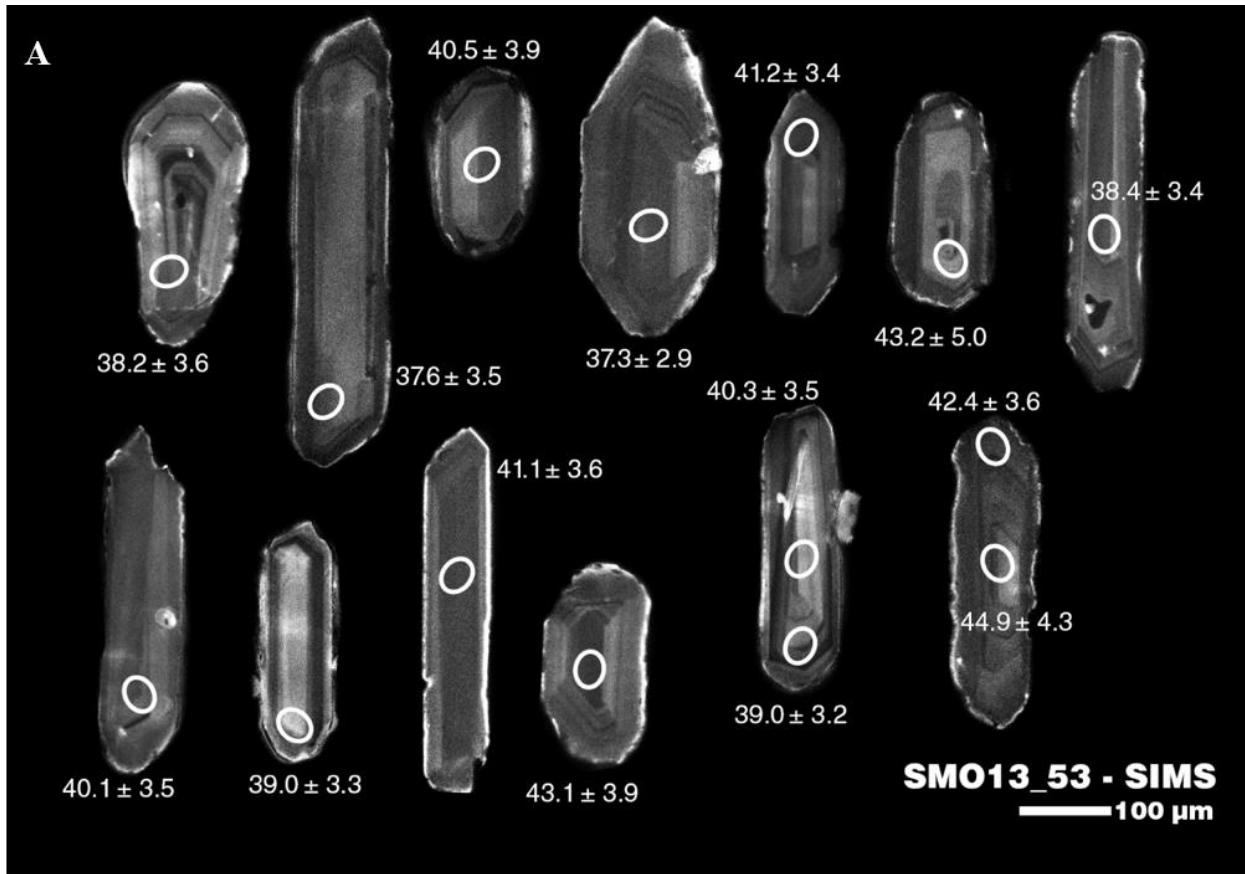


Figure 39. Sample SMO13_53. **A)** Zircons (200-450 μm in length) are distinctly prismatic with good oscillatory zoning and clear cores and rims. SIMS U-Pb dates ($\pm 1\sigma$) for individual sample spots are listed next to each grain. **B)** The sample's weighted mean $^{206}\text{Pb}/^{238}\text{U}$ crystallization age is 39.6 ± 2.0 Ma ($n = 13/15$, MSWD = 0.29, 2σ). Bar heights at 2σ . **C)** Tera-Wasserburg concordia diagram for sample SMO13_53. Error ellipses are at 2σ .

4. Discussion

4.1 Comparison of $^{206}\text{Pb}/^{238}\text{U}$ and $^{40}\text{Ar}/^{39}\text{Ar}$ data from double-dated samples

Double-dating of samples by the U-Pb and $^{40}\text{Ar}/^{39}\text{Ar}$ methods is highly likely to yield more than one valid radiometric age for a single deposit. This is primarily because of the differences in the crystallization conditions of zircon and K-bearing phases during protracted rhyolite petrogenesis, and the differences in closing temperature. Because Ar is a noble gas it readily diffuses out of crystal lattices at elevated temperature; the closing temperatures for phases used in this study are: biotite = 250-350°C, and sanidine 175-350°C. In comparison, the closure temperature for Pb in zircon is ~960°C (i.e. magmatic temperatures). Differences can also be explained by failures in the U-Pb or $^{40}\text{Ar}/^{39}\text{Ar}$ systematics, for example, poor retention of radiogenic ^{206}Pb , ^{207}Pb , or ^{40}Ar due to hydrothermal alteration giving anomalously young ages. However, because the two radiometric systems utilize different mineral phases, they serve as a double-check on each other, and large differences between U-Pb and $^{40}\text{Ar}/^{39}\text{Ar}$ ages in the same rock, i.e. greater than the largest analytical uncertainty, can be used to identify geological processes that have upset one or other of the systems. In other words, minor differences (~1-2 Ma) are to be expected, differences >5 Ma are cause for concern.

Samples SMO13_02 ‘Guadalupe tuff’, SMO13_22, SMO13_35, SMO13_37, SMO13_42 ‘Navarro tuff’, SMO13_43, SMO13_46, and SMO13_48 ‘Ballezas Junction tuff’ were double-dated. In every case the $^{40}\text{Ar}/^{39}\text{Ar}$ age was younger or within error of the corresponding $^{206}\text{Pb}/^{238}\text{U}$ zircon age; this is to be expected as the eruption age defined by cooling through <350°C Ar closure temperature should be younger than the zircon crystallization age with a significantly higher closure temperature. The difference in age (t_{Δ}) between the $^{206}\text{Pb}/^{238}\text{U}$ zircon crystallization age and the $^{40}\text{Ar}/^{39}\text{Ar}$ cooling age ranges from ~4 to ~0 Myr with a mean t_{Δ} of ~2.2 Myr. This indicates that Zr saturation and the onset of zircon crystallization in the magma is ≤ 4 Ma before eruption, and often less than 2.2 Ma; this puts a constraint on the longevity of an individual batch of magma that was eventually erupted as a large ignimbrite. My value of ~2.2 Ma agrees very closely with Bryan et al. (2008)’s values of t_{Δ} (1 – 4 Myr) from their study of seven double-dated SMO ignimbrites. They attributed t_{Δ} of 1 – 4 Myr as the duration over which rhyolitic magma was accumulated in upper crustal magma chambers from diffuse sources in the lower crust.

In four samples (SMO13_02, SMO13_37, SMO13_42, and SMO13_48) t_{Δ} is greater than the largest age error (always $^{206}\text{Pb}/^{238}\text{U}$ zircon) by ~ 1.7 Myrs. In all four samples the $^{206}\text{Pb}/^{238}\text{U}$ zircon crystallization age is statistically reasonable (MSWD < 2), and there is no reason to infer that the zircon crystallization age is too old. The $^{40}\text{Ar}/^{39}\text{Ar}$ cooling age is more easily disturbed by hydrothermal alteration than zircon. Sample SMO13_02 is within the Guadalupe y Calvo mineral districts; the Guadalupe y Calvo silver deposit is hosted within the Guadalupe tuff. The other samples are not proximal to known zones of mineralization but alteration visibly increases in the older, more northeasterly samples (Anderson, *in prep.*) and resetting of the $^{40}\text{Ar}/^{39}\text{Ar}$ cooling ages seems plausible.

4.2 Age relationships in stratigraphic sections

All the composite stratigraphic sections established in the field returned viable age models, i.e. the oldest units were at the base and the youngest units were at the top. This suggests that the sampling strategy in the field and for selecting geochronological samples was successful, and that there is little stratigraphic complexity in the area of the transect (Figure 6), i.e., the stratigraphy is layer-cake over tens of kilometers.

With the exception of the ca. 67 Ma ($^{206}\text{Pb}/^{238}\text{U}$ zircon) Guadalupe tuff (SMO13_02) all the units dated were Oligocene as expected. In the five stratigraphic sections established wholly within Oligocene UVS units, the mean time span between the oldest and youngest ignimbrites dated is 2.1 Myr and the median number of ignimbrites is 4. Therefore, any given location along the transect averages an accumulation of 4 ignimbrites in ca. 2 Myr, at a rate of one ignimbrite emplacement event approximately every 0.5 Myr. Given that this is the first study to attempt to identify all the volcanic stratigraphy along a single radiometrically dated transect, similar data do not exist for the adjacent parts of the SMO (Figure 5).

4.3 Testing of possible correlations between SMO ignimbrites

In an attempt to correlate between stratigraphic sections, I performed a series of correlation tests using the available geochronology, primarily U-Pb, and petrographic, lithological, and geochemical data.

4.3.1 Methodology and scoring rubric

Weighted mean $^{206}\text{Pb}/^{238}\text{U}$ and $^{40}\text{Ar}/^{39}\text{Ar}$ age data were used as first-order correlation tests of units described in the field (e.g., McDowell and McIntosh, 2012). Twenty-three potential pairs were identified and further evaluated on the basis of point count data (Anderson, *in prep.*), whole rock geochemical data, and rock descriptions. These individual correlation components were ranked on a scale of 0-3, where 0 = no evidence of a relationship between the pair, 1 = weak correlation potential between the pair, and 3 = strong correlation potential between the pair. There is no rank '2' to allow strong correlations to stand-out. A weighted overall sum was generated from scaled sums of the individual components. Trace elements were given the greatest weight to reflect their high-precision measurements, resistance to post-emplacement redistribution, and importance to petrological processes. The final correlation results are summarized in Table 3.

4.3.2 Geochronologic comparison, methodology and scoring

Weighted mean $^{206}\text{Pb}/^{238}\text{U}$ ages and associated $\pm 2\sigma$ error bars for all 17 samples were plotted in Excel and visually inspected for overlap (Figure 40). Samples were considered correlation candidates when weighted mean $^{206}\text{Pb}/^{238}\text{U}$ ages were within the error envelope of similarly-aged units. U-Pb age data were also cross-checked for agreement with available $^{40}\text{Ar}/^{39}\text{Ar}$ age data to bolster pick reliability. In total, twenty-three pairs were identified, confined mostly to samples east of SMO13_33 (Figure 6). These pairs are listed in Table 3.

4.3.3 Point count data comparison, methodology and scoring

Point-count data of Anderson (*in prep.*) formed the basis of the petrographic comparisons. These data were collected for all 17 samples. The between-pair differences in total relative abundances of plagioclase, potassium feldspar, quartz, and biotite were assigned a ranking between 0 and 3. Pairs within 5% abundance of each other were given a ranking of 3, pairs within 5 – 10% of each other were given a 1, and pairs with differences >10% were considered mismatched and assigned a ranking of 0. A second petrographic test examined *within-sample* ratios of quartz to plagioclase, plagioclase to potassium feldspar + biotite, potassium feldspar to biotite, and quartz

Tested Pair	Correlation Strength	Point Counts (<i>p</i>)		Trace Elements (<i>g</i>)		Total Correlation (<i>t</i>)	
		Scaled Score (X_p)	\bar{x}_p σ_{xp}	Scaled Score (X_g)	\bar{x}_g σ_{xg}	Weighted Score (X_t)	\bar{x}_t σ_{xt}
46-53	Strong	0.63	0.67 / 0.04	1.00	0.95 / 0.04	0.89	0.87 / 0.02
33-53		0.71		0.93		0.86	
33-46		0.67		0.93		0.85	
43-53	Medium to Weak	0.71	0.54 / 0.32	0.33	0.26 / 0.12	0.45	0.35 / 0.06
33-43		0.58		0.33		0.41	
13-28		0.63		0.26		0.37	
22-37		0.63		0.26		0.37	
43-46		1.00		0.07		0.35	
4-16		0.42		0.26		0.31	
46-48		0.13		0.37		0.30	
28-35		0.79		0.07		0.29	
48-53		0.00		0.41		0.29	
43-48		0.13		0.33		0.27	
33-48	0.04	0.33	0.25				
8-13	No Correlation	0.71	0.45 / 0.21	0.00	0.07 / 0.13	0.21	0.19 / 0.05
13-35		0.67		0.00		0.20	
19-28		0.54		0.04		0.19	
22-42		0.63		0.00		0.19	
13-19		0.38		0.07		0.16	
12-19		0.54		0.00		0.16	
19-35		0.54		0.00		0.16	
8-28		0.42		0.00		0.13	
8-35		0.42		0.00		0.13	

Table 3. Summary of correlation test data.

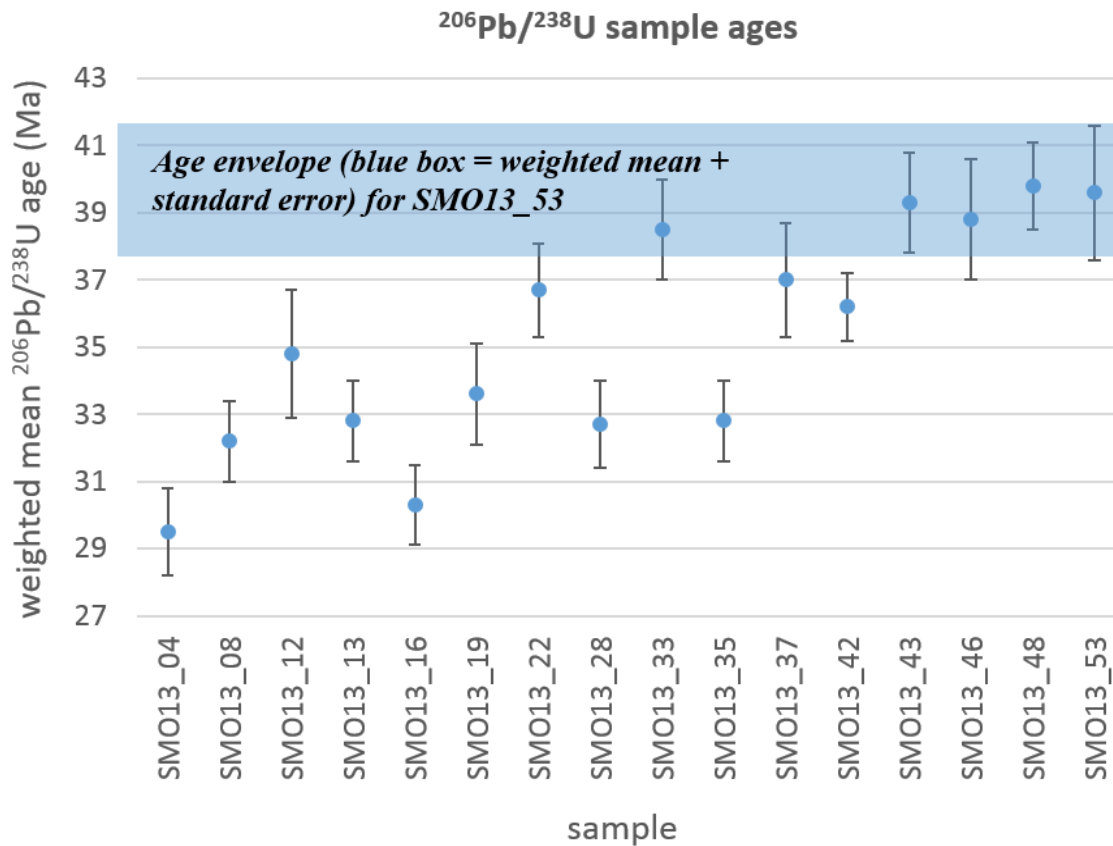


Figure 40. Illustration of the visual inspection process used to determine potential correlation pairs based on geochronological data for SMO13_53. All weighted mean U-Pb sample ages and associated analytical errors ($\pm 2\sigma$) have been plotted. Note that the age envelope (blue box = weighted mean + standard error) for sample SMO13_53 fully encompass the weighted means of samples SMO13_33, SMO13_43, SMO13_46, and SMO13_48. These are considered potential pairings. The envelope also partially overlaps the error bars of sample SMO13_22. However, as it does not encompass the weighted mean for that sample it is not considered a potential pair for SMO13_53.

to biotite + potassium feldspar, similar to the approach used by McDowell and McIntosh (2012). Rankings were limited to 0 or 3: pairs exhibiting identical within-sample relative proportions were assigned a 3 and mismatched pairs were assigned a 0. The sums of the results of these petrographic tests were combined to generate a raw “point-count data” score for each pair. This raw score was then scaled from zero to one for easier comparison (Appendix C).

4.3.4 Geochemical comparison--incompatible trace elements, methodology and scoring

Whole rock geochemical data consisting of the trace elements *Nd*, *Gd*, *Yb*, *Y*, *Zr*, *Nb*, *Ta*, *Rb*, *Sr*, and *Ba* were available for all 17 rocks in the sample suite. Between-pair similarities were evaluated graphically as direct numeric comparisons of the elements were insufficient to prove (or adequately provide evidence for) genetic relationships. For example, while three rocks may possess near-identical Nd content, a second factor such as Gd similarity may tie two of the samples closer together than to the third, reducing the probability that the two similar rocks deserve to be grouped with the outlier (e.g., Figure 41). Therefore, to adequately assess the relatedness of the pairs through trace element similarities, each element was plotted against a common denominator (*Zr*, in ppm) as the abscissa. For a pair of samples, this generates two points whose separation distance can be reasonably inferred to represent relatedness, as two geochemically identical rocks would plot as a single point (i.e. possess the same values of *x* and *y*) and two geochemically dissimilar rocks would plot at greater distances from each other. The distance between these points can be calculated using Pythagorean Theorem because the connecting line forms the hypotenuse of a right triangle whose base is equal to the difference in the values of *Zr* and whose height is equal to the difference in values of the trace element of interest:

$$l = \sqrt{\Delta Zr^2 + \Delta X^2}$$

where *l* = line length, ΔZr^2 = the squared difference in values of zirconium, and ΔX^2 = the squared difference in values of the element of interest.

This graphical process was applied to all nine trace elements. Percentile-based rankings were assigned to the measured lengths to account for variations in y-axis scaling. The shortest distances, whose lengths fell below the 10th percentile of all measured lengths for that particular element, were assigned a 3. Lengths between the 10th and 50th percentile were assigned

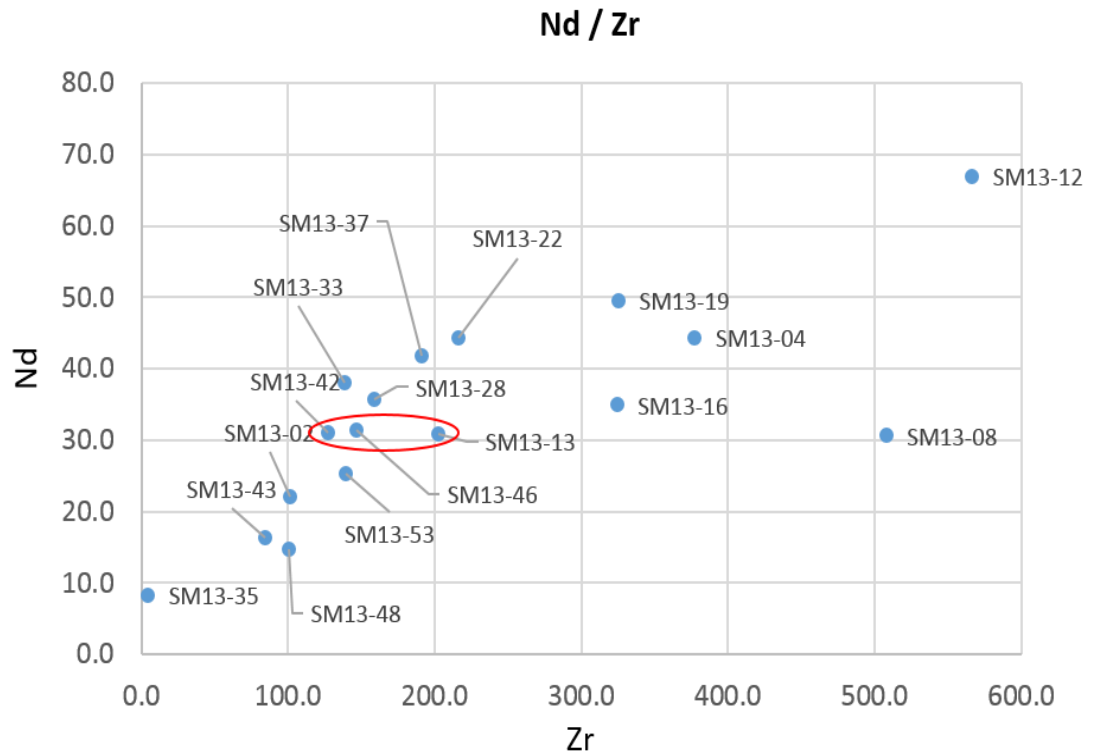


Figure 41. The graphical method for determining the sameness of rock pairs on the basis of trace elements. Note that samples SMO13_13, _42, and _46 (red ellipse) have similar ppm values of Nd. However, when plotted against the common axis Zr (ppm), it becomes clear that samples SMO13_42 and _46 are more related to each other than either is to SMO13_13. This process was repeated for all trace elements tested, always with Zr along the *x*-axis.

a 1, and the remaining pair lengths were assigned a 0. In total, trace element testing produced nine scores (one for each trace element) of 0, 1, or 3 for each of the 23 pairs. These rankings were summed to form a raw “trace element score” which was then scaled from zero to one for easier comparison later. The results are tabulated in Appendix D.

4.3.5 Correlation results

Correlation results are summarized in Table 3. Twenty-three unit pairs were identified based on geochronologic similarity of weighted $^{206}\text{Pb}/^{238}\text{U}$ and $^{40}\text{Ar}/^{39}\text{Ar}$ age data. Pairs were further compared on the basis of petrographic and geochemical similarity. Assigned pair scores, ranging from 0 to 3, were summed and scaled between zero and one, generating a single ‘point-count data’ (X_p) and ‘trace element’ (X_g) score per pair. X_p and X_g were then summed into a final weighted ‘correlation score’ (X_t), with heavier weight toward the more discriminative trace elements.

Total correlation scores (X_t) for the 23 pairs ranged from 0.13 to 0.89. Three samples (SMO13_33, SMO13_46, and SMO13_53) formed three pairs with combined weighted correlation scores above 0.77, which was the 90th percentile of the scaled scores. These pairs were **46-53** ($X_t = 0.89$), **33-53** ($X_t = 0.86$), and **33-46** ($X_t = 0.85$). These pairs matched strongly petrographically. The mean point-count correlation score (\bar{x}_p) for these three samples was 0.67 with a standard deviation (σ_{xp}) of 0.04, indicating a relatively tight cluster of scores, suggesting petrographic sameness. The three samples were nearly identical geochemically. The mean trace element score (\bar{x}_g) for the units was 0.95, with a standard deviation (σ_{xg}) of 0.04. Overall, the average weighted correlation score (\bar{x}_t) for these three strongly matched pairs was 0.87 with a standard deviation (σ_{xt}) of 0.02, indicating only minor variations in scores, suggesting sameness of the units.

Twelve samples (SMO13_53, SMO13_48, SMO13_46, SMO13_43, SMO13_37, SMO13_35, SMO13_33, SMO13_28, SMO13_22, SMO13_16, SMO13_13, and SMO13_04) formed nine pairs with weighted correlation scores greater than or equal to 0.29, which was the 50th percentile of the scaled scores. These pairs were **43-53** ($X_t = 0.45$), **33-43** ($X_t = 0.41$), **13-28** ($X_t = 0.37$), **22-37** ($X_t = 0.37$), **43-46** ($X_t = 0.35$), **04-16** ($X_t = 0.31$), **46-48** ($X_t = 0.30$), **28-35** ($X_t = 0.29$), and **48-53** ($X_t = 0.29$). Overall these pairs were weakly to moderately matched petrographically ($\bar{x}_p = 0.54$, $\sigma_{xp} = 0.32$) and geochemically ($\bar{x}_g = 0.26$, $\sigma_{xg} = 0.12$).

Eleven samples (SMO13_48, SMO13_43, SMO13_42, SMO13_35, SMO13_33, SMO13_28, SMO13_22, SMO13_19, SMO13_13, SMO13_12, and SMO13_08) formed eleven pairs with combined weighted correlation scores less than or equal to 0.27, which is less than the 50th percentile of the scaled scores. These pairs were **43-48** ($X_t = 0.27$), **33-48** ($X_t = 0.25$), **08-13** ($X_t = 0.21$), **13-35** ($X_t = 0.20$), **19-28** ($X_t = 0.19$), **22-42** ($X_t = 0.19$), **13-19** ($X_t = 0.16$), **12-19** ($X_t = 0.16$), **19-35** ($X_t = 0.16$), **08-28** ($X_t = 0.13$), and **08-35** ($X_t = 0.13$). These pairs were broadly similar petrographically ($\bar{x}_p = 0.45$, $\sigma_{xp} = 0.21$), but exhibited virtually no matching potential in the trace elements ($\bar{x}_g = 0.07$, $\sigma_{xg} = 0.13$). For these reasons these eleven pairs were not considered matches.

4.3.6 *The Ojito tuff*

On the basis of these results I tentatively correlate samples SMO13_33, SMO_46, and SMO13_53 to be the same ca. 38.5 Ma deposit currently exposed over a minimum straight-line distance of ~41 km along Highway 24 (Figure 6). I have provisionally named this unit the ‘Ojito tuff’ after the village approximately halfway between the locations of samples SMO13_33 and SMO13_53. Assuming a circular distribution centered on Ojito with a radius of 20.5 km, and a minimum thickness of 20 m (based on SMO13_53), constrains the conservative minimum volume of the extracaldera ignimbrite to be 26 km³. The minimum total volume is usually assumed to be three times the extracaldera ignimbrite (ignimbrite + assumed proximal intracaldera-fill + assumed distal Plinian fall deposits; Mason et al., 2004) giving a volume of ~78 km³. This minimum total volume places the Ojito tuff in volcanic explosivity index (VEI; Newhall and Self, 1982) category 6 (10 – 100 km³), corresponding to Plinian and ultraplinian eruption sizes. VEI 6+ eruptions occur once or twice a century but are typical of many SLIPS (e.g., Snake River Plain; Branney et al., 2008; Etendeka-Parana; Bryan et al., 2010).

This correlation allows for the three oldest stratigraphic sections of the transect to be correlated using the presence of the Ojito tuff. Samples SMO13_43 and SMO13_48 both occur beneath the Ojito tuff in their respective stratigraphic sections but do not correlate (see below).

4.4 The Guadalupe tuff (SMO13_02) and the edge of the UVS

With the exception of SMO13_02, all U-Pb and ⁴⁰Ar/³⁹Ar ages are consistent with known age constraints of the Cenozoic ignimbrite flare-up of North America and the UVS in particular (McDowell and Clabaugh, 1979; Ferrari et al., 2007; Bryan et al., 2008; McDowell and

McIntosh, 2012). SMO13_02's Late Cretaceous age (67.0 Ma) and location (Figure 6) likely make it a felsic volcanic component of the oldest parts of LVC emplaced during the beginning of the Laramide. The sample was collected with the expectation that as a rhyolitic ignimbrite it was part of the UVS and unlikely to be part of the dominantly andesitic-dacitic LVC. Therefore, the Late Cretaceous age of the Guadalupe tuff is surprising, and rhyolitic ignimbrites within the LVC may be more common than previously thought (cf. Clark et al., 1979). The Guadalupe tuff is the first reported occurrence of LVC rocks along the Durango and Chihuahua state border where the UVS is more typically unconformable on the Cretaceous Sinaloa batholith (Figure 3) and its Mesozoic metasedimentary wall-rocks. It is also one of the oldest reported LVC units in the western SMO generally, where most LVC rocks are Eocene andesites (Ferrari et al., 2007). This is particularly important because the voluminous Guadalupe y Calvo silver-gold mineral deposit (<http://edrsilver.com/projects/exploration/guadalupe/>) is hosted largely within the Guadalupe tuff along fractures associated with the Rosario fault zone. The minimum age of the Rosario fault zone is therefore constrained to ca. 67 Ma, and it may not deform the later LVC (i.e. Eocene) or UVS (i.e. Oligocene – Miocene).

When taken with the Oligocene age of the overlying SMO13_04 (29.5 Ma), I can infer an unconformable contact between the UVS and LVC, and locate the western margin of the UVS in the central SMO. The eastern margin of the SMO is easier to identify where SMO13_53 (39.6 Ma) and the overlying SMO13_54 both unconformably overlie folded shales and slates of the Late Jurassic – Early Cretaceous Parral Formation (Grant and Ruiz, 1988).

4.5 SMO zircons as probes of the basement and magma chamber processes

4.5.1 Xenocrystic zircons

The presence of xenocrystic zircons within SMO ignimbrites illuminates the nature of the basement beneath the SMO. Previous work (e.g., Cameron et al., 1992; Cameron and Ward, 1998) has shown that the geochronology of xenoliths in Quaternary basalts adjacent to the SMO can provide temporal (Rudnick and Cameron, 1991) and spatial (Valencia-Moreno et al., 2001) insights on the extents of basement rocks beneath the SMO cover. To the west of the SMO Proterozoic North American ca. 1.8 – 1.6 Ga *Caborca block* basement is inferred to extend to approximately 200 km south of Hermosillo, Sonora, (Figure 2; Valencia-Moreno et al., 2001; Henry et al., 2003). In the east, ca. 1.2 – 1.0 Ga *Grenville-Oaxaquia* basement underlies

extensive parts of Coahuila and eastern and southeastern Chihuahua states beneath the Sierra Madre Oriental (Figure 2; e.g., Rudnick and Cameron, 1991; Centeno-García et al., 2011). Between and to the south of these Proterozoic domains is inferred to be Paleozoic and Mesozoic lithosphere of the accreted Guerrero composite terrane (Centeno-García et al., 2008), which is thought to underlie much of the SMO.

Samples SMO13_08, SMO13_35, and SMO13_48 (Figure 6) yielded concordant $^{207}\text{Pb}/^{206}\text{Pb}$ zircon ages of 1560 Ma, 1057 Ma, and 1237 Ma, respectively. This study shows that rhyolitic SMO magmas incorporated Grenville-Oaxaquia zircons in the east (samples SMO13_35 and SMO13_48) and Caborca zircons in the west (SMO13_08); in both cases these are considerably further south than typically inferred.

Samples SMO13_16, SMO13_19, and SMO13_42 (Figure 6) contain zircons with $^{206}\text{Pb}/^{238}\text{U}$ ages of 157 Ma (Late Jurassic), 176 Ma (Early to Middle Jurassic), and 460 Ma (Ordovician), 371 Ma (Late Devonian) and 150 Ma (Late Jurassic to Early Cretaceous), and 231 Ma (Middle to Late Triassic), respectively, though these ages were not concordant. These ages are typical of range of ages included within the Guerrero composite terrane. The oldest part of the Guerrero is the Ordovician – Early Cretaceous Tahue terrane in Sinaloa and neighboring parts of Chihuahua and Durango states. The Tahue terrane is the only part of the Guerrero to contain Early Paleozoic rocks (Ordovician El Fuerte Complex; Centano-García et al., 2008) and therefore is distinctive. The occurrence of a single Ordovician zircon in SMO13_16 suggests that the El Fuerte Complex underlay the volcanic center that erupted the unnamed SMO13_16 ignimbrite, and that that location was probably close to or to the west of the sample location (Figure 6).

The source of a Devonian zircon in SMO13_19 is unclear as Late Paleozoic sources are not known in northern Mexico or the southern United States. However, Devonian sources may exist in West Africa and may have supplied zircons to the western margin of Mexico via the *Potosi Fan* (Centeno-García, 2005), a major submarine fan system fed by west-flowing rivers in the Triassic. The Potosi Fan supplied turbidites into the basin between Mexico and the off-board Guerrero composite terrane, until opening of the mid-Atlantic and Gulf of Mexico in the Late Triassic and Early Jurassic cut-off the sediment supply from the east. The Potosi Fan was then progressively deformed and accreted to mainland Mexico when the Guerrero composite terrain

was accreted in the Late Jurassic to Late Cretaceous (Laramide; Centeno-García et al., 2008). The Potosi Fan is inferred to underlie much of north-central between 20°N and 25°N, i.e. San Luis Potosi and northern Zacatecas states (Ortega-Flores et al., 2014). The presence of a single Devonian zircon in SMO13_19 suggests, very tentatively, that the Potosi Fan extends further north (i.e. into Durango State) than previously thought, or that erosion accompanying Laramide uplift and recycling of detrital zircons within the Potosi Fan during the Cretaceous redistributed Devonian zircons to the north.

The ca. 231 Ma (Middle to Late Triassic) zircon recovered from sample SMO13_42 (Figure 6) is typical of continental arc magmatism in eastern Mexico during the Permian and Triassic, and preceding opening of the Gulf of Mexico and mid-Atlantic basins. Zircons of this age are common in the remnants of the arc on Oaxaquian basement (northeast Mexico) and throughout the deposits of the Potosi Fan and the eastern parts of the Guerrero composite terrane (Ortega-Flores et al., 2014) with the exception of the Tahue terrane to the far west (Centeno-García et al., 2008). With such a wide dispersal, Triassic zircons could be sourced from almost any part of the eastern Guerrero composite terrane and the Oaxaquian basement, and therefore are very likely to exist in the upper crust beneath the eastern parts of the SMO.

The ca. 176 – 150 Ma zircons in samples SMO13_16 and SMO13_19 are typical of (1) the island arcs and fringing marine sedimentary basins that made up the Guerrero composite terrane (Centeno-García et al., 2008) and (2) the Jurassic to Early Cretaceous continental arcs that developed along the margin of mainland Mexico during accretion of the Guerrero composite terrane and the subduction of the intervening oceanic basin. Without trace element and isotopic characterization of these grains it is impossible to assign them to the ocean or continental arcs with any certainty. However, their presence in western parts of the transect (Figure 6) are more easily explained by underlying Guerrero composite terrane rocks rather than the continental arc that is likely to be considerably further to the east (i.e. beneath or east of Hidalgo de Parral).

4.5.2 *Antecrystic zircons*

Ten ignimbrite samples had significant antecrystic zircon populations, up to 35% (Figure 42). Antecrysts are characterized by minor suites of ages consistently a little older than the inferred eruption age. Because zircon crystallizes throughout rhyolite petrogenesis after zircon saturation is achieved, the range of zircon ages can be extensive, and not just limited to the

Relative percentages of phenocrysts, antecrysts, and xenocrysts in each sample

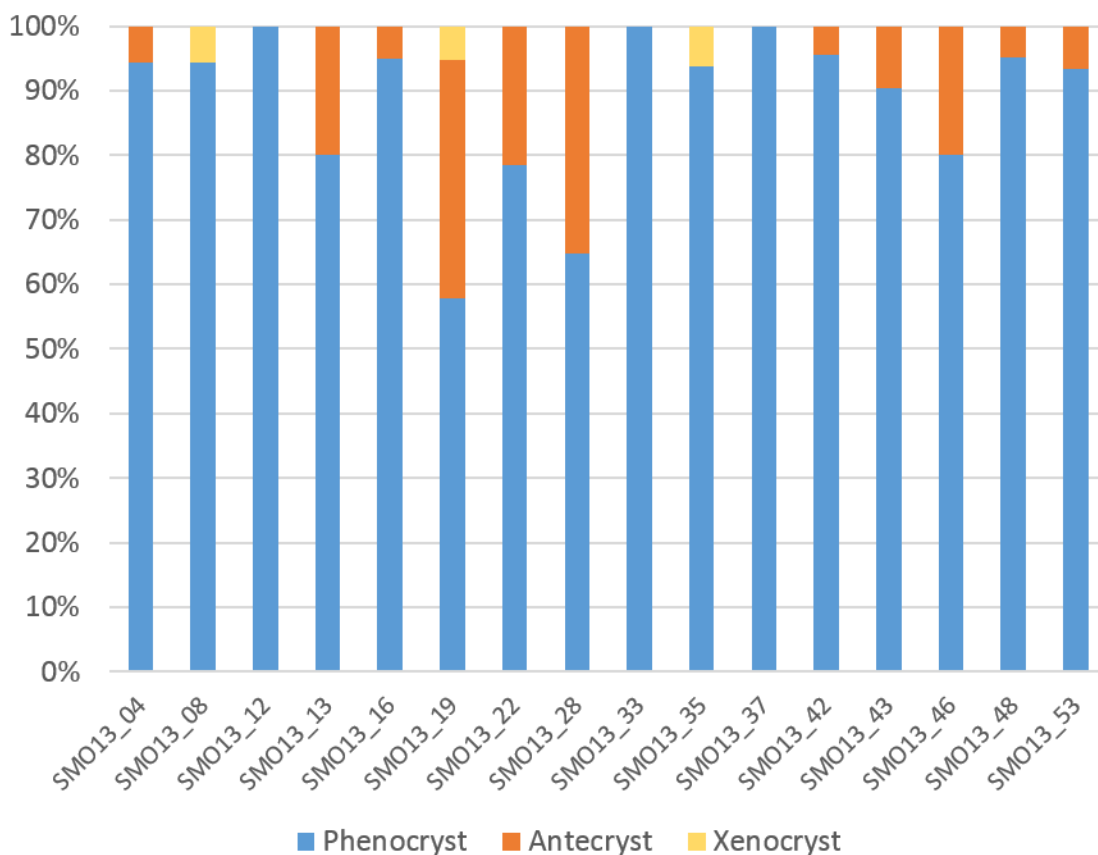


Figure 42. The relative proportions of zircon phenocrysts, antecrysts, and xenocrysts in each sample.

youngest age population that is inferred to be the eruption age. It is because of this long and complex zircon crystallization history that $^{40}\text{Ar}/^{39}\text{Ar}$ ages are so useful because they unambiguously give the eruption age. At some point antecrystic and xenocrystic zircons become difficult to distinguish, especially in long-lived magmatic systems like western Mexico where continental arc magmatism was continuous from the Jurassic to the Miocene. For the purposes of this study I have included all Cretaceous zircons in the Oligocene rhyolites of the SMO13 transect as potential antecrysts.

The greatest proportions of antecrystic zircons are restricted to samples between SMO13_13 and SMO13_28 in the central and western portions of the sample transect, i.e. the unextended core (Figure 6). The antecrysts' $^{206}\text{Pb}/^{238}\text{U}$ crystallization ages range from ca. 40-110 Ma, with the vast majority being Cretaceous (68 – 112 Ma). The most likely sources of Cretaceous antecrystic or xenocrystic zircons are the Laramide Sinaloa batholith (Figure 3) or the Guerrero composite terrane, respectively. If the zircon are scavenged from the Sinaloa batholith then they can be considered antecrystic because they are juvenile, magmatic zircon formed in a continental arc that preceded the SMO arc in the Cenozoic. If they are scavenged from the Guerrero composite terrane they are better considered as xenocrystic because they formed in a different magmatic environment (e.g., an oceanic arc) and may be partially or entirely detrital. Cenozoic zircons notably older than others in the same sample are probably antecrystic and crystallized in the LVC or its plutonic equivalents.

Bryan et al. (2008) suggested that elevated antecryst populations could result from the remelting and disaggregation of igneous rocks formed during Cretaceous to Eocene magmatism (i.e. Sinaloa batholith and LVC). Progressive magmatic underplating, intrusion, and advective heat transfer during sustained arc magmatism thickened and heated the lithosphere beneath the SMO, especially in the younger, western part of the SMO13 transect (Figure 6; Ferrari et al., 2007; Bryan et al., 2008). The increased heat may have accelerated crustal melting in the Sinaloa batholith and surrounding Guerrero composition terrane basement, which would explain why Cretaceous antecrystic zircons are so numerous in the SMO's thick core and western margin, and less abundant in the eastern samples that were erupted through lithosphere that was less influenced by protracted magmatism.

4.6 Patterns and rates of arc migration during roll-back of the Farallon slab

Geochronology data from throughout the SMO indicate that ignimbrite volcanism occurred between ca. 46-40 Ma, ca. 36-28 Ma, and ca. 24-20 Ma (Figure 43; Wark et al., 1990; Bryan et al., 2008; McDowell and McIntosh, 2012; *this study*), of which the 36-28 Ma pulse was most voluminous (McDowell and McIntosh, 2012; Figure 43). Volcanism occurred in broad, NNW-striking belts that became younger to the southwest toward the Gulf of California (McDowell and McIntosh, 2012). Probability density plots for the northern (Figure 44a), central (Figure 44b), and southern (Figure 45) transects (Figure 5) show that peak activity throughout the SMO was not uniform. In the north, activity was strongest around 36 Ma and 30 Ma, with a localized pulse around 45 Ma (Swanson et al., 2006; McDowell and McIntosh, 2012; Murray et al., 2013). Along the central transect (*this study*), activity peaked around 32 Ma and 36 Ma. In the south, peak activity was around 31 Ma and 33 Ma but was much more concentrated, lacking much of the age spectrum evident along the north and central transects, though an early Eocene pulse is present here as well (McDowell and McIntosh, 2012). These pulses likely reflect heat flux caused by slab rollback of the Farallon Plate (Ferrari et al., 2002)

U-Pb and $^{40}\text{Ar}/^{39}\text{Ar}$ age data for SMO units in this study broadly follow this temporal-spatial trend (McDowell and McIntosh, 2012; Figures 6 and 46). Five samples east of (and including) SMO13_33 represent the younger end of the ca. 46-40 Ma pulse (Figure 6). The remaining eight samples west of (and including) SMO13_28, plus SMO13_35 and SMO13_37, and SMO13_42, cover the majority of the unextended SMO core and extended western flank (Figure 6). These samples represent the largest Oligocene ignimbrite pulse (ca. 36-28 Ma) believed to have covered most of western Mexico (Ferrari et al., 2007; Figure 6).

A compilation of published $^{40}\text{Ar}/^{39}\text{Ar}$, K/Ar, and U-Pb age data (Swanson et al., 2006; McDowell and McIntosh, 2012; Murray et al., 2013) and the results of this study reveals the age trends within the SMO (Figure 46). A plot of age versus distance from the Gulf of California coastal plain demonstrates the southwestward younging (Figure 47). The R^2 values for the

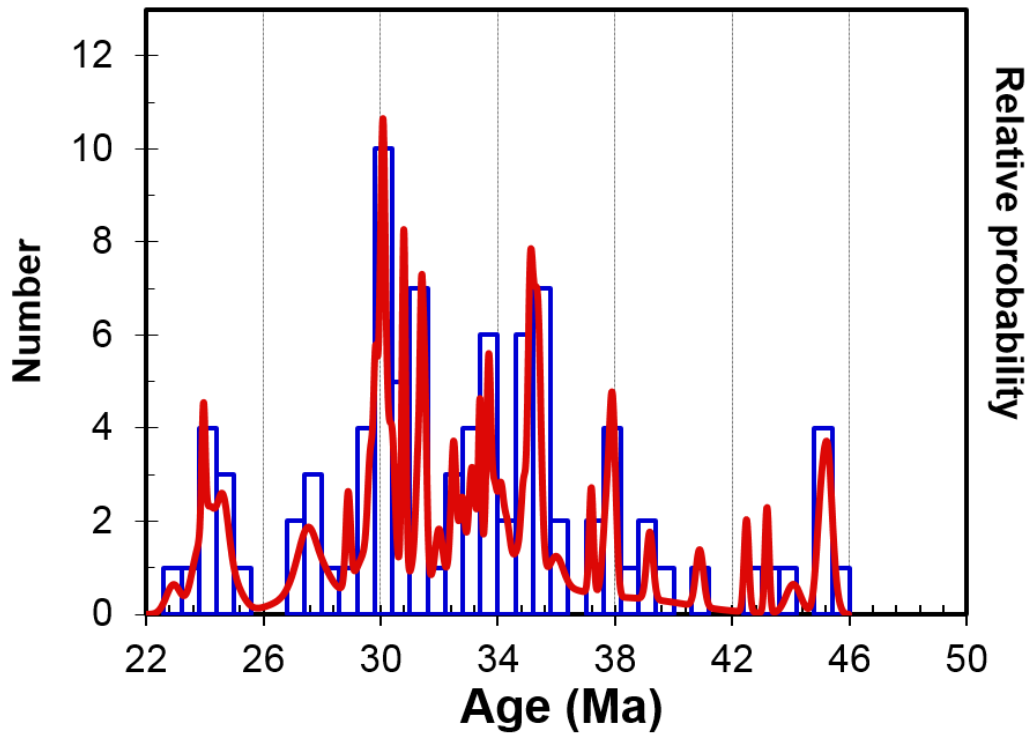


Figure 43. Probability density plot for the northern, central, and southern transects of the SMO (Figure 5 and references therein). Note that volcanic activity was fairly widespread but concentrated in pulses at ~ 25 Ma, ~ 30 Ma, ~ 35 Ma, and ~ 45 Ma. This suggests that peak activity was not consistent through time.

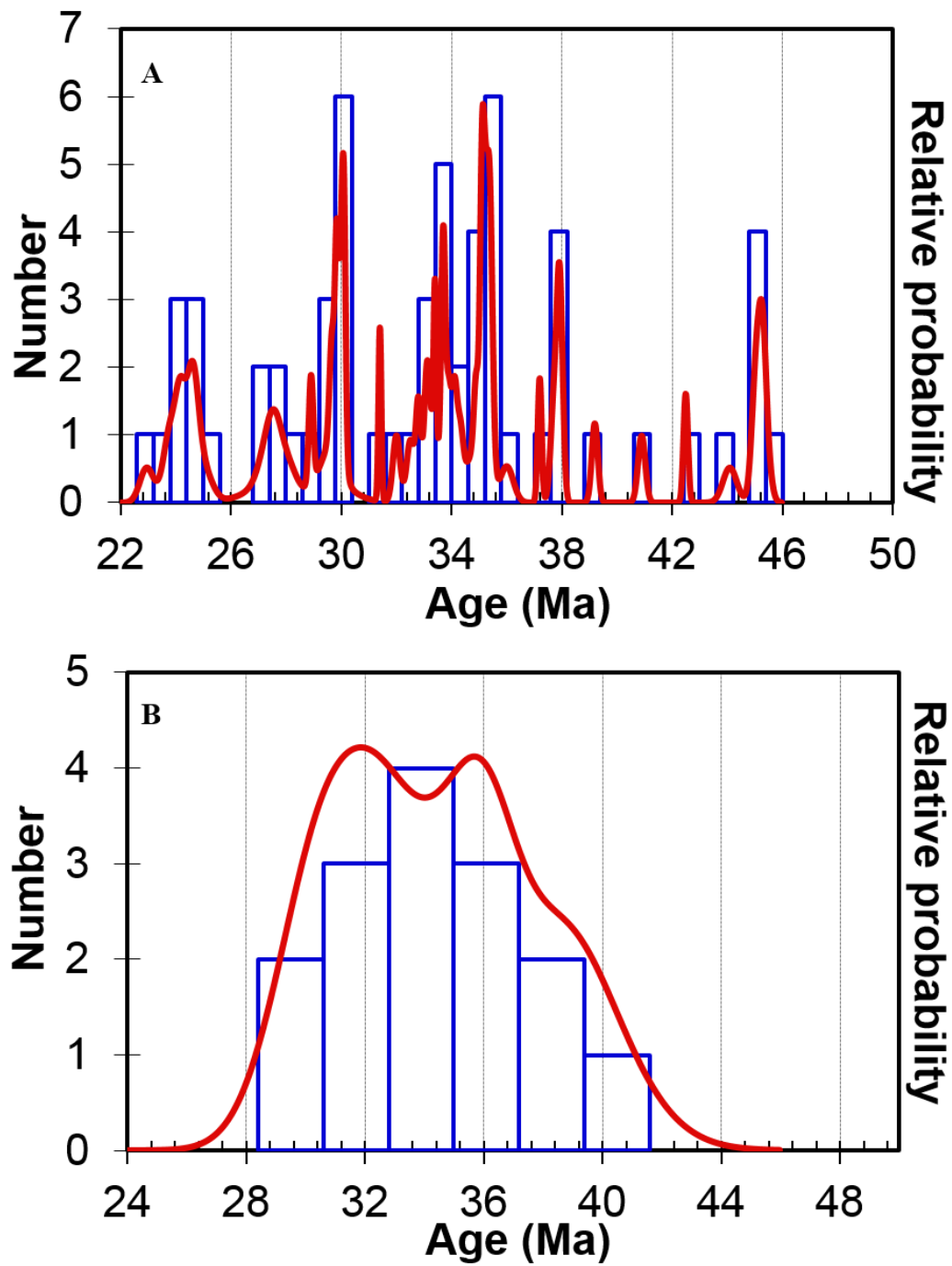


Figure 44. Probability density plots for the **A**) northern sector, and **B**) central sector (Figure 5 and references therein). The northern sector peaks suggest strong activity at ~ 30 Ma and ~ 36 Ma, but in the central sector peak activity was closer to ~ 32 Ma and ~ 36 Ma.

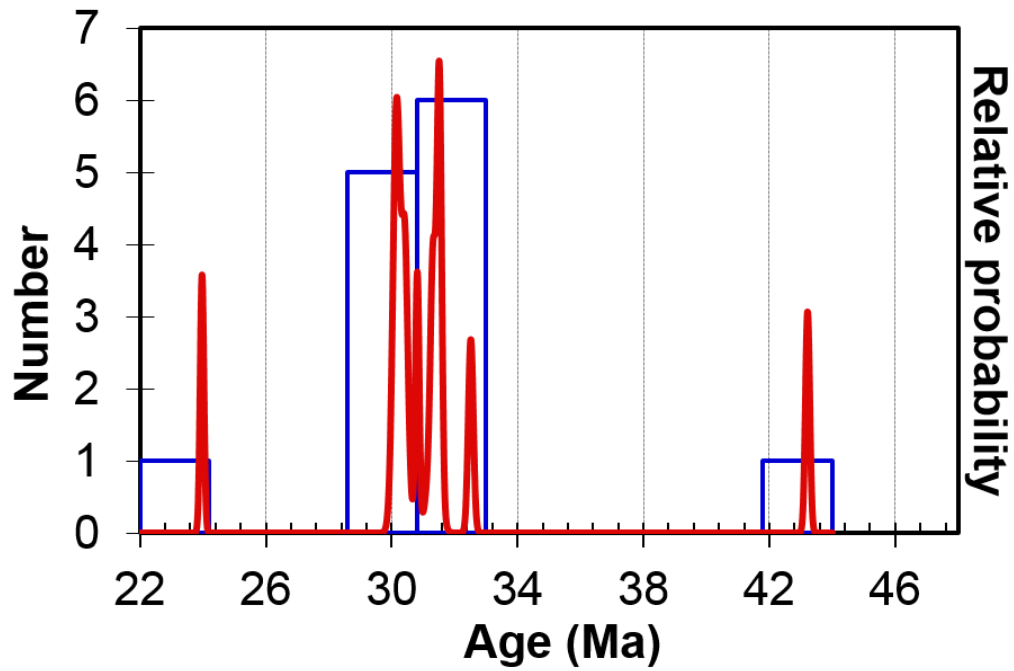


Figure 45. Probability density plot for the southern SMO transect (Figure 5 and references therein). Unlike the northern and southern transects, activity was much more concentrated with less spread of activity than the other transects (Figures 44a and 44b), though this could reflect sampling bias as the southern transect possesses the fewest geochronological data points. Regardless, activity is clearly concentrated at ~ 30 Ma, with localized Eocene and Miocene activity.

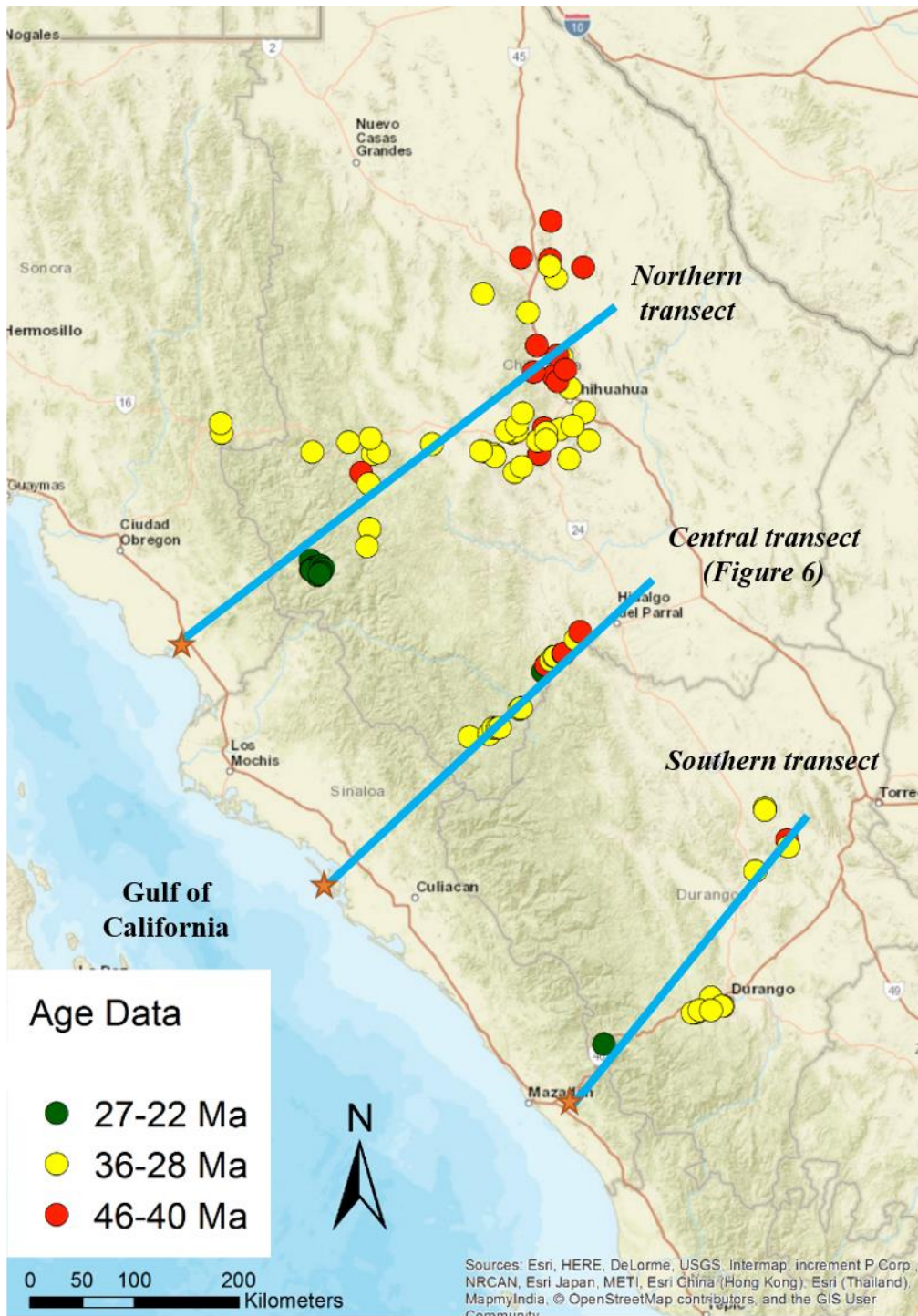


Figure 46. Location data modified from Figure 5 to show ages associated with each sample and sample transect. Samples are older in the northeast and young toward the west. Stars represent arbitrary points along the Gulf of California coast from which each location's position is measured.

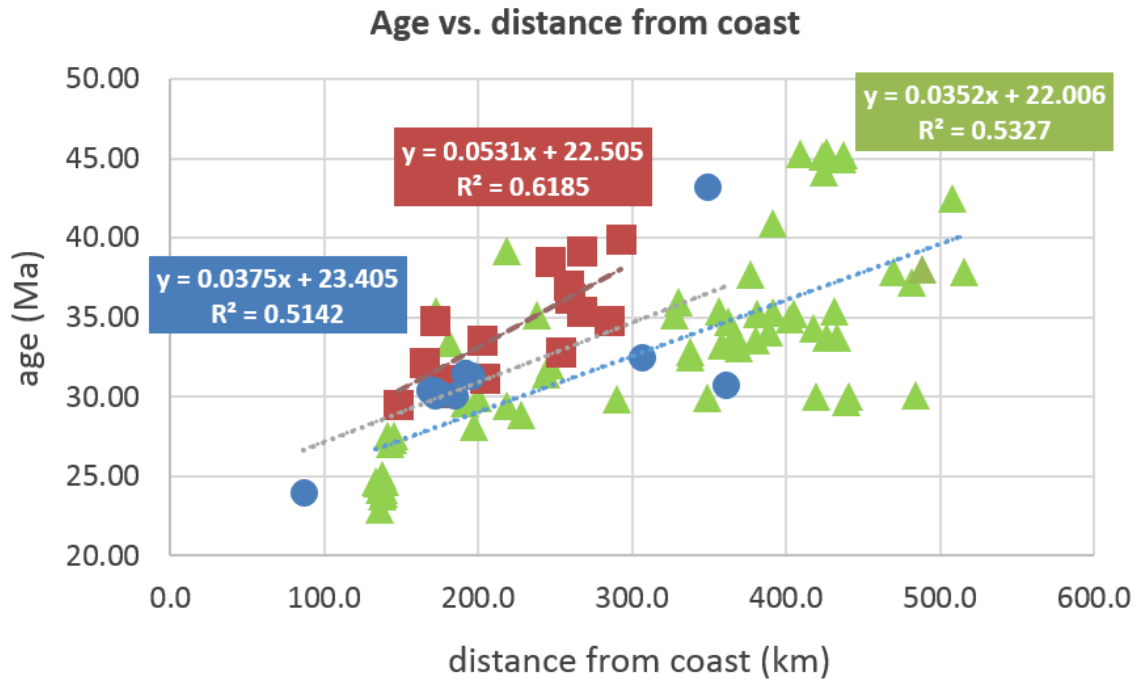


Figure 47. Ages from Figure 5 plotted as a function of distance from the coast (stars, Figure 46) in the northern (green triangles, Figure 5 and references therein), central (red squares, *this study*), and southern (blue circles, Figure 5 and references therein) transects.

northern, central, and southern trendlines are 0.533, 0.619, and 0.513, respectively, implying a fairly strong relationship between distance and age.

The slopes of these trend lines also have implications for the average rate of migration of SMO volcanism. If the axes are reversed then the slope of the trendline is the rate of migration in kilometers per million years (km/Myr; Figure 48). In the northern, central, and southern sectors, volcanism migrated southwestwards at about 15.1, 11.7, and 13.7 km/Myr, respectively. These values are very similar to calculated migration rates in the SMO (10 – 15 km/Myr; 1 – 1.5 cm/yr) published by Henry et al. (2003). These values are within the ranges of arc-trench retreat rates - 0.6 – -1.1 ±3.0 cm/yr) derived from global plate motion models (e.g., Lallemande et al., 2008), where the maximum retreat rate is -12.5 – -14.5 cm/yr in the Tonga arc. An arc-trench rate of 1.5 cm/yr correlates with a subduction rate of ~4 cm/yr (Lallemande et al., 2008). Moderate arc-trench retreat (Figure 49) drives extension (Figure 50) in the over-riding plate that encouraging advective heat transfer from the mantle and increased intrusion of mantle-derived primitive melts into the base of the lithosphere: these are the ingredients necessary to generate voluminous silicic magmatism and a SLIP.

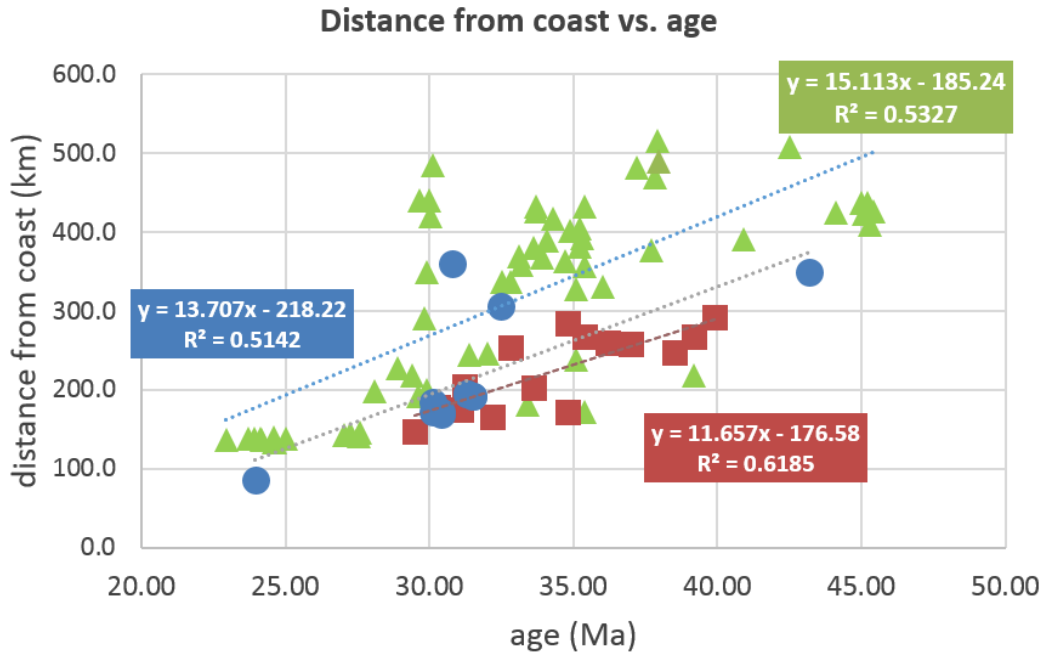


Figure 48. When the axes from Figure 47 are switched the slopes of the resulting trend lines represent a rate of arc-trench migration in terms of km/Myr. The migration rates were not uniform, but broadly consistent with previous estimates of about 10-15 km/Myr (Henry et al., 2003). Northern transect = green triangles (Figure 5 and references therein), central transect = red squares (*this study*), and southern transect = blue circles (Figure 5 and references therein).

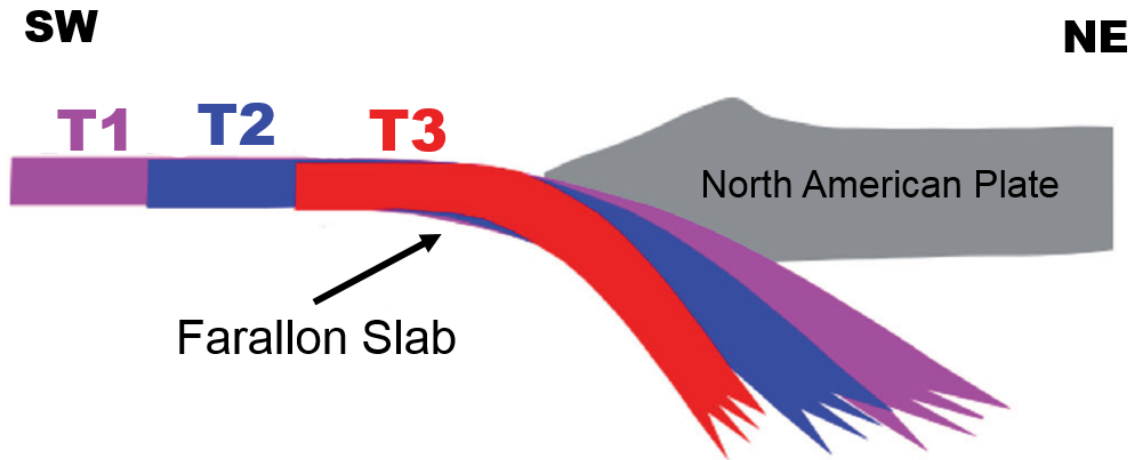


Figure 49. Illustration of slab rollback and the initiation of trench migration. At time T1 the Farallon slab and resulting trench are as far east as they will be. At times T2 and T3, the force of gravity has begun vertically rotating the slab. As the slab rotates, the trench migrates west, away from the original trench. Modified from Niu (2014).

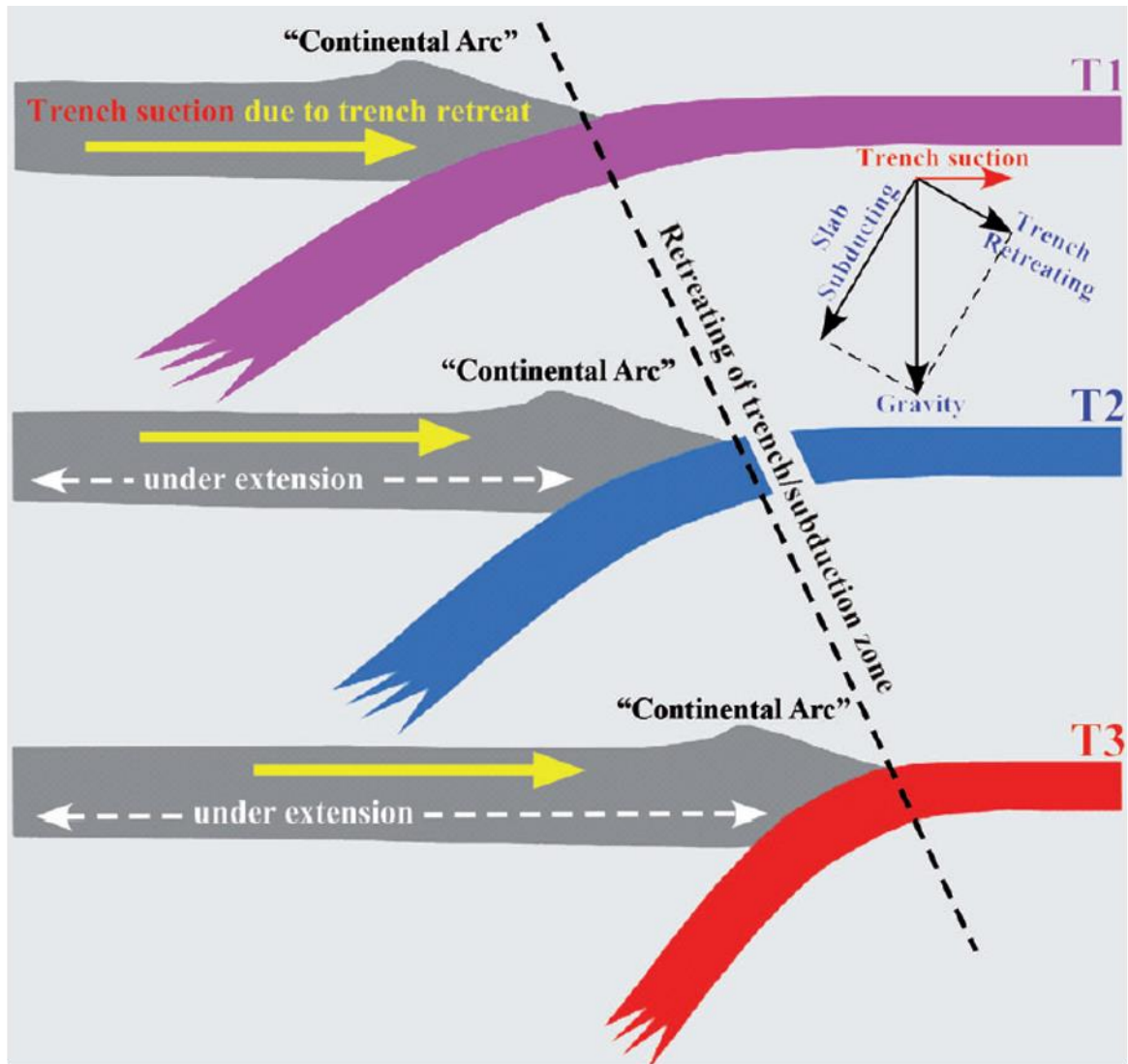


Figure 50. Illustration of migration-induced (Figure 49) extension. As the subducted slab rolls back, the resulting migration of the trench initiates extension in the overriding plate. The new locations of the trench have been marked for times T1, T2, and T3. Modified from Niu (2014).

5. Conclusions

In-situ SIMS U-Pb zircon and $^{40}\text{Ar}/^{39}\text{Ar}$ geochronology analyses were conducted on 17 rhyolitic ignimbrites and lavas collected along a previously unstudied traverse of the Eocene-Oligocene Sierra Madre Occidental silicic large igneous province in Mexico. In all cases $^{206}\text{Pb}/^{238}\text{U}$ zircon crystallization ages were ≤ 2.2 Myr older than the $^{40}\text{Ar}/^{39}\text{Ar}$ cooling ages. The ages of the 17 samples conform to the observed stratigraphy suggesting a relatively simple and layer-cake volcanic stratigraphy along the Chihuahua-Durango state border part of the Sierra Madre Occidental. Using these new age data in conjunction with unpublished geochemical and petrography data, I tentatively correlate samples SMO13_33, SMO13_46, and SMO13_53 to be the same ca. 38.5 Ma, ≥ 26 km³ ignimbrite, the informally named Ojito tuff. Xenocrysts are present in many samples, suggesting input from underlying Paleozoic-Mesozoic composite terranes as well as Proterozoic basement.

The range of ages recorded is broadly consistent with previous models of westward-younging volcanism in the Sierra Madre Occidental (e.g., McDowell and McIntosh, 2012), thought to result from slab rollback of the Farallon Plate beneath North America. The Farallon Plate migrated west at different rates through the north, central, and southern regions of the SMO; westward arc migration was approximately 15.1 km/Myr across the north, 11.7 km/Myr across the central transect, and 13.7 km/Myr across the south. These rates are consistent with those interpreted in the Sierra Madre Occidental by Henry et al. (2003), and estimates of arc-trench migration based on global plate motion models.

References

- Aguirre-Díaz, G.J., and McDowell, F.W., 1991, The volcanic section at Nazas, Durango, Mexico, and the possibility of widespread Eocene volcanism within the Sierra Madre Occidental: *Journal of Geophysical Research*, v. 96, p. 13,373-13,388.
- Aguirre-Díaz, G.J., and McDowell, F.W., 1993, Nature and timing of faulting and synextensional magmatism in the southern Basin and Range, central-eastern Durango, Mexico: *Geological Society of America Bulletin*, v. 105, p. 1,435-1,444.
- Aguirre-Díaz, G.J., and Labarthe-Hernández, G., 2003, Fissure ignimbrites: Fissure-source origin for voluminous ignimbrites of the Sierra Madre Occidental and its relationship with Basin and Range faulting: *Geology*, v. 31, p. 773-776.
- Anderson, T.H., and Silver, L.T., 1981, An overview of Precambrian rocks in Sonora: *Revista Mexicana de Ciencias Geológicas*, v. 5, p. 131-139.
- Anderson, T.H., and Silver, L.T., 2005, The Mojave-Sonora megashear—Field and analytical studies leading to the conception and evolution of the hypothesis, in Anderson, T.H., Nourse, J.A., McKee, J.W., and Steiner, M.B., *eds.*, The Mojave-Sonora megashear hypothesis: Development, assessment, and alternatives: *Geological Society of America Special Paper 393*, p. 1–50.
- Andrews, G.D.M., Davila Harris, P., Brown, S.R., Anderson, L.G., and Moreno, N., 2014, A new sample transect through the Sierra Madre Occidental silicic large igneous province in southern Chihuahua State, Mexico: First stratigraphic, petrologic, and geochemical results: Abstract V33B-4860 presented at 2014 Fall meeting, AGU, San Francisco, California, 13-19 December.
- Bachmann, O., Oberli, F., Dungan, M.A., Meier, M., Mundil, R., and Fischer, H., 2007, $^{40}\text{Ar}/^{39}\text{Ar}$ and U-Pb dating of the Fish Canyon magmatic system, San Juan Volcanic field, Colorado: Evidence for an extended crystallization history: *Chemical Geology*, v. 236, p. 134-166.
- Bateman, P.C., 1992, Plutonism in the central part of the Sierra Nevada batholith, California: U.S. Geological Survey Professional Paper 1483, p. 1-186.
- Bonner, J.L., and Herrin, E.T., 1999, Surface wave studies of the Sierra Madre Occidental of northern Mexico: *Bulletin of Seismological Society of America*, v. 89, p. 1,323-1,337.
- Bowring, S.A., and Schmitz, M.D., 2003, High-precision U-Pb geochronology and the stratigraphic record: *Reviews in Mineralogy and Geochemistry*, v. 53, p. 305-326.
- Branney, M.J., Bonnicksen, B., Andrews, G.D.M., Ellis, B., Barry, T.L. and McCurry, M., 2008, ‘Snake River (SR)-type’ volcanism at the Yellowstone hotspot track: Distinctive products from unusual, high-temperature silicic super-eruptions: *Bulletin of Volcanology*, v. 70, p. 293-314.

- Braun, J., Beek, P.V.D., and Batt, G.E., 2006, Quantitative thermochronology numerical methods for the interpretation of thermochronological data: New York, Cambridge University Press, 270 p.
- Bryan, S.E., 2007, Silicic large igneous provinces: Episodes, v. 30, p. 1-12.
- Bryan, S.E., Ferrari, L., Reiners, P.W., Allen, C.M., Petrone, C.M., Romas-Rosique, A., and Campbell, I.H., 2008, New insights into crustal contributions to large-volume rhyolite generation in the mid-Tertiary Sierra Madre Occidental province, Mexico, revealed by U-Pb geochronology: *Journal of Petrology*, v. 49, p. 44-77.
- Bryan, S.E., and Ferrari, L., 2013, Large igneous provinces and silicic large igneous provinces: Progress in our understanding over the last 25 years: *Geological Society of America Bulletin*, v. 125, p. 1,053-1,080.
- Bryan, S.E., Peate, I.U., Peate, D.W., Self, S., Jerram, D.A., Mawby, M.R., Marsh, J.S. (Goonie), & Miller, J.A., 2010, The largest volcanic eruptions on Earth: *Earth-Science Reviews*, v. 102, p. 207-229.
- Busby, C.J., 2008, Geology of the Sierra Madre Occidental, Mexico: November 2008 LIP of the Month, Large Igneous Provinces Commission, <http://www.largeigneousprovinces.org/08nov> (Accessed May 2016).
- Cameron, K.L., Nimz, G.J., Kuentz, D., Niemeyer, S., and Gunn, S., 1989, Southern Cordilleran Basaltic Andesite suite, southern Chihuahua, Mexico: A link between Tertiary continental arc and flood basalt magmatism in North America: *Journal of Geophysical Research*, v. 94, p. 7,817-7,840.
- Cameron, K.L., Robinson, J.V., Niemeyer, S., Nimz, G.J, Kuentz, C., Harmon, R.S., Bohlen, S.R., and Collerson, K.D., 1992, Contrasting styles of pre-Cenozoic and mid-Tertiary crustal evolution in Northern Mexico: Evidence from deep crustal xenoliths from La Olivina: *Journal of Geophysical Research*, v. 97, p. 17,353-17,376.
- Cameron, K.L., and Ward, R.L., 1998, Xenoliths of Grenvillian granulite basement constrain models for the origin of voluminous Tertiary rhyolites, Davis Mountains, west Texas: *Geology*, v. 26, p. 1,087-1,090.
- Campa, M. F., and Coney, P.J., 1983, Tectono-stratigraphic terranes and mineral resource distributions in Mexico: *Canadian Journal of Earth Sciences*, v. 20, p. 1,040-1,051.
- Centeno-García, E., 2005, Review of Upper Paleozoic and Lower Mesozoic stratigraphy and depositional environments of central and west Mexico: Constraints on terrane analysis and paleogeography, *in* Anderson, T.H., Nourse, J.A., Mc Kee, J.W., and Steiner, M.B., *eds.*, The Mojave-Sonora megashear hypothesis: Development, assessment, and alternatives: *Geological Society of America Special Papers* 393, p. 233–258.

- Centeno-García, E., Guerrero-Suastegui, M., and Talavera-Mendoza, O., 2008, The Guerrero Composite Terrane of western Mexico: Collision and subsequent rifting in a supra-subduction zone, *in* Draut, A., Clift, P.D., and Scholl, D.W., *eds.*, Formation and Applications of the Sedimentary Record in Arc Collision Zones: Geological Society of America Special Paper 436, p. 279–308.
- Centeno-García, E., Busby, C., Busby, M., and Gehrels, G., 2011, Evolution of the Guerrero composite terrane along the Mexican margin, from extensional fringing arc to the contractional continental arc: Geological Society of America Bulletin, v. 123, p. 1,776-1,797.
- Clark, K.F., Dow, R.R., and Knowling, R.D., 1979, Fissure-vein deposits related to continental volcanic and subvolcanic terranes in Sierra Madre Occidental province, Mexico, *in* Ridge, J.D. *ed.*, Papers on Mineral Deposits of Western North America: Proceedings of the Fifth IAGOD Quadrennial Symposium, Nevada Bureau of Mines and Geology Report 33, p. 189-201.
- Coenraads, R.R., Sutherland, F.L., and Kinny, P.D., 1990, The origin of sapphires: U-Pb dating of zircon inclusions sheds new light: Mineralogical Magazine, v. 54, p. 113-122.
- Colón, D.P., Bindeman, I.N., Ellis, B.S., Schmitt, A.K., and Fisher, C.M., 2015, Hydrothermal alteration and melting of the crust during the Columbia River Basalt-Snake River Plain transition and the origin of low-d¹⁸O rhyolites of the central Snake River Plain: Lithos, v. 224-225, p. 310-323.
- Coney, P.J., Reynolds, S.J., 1977, Cordilleran Benioff zones: Nature, v. 270, p. 403-406.
- Crowley, J.L., Schoene, B., and Bowring, S.A., 2007, U-Pb dating of zircon in the Bishop Tuff at the millennial scale: Geology, v. 35, p. 1,123-1,126.
- Damon, P.E., Shafiqullah, M., and Clark, K.F., 1981, Geochronology of the porphyry copper deposits and related mineralization of Mexico: Canadian Journal of Earth Sciences, v. 20, p. 1,052-1,071.
- Dodson, M.H., 1973, Closure temperature in cooling geochronological and petrological systems: Contributions to Mineralogy and Petrology, v. 40, p. 259-274.
- Ferrari, L., López-Martínez, M., and Rosas-Elguera, J., 2002, Ignimbrite flare-up and deformation in the southern Sierra Madre Occidental, western Mexico: Implications for the late subduction history of the Farrallon plate: Tectonics, v. 21, p. 1-24.
- Ferrari, L., Valencia-Moreno, M., and Bryan, S., 2007, Magmatism and tectonics of the Sierra Madre Occidental and its relation with the evolution of the western margin of North America, *in* Alaniz-Álvarez, S.A., and Nieto-Samaniego, Á.F., *eds.*, Geology of México: Celebrating the Centenary of the Geological Society of México: Geological Society of America Special Paper 422, p. 1–39.
- Ferrari, L., Bryan, S.E., Rosique, A.R., Allen, C., López, M., and Rankin, A., 2010, Relationships between rates of silicic magma generation, eruption and extensional tectonics: Insights from the Bolaños Graben, Southern Sierra Madre Occidental, Mexico: Geophysical Research Abstracts, v. 12, EGU2010-3825-1, EGU General Assembly 2010.

- Gans, P.B., 1997, Large-magnitude Oligo-Miocene extension in southern Sonora: Implications for the tectonic evolution of northwestern Mexico: *Tectonics*, v. 16, p. 388-408.
- González León, C.M., McIntosh, W.C., Lozano-Santacruz, R., Valencia-Moreno, M., Amaya-Martínez, R., and Rodríguez-Castañeda, J.L., 2000, Cretaceous and Tertiary sedimentary, magmatic, and tectonic evolution of north-central Sonora (Arizpe and Bacanuchi Quadrangles), northwest Mexico: *Geological Society of America Bulletin*, v. 112, p. 600-610.
- Grant, G.J., and Ruiz, J., 1988, The Pb-Zn-Cu-Ag deposits of the Granadena Mine, San Francisco del Oro - Santa Barbara district, Chihuahua, Mexico: *Economic Geology*, v. 83, p. 1,683-1,702.
- Henry, C.D., and Aranda-Gomez, J.J., 1992, The real southern Basin and Range: Mid- to late Cenozoic extension in Mexico: *Geology*, v. 20, p. 701-704.
- Henry, C.D., and Aranda-Gomez, J.J., 2000, Plate interactions control middle-late Miocene, proto-Gulf and Basin and Range extension in the southern Basin and Range: *Tectonophysics*, v. 318, p. 1-26.
- Henry, C.D., McDowell, F.W., and Silver, L.T., 2003, Geology and geochronology of granitic batholithic complex, Sinaloa, México: Implications for Cordilleran magmatism and tectonics, *in* Johnson, S.E., Paterson, S.R., Fletcher, J.M., Girty, G.H., Kimbrough, D.L., and Martín-Barajas, A., *eds.*, *Tectonic evolution of north-western México and the southwestern USA*: Boulder, Colorado, Geological Society of America Special Paper 374, p. 237-273.
- Hodges, K.V., 2013, Thermochronology in orogenic systems, *in* Holland, H.D. and Turekian, K.K., *Treatise on Geochemistry* (2nd edition), v. 4, p. 281-308. Oxford: Elsevier.
- Hora, J.M., Singer, B.S., Jicha, B.R., Beard, B.L., Johnson, C.M., de Silva, S., and Salisbury, M., 2010, Volcanic biotite-sanidine ⁴⁰Ar/³⁹Ar age discordances reflect Ar partitioning and pre-eruption closure in biotite: *Geology*, v. 38, p. 923-926.
- Humphreys, E.D., 1995, Post-Laramide removal of the Farallon slab, western United States: *Geology*, v. 23, p. 987-990.
- Ireland, T.R., and Williams, I.S., 2003, Considerations in zircon geochronology by SIMS: *Reviews in Mineralogy and Geochemistry*, v. 53, p. 215-241.
- Kelley, S., 2002, K-Ar and Ar-Ar dating: *Reviews in Mineralogy and Geochemistry*, v. 47, p. 785-818.
- Lallemande, S., Heuret, A., Faccenna, C., and Funicello, F., 2008, Subduction dynamics as revealed by trench migration: *Tectonics*, v. 27, p. 1-15.
- Lanphere, MA., Cameron, K.L., and Cameron, M., 1980, Sr isotopic geochemistry of voluminous rhyolitic ignimbrites and related rocks, Batopilas area, western Mexico: *Nature*, v. 286, p. 594-596.
- Lang, B., Steinitz, G., Sawkins, F.J., and Simmons, S.F., 1988, K-Ar age studies in the Fresnillo Silver District, Zacatecas, Mexico: *Economic Geology*, v. 83, p. 1,642-1,646.

- Lee, J.K.W., 2015, Single-crystal laser fusion: *in* Rink, W., and Thompson, J., *eds.*, *Encyclopedia of Scientific Dating Methods*, p. 760-763.
- Ludwig, K.R., 2012, *Isoplot 3.75: A geochronological toolkit for Microsoft Excel*: Berkeley Geochronology Center, Special Publication no. 5, p. 1-75.
- Luhr, J.F., Henry, C.D., Housh, T.B., Aranda-Gómez, J.J., and McIntosh, W.C., 2001, Early extension and associated mafic alkali volcanism from the southern Basin and Range Province: Geology and petrology of the Rodeo and Nazas volcanic fields, Durango, Mexico: *Geological Society of America Bulletin*, v. 113, p. 760-773.
- Mason, B.G., Pyle, D.M. and Oppenheimer, C., 2004, The size and frequency of the largest explosive eruptions on Earth: *Bulletin of Volcanology*, v. 66, p. 735-748.
- Matmon, A., Briner, J.P., Carver, G.A., Bierman, P., and Finkel, R.C., 2010, Moraine chronosequence of the Donnelly Dome region, Alaska: *Quaternary Research*, v. 74, p. 63-72.
- McDowell, F.W., and Keizer, R.P., 1977, Timing of mid-Tertiary volcanism in the Sierra Madre Occidental between Durango City and Mazatlan, Mexico: *Geological Society of America Bulletin*, v. 88, p. 1,479-1,487.
- McDowell, F.W., Clabaugh, S.E., 1979, Ignimbrites of the Sierra Madre Occidental and their relation to the tectonic history of western Mexico, *in* Chapin, C.E., and Elston, W.E., *eds.*, *Geological Society of America Special Paper 180*, p. 113–124.
- McDowell, F.W., and Mauger, R.L., 1994, K-Ar and U-Pb zircon chronology of Late Cretaceous and Tertiary magmatism in central Chihuahua State, Mexico: *Geological Society of America Bulletin*, v. 106, p. 118-132.
- McDowell, F.W., Roldán-Quintana, J., and Connelly, J.N., 2001, Duration of Late Cretaceous-early Tertiary magmatism in east-central Sonora, Mexico: *Geological Society of America Bulletin*, v. 113, p. 521-531.
- McDowell, F.W., and McIntosh, W.C., 2012, Timing of intense magmatic episodes in the northern and central Sierra Madre Occidental, western Mexico: *Geosphere*, v. 8, p. 1,505-1,526.
- Murray, B.P., Busby, C.J., Ferrari, L., and Solari, L.A., 2013, Synvolcanic crustal extension during the mid-Cenozoic ignimbrite flare-up in the northern Sierra Madre Occidental, Mexico: Evidence from the Guazapares Mining District region, western Chihuahua: *Geosphere*, v. 9, p. 1-35.
- Newhall, C.G., and Self, S., 1982, The volcanic explosivity index (VEI) – an estimate of explosive magnitude for historical volcanism: *Journal of Geophysical Research*, v. 87, p. 1,231–1,238.
- Niu, Y., 2014, Geological understanding of plate tectonics: Basic concepts, illustrations, examples and new perspectives: *Global Tectonics and Metallogeny*, v. 10, p. 23-46.

- Ortega-Flores, B., Solari, L., Lawton, T.F., and Ortega-Obregón, C., 2014, Detrital-zircon record of major Middle Triassic–Early Cretaceous provenance shift, central Mexico: demise of Gondwanan continental fluvial systems and onset of back-arc volcanism and sedimentation: *International Geology Review*, v. 56, p. 237-261.
- Paces, J.B., and Miller, J.D., 1993, Precise U-Pb ages of Duluth Complex and related mafic intrusions, Northeastern Minnesota: Geochronological insights to physical, petrogenetic, paleomagnetic, and tectonomagmatic processes associated with the 1.1 Ga midcontinent rift system: *Journal of Geophysical Research*, v. 98, p. 13,997-14,013.
- Pérez-Segura, E., González-Partida, E., and Valencia, V.A., 2009, Late Cretaceous adakitic magmatism in east-central Sonora, Mexico, and its relation to Cu-Zn-Ni-Co skarns: *Revista Mexicana de Ciencias Geológicas*, v. 26, p. 411-427.
- Roldán-Quintana, J., 1991, Geology and chemical composition of the Jaralito and Aconchi batholiths in east-central Sonora, Mexico: *in* Pérez-Segura, E., and Jacques-Ayala, C., *eds.*, *Studies of Sonoran Geology: Geological Society of America Special Paper 254*, p. 69-80.
- Rudnick, R.L., and Cameron, K.L., 1991, Age diversity of the deep crust in northern Mexico: *Geology*, v. 18, p. 1,197-1,200.
- Schaltegger, U., Schmitt, A.K., and Horstwood, M.S.A., 2015, U-Th-Pb zircon geochronology by ID-TIMS, SIMS, and laser ablation ICP-MS: Recipes, interpretations, and opportunities: *Chemical Geology*, v. 402, p. 89-110.
- Scheubel, F.R., Clark, K.F., and Porter, E.W., 1988, Geology, tectonic environment, and structural controls in the San Martín de Bolaños district, Jalisco, Mexico: *Economic Geology*, v. 83, p. 1,703-1,720.
- Schoene, B., 2013, U-Th-Pb Geochronology, *in* Holland, H.D. and Turekian, K.K., *Treatise on Geochemistry (2nd edition)*, v. 4, p. 341-378. Oxford: Elsevier.
- Sedlock, R.L., Ortega-Gutiérrez, F., and Speed, R.C., 1993, Tectonostratigraphic terranes and tectonic evolution of Mexico: Boulder, Colorado, Geological Society of America Special Paper 278, p. 1-142.
- Steiger, R.H., and Jäger, E., 1977, Subcommittee on geochronology: Convention on the use of decay constants in geo- and cosmochemistry: *Earth and Planetary Science Letters*, v. 36, p. 359-362.
- Stewart, J.H., 1978, Basin-range structure in western North America: A review: *Geological Society of America, Memoir 152*, p. 1-32.
- Swanson, E.R., Keizer, R.P., Lyons, J.I., and Clabaugh, S.E., 1978, Tertiary volcanism and caldera development near Durango City, Sierra Madre Occidental, Mexico: *Geological Society of America Bulletin*, v. 89, p. 1,000-1,012.

- Swanson, E.R., and McDowell, F.W., 1984, Calderas of the Sierra Madre Occidental volcanic field western Mexico: *Journal of Geophysical Research*, v. 89, p. 8,787-8,799.
- Swanson, E.R., Kempter, K.A., McDowell, F.W., and McIntosh, W.C., 2006, Major ignimbrites and volcanic centers of the Copper Canyon area: A view into the core of Mexico's Sierra Madre Occidental: *Geosphere*, v. 2, p. 125-141.
- USRG, 2008, Macquarie University U-series research group: <https://research.science.mq.edu.au/u-series-research-group/facil.html> (accessed May 2016).
- Valencia-Moreno, M. Ruiz, J., Patchett, P.J., Zurcher, L., and Hodkinson, D.G., and Roldán-Quintana, J., 2001, A chemical isotopic study of the Laramide granitic belt of northwestern Mexico: Identification of the southern edge of the North American Precambrian basement: *Geological Society of America Bulletin*, v. 113, p. 1,409-1,422.
- Wark, D.A., Kempter, K.A., and McDowell, F.W., 1990, Evolution of waning, subduction-related magmatism, northern Sierra Madre Occidental, Mexico: *Geological Society of America Bulletin*, v. 102, p. 1,555-1,564.
- Wark, D.A., 1991, Oligocene ash flow volcanism, northern Sierra Madre Occidental: Role of mafic and intermediate-composition magmas in rhyolite genesis: *Journal of Geophysical Research*, v. 96, p. 13,389-13,411.
- Wetherill, G.W., 1956, Discordant uranium-lead ages, I: *Transactions, American Geophysical Union*, v. 37, p. 320-326.
- WiscAr Geochronology Lab, 2016, Analytical approaches: <http://geochronology.geoscience.wisc.edu/analytical-approaches> (accessed May 2016).

Appendix A –U-Pb Data

Sample	Isotopic Ratios					$^{206}\text{Pb}/^{238}\text{U}$		$^{207}\text{Pb}/^{235}\text{U}$		$^{207}\text{Pb}/^{206}\text{Pb}$		Common Pb			
	$^{207}\text{Pb}/^{235}\text{U}$	$\pm 1\sigma$ (%)	$^{206}\text{Pb}/^{238}\text{U}$	$\pm 1\sigma$ (%)	Correlation of Concordia Ellipses	Age (Ma)	$\pm 1\sigma$	Age (Ma)	$\pm 1\sigma$	Age (Ma)	$\pm 1\sigma$	$^{206}\text{Pb}/^{204}\text{Pb}$	$^{207}\text{Pb}/^{204}\text{Pb}$	$^{208}\text{Pb}/^{204}\text{Pb}$	Pb corr.
SMO13_02	0.03366	7.79	0.005316	5.08	0.688	34.2	1.7	33.62	2.58	-1	0.0026	18.86	15.62	38.34	(204Pb)
	0.04009	7.03	0.005929	6.69	0.96	38.1	2.5	39.91	2.75	150	46.4	18.86	15.62	38.34	(204Pb)
	0.08939	23.4	0.008184	22.4	0.852	53	12	86.94	19.5	1178	247	18.86	15.62	38.34	(204Pb)
	0.05447	13.9	0.009327	8.2	0.662	59.9	4.9	53.85	7.31	-1	0.00444	18.86	15.62	38.34	(204Pb)
	0.03375	53.2	0.009581	6.97	0.337	61.5	4.3	33.71	17.6	-1	0.0131	18.86	15.62	38.34	(204Pb)
	0.05774	19.2	0.009599	6.86	0.426	61.6	4.2	57	10.6	-1	0.00759	18.86	15.62	38.34	(204Pb)
	0.0615	8.55	0.009976	5.43	0.699	64.0	3.5	60.6	5.03	-1	0.00275	18.86	15.62	38.34	(204Pb)
	0.07055	10.2	0.01005	7.41	0.738	64.4	4.8	69.22	6.82	237.8	159	18.86	15.62	38.34	(204Pb)
	0.06513	42.4	0.01014	32.6	0.748	65	21	64.07	26.3	26.85	676	18.86	15.62	38.34	(204Pb)
	0.05869	12.6	0.01067	7.68	0.653	68.5	5.2	57.91	7.1	-1	0.00382	18.86	15.62	38.34	(204Pb)
	0.06391	13.6	0.01074	7.74	0.6	68.9	5.3	62.91	8.31	-1	0.00471	18.86	15.62	38.34	(204Pb)
	0.06043	16.1	0.0108	8.13	0.583	69.3	5.6	59.58	9.3	-1	0.00532	18.86	15.62	38.34	(204Pb)
	0.06845	14.7	0.01089	8.13	0.621	69.8	5.7	67.22	9.55	-1	0.00526	18.86	15.62	38.34	(204Pb)
	0.05344	20	0.01089	8.85	0.515	69.8	6.1	52.86	10.3	-1	0.00612	18.86	15.62	38.34	(204Pb)
	0.07533	9.22	0.01099	7.75	0.833	70.5	5.4	73.74	6.56	180.8	119	18.86	15.62	38.34	(204Pb)
	0.07686	11.4	0.0116	8.65	0.811	74.4	6.4	75.19	8.26	102	158	18.86	15.62	38.34	(204Pb)
	0.0137	358	0.01207	85.5	0.239	77	66	13.82	49.1	-1	0.0286	18.86	15.62	38.34	(204Pb)
0.1406	13.8	0.01271	10.1	0.773	81.4	8.2	133.6	17.3	1203	173	18.86	15.62	38.34	(204Pb)	
0.0733	11.9	0.01323	7.61	0.66	84.7	6.4	71.83	8.24	-1	0.00359	18.86	15.62	38.34	(204Pb)	
SMO13_04	-0.1155	-35.7	0.002992	12.9	0.841	19.3	2.5	-124.6	47.3	-1	-0.132	18.86	15.62	38.34	(204Pb)
	-0.005345	-475	0.00404	8.79	0.527	26.0	2.3	-5.442	25.9	-1	-0.0461	18.86	15.62	38.34	(204Pb)
	0.01946	54.2	0.004111	5.56	0.462	26.5	1.5	19.57	10.5	-1	0.0178	18.86	15.62	38.34	(204Pb)
	-0.00001924	-6.11E+04	0.004264	9.33	0.249	27.4	2.6	-0.01953	11.9	-1	-0.02	18.86	15.62	38.34	(204Pb)
	0.01369	117	0.004516	9.2	0.378	29.1	2.7	13.81	16.1	-1	0.0251	18.86	15.62	38.34	(204Pb)
	0.048	22.3	0.004548	6.28	0.664	29.3	1.8	47.6	10.4	1109	375	18.86	15.62	38.34	(204Pb)
	0.02881	49.2	0.004566	9.23	0.45	29.4	2.7	28.84	14	-1	0.021	18.86	15.62	38.34	(204Pb)
	0.003714	696	0.004575	10.2	0.479	29.4	3.0	3.764	26.2	-1	0.0407	18.86	15.62	38.34	(204Pb)
	-0.01419	-228	0.004683	11.8	0.462	30.1	3.5	-14.51	33.3	-1	-0.0513	18.86	15.62	38.34	(204Pb)
	-0.0005843	-2.81E+03	0.004738	10.4	0.268	30.5	3.2	-0.5934	16.7	-1	-0.0251	18.86	15.62	38.34	(204Pb)
	0.02708	27.5	0.004761	9.02	0.416	30.6	2.8	27.13	7.37	-1	0.0104	18.86	15.62	38.34	(204Pb)
	0.0488	22.6	0.004971	9.26	0.552	32.0	3.0	48.38	10.7	963.1	390	18.86	15.62	38.34	(204Pb)
	0.06778	18.7	0.005011	8.84	0.505	32.2	2.8	66.59	12	1588	301	18.86	15.62	38.34	(204Pb)
	0.05771	22.9	0.00514	9.7	0.6	33.1	3.2	56.97	12.7	1232	369	18.86	15.62	38.34	(204Pb)
	0.01901	46	0.005191	9.6	0.341	33.4	3.2	19.12	8.7	-1	0.0116	18.86	15.62	38.34	(204Pb)
	0.04681	22.5	0.005384	9.3	0.543	34.6	3.2	46.45	10.2	710.3	407	18.86	15.62	38.34	(204Pb)
	0.03294	63.7	0.005522	10.9	0.448	35.5	3.9	32.91	20.6	-1	0.0258	18.86	15.62	38.34	(204Pb)
0.1024	29.3	0.005853	6.85	0.739	37.6	2.6	98.96	27.7	2055	436	18.86	15.62	38.34	(204Pb)	
SMO13_08	0.03797	19	0.002965	4.44	0.495	19.1	0.8	37.84	7.04	1485	326	18.86	15.62	38.34	(204Pb)
	0.06311	22.6	0.003586	5.98	0.728	23.1	1.4	62.14	13.6	2066	330	18.86	15.62	38.34	(204Pb)
	0.079	28.9	0.004368	6.29	0.636	28.1	1.8	77.21	21.5	2114	445	18.86	15.62	38.34	(204Pb)
	0.06679	31.3	0.004748	7.66	0.687	30.5	2.3	65.65	19.9	1662	493	18.86	15.62	38.34	(204Pb)

	0.03439	35.3	0.004763	4.97	0.532	30.6	1.5	34.33	11.9	301.1	751	18.86	15.62	38.34	(204Pb)
	0.06297	16.3	0.004945	5.77	0.684	31.8	1.8	62.01	9.83	1475	248	18.86	15.62	38.34	(204Pb)
	0.03863	9.77	0.004967	4.24	0.601	31.9	1.4	38.48	3.69	468.2	177	18.86	15.62	38.34	(204Pb)
	0.0458	10.6	0.005202	5.26	0.577	33.5	1.8	45.47	4.7	736.9	184	18.86	15.62	38.34	(204Pb)
	0.08173	29.5	0.005302	7.8	0.684	34.1	2.7	79.77	22.7	1829	450	18.86	15.62	38.34	(204Pb)
	0.09781	11.7	0.005342	5.12	0.697	34.4	1.8	94.75	10.6	2135	156	18.86	15.62	38.34	(204Pb)
	0.04327	23.7	0.005443	5.95	0.525	35.0	2.1	43.01	10	516.6	466	18.86	15.62	38.34	(204Pb)
	0.06389	108	0.00549	13.3	0.785	35.3	4.7	62.88	65.7	1302	1.90E+03	18.86	15.62	38.34	(204Pb)
	0.1655	52.7	0.005745	14.1	0.805	36.9	5.2	155.5	76	2897	684	18.86	15.62	38.34	(204Pb)
	0.237	20.7	0.006194	9.16	0.868	39.8	3.6	216	40.2	3349	211	18.86	15.62	38.34	(204Pb)
	0.3998	19.1	0.007499	10.6	0.921	48.2	5.1	341.5	55.5	3858	154	18.86	15.62	38.34	(204Pb)
	0.7463	21.5	0.01092	14.9	0.952	70	10	566.1	93.4	4228	128	18.86	15.62	38.34	(204Pb)
	0.1825	5.38	0.01369	4.86	0.908	87.7	4.2	170.2	8.43	1560	42.4	18.86	15.62	38.34	(204Pb)
	1.213	19.7	0.01475	15.8	0.951	94	15	806.4	110	4499	98.5	18.86	15.62	38.34	(204Pb)
SMO13_12	0.03006	14.4	0.003209	4.25	0.626	20.7	0.9	30.08	4.26	867	252	18.86	15.62	38.34	(204Pb)
	0.004097	1.13E+03	0.004409	10.4	0.748	28.4	3.0	4.152	46.6	-1	0.0753	18.86	15.62	38.34	(204Pb)
	0.01664	609	0.004688	19.5	0.86	30.2	5.9	16.75	101	-1	0.152	18.86	15.62	38.34	(204Pb)
	0.1052	36.1	0.005022	9.82	0.697	32.3	3.2	101.6	34.9	2368	513	18.86	15.62	38.34	(204Pb)
	0.09684	11.3	0.005307	5.71	0.732	34.1	1.9	93.85	10.1	2129	141	18.86	15.62	38.34	(204Pb)
	0.1438	31.3	0.00535	10.7	0.806	34.4	3.7	136.4	40	2784	386	18.86	15.62	38.34	(204Pb)
	0.1162	15.5	0.005481	6.13	0.717	35.2	2.2	111.7	16.4	2389	202	18.86	15.62	38.34	(204Pb)
	0.1848	29.1	0.005483	9.78	0.728	35.3	3.4	172.2	46.1	3149	364	18.86	15.62	38.34	(204Pb)
	0.08394	81.1	0.005506	13.1	0.803	35.4	4.6	81.84	63.8	1809	1.29E+03	18.86	15.62	38.34	(204Pb)
	0.1763	28.3	0.005938	10.9	0.817	38.2	4.2	164.8	43	2946	328	18.86	15.62	38.34	(204Pb)
	0.1844	27.9	0.006072	10.3	0.829	39.0	4.0	171.8	44.1	2982	325	18.86	15.62	38.34	(204Pb)
	0.2014	35.3	0.006316	12.3	0.817	40.6	5.0	186.3	60.1	3061	419	18.86	15.62	38.34	(204Pb)
	0.1945	22.9	0.006516	9.87	0.838	41.9	4.1	180.4	37.8	2955	251	18.86	15.62	38.34	(204Pb)
	0.35	30.6	0.007085	14.2	0.893	45.5	6.4	304.7	80.5	3743	289	18.86	15.62	38.34	(204Pb)
	0.5668	21.5	0.009442	12.9	0.911	60.6	7.8	455.9	79	4036	165	18.86	15.62	38.34	(204Pb)
	1.208	21.6	0.01396	14.9	0.944	89	13	804.1	120	4573	130	18.86	15.62	38.34	(204Pb)
	1.189	23.6	0.01404	16.9	0.976	90	15	795.7	130	4542	116	18.86	15.62	38.34	(204Pb)
SMO13_13	-0.1505	-24	0.002029	14.8	0.523	13.1	1.9	-165.6	43.1	-1	-0.184	18.86	15.62	38.34	(204Pb)
	-0.07116	-69.2	0.003386	13.4	0.629	21.8	2.9	-74.96	53.9	-1	-0.12	18.86	15.62	38.34	(204Pb)
	0.0243	33.5	0.003763	5.02	0.46	24.2	1.2	24.38	8.07	41.05	753	18.86	15.62	38.34	(204Pb)
	0.01261	69.8	0.004184	5.53	0.333	26.9	1.5	12.73	8.82	-1	0.0149	18.86	15.62	38.34	(204Pb)
	0.07923	53.3	0.004606	9.93	0.634	29.6	2.9	77.42	39.7	2025	843	18.86	15.62	38.34	(204Pb)
	0.05763	28.2	0.004611	5.85	0.583	29.7	1.7	56.89	15.6	1439	481	18.86	15.62	38.34	(204Pb)
	0.03067	7.7	0.004786	5.84	0.773	30.8	1.8	30.67	2.33	22.26	117	18.86	15.62	38.34	(204Pb)
	0.03198	27.3	0.0049	6.34	0.395	31.5	2.0	31.96	8.58	65.92	606	18.86	15.62	38.34	(204Pb)
	0.05688	10.9	0.005089	6.46	0.639	32.7	2.1	56.17	5.95	1223	165	18.86	15.62	38.34	(204Pb)
	0.06727	9.62	0.005155	6.12	0.749	33.2	2.0	66.1	6.16	1521	122	18.86	15.62	38.34	(204Pb)
	0.09619	14.9	0.005216	6.61	0.688	33.5	2.2	93.25	13.3	2148	200	18.86	15.62	38.34	(204Pb)
	0.05341	8.82	0.005228	6.34	0.801	33.6	2.1	52.83	4.54	1044	108	18.86	15.62	38.34	(204Pb)
	0.06789	9.38	0.005258	5.71	0.707	33.8	1.9	66.7	6.06	1501	127	18.86	15.62	38.34	(204Pb)
	0.112	14.2	0.005397	6.16	0.702	34.7	2.1	107.8	14.5	2352	184	18.86	15.62	38.34	(204Pb)
	0.07564	10.2	0.005485	6.63	0.616	35.3	2.3	74.04	7.28	1625	149	18.86	15.62	38.34	(204Pb)
	0.03815	9.18	0.005717	7.38	0.762	36.8	2.7	38.02	3.42	118.8	140	18.86	15.62	38.34	(204Pb)

	0.2194	16.4	0.006213	7.33	0.838	39.9	2.9	201.4	30	3223	174	18.86	15.62	38.34	(204Pb)
	0.2137	14.9	0.006314	7.47	0.839	40.6	3.0	196.7	26.6	3156	151	18.86	15.62	38.34	(204Pb)
	0.4353	14.1	0.008357	8.24	0.932	53.7	4.4	366.9	43.3	3823	107	18.86	15.62	38.34	(204Pb)
	0.1016	6.24	0.01465	5.23	0.835	93.7	4.9	98.26	5.84	209.7	79.6	18.86	15.62	38.34	(204Pb)
	1.511	15.2	0.01755	12.1	0.99	112	14	935	92.9	4566	52.7	18.86	15.62	38.34	(204Pb)
SMO13_16	0.08746	97.8	0.001017	109	0.871	6.6	7.2	85.13	79.9	4564	778	18.86	15.62	38.34	(204Pb)
	-0.04972	-67.5	0.003108	10.3	0.774	20.0	2.1	-51.79	35.9	-1	-0.0879	18.86	15.62	38.34	(204Pb)
	0.01774	307	0.003637	13.9	0.635	23.4	3.2	17.86	54.3	-1	0.106	18.86	15.62	38.34	(204Pb)
	0.01762	136	0.003966	8.48	0.578	25.5	2.2	17.73	23.9	-1	0.0423	18.86	15.62	38.34	(204Pb)
	0.01703	165	0.004057	8.24	0.691	26.1	2.2	17.15	28.1	-1	0.0486	18.86	15.62	38.34	(204Pb)
	0.2313	13.6	0.004241	10.3	0.779	27.3	2.8	211.3	25.9	3892	128	18.86	15.62	38.34	(204Pb)
	0.03166	30.6	0.00461	6.72	0.384	29.7	2.0	31.65	9.55	186.1	669	18.86	15.62	38.34	(204Pb)
	0.02893	16.3	0.004645	5.1	0.482	29.9	1.5	28.95	4.65	-1	0.00657	18.86	15.62	38.34	(204Pb)
	0.05151	23.6	0.004651	6.7	0.474	29.9	2.0	51	11.8	1205	420	18.86	15.62	38.34	(204Pb)
	0.04161	37.4	0.004652	7.05	0.513	29.9	2.1	41.4	15.2	770.5	722	18.86	15.62	38.34	(204Pb)
	0.0273	43.7	0.004715	6.67	0.432	30.3	2.0	27.35	11.8	-1	0.0173	18.86	15.62	38.34	(204Pb)
	0.04128	29.5	0.004715	6.38	0.48	30.3	1.9	41.08	11.9	725	574	18.86	15.62	38.34	(204Pb)
	0.07522	13.7	0.004915	6.29	0.567	31.6	2.0	73.64	9.74	1816	207	18.86	15.62	38.34	(204Pb)
	0.03475	42.8	0.004996	6.85	0.495	32.1	2.2	34.69	14.6	215.8	923	18.86	15.62	38.34	(204Pb)
	0.02781	27.3	0.005071	6.02	0.375	32.6	2.0	27.85	7.49	-1	0.0102	18.86	15.62	38.34	(204Pb)
	0.1436	18	0.005713	6.89	0.721	36.7	2.5	136.3	22.9	2674	229	18.86	15.62	38.34	(204Pb)
	0.2366	16.3	0.006609	8.17	0.841	42.5	3.5	215.6	31.7	3244	164	18.86	15.62	38.34	(204Pb)
	0.3142	10.2	0.006976	7.82	0.845	44.8	3.5	277.4	24.8	3602	84.9	18.86	15.62	38.34	(204Pb)
	2.28	15.4	0.02467	12.9	0.991	157	20	1206	109	4668	45.8	18.86	15.62	38.34	(204Pb)
	2.661	7.77	0.02774	7.81	0.964	176	14	1318	57.3	4722	30.1	18.86	15.62	38.34	(204Pb)
	7.953	15.9	0.07401	15.3	0.999	460	68	2226	144	4884	12.5	18.86	15.62	38.34	(204Pb)
SMO13_19	0.01469	246	0.004499	11.4	0.603	28.9	3.3	14.81	36.2	-1	0.0568	18.86	15.62	38.34	(204Pb)
	0.02718	26.2	0.004558	7.72	0.358	29.3	2.3	27.23	7.03	-1	0.0106	18.86	15.62	38.34	(204Pb)
	0.006308	674	0.004931	11.7	0.628	31.7	3.7	6.385	42.9	-1	0.0619	18.86	15.62	38.34	(204Pb)
	0.04932	32.6	0.004946	7.92	0.471	31.8	2.5	48.88	15.5	994.7	603	18.86	15.62	38.34	(204Pb)
	0.02601	83	0.005058	8.66	0.497	32.5	2.8	26.07	21.4	-1	0.0295	18.86	15.62	38.34	(204Pb)
	0.02922	18.7	0.005186	7.09	0.468	33.4	2.4	29.24	5.4	-1	0.0068	18.86	15.62	38.34	(204Pb)
	0.02963	13.2	0.005354	8.08	0.573	34.4	2.8	29.65	3.85	-1	0.00433	18.86	15.62	38.34	(204Pb)
	0.03649	48.8	0.005414	8.08	0.442	34.8	2.8	36.39	17.5	142	1.08E+03	18.86	15.62	38.34	(204Pb)
	-0.02533	-174	0.005484	12.3	0.523	35.3	4.3	-26.05	45.9	-1	-0.0605	18.86	15.62	38.34	(204Pb)
	0.03824	40.9	0.005545	7.41	0.452	35.6	2.6	38.1	15.3	195.9	886	18.86	15.62	38.34	(204Pb)
	0.0362	23.7	0.005553	5.47	0.452	35.7	2.0	36.11	8.42	63.29	519	18.86	15.62	38.34	(204Pb)
	0.1534	11	0.006055	7.4	0.608	38.9	2.9	144.9	14.8	2687	145	18.86	15.62	38.34	(204Pb)
	0.3846	13.8	0.009182	7.31	0.787	58.9	4.3	330.4	38.9	3490	142	18.86	15.62	38.34	(204Pb)
	0.06222	13.9	0.00992	7.05	0.585	63.6	4.5	61.29	8.24	-1	0.00513	18.86	15.62	38.34	(204Pb)
	1.021	7.16	0.01363	6.07	0.961	87.3	5.3	714.3	36.7	4363	31.3	18.86	15.62	38.34	(204Pb)
	1.245	9.33	0.01537	8.08	0.941	98.3	7.9	821.1	52.5	4477	47.1	18.86	15.62	38.34	(204Pb)
	0.6648	8.11	0.0155	6.68	0.918	99.2	6.6	517.6	32.9	3526	50.9	18.86	15.62	38.34	(204Pb)
	2.242	10.7	0.02349	9.37	0.978	150	14	1194	75.2	4715	35.9	18.86	15.62	38.34	(204Pb)
	1.232	6.25	0.05925	5.81	0.921	371	21	815.1	35	2355	41.7	18.86	15.62	38.34	(204Pb)
SMO13_22	0.03923	20.4	0.004516	5.51	0.435	29.0	1.6	39.07	7.82	708.3	397	18.86	15.62	38.34	(204Pb)

	0.03315	8.39	0.004579	5.11	0.636	29.5	1.5	33.12	2.73	307.7	148	18.86	15.62	38.34	(204Pb)
	0.09007	8.18	0.004901	4.8	0.655	31.5	1.5	87.57	6.87	2142	109	18.86	15.62	38.34	(204Pb)
	0.03433	5.39	0.005209	5.03	0.944	33.5	1.7	34.27	1.82	89.09	42.3	18.86	15.62	38.34	(204Pb)
	0.03571	7.11	0.005475	7	0.985	35.2	2.5	35.63	2.49	64.79	28.8	18.86	15.62	38.34	(204Pb)
	0.03619	5.66	0.005483	5.09	0.925	35.3	1.8	36.1	2.01	92.73	51	18.86	15.62	38.34	(204Pb)
	0.03775	7.04	0.005531	6.45	0.928	35.6	2.3	37.63	2.6	172.1	61.4	18.86	15.62	38.34	(204Pb)
	0.03268	16.7	0.005742	7.09	0.493	36.9	2.6	32.65	5.37	-1	0.00602	18.86	15.62	38.34	(204Pb)
	0.03603	11.6	0.005914	5.19	0.517	38.0	2.0	35.94	4.11	-1	0.00442	18.86	15.62	38.34	(204Pb)
	0.04214	13.6	0.006001	7.55	0.606	38.6	2.9	41.91	5.58	237.4	250	18.86	15.62	38.34	(204Pb)
	0.03959	10.1	0.006026	4.9	0.569	38.7	1.9	39.42	3.91	81.82	199	18.86	15.62	38.34	(204Pb)
	0.0376	11.4	0.006365	5.5	0.613	40.9	2.2	37.48	4.18	-1	0.0039	18.86	15.62	38.34	(204Pb)
	0.1386	8.22	0.007188	5.39	0.791	46.2	2.5	131.8	10.2	2225	89.2	18.86	15.62	38.34	(204Pb)
	0.1583	8.44	0.00722	5.72	0.833	46.4	2.7	149.2	11.7	2445	82.1	18.86	15.62	38.34	(204Pb)
	0.09591	10.6	0.007378	5.7	0.6	47.4	2.7	92.99	9.39	1514	160	18.86	15.62	38.34	(204Pb)
SMO13_28	0.04065	9.46	0.004196	3.88	0.713	27.0	1.0	40.46	3.75	936.2	148	18.86	15.62	38.34	(204Pb)
	0.04235	10.7	0.004258	4.18	0.618	27.4	1.1	42.11	4.4	989.3	178	18.86	15.62	38.34	(204Pb)
	0.175	16.5	0.004736	7.17	0.929	30.5	2.2	163.8	25	3294	160	18.86	15.62	38.34	(204Pb)
	0.09595	16.9	0.004835	5.37	0.815	31.1	1.7	93.04	15.1	2275	223	18.86	15.62	38.34	(204Pb)
	0.05247	13.5	0.00487	5.34	0.685	31.3	1.7	51.93	6.84	1151	210	18.86	15.62	38.34	(204Pb)
	0.0586	15.2	0.004889	4.89	0.748	31.4	1.5	57.82	8.52	1359	230	18.86	15.62	38.34	(204Pb)
	0.06307	13.5	0.005101	5.24	0.658	32.8	1.7	62.11	8.12	1419	206	18.86	15.62	38.34	(204Pb)
	0.07615	15.5	0.005146	5.51	0.739	33.1	1.8	74.52	11.1	1755	220	18.86	15.62	38.34	(204Pb)
	0.09271	11	0.005698	5.39	0.761	36.6	2.0	90.03	9.51	1926	139	18.86	15.62	38.34	(204Pb)
	0.1519	15.5	0.006058	6.41	0.856	38.9	2.5	143.6	20.8	2670	175	18.86	15.62	38.34	(204Pb)
	0.1653	16.8	0.006092	6.92	0.861	39.2	2.7	155.3	24.2	2800	187	18.86	15.62	38.34	(204Pb)
	0.1646	10.9	0.006202	5.17	0.798	39.9	2.1	154.7	15.6	2763	122	18.86	15.62	38.34	(204Pb)
	0.06683	14	0.00638	6.12	0.775	41.0	2.5	65.69	8.89	1094	200	18.86	15.62	38.34	(204Pb)
	0.07796	11.8	0.006415	5.17	0.686	41.2	2.1	76.22	8.7	1386	175	18.86	15.62	38.34	(204Pb)
	0.09379	16.2	0.00645	5.43	0.579	41.5	2.2	91.03	14.1	1722	254	18.86	15.62	38.34	(204Pb)
	0.3687	18	0.007867	9.48	0.957	50.5	4.8	318.7	49.3	3662	143	18.86	15.62	38.34	(204Pb)
	0.9958	28.8	0.01355	20.5	0.988	87	18	701.7	146	4335	134	18.86	15.62	38.34	(204Pb)
SMO13_33	0.004526	369	0.005202	7.44	0.375	33.5	2.5	4.586	16.9	-1	0.0231	18.86	15.62	38.34	(204Pb)
	0.01589	122	0.005549	7.4	0.434	35.7	2.6	16.01	19.4	-1	0.0247	18.86	15.62	38.34	(204Pb)
	0.03349	55.3	0.005588	10.9	0.406	35.9	3.9	33.45	18.2	-1	0.0225	18.86	15.62	38.34	(204Pb)
	0.02593	27.7	0.005801	6.66	0.377	37.3	2.5	25.99	7.1	-1	0.00839	18.86	15.62	38.34	(204Pb)
	0.03382	16	0.006012	7.73	0.526	38.6	3.0	33.77	5.31	-1	0.00556	18.86	15.62	38.34	(204Pb)
	0.02543	34.8	0.006023	6.37	0.361	38.7	2.5	25.49	8.77	-1	0.0101	18.86	15.62	38.34	(204Pb)
	0.04278	23.5	0.006058	8.8	0.532	38.9	3.4	42.53	9.79	250.3	466	18.86	15.62	38.34	(204Pb)
	0.03895	30.4	0.006134	7.65	0.404	39.4	3.0	38.8	11.6	0.5687	679	18.86	15.62	38.34	(204Pb)
	0.005962	201	0.006134	7.64	0.252	39.4	3.0	6.036	12.1	-1	0.014	18.86	15.62	38.34	(204Pb)
	-0.007874	-436	0.006229	8.66	0.467	40.0	3.5	-8.027	35.1	-1	-0.0404	18.86	15.62	38.34	(204Pb)
	0.03003	43.8	0.00624	6.85	0.379	40.1	2.7	30.04	13	-1	0.0145	18.86	15.62	38.34	(204Pb)
	0.02694	32.6	0.006246	7.42	0.345	40.1	3.0	26.99	8.69	-1	0.00965	18.86	15.62	38.34	(204Pb)
	0.0391	13.2	0.006391	6.98	0.546	41.1	2.9	38.94	5.03	-1	0.0049	18.86	15.62	38.34	(204Pb)
	0.04266	22.2	0.006452	9.48	0.52	41.5	3.9	42.42	9.21	97.28	451	18.86	15.62	38.34	(204Pb)
	0.0458	16.7	0.006463	7.04	0.484	41.5	2.9	45.47	7.41	258.9	336	18.86	15.62	38.34	(204Pb)

SMO13_35	0.0242	26.2	0.004865	6.54	0.375	31.3	2.0	24.28	6.29	-1	0.00885	18.86	15.62	38.34	(204Pb)
	0.03548	8.88	0.004871	6.76	0.766	31.3	2.1	35.4	3.09	321.3	130	18.86	15.62	38.34	(204Pb)
	0.02653	19.8	0.004905	6.93	0.414	31.5	2.2	26.59	5.2	-1	0.0071	18.86	15.62	38.34	(204Pb)
	0.03365	14.5	0.004938	6.44	0.527	31.8	2.0	33.6	4.78	167.8	289	18.86	15.62	38.34	(204Pb)
	0.02872	13.7	0.005101	6.62	0.541	32.8	2.2	28.75	3.89	-1	0.00472	18.86	15.62	38.34	(204Pb)
	0.02885	16.8	0.005101	6.66	0.486	32.8	2.2	28.88	4.77	-1	0.00604	18.86	15.62	38.34	(204Pb)
	0.03409	16.8	0.005106	6.72	0.531	32.8	2.2	34.04	5.62	119.8	339	18.86	15.62	38.34	(204Pb)
	0.02379	22.6	0.005124	6.82	0.411	32.9	2.2	23.88	5.33	-1	0.00698	18.86	15.62	38.34	(204Pb)
	0.03408	20.4	0.005161	6.7	0.385	33.2	2.2	34.03	6.84	93.96	447	18.86	15.62	38.34	(204Pb)
	0.02219	20.3	0.005173	6.61	0.412	33.3	2.2	22.29	4.48	-1	0.00578	18.86	15.62	38.34	(204Pb)
	0.03143	15.1	0.005175	6.94	0.58	33.3	2.3	31.43	4.67	-1	0.00547	18.86	15.62	38.34	(204Pb)
	-0.0005357	-8.90E+03	0.005198	11	0.699	33.4	3.7	-0.544	48.4	-1	-0.0665	18.86	15.62	38.34	(204Pb)
	0.03134	9.81	0.005331	6.67	0.677	34.3	2.3	31.34	3.03	-1	0.00308	18.86	15.62	38.34	(204Pb)
	0.04479	16	0.005355	7	0.608	34.4	2.4	44.49	6.97	627.5	280	18.86	15.62	38.34	(204Pb)
	0.01051	105	0.005559	7.97	0.271	35.7	2.8	10.61	11.1	-1	0.0141	18.86	15.62	38.34	(204Pb)
	1.176	6.24	0.1144	6.23	0.987	698	41	789.5	34.3	1057	20.2	18.86	15.62	38.34	(204Pb)
SMO13_37	0.02031	18.4	0.003335	16.8	0.854	21.5	3.6	20.42	3.72	-1	0.00425	18.86	15.62	38.34	(204Pb)
	0.04164	17.3	0.003801	16.3	0.856	24.5	4.0	41.42	7.04	1183	179	18.86	15.62	38.34	(204Pb)
	0.02677	10.1	0.004884	10.5	0.747	31.4	3.3	26.83	2.68	-1	0.00291	18.86	15.62	38.34	(204Pb)
	0.03244	11.1	0.005284	9.61	0.875	34.0	3.3	32.42	3.54	-1	0.00239	18.86	15.62	38.34	(204Pb)
	0.05707	6.93	0.005408	6.1	0.894	34.8	2.1	56.36	3.8	1109	62	18.86	15.62	38.34	(204Pb)
	0.03523	7.16	0.005413	5.88	0.833	34.8	2.0	35.15	2.47	59.48	94.3	18.86	15.62	38.34	(204Pb)
	0.03471	9.47	0.005569	9.14	0.958	35.8	3.3	34.65	3.23	-1	0.00123	18.86	15.62	38.34	(204Pb)
	0.0533	13.2	0.005826	9.48	0.719	37.5	3.5	52.72	6.77	817.4	191	18.86	15.62	38.34	(204Pb)
	0.03459	11.5	0.00585	9.53	0.86	37.6	3.6	34.53	3.9	-1	0.00252	18.86	15.62	38.34	(204Pb)
	0.03897	9.34	0.005853	9.08	0.959	37.6	3.4	38.81	3.56	113	62.8	18.86	15.62	38.34	(204Pb)
	0.03851	9.24	0.005994	8.91	0.972	38.5	3.4	38.37	3.48	28.7	52.3	18.86	15.62	38.34	(204Pb)
	0.0403	9.65	0.006016	9.32	0.97	38.7	3.6	40.11	3.8	127.6	55.4	18.86	15.62	38.34	(204Pb)
	0.0394	11.3	0.006081	10.7	0.95	39.1	4.2	39.23	4.35	48.59	84.6	18.86	15.62	38.34	(204Pb)
	0.04972	9.29	0.006165	8.94	0.939	39.6	3.5	49.27	4.47	548.3	70	18.86	15.62	38.34	(204Pb)
	0.03004	23.2	0.0066	10.5	0.502	42.4	4.4	30.05	6.87	-1	0.00663	18.86	15.62	38.34	(204Pb)
	0.03409	23.9	0.006814	9.02	0.488	43.8	3.9	34.04	7.99	-1	0.00762	18.86	15.62	38.34	(204Pb)
0.04378	10.7	0.007141	9.27	0.882	45.9	4.2	43.51	4.57	-1	0.00225	18.86	15.62	38.34	(204Pb)	
0.05587	54.4	0.009195	51.9	0.985	59	31	55.2	29.2	-1	0.00423	18.86	15.62	38.34	(204Pb)	
SMO13_42	0.03984	19.7	0.004795	5.79	0.516	30.8	1.8	39.66	7.67	612.5	377	18.86	15.62	38.34	(204Pb)
	0.0349	20	0.004892	4.96	0.506	31.5	1.6	34.84	6.86	274.5	413	18.86	15.62	38.34	(204Pb)
	0.04159	20.8	0.005039	6.07	0.511	32.4	2.0	41.38	8.44	598.6	400	18.86	15.62	38.34	(204Pb)
	0.05152	12.5	0.005272	5.4	0.706	33.9	1.8	51.01	6.2	953.9	194	18.86	15.62	38.34	(204Pb)
	0.07325	30.3	0.005305	6.85	0.591	34.1	2.3	71.78	21	1627	498	18.86	15.62	38.34	(204Pb)
	0.03738	7.03	0.005354	4.74	0.743	34.4	1.6	37.27	2.57	224.3	109	18.86	15.62	38.34	(204Pb)
	0.05416	11	0.005358	5.27	0.736	34.5	1.8	53.56	5.76	1023	162	18.86	15.62	38.34	(204Pb)
	0.04584	14.2	0.005359	5.44	0.633	34.5	1.9	45.51	6.34	675.7	248	18.86	15.62	38.34	(204Pb)
	0.03779	7.52	0.005451	5.36	0.788	35.1	1.9	37.66	2.78	207.8	108	18.86	15.62	38.34	(204Pb)
	0.05892	20.7	0.00554	5.48	0.528	35.6	2.0	58.13	11.7	1125	367	18.86	15.62	38.34	(204Pb)
	0.03942	7.52	0.005639	5.4	0.755	36.3	2.0	39.26	2.9	227.2	114	18.86	15.62	38.34	(204Pb)
	0.08282	19.2	0.005748	6.49	0.668	37.0	2.4	80.79	14.9	1705	288	18.86	15.62	38.34	(204Pb)
	0.05258	10.3	0.005776	6.01	0.625	37.1	2.2	52.03	5.21	807.1	168	18.86	15.62	38.34	(204Pb)

	0.05554	12.9	0.005795	5.89	0.617	37.3	2.2	54.89	6.91	913.9	214	18.86	15.62	38.34	(204Pb)
	0.04697	8.97	0.005809	6.06	0.767	37.3	2.3	46.6	4.09	553.8	127	18.86	15.62	38.34	(204Pb)
	0.05744	8.23	0.005928	6.66	0.835	38.1	2.5	56.71	4.54	936.4	93	18.86	15.62	38.34	(204Pb)
	0.04558	6.86	0.005975	6.26	0.891	38.4	2.4	45.26	3.04	425.3	69.5	18.86	15.62	38.34	(204Pb)
	0.1459	16.2	0.006142	6.52	0.796	39.5	2.6	138.3	20.9	2580	195	18.86	15.62	38.34	(204Pb)
	0.05452	8.96	0.006205	5.66	0.513	39.9	2.3	53.9	4.7	732.6	164	18.86	15.62	38.34	(204Pb)
	0.07799	10.1	0.006277	6.15	0.726	40.3	2.5	76.25	7.41	1428	134	18.86	15.62	38.34	(204Pb)
	0.1072	9.99	0.006379	6.15	0.756	41.0	2.5	103.4	9.82	1983	119	18.86	15.62	38.34	(204Pb)
	0.6505	12.7	0.01138	8.35	0.953	72.9	6.1	508.8	50.8	3963	80.5	18.86	15.62	38.34	(204Pb)
	4.133	19.5	0.0364	15.5	0.945	231	35	1661	159	4963	99.5	18.86	15.62	38.34	(204Pb)
SMO13_43	0.02639	16.3	0.004879	4.87	0.456	31.4	1.5	26.45	4.25	-1	0.00577	18.86	15.62	38.34	(204Pb)
	0.02185	68.8	0.005248	5.91	0.437	33.7	2.0	21.94	14.9	-1	0.0201	18.86	15.62	38.34	(204Pb)
	0.03463	18.3	0.005275	5.69	0.413	33.9	1.9	34.57	6.22	80.15	398	18.86	15.62	38.34	(204Pb)
	0.01436	90.2	0.005279	6.47	0.379	33.9	2.2	14.48	13	-1	0.0174	18.86	15.62	38.34	(204Pb)
	0.01859	95.2	0.005586	7.13	0.426	35.9	2.6	18.7	17.6	-1	0.0223	18.86	15.62	38.34	(204Pb)
	0.04228	8.99	0.005665	5.25	0.716	36.4	1.9	42.05	3.7	376.7	144	18.86	15.62	38.34	(204Pb)
	0.04712	21.5	0.005717	5.4	0.542	36.8	2.0	46.75	9.84	595.3	415	18.86	15.62	38.34	(204Pb)
	0.03707	52.1	0.005764	5.59	0.533	37.1	2.1	36.96	18.9	30.8	1.18E+03	18.86	15.62	38.34	(204Pb)
	0.02272	46.9	0.005777	5.07	0.397	37.1	1.9	22.82	10.6	-1	0.0129	18.86	15.62	38.34	(204Pb)
	0.04391	8.06	0.00586	4.92	0.723	37.7	1.9	43.64	3.44	385.6	127	18.86	15.62	38.34	(204Pb)
	0.08004	7.01	0.006003	5.34	0.796	38.6	2.1	78.19	5.27	1562	79.7	18.86	15.62	38.34	(204Pb)
	0.03388	15.5	0.006445	6.08	0.503	41.4	2.5	33.83	5.17	-1	0.00516	18.86	15.62	38.34	(204Pb)
	0.04508	10.7	0.006517	6.15	0.623	41.9	2.6	44.77	4.68	202.8	195	18.86	15.62	38.34	(204Pb)
	0.04172	6.23	0.006594	5.7	0.924	42.4	2.4	41.5	2.53	-1	0.0011	18.86	15.62	38.34	(204Pb)
	0.0432	7.38	0.006731	6.11	0.85	43.2	2.6	42.94	3.1	26.13	93.4	18.86	15.62	38.34	(204Pb)
	0.04561	9.39	0.006747	5.9	0.532	43.4	2.6	45.29	4.16	149.4	188	18.86	15.62	38.34	(204Pb)
	0.04149	9.21	0.006781	7.67	0.86	43.6	3.3	41.28	3.73	-1	0.00209	18.86	15.62	38.34	(204Pb)
	0.04402	6.86	0.007102	6.27	0.93	45.6	2.9	43.74	2.94	-1	0.00114	18.86	15.62	38.34	(204Pb)
	0.1387	6.74	0.008039	6.04	0.926	51.6	3.1	131.8	8.34	2030	45.2	18.86	15.62	38.34	(204Pb)
	0.2508	14.2	0.008248	6.88	0.852	53.0	3.6	227.2	28.9	2985	146	18.86	15.62	38.34	(204Pb)
	0.4888	14.4	0.01067	8.28	0.926	68.4	5.6	404.1	47.9	3628	113	18.86	15.62	38.34	(204Pb)
SMO13_46	0.03186	40	0.005666	7.67	0.425	36.4	2.8	31.84	12.5	-1	0.0152	18.86	15.62	38.34	(204Pb)
	0.03203	17.7	0.005702	6.87	0.496	36.7	2.5	32.01	5.57	-1	0.0063	18.86	15.62	38.34	(204Pb)
	0.04001	8.09	0.005845	7.52	0.904	37.6	2.8	39.83	3.16	178.3	81	18.86	15.62	38.34	(204Pb)
	0.03103	38.9	0.005887	8.62	0.394	37.8	3.3	31.03	11.9	-1	0.0139	18.86	15.62	38.34	(204Pb)
	0.03752	26.8	0.0059	7.93	0.498	37.9	3.0	37.4	9.83	4.203	574	18.86	15.62	38.34	(204Pb)
	0.02247	56.7	0.005976	7.92	0.353	38.4	3.0	22.56	12.7	-1	0.0148	18.86	15.62	38.34	(204Pb)
	0.03641	20.9	0.006071	9.74	0.546	39.0	3.8	36.31	7.46	-1	0.00766	18.86	15.62	38.34	(204Pb)
	0.03873	17.8	0.006146	7.48	0.488	39.5	3.0	38.58	6.74	-1	0.00712	18.86	15.62	38.34	(204Pb)
	0.0369	13.9	0.006333	8.06	0.613	40.7	3.3	36.79	5.04	-1	0.00466	18.86	15.62	38.34	(204Pb)
	0.02653	31.2	0.006373	8.01	0.378	41.0	3.3	26.59	8.19	-1	0.0088	18.86	15.62	38.34	(204Pb)
	0.04654	10.7	0.006453	9.07	0.849	41.5	3.8	46.19	4.82	299	128	18.86	15.62	38.34	(204Pb)
	0.04045	31.4	0.006499	7.96	0.438	41.8	3.3	40.27	12.4	-1	0.013	18.86	15.62	38.34	(204Pb)
	0.03625	20.2	0.006499	8.21	0.498	41.8	3.4	36.16	7.17	-1	0.00712	18.86	15.62	38.34	(204Pb)
	0.0262	33.3	0.006523	8.97	0.393	41.9	3.8	26.26	8.64	-1	0.00901	18.86	15.62	38.34	(204Pb)
	0.04252	10.8	0.006701	8.87	0.816	43.1	3.8	42.28	4.47	-1	0.00287	18.86	15.62	38.34	(204Pb)

SMO13_48	0.01468	83.7	0.005053	5.42	0.393	32.5	1.8	14.8	12.3	-1	0.0172	18.86	15.62	38.34	(204Pb)
	0.03361	18.2	0.005071	4.68	0.505	32.6	1.5	33.56	6.02	102.8	387	18.86	15.62	38.34	(204Pb)
	0.04	67.3	0.005102	7.73	0.554	32.8	2.5	39.82	26.3	486	1.40E+03	18.86	15.62	38.34	(204Pb)
	0.03099	9.63	0.005241	5.72	0.558	33.7	1.9	30.99	2.94	-1	0.00343	18.86	15.62	38.34	(204Pb)
	-0.05097	-64.9	0.005308	9.7	0.423	34.1	3.3	-53.12	35.4	-1	-0.0485	18.86	15.62	38.34	(204Pb)
	0.04112	6.83	0.005823	4.47	0.769	37.4	1.7	40.92	2.74	250.4	102	18.86	15.62	38.34	(204Pb)
	0.03555	11.4	0.005853	6.75	0.612	37.6	2.5	35.47	3.99	-1	0.00399	18.86	15.62	38.34	(204Pb)
	0.03504	15.2	0.005855	6.21	0.522	37.6	2.3	34.97	5.23	-1	0.00568	18.86	15.62	38.34	(204Pb)
	0.04016	9.36	0.005963	6.77	0.749	38.3	2.6	39.98	3.67	140.4	146	18.86	15.62	38.34	(204Pb)
	0.04017	21.2	0.00612	4.73	0.463	39.3	1.9	39.99	8.32	79.64	463	18.86	15.62	38.34	(204Pb)
	0.04475	18	0.006131	6.6	0.518	39.4	2.6	44.45	7.81	326.2	354	18.86	15.62	38.34	(204Pb)
	0.03836	9.72	0.006361	7.06	0.756	40.9	2.9	38.22	3.65	-1	0.00279	18.86	15.62	38.34	(204Pb)
	0.04	20.3	0.006373	6.5	0.446	41.0	2.7	39.82	7.92	-1	0.00834	18.86	15.62	38.34	(204Pb)
	0.03704	24.1	0.006434	6.92	0.409	41.3	2.9	36.93	8.74	-1	0.00926	18.86	15.62	38.34	(204Pb)
	0.0345	13.2	0.006436	6.76	0.541	41.4	2.8	34.44	4.47	-1	0.00431	18.86	15.62	38.34	(204Pb)
	0.04559	8.47	0.006445	6.83	0.838	41.4	2.8	45.26	3.75	254.5	107	18.86	15.62	38.34	(204Pb)
	0.03869	11.1	0.006541	6.68	0.616	42.0	2.8	38.54	4.2	-1	0.00376	18.86	15.62	38.34	(204Pb)
	0.04003	10.4	0.006557	6.35	0.633	42.1	2.7	39.86	4.05	-1	0.00355	18.86	15.62	38.34	(204Pb)
	0.06487	7.2	0.00676	6.76	0.954	43.4	2.9	63.82	4.45	916.5	44.6	18.86	15.62	38.34	(204Pb)
	0.1123	16.4	0.007677	6.13	0.607	49.3	3.0	108.1	16.8	1734	249	18.86	15.62	38.34	(204Pb)
2.293	7.23	0.2036	6.9	0.981	1195	75	1210	51.2	1237	27.7	18.86	15.62	38.34	(204Pb)	
SMO13_53	0.03823	24.1	0.005796	7.84	0.431	37.3	2.9	38.09	9.01	91.26	519	18.86	15.62	38.34	(204Pb)
	0.007028	266	0.00585	9.37	0.296	37.6	3.5	7.111	18.8	-1	0.0229	18.86	15.62	38.34	(204Pb)
	0.02572	40	0.005947	9.41	0.356	38.2	3.6	25.79	10.2	-1	0.0118	18.86	15.62	38.34	(204Pb)
	0.0129	86.9	0.005969	8.81	0.273	38.4	3.4	13.01	11.2	-1	0.0133	18.86	15.62	38.34	(204Pb)
	0.0395	10.5	0.006064	8.11	0.816	39.0	3.2	39.33	4.05	61.08	145	18.86	15.62	38.34	(204Pb)
	0.02628	60.3	0.006066	8.52	0.38	39.0	3.3	26.34	15.7	-1	0.0181	18.86	15.62	38.34	(204Pb)
	0.03994	18.9	0.006238	8.83	0.538	40.1	3.5	39.76	7.37	20.08	384	18.86	15.62	38.34	(204Pb)
	0.03502	17.6	0.006271	8.59	0.565	40.3	3.5	34.95	6.05	-1	0.00591	18.86	15.62	38.34	(204Pb)
	0.03062	40.3	0.006304	9.69	0.387	40.5	3.9	30.62	12.1	-1	0.0132	18.86	15.62	38.34	(204Pb)
	0.03139	20.8	0.006398	8.8	0.457	41.1	3.6	31.39	6.44	-1	0.0066	18.86	15.62	38.34	(204Pb)
	0.03465	14.3	0.006409	8.38	0.64	41.2	3.4	34.59	4.87	-1	0.00432	18.86	15.62	38.34	(204Pb)
	0.03321	22.4	0.006591	8.54	0.487	42.4	3.6	33.18	7.33	-1	0.00722	18.86	15.62	38.34	(204Pb)
	0.02574	33.8	0.006701	9.08	0.32	43.1	3.9	25.8	8.61	-1	0.00893	18.86	15.62	38.34	(204Pb)
	-0.06555	-73.4	0.00673	11.6	0.391	43.2	5.0	-68.84	52.3	-1	-0.0556	18.86	15.62	38.34	(204Pb)
	0.0564	17.4	0.006984	9.51	0.61	44.9	4.3	55.72	9.41	551.3	301	18.86	15.62	38.34	(204Pb)

Appendix A. Summary of U-Pb data. Asterisks denote radiogenic product.

Appendix B – ⁴⁰Ar/³⁹Ar Data

Sample	p ¹	i ²	40 V ³	39 V	38 V	37 V	36 V	Moles ⁴⁰ Ar*	%Rad ⁴	R	Age (Ma)	±σ						
SMO13_02	au29.1b.ksp.19a.txt	2	20	2.7E-01	6.4E-04	2.9E-02	2.7E-04	5.2E-04	2.8E-05	4.4E-04	2.9E-05	1.6E-04	1.0E-05	1.75E-15	0.826	7.660	54.504	0.983
<i>Sanidine</i>	au29.1b.ksp.16a.txt	2	20	9.8E-01	1.3E-03	1.1E-01	3.6E-04	1.4E-03	3.8E-05	7.4E-04	3.1E-05	3.4E-04	1.2E-05	6.34E-15	0.897	7.994	56.844	0.327
<i>Total Fusion</i>	au29.1b.ksp.21a.txt	2	20	4.3E-01	5.5E-04	4.7E-02	2.4E-04	6.4E-04	3.0E-05	5.2E-04	2.0E-05	1.8E-04	1.0E-05	2.78E-15	0.873	8.001	56.891	0.584
	au29.1b.ksp.7a.txt	2	15	1.4E+00	9.4E-04	3.4E-02	1.1E-04	1.2E-03	2.6E-05	5.8E-04	3.0E-05	3.7E-03	4.4E-05	8.82E-15	0.201	8.031	57.103	2.967
J-Value	au29.1b.ksp.12a.txt	2	20	1.1E+00	1.1E-03	1.3E-01	4.0E-04	1.8E-03	2.8E-05	1.4E-03	3.2E-05	3.0E-04	8.7E-06	7.37E-15	0.923	8.174	58.099	0.249
0.008 ± 8E-6	au29.1b.ksp.6a.txt	2	15	5.3E-01	1.4E-03	6.2E-02	3.1E-04	8.0E-04	1.4E-05	5.5E-04	2.2E-05	4.8E-05	6.5E-06	7.17E-15	0.973	8.285	58.876	0.412
	au29.1b.ksp.8a.txt	2	20	1.3E+01	8.6E-03	1.5E+00	2.1E-03	2.0E-02	1.8E-04	9.1E-03	1.3E-04	3.1E-04	1.6E-05	8.70E-14	0.993	8.854	62.848	0.099
	au29.1b.ksp.18a.txt	2	20	2.3E+01	1.0E-02	2.6E+00	2.7E-03	3.4E-02	1.5E-04	1.5E-02	4.3E-05	1.2E-03	2.2E-05	1.52E-13	0.985	8.854	62.851	0.074
	au29.1b.ksp.17a.txt	2	20	1.7E+01	8.3E-03	1.9E+00	2.1E-03	2.4E-02	1.7E-04	1.1E-02	7.4E-05	2.5E-04	2.0E-05	1.08E-13	0.996	8.869	62.957	0.081
	au29.1b.ksp.22a.txt	2	20	1.4E+01	5.7E-03	1.5E+00	1.9E-03	2.0E-02	1.4E-04	8.8E-03	5.3E-05	2.6E-04	1.2E-05	8.95E-14	0.994	8.874	62.993	0.085
	au29.1b.ksp.23a.txt	2.2	20	1.1E+01	4.6E-03	1.2E+00	2.1E-03	1.6E-02	8.3E-05	7.1E-03	4.9E-05	1.1E-03	1.8E-05	7.18E-14	0.970	8.878	63.016	0.120
	au29.1b.ksp.24a.txt	2.2	20	1.2E+01	7.9E-03	1.3E+00	2.2E-03	1.7E-02	1.3E-04	1.0E-02	8.5E-05	2.1E-03	1.8E-05	7.80E-14	0.948	8.888	63.091	0.124
	au29.1b.ksp.3a.txt	1.8	15	2.1E+01	1.6E-02	2.3E+00	1.7E-03	3.0E-02	2.1E-04	1.4E-02	1.5E-04	2.8E-04	2.3E-05	1.58E-13	0.996	8.891	63.107	0.072
	au29.1b.ksp.14a.txt	2	20	1.2E+01	7.4E-03	1.3E+00	3.0E-03	1.7E-02	9.2E-05	8.1E-03	8.1E-05	3.1E-04	1.7E-05	7.68E-14	0.992	8.894	63.127	0.150
	au29.1b.ksp.13a.txt	2	20	1.8E+01	5.4E-03	2.0E+00	2.3E-03	2.6E-02	1.7E-04	1.2E-02	7.3E-05	2.2E-04	2.5E-05	1.18E-13	0.996	8.898	63.160	0.078
	au29.1b.ksp.4a.txt	1.8	15	1.7E+01	1.6E-02	1.9E+00	1.8E-03	2.5E-02	1.7E-04	1.1E-02	7.6E-05	5.1E-05	2.3E-05	1.31E-13	0.999	8.908	63.227	0.088
	au29.1b.ksp.15a.txt	2	20	1.5E+01	1.3E-02	1.7E+00	1.9E-03	2.2E-02	3.1E-04	9.5E-03	7.0E-05	1.3E-04	2.1E-05	9.85E-14	0.997	8.910	63.245	0.093
	au29.1b.ksp.20a.txt	2	20	2.3E+00	2.6E-03	2.5E-01	6.3E-04	3.1E-03	6.7E-05	1.6E-03	4.1E-05	1.0E-04	1.3E-05	1.47E-14	0.987	9.016	63.981	0.209
SMO13_02	au29.1c.bio.81a.txt	2.2	20	1.9E+01	6.8E-03	2.0E+00	1.5E-03	1.2E-01	7.9E-04	3.0E-03	4.8E-05	3.9E-03	3.6E-05	1.20E-13	0.938	8.902	62.997	0.069
<i>Biotite</i>	au29.1c.bio.82a.txt	2.2	20	1.3E+01	1.2E-02	1.4E+00	2.1E-03	8.4E-02	4.7E-04	2.1E-03	4.8E-05	2.4E-03	2.4E-05	8.57E-14	0.946	8.914	63.082	0.123
<i>Step Heating</i>	au29.1c.bio.85a.txt	2.2	20	7.7E+00	7.6E-03	8.3E-01	2.1E-03	4.9E-02	3.0E-04	2.4E-03	5.9E-05	1.4E-03	1.6E-05	5.00E-14	0.947	8.822	62.444	0.184
	au29.1c.bio.86a.txt	2.2	20	1.8E+01	1.2E-02	2.0E+00	2.2E-03	1.2E-01	5.1E-04	9.3E-02	3.2E-04	2.8E-03	1.18E-13	0.958	8.859	62.698	0.090	
J-Value	au29.1c.bio.87a.txt	2.2	20	8.1E+00	1.0E-02	8.8E-01	1.2E-03	5.3E-02	2.8E-04	4.6E-03	9.7E-05	2.6E-04	1.9E-05	5.24E-14	0.967	8.910	63.055	0.127
0.008 ± 8E-6	au29.1c.bio.84a.txt	0.4	30	-1.6E-04	1.5E-04	-1.2E-04	6.8E-05	-2.6E-05	-1.9E-04	3.0E-05	1.1E-05	1.7E-05	-1.04E-18	20.965	28.957	197.913	311.708	
	au29.1c.bio.84b.txt	0.45	30	1.1E-03	1.8E-04	1.4E-04	7.6E-05	-1.6E-05	2.4E-05	-8.4E-05	2.8E-05	-7.0E-06	1.2E-05	7.30E-18	2.839	7.963	56.625	191.041
	au29.1c.bio.84c.txt	0.5	30	2.3E-03	2.3E-04	1.5E-04	5.3E-05	-2.9E-05	2.3E-05	-1.6E-04	3.8E-05	-1.4E-05	1.4E-05	1.47E-17	2.771	15.534	108.863	210.991
	au29.1c.bio.84d.txt	0.55	30	9.9E-03	2.4E-04	8.8E-04	6.8E-05	-3.5E-06	2.1E-05	3.7E-05	3.2E-05	6.3E-06	1.0E-05	6.45E-17	0.814	9.160	64.984	25.603
	au29.1c.bio.84e.txt	0.6	30	3.2E-02	3.5E-04	2.6E-03	7.5E-05	1.1E-04	2.9E-05	4.1E-05	5.2E-05	1.5E-05	1.1E-05	2.11E-16	0.860	10.553	74.662	9.021
	au29.1c.bio.84f.txt	0.65	30	4.2E-02	3.5E-04	3.8E-03	8.4E-05	1.5E-04	2.0E-05	1.4E-04	3.8E-05	1.4E-05	1.1E-05	2.74E-16	0.901	9.948	70.466	6.141
	au29.1c.bio.84g.txt	0.7	30	4.0E-02	2.7E-04	3.9E-03	9.7E-05	1.7E-04	2.9E-05	6.2E-05	3.3E-05	1.6E-05	9.1E-06	2.58E-16	0.884	9.067	64.338	5.263
	au29.1c.bio.84h.txt	0.75	30	5.2E-02	3.0E-04	4.8E-03	1.0E-04	2.4E-04	2.0E-05	-1.3E-04	7.9E-05	1.9E-05	1.2E-05	3.35E-16	0.893	9.698	68.729	5.457
	au29.1c.bio.84i.txt	0.8	30	5.2E-02	2.0E-04	3.7E-03	1.2E-04	1.8E-04	2.7E-05	2.3E-05	3.8E-05	5.6E-05	1.1E-05	3.37E-16	0.683	9.555	67.732	7.090
	au29.1c.bio.84j.txt	0.85	30	4.5E-02	3.7E-04	3.6E-03	1.1E-04	2.0E-04	3.0E-05	4.7E-05	5.5E-05	3.4E-05	9.1E-06	2.89E-16	0.774	9.566	67.808	6.019
	au29.1c.bio.84k.txt	0.92	30	6.8E-02	2.1E-04	5.6E-03	1.3E-04	3.0E-04	2.5E-05	5.7E-05	3.4E-05	5.9E-05	8.9E-06	4.39E-16	0.744	9.066	64.329	3.956
	au29.1c.bio.84l.txt	1	30	1.0E-01	2.6E-04	9.2E-03	1.5E-04	5.3E-04	2.6E-05	9.4E-05	3.8E-05	6.7E-05	1.0E-05	6.60E-16	0.805	8.937	63.430	2.717
	au29.1c.bio.84m.txt	1.1	30	2.8E-01	4.7E-04	2.6E-02	9.9E-05	1.6E-03	2.9E-05	2.4E-05	3.4E-05	1.8E-04	9.5E-06	1.84E-15	0.815	8.813	62.565	0.825
	au29.1c.bio.84n.txt	1.2	30	8.6E-01	8.8E-04	9.2E-02	3.4E-04	5.8E-03	9.4E-05	1.0E-04	3.2E-05	1.2E-04	1.3E-05	5.57E-15	0.959	8.953	63.543	0.392
	au29.1c.bio.84o.txt	1.3	30	1.8E+00	1.6E-03	2.0E-01	6.7E-04	1.2E-02	6.6E-05	2.0E-04	2.7E-05	2.4E-04	1.0E-05	1.18E-14	0.961	8.864	62.920	0.255
	au29.1c.bio.84p.txt	1.4	20	3.2E+00	2.0E-03	3.5E-01	9.9E-04	2.2E-02	2.4E-04	3.0E-04	3.0E-05	1.7E-04	1.1E-05	2.07E-14	0.984	8.933	63.402	0.198
	au29.1c.bio.84q.txt	1.6	20	2.0E+00	1.5E-03	2.1E-01	5.1E-04	1.3E-02	9.0E-05	1.2E-04	5.3E-05	3.3E-04	1.4E-05	1.29E-14	0.952	8.929	63.376	0.217
	au29.1c.bio.84r.txt	1.8	20	1.7E-01	3.9E-04	1.1E-02	2.0E-04	5.6E-04	2.8E-05	1.1E-04	4.1E-05	2.6E-04	9.7E-06	1.12E-15	0.560	8.515	60.483	2.775
SMO13_22	au29.1d.ksp.43a.txt	2.2	20	3.1E-01	3.8E-04	5.4E-02	2.4E-04	7.4E-04	2.9E-05	2.0E-01	6.4E-04	3.2E-04	1.6E-05	1.98E-15	0.688	4.232	30.313	0.658
<i>Sanidine</i>	au29.1d.ksp.41a.txt	2.2	20	1.5E+00	1.7E-03	1.0E-01	4.8E-04	2.2E-03	2.8E-05	4.2E-01	1.3E-03	3.8E-03	5.5E-05	9.88E-15	0.260	4.236	30.346	1.297
<i>Total Fusion</i>	au29.1d.ksp.38a.txt	2.2	20	9.7E-01	6.5E-04	1.3E-01	5.8E-04	1.9E-03	4.5E-05	1.5E-01	6.5E-04	1.5E-03	3.2E-05	6.29E-15	0.536	4.237	30.351	0.611
	au29.1d.ksp.37a.txt	2.2	20	1.8E+00	2.4E-03	2.2E-01	3.6E-04	3.3E-03	3.0E-05	8.4E-02	6.0E-04	3.1E-03	3.6E-05	1.19E-14	0.506	4.334	31.039	0.381
J-Value	au29.1d.ksp.34a.txt	2.2	20	8.9E-01	1.2E-03	1.2E-01	2.6E-04	1.9E-03	3.9E-05	2.0E-01	4.0E-04	1.3E-03	2.8E-05	5.80E-15	0.573	4.351	31.162	0.508
0.008 ± 8E-6	au29.1d.ksp.42a.txt	2.2	20	9.8E-01	1.2E-03	1.5E-01	5.9E-04	2.3E-03	3.9E-05	3.2E-01	1.0E-03	1.1E-03	1.9E-05	6.35E-15	0.668	4.414	31.604	0.317
	au29.1d.ksp.27a.txt	2.2	20	9.1E-01	1.3E-03	1.5E-01	4.1E-04	2.2E-03	4.1E-05	3.3E-01	9.3E-04	9.3E-04	2.3E-05	5.89E-15	0.697	4.438	31.779	0.359
	au29.1d.ksp.35a.txt	2.2	20	7.1E-01	1.2E-03	1.1E-01	2.3E-04	1.9E-03	2.2E-05	3.3E-01	8.2E-04	7.8E-04	1.5E-05	4.58E-15	0.675	4.444	31.819	0.312
	au29.1d.ksp.39a.txt	2.2	20	8.4E-01	9.6E-04	1.7E-01	6.0E-04	2.5E-03	3.1E-05	6.6E-01	1.1E-03	5.2E-04	1.6E-05	5.47E-15	0.819	4.458	31.921	0.246
	au29.1d.ksp.40a.txt	2.2	20	4.7E-01	8.3E-04	9.8E-02	4.9E-04	1.7E-03	2.9E-05	4.2E-01	1.1E-03	2.4E-04	2.0E-05	3.04E-15	0.852	4.476	32.048	0.47

	au29.1d.ksp.31a.txt	2.2	20	6.8E-01	1.1E-03	9.0E-02	2.9E-04	1.4E-03	2.8E-05	3.3E-01	5.9E-04	1.0E-03	1.2E-05	4.41E-15	0.558	4.557	32.623	0.352
	au29.1d.ksp.33a.txt	2.2	20	1.4E+00	1.3E-03	1.7E-01	4.4E-04	2.7E-03	4.0E-05	3.3E-01	8.6E-04	2.4E-03	1.7E-05	9.24E-15	0.509	4.563	32.661	0.287
	au29.1d.ksp.26a.txt	2.2	20	7.7E+01	1.1E-03	1.2E-01	4.7E-04	1.7E-03	2.7E-05	3.6E-01	1.5E-03	8.8E-04	1.2E-05	5.01E-15	0.663	4.620	33.072	0.295
	au29.1d.ksp.29a.txt	2.2	20	4.1E-01	8.8E-04	7.7E-02	3.9E-04	1.2E-03	2.7E-05	2.3E-01	5.1E-04	2.5E-04	2.2E-05	2.68E-15	0.820	4.689	33.554	0.643
	au29.1d.ksp.32a.txt	2.2	20	8.6E-01	1.0E-03	6.6E-02	3.0E-04	2.1E-03	4.2E-05	5.3E-01	1.3E-03	2.0E-03	1.4E-05	5.58E-15	0.318	4.874	34.868	0.689
	au29.1d.ksp.28a.txt	2.2	20	3.0E-01	8.9E-04	4.1E-03	8.1E-05	1.2E-04	2.2E-05	2.9E+00	2.7E-03	1.7E-03	1.6E-05	1.94E-15	-0.724	23.623	163.053	21.673
SMO13_35	au29.1h.ksp.45a.txt	2.2	20	1.2E+01	8.7E-03	2.6E+00	2.6E-03	3.4E-02	2.1E-04	9.8E-02	3.6E-04	1.1E-03	1.9E-05	7.59E-14	0.972	4.406	31.548	0.044
Sanidine	au29.1h.ksp.46a.txt	2.2	20	1.3E+01	7.0E-03	2.8E+00	3.0E-03	3.7E-02	3.4E-04	1.2E-01	5.7E-04	1.1E-03	1.6E-05	8.23E-14	0.973	4.417	31.628	0.041
Total Fusion	au29.1h.ksp.47a.txt	2.2	20	1.1E+01	6.0E-03	2.6E+00	2.0E-03	3.4E-02	3.0E-04	1.0E-01	5.6E-04	5.2E-04	1.6E-05	7.46E-14	0.987	4.407	31.560	0.033
	au29.1h.ksp.48a.txt	2.2	20	6.4E+00	7.3E-03	1.4E+00	1.5E-03	1.8E-02	1.4E-04	4.3E-02	5.4E-04	8.8E-04	1.3E-05	4.16E-14	0.960	4.422	31.663	0.056
J-Value	au29.1h.ksp.49a.txt	2.2	20	6.5E+00	4.5E-03	1.4E+00	1.0E-03	1.9E-02	1.5E-04	6.0E-02	3.9E-04	9.0E-04	1.9E-05	4.24E-14	0.959	4.422	31.667	0.043
0.008 ± 8E-6	au29.1h.ksp.50a.txt	2.2	20	9.9E+00	9.5E-03	2.2E+00	3.1E-03	2.8E-02	1.3E-04	7.4E-02	5.6E-04	1.1E-03	1.9E-05	6.43E-14	0.968	4.417	31.626	0.059
	au29.1h.ksp.51a.txt	2.2	20	8.6E+00	7.7E-03	1.9E+00	1.1E-03	2.4E-02	1.3E-04	5.8E-02	3.7E-04	7.4E-04	1.8E-05	5.57E-14	0.974	4.423	31.672	0.041
	au29.1h.ksp.52a.txt	2.2	20	1.1E+01	9.2E-03	2.5E+00	2.7E-03	3.3E-02	1.9E-04	7.9E-02	5.7E-04	8.4E-04	1.8E-05	7.32E-14	0.978	4.421	31.658	0.046
	au29.1h.ksp.53a.txt	2.2	20	1.3E+01	6.9E-03	2.8E+00	2.4E-03	3.7E-02	3.1E-04	1.0E-01	4.1E-04	6.8E-04	2.5E-05	8.24E-14	0.984	4.416	31.619	0.037
	au29.1h.ksp.54a.txt	2.2	20	9.0E+00	5.9E-03	2.0E+00	2.0E-03	2.6E-02	1.7E-04	6.3E-02	3.3E-04	5.1E-04	1.5E-05	5.85E-14	0.983	4.421	31.654	0.042
	au29.1h.ksp.55a.txt	2.2	20	1.2E+01	1.0E-02	2.7E+00	2.7E-03	3.4E-02	2.2E-04	6.9E-02	4.2E-04	5.9E-04	3.3E-05	7.70E-14	0.985	4.410	31.578	0.050
	au29.1h.ksp.56a.txt	2.2	20	6.1E+00	5.9E-03	1.4E+00	1.9E-03	1.8E-02	1.3E-04	7.7E-02	8.2E-04	3.5E-04	1.2E-05	3.94E-14	0.983	4.426	31.693	0.058
	au29.1h.ksp.60a.txt	2.2	20	6.5E+00	6.2E-03	1.5E+00	1.6E-03	1.9E-02	1.9E-04	5.3E-02	2.3E-04	2.9E-04	1.3E-05	4.24E-14	0.987	4.416	31.621	0.050
	au29.1h.ksp.58a.txt	2.2	20	1.0E+01	1.4E-02	2.3E+00	2.9E-03	2.9E-02	1.7E-04	7.5E-02	4.1E-04	6.4E-04	2.6E-05	6.62E-14	0.982	4.416	31.623	0.065
	au29.1h.ksp.59a.txt	2.2	20	1.4E+01	9.9E-03	3.1E+00	3.2E-03	4.1E-02	2.7E-04	1.2E-01	3.6E-04	6.3E-04	2.0E-05	9.10E-14	0.987	4.425	31.685	0.029
	au29.1h.ksp.60a.txt	2.2	20	1.3E+01	9.5E-03	2.9E+00	1.6E-03	3.8E-02	2.5E-04	9.3E-02	5.0E-04	4.5E-04	3.7E-05	8.36E-14	0.990	4.413	31.601	0.054
	au29.1g.ksp.61a.txt	2.2	20	5.1E+00	3.6E-03	1.1E+00	1.4E-03	1.5E-02	1.5E-04	4.3E-02	5.5E-04	3.6E-04	1.0E-05	3.32E-14	0.979	4.432	31.735	0.049
	au29.1g.ksp.62a.txt	2.2	20	3.9E+00	2.9E-03	8.7E-01	1.5E-03	1.1E-02	7.3E-05	3.7E-02	5.2E-04	1.8E-04	1.1E-05	2.51E-14	0.986	4.415	31.616	0.068
	au29.1g.ksp.63a.txt	2.2	20	6.3E+00	4.7E-03	1.4E+00	2.3E-03	1.8E-02	1.1E-04	4.0E-02	4.6E-04	4.0E-04	1.3E-05	4.06E-14	0.981	4.400	31.505	0.061
	au29.1g.ksp.64a.txt	2.2	20	3.2E+00	2.2E-03	7.1E-01	7.2E-04	9.5E-03	7.0E-05	2.2E-02	2.8E-04	1.5E-04	1.0E-05	2.06E-14	0.986	4.402	31.522	0.049
SMO13_37	au29.1k.ksp.65a.txt	2.2	20	1.2E+01	5.6E-03	2.5E+00	3.1E-03	3.3E-02	2.5E-04	3.8E-02	2.9E-04	3.1E-03	3.4E-05	7.89E-14	0.924	4.466	31.977	0.054
Sanidine	au29.1k.ksp.66a.txt	2.2	20	1.1E+01	7.2E-03	2.3E+00	2.2E-03	3.0E-02	3.0E-04	3.7E-02	2.6E-04	6.5E-04	2.7E-05	6.83E-14	0.982	4.466	31.974	0.045
Total Fusion	au29.1k.ksp.67a.txt	2.2	20	5.1E+00	4.2E-03	1.1E+00	1.7E-03	1.5E-02	1.3E-04	2.1E-02	2.4E-04	2.3E-04	1.3E-05	3.33E-14	0.987	4.458	31.920	0.060
	au29.1k.ksp.68a.txt	2.2	20	7.5E+00	9.7E-03	1.6E+00	1.3E-03	2.1E-02	1.5E-04	2.7E-02	3.5E-04	1.1E-03	1.7E-05	4.84E-14	0.956	4.447	31.844	0.056
J-Value	au29.1k.ksp.69a.txt	2.2	20	8.7E+00	9.6E-03	1.9E+00	2.5E-03	2.5E-02	1.4E-04	3.6E-02	2.1E-04	6.1E-04	1.2E-05	5.67E-14	0.980	4.465	31.969	0.057
0.008 ± 8E-6	au29.1k.ksp.70a.txt	2.2	20	4.9E+00	2.7E-03	1.1E+00	1.0E-03	1.4E-02	1.3E-04	1.6E-02	2.4E-04	6.7E-05	2.1E-05	3.17E-14	0.996	4.477	32.057	0.054
	au29.1k.ksp.71a.txt	2.2	20	2.3E+00	1.5E-03	5.0E-01	1.1E-03	6.3E-03	6.2E-05	7.2E-03	1.1E-04	8.2E-05	1.1E-05	1.46E-14	0.989	4.476	32.045	0.091
	au29.1k.ksp.72a.txt	2.2	20	4.9E+00	3.2E-03	1.1E+00	1.2E-03	1.4E-02	8.9E-05	1.5E-02	1.1E-04	7.4E-05	2.1E-05	3.15E-14	0.996	4.478	32.065	0.059
	au29.1k.ksp.73a.txt	2.2	20	5.4E+00	3.4E-03	1.2E+00	1.6E-03	1.6E-02	1.3E-04	1.8E-02	1.1E-04	1.4E-04	1.2E-05	3.53E-14	0.993	4.460	31.935	0.051
	au29.1k.ksp.74a.txt	2.2	20	4.3E+00	3.1E-03	9.6E-01	1.1E-03	1.2E-02	8.1E-05	1.6E-02	2.0E-04	1.8E-04	2.0E-05	2.82E-14	0.988	4.477	32.053	0.062
	au29.1k.ksp.75a.txt	2.2	20	6.6E+00	3.5E-03	1.5E+00	1.4E-03	1.9E-02	2.2E-04	2.0E-02	2.6E-04	3.9E-04	1.1E-05	4.31E-14	0.983	4.472	32.020	0.040
	au29.1k.ksp.76a.txt	2.2	20	4.6E+00	5.3E-03	1.0E+00	1.9E-03	1.3E-02	8.3E-05	1.2E-02	2.4E-04	1.3E-04	1.2E-05	2.97E-14	0.992	4.482	32.091	0.075
	au29.1k.ksp.77a.txt	2.2	20	8.0E+00	7.2E-03	1.8E+00	1.4E-03	2.3E-02	1.3E-04	2.9E-02	4.2E-04	4.4E-04	2.1E-05	5.18E-14	0.984	4.484	32.104	0.047
	au29.1k.ksp.78a.txt	2.2	20	1.2E+01	7.3E-03	2.6E+00	2.7E-03	3.4E-02	2.6E-04	4.4E-02	1.7E-04	2.2E-03	2.4E-05	7.94E-14	0.946	4.457	31.910	0.045
	au29.1k.ksp.79a.txt	2.2	20	4.5E+00	4.4E-03	1.0E+00	1.1E-03	1.3E-02	7.2E-05	1.2E-02	1.0E-04	1.8E-04	1.3E-05	2.93E-14	0.988	4.469	31.997	0.054
	au29.1k.ksp.80a.txt	2.2	20	6.5E+00	4.4E-03	1.4E+00	1.5E-03	1.9E-02	1.4E-04	2.0E-02	2.4E-04	1.6E-04	1.9E-05	4.22E-14	0.993	4.477	32.057	0.050
	au29.1k.ksp.81a.txt	2.2	20	7.4E+00	7.2E-03	1.6E+00	2.5E-03	2.1E-02	1.6E-04	2.3E-02	2.0E-04	4.8E-04	1.2E-05	4.78E-14	0.981	4.455	31.896	0.062
	au29.1k.ksp.82a.txt	2.2	20	4.1E+00	2.4E-03	9.0E-01	1.0E-03	1.2E-02	9.1E-05	1.3E-02	2.2E-04	2.3E-04	1.0E-05	2.67E-14	0.983	4.479	32.069	0.048
	au29.1k.ksp.83a.txt	2.2	20	6.1E+00	5.0E-03	1.3E+00	2.4E-03	1.7E-02	1.0E-04	2.0E-02	2.9E-04	4.9E-04	1.2E-05	3.99E-14	0.977	4.469	31.998	0.067
	au29.1k.ksp.84a.txt	2.2	20	3.2E+00	3.3E-03	6.7E-01	7.3E-04	8.9E-03	1.0E-04	1.4E-02	1.6E-04	5.5E-04	2.2E-05	2.05E-14	0.948	4.476	32.049	0.087
SMO13_42	au29.1r.ksp.109a.txt	2.2	20	2.4E+00	1.8E-03	4.8E-01	1.4E-03	6.1E-03	6.6E-05	4.6E-03	8.0E-05	1.7E-04	1.2E-05	1.54E-14	0.979	4.821	34.496	0.119
Sanidine	au29.1r.ksp.110a.txt	2.2	20	1.2E+00	1.2E-03	2.4E-01	7.4E-04	3.0E-03	5.0E-05	2.0E-03	4.3E-05	1.6E-04	1.3E-05	7.71E-15	0.961	4.818	34.469	0.164
Total Fusion	au29.1r.ksp.115a.txt	2.2	20	5.2E+00	3.2E-03	1.1E+00	1.5E-03	1.4E-02	1.4E-04	9.3E-03	9.1E-05	5.5E-04	1.5E-05	3.40E-14	0.969	4.809	34.407	0.063
	au29.1r.ksp.118a.txt	2.2	20	2.3E+00	2.1E-03	4.7E-01	7.3E-04	6.1E-03	5.9E-05	4.2E-03	5.5E-05	2.7E-04	2.2E-05	1.50E-14	0.965	4.772	34.150	0.117
J-Value	au29.1r.ksp.113a.txt	2.2	20	8.1E+01	9.8E-04	1.6E-01	4.0E-04	2.0E-03	4.3E-05	1.4E-03	5.9E-05	2.2E-04	1.4E-05	5.27E-15	0.921	4.737	33.895	0.213
0.008 ± 7.7E-6	au29.1r.ksp.114a.txt	2.2	20	9.3E-01	1.2E-03	1.9E-01	4.8E-04	2.4E-03	4.8E-05	1.8E-03	5.8E-05	2.0E-04	2.0E-05	6.03E-15	0.936	4.702	33.648	0.249
	au29.1r.ksp.117a.txt	2.2	20	1.9E+00	8.6E-04	3.8E-01	3.4E-04	5.0E-03	8.0E-05	3.2E-03	5.3E-05	5.0E-04	1.6E-05	1.22E-14	0.922	4.593	32.876	0.096
	au29.1r.ksp.108a.txt	2.2	20	2.2E+00	1.4E-03	4.2E-01	8.1E-04	5.7E-03	1.1E-04	3.5E-03	4.1E-05	9.1E-04	1.8E-05	1.41E-14	0.876	4.566	32.684	0.120
	au29.1r.ksp.116a.txt	2.2	20	2.7E-01	5.3E-04	4.3E-02	2.1E-04	6.7E-04	3.7E-05	7.4E-04	4.5E-05	4.8E-04	1.5E-05	1.76E-15	0.472	2.996	21.515	0.812
SMO13_42	au29.1j.bio.93a.txt	2.2	20	6.8E+00	5.0E-03	1.0E+00	1.5E-03	5.3E-02	3.5E-04	6.5E-02	3.9E-04	6.5E-03	6.6E-05	4.44E-14	0.717	4.796	34.215	0.158

<i>Biotite</i>	au29.1j.bio.94a.txt	2.2	20	3.3E+00	1.7E-03	4.3E-01	9.9E-04	2.1E-02	2.3E-04	5.3E-03	8.2E-05	3.8E-03	2.2E-05	2.17E-14	0.659	5.063	36.101	0.172
	au29.1j.bio.95a.txt	2.2	20	3.9E+00	3.0E-03	5.0E-01	1.0E-03	2.1E-02	1.6E-04	4.8E-03	1.1E-04	5.2E-03	4.8E-05	2.56E-14	0.608	4.814	34.344	0.240
<i>Step Heating</i>	au29.1j.bio.96a.txt	2.2	20	6.3E+00	5.3E-03	1.0E+00	9.3E-04	4.6E-02	2.7E-04	1.9E-02	1.5E-04	4.0E-03	4.7E-05	4.08E-14	0.811	4.869	34.728	0.109
	au29.1j.bio.97a.txt	2.2	20	8.4E+00	9.6E-03	1.4E+00	2.3E-03	7.0E-02	3.9E-04	7.2E-03	9.8E-05	6.0E-03	6.5E-05	5.42E-14	0.789	4.755	33.927	0.132
J-Value 0.008 ± 8E-6	au29.1j.bio.91a.txt	0.4	30	8.6E-03	2.6E-04	7.6E-04	9.4E-05	1.1E-05	1.9E-05	6.4E-05	3.3E-05	3.8E-05	1.2E-05	5.56E-17	-0.327	-3.701	-26.933	-38.349
	au29.1j.bio.91b.txt	0.5	30	1.1E-01	3.5E-04	9.8E-03	1.6E-04	2.5E-04	2.1E-05	2.8E-04	6.1E-05	2.5E-04	1.5E-05	7.42E-16	0.347	4.069	29.154	3.564
	au29.1j.bio.91c.txt	0.6	30	3.3E-01	9.7E-04	2.1E-02	8.4E-05	8.0E-04	1.8E-05	6.7E-04	3.1E-05	7.5E-04	1.4E-05	2.11E-15	0.322	4.893	35.007	1.493
	au29.1j.bio.91d.txt	0.65	30	1.2E-01	2.6E-04	1.4E-02	1.1E-04	5.5E-04	1.9E-05	5.8E-04	2.1E-05	1.6E-04	1.0E-05	7.60E-16	0.586	4.785	34.242	1.599
	au29.1j.bio.91e.txt	0.7	30	9.1E-02	5.0E-04	1.1E-02	1.2E-04	4.1E-04	4.1E-05	7.8E-04	3.0E-05	1.2E-04	1.1E-05	5.88E-16	0.607	4.942	35.350	2.175
	au29.1j.bio.91f.txt	0.75	30	7.2E-02	3.4E-04	9.9E-03	1.2E-04	4.8E-04	2.0E-05	8.6E-04	2.6E-05	7.9E-05	1.1E-05	4.66E-16	0.677	4.935	35.302	2.563
	au29.1j.bio.91g.txt	0.8	30	7.4E-02	3.0E-04	1.0E-02	1.7E-04	5.4E-04	2.2E-05	1.0E-03	4.4E-05	8.2E-05	1.3E-05	4.81E-16	0.672	5.003	35.783	2.898
	au29.1j.bio.91h.txt	0.85	30	1.2E-01	5.8E-04	1.5E-02	1.4E-04	7.4E-04	2.0E-05	1.2E-03	5.0E-05	1.4E-04	1.2E-05	7.49E-16	0.646	5.071	36.266	1.898
	au29.1j.bio.91i.txt	0.9	30	2.1E-01	4.4E-04	2.7E-02	9.3E-05	1.4E-03	3.2E-05	1.3E-03	4.3E-05	2.6E-04	1.2E-05	1.38E-15	0.635	5.098	36.455	0.961
	au29.1j.bio.91j.txt	1	30	8.6E-01	5.4E-04	1.2E-01	4.1E-04	6.4E-03	7.8E-05	2.3E-03	6.0E-05	9.1E-04	1.3E-05	5.57E-15	0.686	4.909	35.115	0.297
	au29.1j.bio.91k.txt	1.1	30	1.1E+00	1.1E-03	1.8E-01	2.3E-04	9.9E-03	1.2E-04	2.5E-03	4.2E-05	8.1E-04	1.5E-05	7.41E-15	0.789	4.879	34.906	0.183
	au29.1j.bio.91l.txt	1.2	20	1.0E+00	9.1E-04	1.6E-01	2.7E-04	8.7E-03	6.2E-05	3.3E-03	6.9E-05	7.0E-04	2.3E-05	6.61E-15	0.796	4.936	35.311	0.302
	au29.1j.bio.91m.txt	1.3	20	1.4E+00	1.0E-03	2.4E-01	6.8E-04	1.3E-02	1.1E-04	4.9E-03	7.0E-05	8.3E-04	1.5E-05	9.31E-15	0.829	4.897	35.033	0.179
	au29.1j.bio.91n.txt	1.4	20	1.0E+00	1.3E-03	1.7E-01	4.0E-04	9.3E-03	1.1E-04	3.0E-03	3.9E-05	5.3E-04	1.2E-05	6.48E-15	0.844	4.859	34.765	0.185
	au29.1j.bio.91o.txt	1.6	20	1.0E+00	4.7E-04	1.8E-01	4.4E-04	9.6E-03	8.2E-05	3.1E-03	6.2E-05	4.8E-04	1.3E-05	6.73E-15	0.864	4.905	35.089	0.177
	au29.1j.bio.91p.txt	1.8	20	2.0E-01	6.0E-04	3.4E-02	1.1E-04	1.9E-03	3.7E-05	6.6E-04	4.4E-05	9.9E-05	1.3E-05	1.27E-15	0.851	4.895	35.018	0.844
	au29.1j.bio.91q.txt	1.9	20	5.0E-02	3.5E-04	8.9E-03	1.3E-04	5.0E-04	2.9E-05	1.8E-04	3.2E-05	3.2E-05	1.2E-05	3.24E-16	0.808	4.542	32.519	2.823
	au29.1j.bio.91r.txt	2	20	3.5E-02	2.7E-04	6.1E-03	1.2E-04	4.7E-04	1.3E-05	1.8E-04	5.2E-05	1.3E-05	1.2E-05	2.26E-16	0.890	5.110	36.539	4.315
	au29.1j.bio.91s.txt	2.1	20	3.6E-03	2.2E-04	5.8E-04	8.6E-05	9.2E-05	2.0E-05	3.9E-05	3.1E-05	1.0E-06	1.0E-05	2.32E-17	0.917	5.664	40.456	37.627
	au29.1j.bio.91t.txt	2.2	20	2.0E-03	2.1E-04	1.8E-04	7.3E-05	1.2E-04	1.7E-05	3.2E-05	3.2E-05	1.7E-05	1.2E-05	1.32E-17	-1.495	-16.862	-126.112	-175.512
	au29.1j.bio.92a.txt	0.4	30	1.3E-03	2.5E-04	1.6E-04	7.0E-05	1.4E-05	2.3E-05	6.3E-05	3.9E-05	1.5E-05	1.1E-05	8.54E-18	-2.434	-19.879	-149.636	-182.945
	au29.1j.bio.92b.txt	0.45	30	7.2E-03	2.7E-04	9.2E-04	8.1E-05	2.8E-05	2.8E-05	-1.2E-04	5.6E-05	1.2E-05	1.1E-05	4.68E-17	0.500	3.900	27.954	26.259
	au29.1j.bio.92c.txt	0.5	30	3.0E-02	3.3E-04	3.5E-03	9.7E-05	6.0E-05	1.7E-05	5.1E-06	3.6E-05	4.5E-05	1.1E-05	1.97E-16	0.557	4.773	34.150	7.002
	au29.1j.bio.92d.txt	0.55	30	5.1E-02	3.9E-04	8.4E-03	1.1E-04	2.1E-04	1.9E-05	6.5E-05	3.3E-05	4.2E-05	1.3E-05	3.33E-16	0.761	4.663	33.371	3.474
	au29.1j.bio.92e.txt	0.6	30	1.6E-01	3.2E-04	2.1E-02	1.2E-04	5.2E-04	2.0E-05	1.6E-04	3.1E-05	2.4E-04	2.3E-05	1.05E-15	0.555	4.350	31.156	2.419
	au29.1j.bio.92f.txt	0.65	30	1.1E-01	2.5E-04	1.2E-02	2.0E-04	4.1E-04	3.2E-05	1.5E-04	5.0E-05	1.1E-04	2.2E-05	7.02E-16	0.699	6.193	44.193	3.905
	au29.1j.bio.92g.txt	0.7	30	1.3E-01	6.3E-04	1.6E-02	1.4E-04	5.7E-04	2.2E-05	1.4E-04	4.3E-05	1.8E-04	1.3E-05	8.68E-16	0.598	5.082	36.343	1.904
	au29.1j.bio.92h.txt	0.75	30	3.0E-01	4.6E-04	2.7E-02	2.2E-04	1.2E-03	2.6E-05	2.3E-04	3.6E-05	5.5E-04	1.4E-05	1.98E-15	0.465	5.333	38.122	1.350
	au29.1j.bio.92i.txt	0.8	30	2.6E-01	5.6E-04	2.6E-02	1.1E-04	1.0E-03	2.7E-05	2.5E-04	3.9E-05	4.2E-04	1.2E-05	1.67E-15	0.518	5.117	36.588	1.055
	au29.1j.bio.92j.txt	0.85	30	2.1E-01	5.0E-04	2.5E-02	9.7E-05	1.1E-03	2.2E-05	2.7E-04	4.6E-05	2.9E-04	1.3E-05	1.37E-15	0.597	5.037	36.022	1.136
	au29.1j.bio.92k.txt	0.92	30	3.6E-01	7.3E-04	4.5E-02	1.8E-04	2.2E-03	3.1E-05	3.6E-04	2.5E-05	4.6E-04	1.3E-05	2.36E-15	0.625	5.025	35.936	0.664
	au29.1j.bio.92l.txt	1	30	6.7E-01	8.1E-04	9.7E-02	2.5E-04	5.0E-03	6.9E-05	4.4E-04	3.6E-05	6.4E-04	1.4E-05	4.35E-15	0.717	4.957	35.461	0.334
	au29.1j.bio.92m.txt	1.1	30	1.1E+00	1.1E-03	1.8E-01	4.6E-04	9.0E-03	8.3E-05	7.3E-04	4.5E-05	8.7E-04	1.3E-05	7.34E-15	0.773	4.859	34.764	0.195
	au29.1j.bio.92n.txt	1.2	30	1.2E+00	1.0E-03	1.9E-01	3.5E-04	1.0E-02	1.0E-04	7.3E-04	5.0E-05	7.7E-04	1.4E-05	7.58E-15	0.806	4.843	34.651	0.173
	au29.1j.bio.92o.txt	1.3	30	1.1E+00	1.0E-03	1.9E-01	5.4E-04	1.0E-02	7.0E-05	5.7E-04	3.9E-05	6.3E-04	1.3E-05	7.24E-15	0.834	4.865	34.802	0.195
	au29.1j.bio.92p.txt	1.4	20	9.2E-01	8.3E-04	1.6E-01	5.7E-04	8.7E-03	9.4E-05	4.7E-04	6.9E-05	4.9E-04	1.2E-05	5.94E-15	0.842	4.822	34.498	0.217
	au29.1j.bio.92q.txt	1.6	20	8.6E-01	8.5E-04	1.5E-01	3.9E-04	8.1E-03	1.0E-04	4.1E-04	5.4E-05	4.6E-04	1.3E-05	5.57E-15	0.843	4.795	34.308	0.219
	au29.1j.bio.92r.txt	1.8	20	4.1E-01	4.9E-04	7.1E-02	2.8E-04	3.8E-03	4.4E-05	2.3E-04	5.0E-05	2.5E-04	1.3E-05	2.67E-15	0.824	4.771	34.142	0.412
	au29.1j.bio.92s.txt	2	20	4.4E-01	7.9E-04	7.6E-02	3.1E-04	4.0E-03	3.3E-05	1.9E-04	3.1E-05	2.4E-04	1.3E-05	2.83E-15	0.840	4.797	34.321	0.413
	au29.1j.bio.92t.txt	2.2	20	2.6E-02	2.6E-04	3.4E-03	7.2E-05	2.4E-04	1.8E-05	2.0E-04	2.6E-05	4.4E-05	1.3E-05	1.69E-16	0.503	3.841	27.538	8.256
SMO13_43	au29.1l.bio.99a.txt	2.2	20	5.2E+00	2.8E-03	8.5E-01	9.0E-04	2.4E-02	1.4E-04	1.3E-02	2.1E-04	1.5E-03	1.6E-05	3.39E-14	0.917	5.625	40.065	0.065
	au29.1l.bio.102a.txt	2.2	20	2.6E+00	1.9E-03	3.9E-01	6.9E-04	1.1E-02	9.9E-05	6.9E-03	9.5E-05	1.6E-03	2.0E-05	1.70E-14	0.818	5.472	38.987	0.140
<i>Step Heating</i>	au29.1l.bio.103a.txt	2.2	20	5.7E+00	3.3E-03	9.8E-01	1.2E-03	2.9E-02	1.4E-04	2.5E-02	2.8E-04	7.3E-04	1.8E-05	3.70E-14	0.962	5.575	39.711	0.068
	au29.1l.bio.105a.txt	2.2	20	3.6E+00	2.7E-03	5.9E-01	8.5E-04	1.7E-02	1.4E-04	9.1E-03	1.9E-04	9.4E-04	1.6E-05	2.35E-14	0.923	5.614	39.982	0.091
J-Value 0.008 ± 8E-6	au29.1l.bio.106a.txt	2.2	20	1.8E+00	2.7E-03	2.9E-01	9.4E-04	8.4E-03	1.2E-04	2.3E-03	4.8E-05	6.2E-04	2.3E-05	1.19E-14	0.899	5.717	40.709	0.235
	au29.1l.bio.100a.txt	0.4	30	-5.6E-04	2.5E-04	1.1E-04	7.1E-05	4.3E-05	2.9E-05	-5.2E-06	2.2E-05	2.5E-05	1.2E-05	-3.63E-18	13.971	-69.396	-587.317	-437.342
	au29.1l.bio.100b.txt	0.45	30	-5.9E-04	2.5E-04	2.9E-05	8.5E-05	4.5E-05	3.2E-05	-4.3E-05	3.3E-05	1.6E-05	1.3E-05	-3.84E-18	9.238	-188.633	-2539.675	-6943.185
	au29.1l.bio.100c.txt	0.5	30	5.8E-04	2.5E-04	2.2E-04	9.2E-05	-1.3E-05	3.7E-05	-3.9E-05	4.1E-05	-8.6E-06	1.9E-05	3.75E-18	5.390	2.567	18.	

	au29.11.bio.100k.txt	0.92	30	2.3E-01	4.5E-04	3.7E-02	2.4E-04	1.1E-03	3.6E-05	5.8E-04	5.5E-05	5.8E-05	1.4E-05	1.47E-15	0.924	5.618	40.134	0.856
	au29.11.bio.100l.txt	1	30	4.1E-01	8.7E-04	6.7E-02	3.1E-04	2.0E-03	6.5E-05	1.3E-03	7.2E-05	1.3E-04	1.3E-05	2.63E-15	0.905	5.498	39.282	0.475
	au29.11.bio.100m.txt	1.1	30	6.3E-01	7.3E-04	1.0E-01	2.9E-04	3.0E-03	2.4E-05	2.8E-03	3.8E-05	1.6E-04	1.3E-05	4.07E-15	0.924	5.583	39.885	0.295
	au29.11.bio.100n.txt	1.2	30	9.2E-01	5.7E-04	1.6E-01	4.2E-04	4.8E-03	6.7E-05	5.0E-03	1.1E-04	2.1E-04	1.3E-05	5.98E-15	0.932	5.517	39.420	0.206
	au29.11.bio.100o.txt	1.3	30	1.6E+00	1.8E-03	2.7E-01	5.5E-04	7.8E-03	9.5E-05	6.6E-03	4.7E-05	2.4E-04	1.3E-05	1.03E-14	0.956	5.527	39.491	0.141
	au29.11.bio.100p.txt	1.4	20	1.4E+00	1.5E-03	2.5E-01	3.9E-04	7.5E-03	1.5E-04	4.1E-03	5.8E-05	1.3E-04	1.2E-05	9.40E-15	0.974	5.587	39.911	0.126
	au29.11.bio.100q.txt	1.6	20	1.7E+00	1.5E-03	3.0E-01	6.2E-04	8.8E-03	7.2E-05	8.8E-03	1.5E-04	1.7E-04	1.3E-05	1.10E-14	0.970	5.530	39.512	0.129
	au29.11.bio.100r.txt	1.8	20	6.4E-01	1.1E-03	1.1E-01	4.1E-04	3.4E-03	6.0E-05	7.6E-03	1.1E-04	1.1E-04	1.1E-05	4.17E-15	0.950	5.484	39.189	0.272
	au29.11.bio.100s.txt	2	20	1.0E-01	3.6E-04	1.6E-02	1.3E-04	5.0E-04	2.8E-05	1.3E-03	5.3E-05	4.8E-05	1.2E-05	6.69E-16	0.861	5.431	38.809	1.558
	au29.11.bio.100t.txt	2.2	20	4.4E-02	2.7E-04	6.1E-03	9.8E-05	1.5E-04	3.0E-05	3.3E-04	2.6E-05	1.8E-05	1.7E-05	2.83E-16	0.881	6.310	45.013	5.821
SMO13_43	au29.1m.ksp.89a.txt	2.2	20	2.4E+00	1.9E-03	1.5E-01	6.3E-04	2.9E-03	2.8E-05	1.4E-01	5.3E-04	5.5E-03	4.5E-05	1.54E-14	0.312	5.181	37.046	0.897
Feldspar	au29.1m.ksp.92a.txt	2.2	20	7.8E-01	8.4E-04	1.0E-01	5.6E-04	1.6E-03	3.8E-05	2.7E-01	6.6E-04	9.4E-04	1.6E-05	5.04E-15	0.644	5.240	37.459	0.475
Total Fusion	au29.1m.ksp.100a.txt	2.2	20	1.1E+00	1.3E-03	2.1E-01	6.0E-04	2.7E-03	4.6E-05	1.0E-01	4.2E-04	3.4E-04	1.1E-05	7.27E-15	0.911	4.882	34.929	0.165
	au29.1m.ksp.99a.txt	2.2	20	3.7E+00	1.6E-03	6.5E-01	1.2E-03	8.5E-03	7.3E-05	4.7E-01	9.6E-04	2.1E-03	2.1E-05	2.43E-14	0.834	4.892	34.998	0.103
J-Value	au29.1m.ksp.101a.txt	2.2	20	2.3E+00	1.4E-03	3.3E-01	5.9E-04	4.7E-03	3.6E-05	4.5E-01	1.9E-03	2.3E-03	2.0E-05	1.49E-14	0.699	5.004	35.788	0.162
0.008 ± 7.7E-6	au29.1m.ksp.97a.txt	2.2	20	2.3E+00	1.5E-03	3.7E-01	7.0E-04	5.2E-03	8.2E-05	4.2E-01	1.4E-03	1.6E-03	1.6E-05	1.49E-14	0.797	5.050	36.113	0.127
	au29.1m.ksp.103a.txt	2.2	20	5.0E-01	8.4E-04	8.9E-02	3.4E-04	1.1E-03	2.6E-05	1.7E-01	1.1E-03	2.0E-04	1.3E-05	3.22E-15	0.881	5.089	36.391	0.352
	au29.1m.ksp.98a.txt	2.2	20	2.2E+00	2.0E-03	3.4E-01	9.3E-04	4.6E-03	6.1E-05	6.2E-01	1.6E-03	1.9E-03	2.0E-05	1.43E-14	0.752	5.106	36.512	0.189
	au29.1m.ksp.88a.txt	2.2	20	1.0E+00	1.4E-03	1.7E-01	4.5E-04	2.3E-03	2.9E-05	3.7E-01	1.0E-03	6.2E-04	1.3E-05	6.67E-15	0.822	5.112	36.556	0.202
	au29.1m.ksp.93a.txt	2.2	20	9.8E-01	8.4E-04	1.5E-01	5.7E-04	2.0E-03	3.4E-05	1.9E-01	5.0E-04	7.0E-04	1.3E-05	6.35E-15	0.787	5.207	37.228	0.261
	au29.1m.ksp.90a.txt	2.2	20	1.3E+00	1.4E-03	1.6E-01	6.7E-04	2.4E-03	4.4E-05	3.5E-01	1.5E-03	1.5E-03	2.0E-05	8.37E-15	0.653	5.329	38.093	0.361
	au29.1m.ksp.102a.txt	2.2	20	2.3E+00	1.6E-03	3.5E-01	6.8E-04	4.7E-03	3.2E-05	8.0E-01	1.6E-03	1.9E-03	1.7E-05	1.51E-14	0.763	5.332	38.109	0.144
	au29.1m.ksp.96a.txt	2.2	20	1.0E+00	9.7E-04	1.2E-01	3.5E-04	1.7E-03	4.0E-05	1.7E-01	6.8E-04	1.4E-03	2.0E-05	6.52E-15	0.596	5.342	38.179	0.424
	au29.1m.ksp.104a.txt	2.2	20	8.2E-01	1.2E-03	1.2E-01	3.1E-04	1.7E-03	4.3E-05	3.1E-01	1.4E-03	6.2E-04	1.3E-05	5.33E-15	0.778	5.372	38.391	0.268
	au29.1m.ksp.86a.txt	2.2	20	1.1E+00	5.5E-04	1.9E-01	6.4E-04	2.5E-03	3.4E-05	3.8E-01	6.0E-04	4.8E-04	1.3E-05	7.22E-15	0.873	5.427	38.780	0.215
	au29.1m.ksp.85a.txt	2.2	20	7.7E-01	8.3E-04	1.3E-01	4.0E-04	1.7E-03	2.5E-05	3.1E-01	8.2E-04	3.4E-04	1.3E-05	5.03E-15	0.869	5.427	38.781	0.251
	au29.1m.ksp.95a.txt	2.2	20	2.0E+00	1.6E-03	3.6E-01	6.8E-04	4.4E-03	5.6E-05	9.5E-03	8.1E-05	1.3E-04	1.1E-05	1.29E-14	0.981	5.464	39.047	0.106
	au29.1m.ksp.87a.txt	2.2	20	1.2E+01	4.1E-03	1.8E+00	1.9E-03	2.4E-02	1.3E-04	4.1E-02	1.5E-04	5.8E-03	7.7E-05	7.65E-14	0.856	5.472	39.104	0.102
	au29.1m.ksp.91a.txt	2.2	20	6.3E+00	3.2E-03	1.1E+00	1.2E-03	1.4E-02	1.3E-04	3.9E-02	2.3E-04	6.9E-04	1.4E-05	4.08E-14	0.967	5.544	39.610	0.056
	au29.1m.ksp.94a.txt	2.2	20	4.5E-01	6.1E-04	5.4E-02	1.2E-04	9.6E-04	3.0E-05	2.3E-01	6.8E-04	5.0E-04	1.2E-05	2.89E-15	0.665	5.856	41.813	0.492
SMO13_46	au29.1n.ksp.115a.txt	2.2	20	1.3E+01	7.4E-03	2.4E+00	2.3E-03	3.0E-02	1.9E-04	2.3E-02	9.9E-05	7.6E-04	1.8E-05	8.21E-14	0.982	5.290	37.816	0.046
Feldspar	au29.1n.ksp.118a.txt	2.2	20	7.5E+00	6.5E-03	1.4E+00	1.6E-03	1.8E-02	1.3E-04	1.1E-02	1.4E-04	2.5E-04	1.2E-05	4.85E-14	0.990	5.291	37.818	0.059
Total Fusion	au29.1n.ksp.117a.txt	2.2	20	1.2E+01	5.7E-03	2.3E+00	2.9E-03	3.0E-02	2.5E-04	3.9E-02	2.0E-04	3.6E-04	1.5E-05	8.10E-14	0.991	5.302	37.900	0.053
	au29.1n.ksp.6a.txt	2.2	20	1.9E+01	7.4E-03	3.5E+00	2.7E-03	4.5E-02	3.2E-04	4.1E-02	2.4E-04	1.1E-03	4.2E-05	1.21E-13	0.983	5.303	37.909	0.042
J-Value	au29.1n.ksp.109a.txt	2.2	20	7.9E+00	9.0E-03	1.5E+00	1.9E-03	1.9E-02	1.9E-04	8.7E-03	1.0E-04	4.5E-04	1.4E-05	5.10E-14	0.983	5.306	37.924	0.069
0.008 ± 1.1E-5	au29.1n.ksp.114a.txt	2.2	20	9.7E+00	1.2E-02	1.8E+00	2.6E-03	2.3E-02	1.3E-04	1.0E-02	1.1E-04	3.9E-04	1.2E-05	6.32E-14	0.988	5.307	37.932	0.075
	au29.1n.ksp.4a.txt	2.2	20	8.4E+00	1.0E-02	1.6E+00	2.6E-03	2.0E-02	1.9E-04	9.9E-03	1.5E-04	3.9E-04	1.3E-05	5.46E-14	0.986	5.310	37.958	0.082
	au29.1n.ksp.108a.txt	2.2	20	1.2E+01	1.1E-02	2.2E+00	1.5E-03	2.9E-02	2.4E-04	3.3E-02	2.0E-04	7.2E-04	3.2E-05	7.81E-14	0.982	5.315	37.994	0.053
	au29.1n.ksp.3a.txt	2.2	20	1.3E+01	7.2E-03	2.2E+00	2.6E-03	2.8E-02	1.3E-04	2.3E-02	1.5E-04	3.0E-03	2.6E-05	8.15E-14	0.930	5.325	38.061	0.060
	au29.1n.ksp.107a.txt	2.2	20	9.9E+00	9.8E-03	1.8E+00	2.5E-03	2.3E-02	1.4E-04	1.5E-02	1.1E-04	4.3E-04	1.1E-05	6.45E-14	0.987	5.325	38.065	0.066
	au29.1n.ksp.113a.txt	2.2	20	9.4E+00	1.0E-02	1.7E+00	2.4E-03	2.2E-02	1.0E-04	1.3E-02	1.7E-04	4.4E-04	1.4E-05	6.09E-14	0.986	5.327	38.075	0.070
	au29.1n.ksp.110a.txt	2.2	20	9.5E+00	4.9E-03	1.8E+00	1.8E-03	2.3E-02	1.8E-04	1.2E-02	2.0E-04	1.8E-04	2.1E-05	6.19E-14	0.994	5.328	38.087	0.050
	au29.1n.ksp.5a.txt	2.2	20	5.0E+00	3.3E-03	9.3E-01	8.4E-04	1.2E-02	1.1E-04	6.1E-03	8.3E-05	3.0E-04	2.1E-05	3.27E-14	0.982	5.336	38.141	0.065
	au29.1n.ksp.7a.txt*	2.2	20	3.3E-01	5.7E-04	4.8E-02	3.7E-04	8.8E-04	3.4E-05	1.9E-01	9.1E-04	3.0E-04	2.3E-05	2.14E-15	0.735	5.361	38.319	1.090
	au29.1n.ksp.8a.txt*	2.2	20	4.3E-01	4.2E-04	6.3E-02	2.8E-04	1.1E-03	3.5E-05	2.5E-01	8.0E-04	3.6E-04	2.5E-05	2.78E-15	0.752	5.473	39.107	0.856
	au29.1n.ksp.105a.txt*	2.2	20	2.6E-01	5.0E-04	4.4E-02	1.0E-04	5.7E-04	3.8E-05	2.1E-01	6.9E-04	1.6E-04	1.0E-05	1.70E-15	0.819	5.323	38.049	0.514
	au29.1n.ksp.106a.txt*	2.2	20	3.7E-01	4.5E-04	3.9E-02	1.4E-04	5.3E-04	3.3E-05	2.4E-01	1.1E-03	5.3E-04	1.2E-05	2.42E-15	0.576	6.150	43.889	0.715
	au29.1n.ksp.116a.txt*	2.2	20	2.6E-01	7.3E-04	3.6E-02	2.8E-04	5.3E-04	3.4E-05	1.9E-01	5.8E-04	2.7E-04	1.1E-05	1.70E-15	0.690	5.479	39.151	0.772
	*plagioclase																	
SMO13_46	au29.2a.bio.63a.txt	2.2	20	1.6E+01	9.4E-03	2.7E+00	2.7E-03	8.3E-02	2.7E-04	2.6E-02	2.1E-04	5.8E-03	7.1E-05	1.05E-13	0.895	5.403	38.500	0.075
Biotite	au29.2a.bio.66a.txt	2.2	20	1.5E+01	9.8E-03	2.5E+00	2.6E-03	8.2E-02	4.9E-04	2.9E-02	1.6E-04	4.9E-03	6.5E-05	9.60E-14	0.903	5.353	38.147	0.077
Step Heating	au29.2a.bio.67a.txt	2.2	20	7.4E+00	9.1E-03	1.2E+00	1.6E-03	4.1E-02	1.8E-04	8.1E-03	1.5E-04	3.0E-03	4.7E-05	4.79E-14	0.881	5.384	38.368	0.114
	au29.2a.bio.69a.txt	2.2	20	1.9E+01	1.1E-02	3.2E+00	3.7E-03	1.1E-01	4.7E-04	2.8E-02	1.1E-04	5.5E-03	8.6E-05	1.22E-13	0.913	5.334	38.009	0.078
J-Value	au29.2a.bio.70a.txt	2.2	20	4.4E+00	5.3E-03	6.8E-01	9.8E-04	2.3E-02	2.4E-04	9.9E-03	9.8E-05	2.7E-03	1.9E-05	2.84E-14	0.819	5.252	37.435	0.105
0.008 ± 8.9E-6	au29.2a.bio.68a.txt	0.4	30	7.8E-03	2.2E-04	3.6E-04	7.4E-05	3.0E-06	2.9E-05	3.1E-05	2.5E-05	2.2E-05	1.1E-05	5.06E-17	0.176	3.802	27.258	78.189
	au29.2a.bio.68b.txt	0.5	30	7.0E-02	4.4E-04	3.3E-03	9.0E-05	8.3E-05	2.3E-05	3.8E-04	3.8E-05	1.4E-04	2.0E-05	4.55E-16	0.411	8.827	62.666	13.761
	au29.2a.bio.68c.txt	0.55	30	1.2E-01	4.9E-04	6.8E-03	1.1E-04	1.3E-04	2.1E-05	5.8E-04	3.5E-05	2.1E-04	1.7E-05	7.53E-16	0.473	8.065	57.339	5.671

	au29.2a.bio.68d.txt	0.6	30	1.7E-01	4.7E-04	1.9E-02	9.4E-05	3.4E-04	2.9E-05	1.0E-03	4.1E-05	1.9E-04	1.9E-05	1.10E-15	0.673	5.920	42.266	2.124
	au29.2a.bio.68e.txt	0.65	30	2.3E-01	2.5E-04	3.7E-02	2.4E-04	5.2E-04	2.4E-05	1.7E-03	4.3E-05	7.6E-05	1.3E-05	1.50E-15	0.903	5.668	40.488	0.778
	au29.2a.bio.68f.txt	0.7	30	2.3E-01	2.5E-04	3.7E-02	2.1E-04	5.4E-04	2.9E-05	1.4E-03	5.0E-05	6.1E-05	1.2E-05	1.48E-15	0.920	5.681	40.579	0.725
	au29.2a.bio.68g.txt	0.75	30	2.9E-01	6.2E-04	4.7E-02	2.4E-04	1.0E-03	3.4E-05	1.4E-03	4.4E-05	1.1E-04	1.0E-05	1.90E-15	0.890	5.565	39.758	0.525
	au29.2a.bio.68h.txt	0.8	30	2.2E-01	2.3E-04	3.5E-02	2.6E-04	1.0E-03	3.1E-05	6.5E-04	3.6E-05	7.9E-05	1.7E-05	1.42E-15	0.893	5.634	40.249	1.076
	au29.2a.bio.68i.txt	0.85	30	2.1E-01	4.9E-04	3.4E-02	3.5E-04	1.1E-03	3.5E-05	6.1E-04	6.6E-05	6.2E-05	1.7E-05	1.38E-15	0.914	5.746	41.038	1.165
	au29.2a.bio.68j.txt	0.92	30	2.4E-01	3.7E-04	3.8E-02	1.6E-04	1.4E-03	3.0E-05	6.0E-04	3.9E-05	4.1E-05	1.0E-05	1.54E-15	0.949	5.872	41.923	0.604
	au29.2a.bio.68k.txt	1	30	4.0E-01	6.3E-04	6.6E-02	3.4E-04	2.2E-03	4.1E-05	8.0E-04	4.2E-05	7.9E-05	2.3E-05	2.62E-15	0.942	5.774	41.232	0.760
	au29.2a.bio.68l.txt	1.1	30	4.8E-01	5.1E-04	7.9E-02	3.0E-04	2.5E-03	2.6E-05	7.6E-04	3.3E-05	1.8E-04	2.7E-05	3.13E-15	0.890	5.467	39.066	0.739
	au29.2a.bio.68m.txt	1.2	30	6.9E-01	6.0E-04	1.1E-01	4.6E-04	3.7E-03	4.3E-05	1.2E-03	4.1E-05	2.2E-04	1.2E-05	4.48E-15	0.905	5.480	39.157	0.287
	au29.2a.bio.68n.txt	1.3	30	1.4E+00	1.6E-03	2.4E-01	8.8E-04	8.0E-03	7.8E-05	2.0E-03	3.9E-05	3.4E-04	2.3E-05	9.11E-15	0.928	5.458	39.004	0.261
	au29.2a.bio.68o.txt	1.4	30	1.8E+00	2.0E-03	3.2E-01	7.3E-04	1.0E-02	1.3E-04	1.2E-03	5.4E-05	3.3E-04	2.9E-05	1.18E-14	0.947	5.414	38.692	0.217
	au29.2a.bio.68p.txt	1.5	20	2.2E+00	1.8E-03	3.9E-01	1.0E-03	1.3E-02	1.2E-04	9.6E-04	5.1E-05	3.3E-04	1.4E-05	1.43E-14	0.955	5.404	38.622	0.132
	au29.2a.bio.68q.txt	1.6	20	9.1E-01	1.2E-03	1.6E-01	5.9E-04	5.3E-03	1.1E-04	2.0E-04	5.3E-05	9.6E-05	2.2E-05	5.90E-15	0.969	5.454	38.977	0.331
	au29.2a.bio.68r.txt	1.8	20	9.4E-01	1.8E-03	1.7E-01	7.1E-04	5.5E-03	9.3E-05	2.3E-04	3.0E-05	1.1E-04	1.2E-05	6.08E-15	0.965	5.407	38.639	0.244
	au29.2a.bio.68s.txt	2	20	2.6E-01	5.4E-04	4.7E-02	1.9E-04	1.5E-03	3.6E-05	1.0E-04	2.0E-05	1.6E-05	1.1E-05	1.71E-15	0.982	5.561	39.733	0.512
	au29.2a.bio.68t.txt	2.2	20	1.1E-01	5.0E-04	1.9E-02	7.3E-05	6.1E-04	3.0E-05	-2.7E-04	9.4E-05	7.1E-06	1.1E-05	7.02E-16	0.981	5.545	39.618	1.238
SMO13_48	au29.1o.ksp.98a.txt	2.2	20	7.5E-01	9.3E-04	1.3E-01	5.1E-04	1.7E-03	3.7E-05	6.6E-02	7.3E-04	5.1E-04	1.4E-05	4.89E-15	0.801	4.733	33.872	0.295
Sanidine	au29.1o.ksp.16a.txt	2.2	20	1.3E+00	1.2E-03	2.0E-01	5.7E-04	2.7E-03	4.3E-05	2.2E-01	7.0E-04	1.1E-03	2.6E-05	8.29E-15	0.744	4.964	35.504	0.321
Total Fusion	au29.1o.ksp.97a.txt	2.2	20	1.1E+00	9.9E-04	2.0E-01	5.8E-04	2.6E-03	3.7E-05	1.3E-01	6.8E-04	4.5E-04	1.2E-05	7.28E-15	0.882	4.998	35.746	0.179
	au29.1o.ksp.22a.txt	2.2	20	4.8E+00	4.0E-03	6.8E-01	9.4E-04	9.6E-03	6.3E-05	3.5E-01	1.1E-03	4.7E-03	4.4E-05	3.10E-14	0.708	5.004	35.790	0.159
J-Value	au29.1o.ksp.13a.txt	2.2	20	3.9E+00	4.0E-03	5.1E-01	8.2E-04	7.7E-03	1.2E-04	2.2E-01	3.7E-04	4.5E-03	4.2E-05	2.53E-14	0.656	5.007	35.808	0.201
0.008 ± 7.7E-6	au29.1o.ksp.18a.txt	2.2	20	7.8E+00	4.7E-03	1.0E+00	8.4E-04	1.6E-02	1.1E-04	6.0E-01	1.7E-03	8.9E-03	7.2E-05	5.07E-14	0.665	5.019	35.899	0.156
	au29.1o.ksp.96a.txt	2.2	20	1.7E+00	2.1E-03	2.8E-01	5.6E-04	3.9E-03	7.9E-05	1.4E-01	7.5E-04	9.2E-04	1.5E-05	1.09E-14	0.838	5.023	35.925	0.151
	au29.1o.ksp.92a.txt	2.2	20	1.8E+00	1.0E-03	3.1E-01	6.8E-04	4.0E-03	4.6E-05	1.2E-01	1.1E-03	7.0E-04	1.5E-05	1.15E-14	0.883	5.035	36.012	0.136
	au29.1o.ksp.17a.txt	2.2	20	2.4E+00	1.9E-03	4.1E-01	8.2E-04	5.7E-03	6.7E-05	1.4E-01	7.9E-04	9.9E-04	1.6E-05	1.53E-14	0.876	5.039	36.039	0.120
	au29.1o.ksp.19a.txt	2.2	20	5.4E+00	5.1E-03	4.1E-01	6.3E-04	7.5E-03	1.0E-04	2.9E-01	8.7E-04	1.2E-02	6.3E-05	3.53E-14	0.374	5.081	36.334	0.381
	au29.1o.ksp.95a.txt	2.2	20	6.9E-01	1.3E-03	1.1E-01	4.4E-04	1.4E-03	3.2E-05	7.5E-02	6.1E-04	5.2E-04	1.3E-05	4.51E-15	0.778	5.113	36.565	0.337
	au29.1o.ksp.20a.txt	2.2	20	3.9E+00	3.8E-03	5.4E-01	9.1E-04	8.0E-03	1.4E-04	3.9E-01	7.5E-04	4.1E-03	5.4E-05	2.56E-14	0.693	5.135	36.721	0.237
	au29.1o.ksp.14a.txt	2.2	20	4.0E+00	2.4E-03	5.6E-01	5.4E-04	7.9E-03	6.2E-05	3.7E-01	5.2E-04	4.0E-03	5.2E-05	2.62E-14	0.710	5.147	36.805	0.203
	au29.1o.ksp.15a.txt	2.2	20	2.4E+00	2.0E-03	3.9E-01	4.9E-04	5.1E-03	4.1E-05	2.1E-01	6.9E-04	1.3E-03	2.8E-05	1.55E-14	0.843	5.154	36.852	0.164
	au29.1o.ksp.94a.txt	2.2	20	1.3E+00	7.4E-04	1.6E-01	6.1E-04	2.3E-03	3.6E-05	1.1E-01	7.6E-04	1.5E-03	1.8E-05	8.16E-15	0.638	5.167	36.945	0.344
	au29.1o.ksp.21a.txt	2.2	20	1.6E+00	1.2E-03	2.5E-01	6.4E-04	3.2E-03	3.4E-05	1.4E-01	5.0E-04	9.7E-04	1.5E-05	1.01E-14	0.816	5.182	37.051	0.176
	au29.1o.ksp.93a.txt	2.2	20	9.1E-01	1.2E-03	1.1E-01	4.3E-04	1.7E-03	2.7E-05	8.1E-02	6.2E-04	1.2E-03	1.5E-05	5.92E-15	0.617	5.194	37.134	0.389
	au29.1o.ksp.25a.txt	2.2	20	5.9E+00	3.8E-03	6.1E-01	1.1E-03	9.4E-03	6.4E-05	4.6E-01	8.8E-04	9.2E-03	6.4E-05	3.83E-14	0.539	5.314	37.983	0.268
	au29.1o.ksp.24a.txt	2.2	20	1.8E+00	1.4E-03	2.4E-01	4.8E-04	3.3E-03	4.9E-05	2.2E-01	8.3E-04	1.7E-03	1.9E-05	1.17E-14	0.717	5.484	39.186	0.208
	au29.1o.ksp.24a.txt	2.2	20	1.8E+00	1.4E-03	2.4E-01	4.9E-04	3.2E-03	4.8E-05	2.2E-01	8.3E-04	1.7E-03	1.9E-05	1.17E-14	0.721	5.517	39.420	0.209
SMO13_48	au29.2d.bio.72a.txt	2.2	20	8.1E+00	6.4E-03	8.3E-01	1.6E-03	2.8E-02	1.7E-04	1.4E-02	9.5E-05	1.2E-02	7.6E-05	5.27E-14	0.58	5.68428	40.480	0.247
Biotite	au29.2d.bio.77a.txt	2.2	20	5.7E+00	4.0E-03	6.0E-01	9.8E-04	1.6E-02	1.9E-04	1.0E-02	1.1E-04	8.0E-03	6.7E-05	3.72E-14	0.59	5.64192	40.182	0.270
Step Heating	au29.2d.bio.78a.txt	2.2	20	6.8E+00	8.1E-03	7.2E-01	1.5E-03	2.6E-02	1.3E-04	1.4E-02	1.4E-04	8.1E-03	6.9E-05	4.39E-14	0.64	6.06456	43.156	0.265
J-Value	au29.2d.bio.79a.txt	2.2	20	2.7E+00	2.3E-03	3.5E-01	6.5E-04	1.2E-02	1.3E-04	3.9E-03	3.9E-05	2.2E-03	3.8E-05	1.77E-14	0.76	5.88001	41.858	0.256
0.008 ± 8.9E-6	au29.2d.bio.80a.txt	2.2	20	4.0E+00	5.5E-03	4.0E-01	1.4E-03	1.4E-02	1.6E-04	6.6E-03	7.1E-05	4.9E-03	5.6E-05	2.57E-14	0.63	6.22285	44.269	0.399

Appendix C. ⁴⁰Ar/³⁹Ar Age Data Summary.

¹Laser power. ²Length of time (in seconds) of laser fusion. ³Voltages of the argon isotopes as measured by the mass spectrometer. ⁴Percentage of the sample that was radiogenic.

Appendix C – Point Count Correlation Data

Pair	Between-Sample Petrographic Similary								Within-sample petrographic similarity					TOTALS		
	<i>Plagioclase</i>		<i>Potassium Feldspar</i>		<i>Quartz</i>		<i>Biotite</i>		SUM	Qtz and Pl	Pl v. k + b	k and bio.	Qtz and k+ b	SUM	RAW	SCALED
	Δ^1	Rank	Δ	Rank	Δ	Rank	Δ	Rank								
4-16	8.8	1	4.6	3	12.7	0	14.8	0	4	3	3	0	0	6	10	0.42
8-13	4.4	3	5.6	1	3.8	3	6.9	1	8	3	3	0	3	9	17	0.71
8-28	29.7	0	17.4	0	18.2	0	6.0	1	1	3	3	0	3	9	10	0.42
8-35	17.7	0	13.4	0	12.4	0	8.1	1	1	3	3	0	3	9	10	0.42
12-19	6.1	1	24.8	0	3.3	3	27.6	0	4	3	3	0	3	9	13	0.54
13-19	19.8	0	15.6	0	18.8	0	26.0	0	0	3	3	0	3	9	9	0.38
13-28	25.3	0	11.8	0	22.0	0	0.9	3	3	3	3	3	3	12	15	0.63
13-35	13.3	0	7.7	1	16.2	0	1.3	3	4	3	3	3	3	12	16	0.67
19-28	5.5	1	27.4	0	3.2	3	25.1	0	4	3	3	0	3	9	13	0.54
19-35	6.5	1	23.4	0	2.6	3	27.3	0	4	3	3	0	3	9	13	0.54
22-37	2.8	3	9.8	1	6.8	1	9.7	1	6	3	3	0	3	9	15	0.63
22-42	40.8	0	1.0	3	49.6	0	3.7	3	6	0	3	3	3	9	15	0.63
28-35	12.0	0	4.1	3	5.8	1	2.2	3	7	3	3	3	3	12	19	0.79
33-43	1.3	3	8.3	1	15.3	0	7.2	1	5	3	3	3	0	9	14	0.58
33-46	3.0	3	4.1	3	13.8	0	8.8	1	7	3	3	3	0	9	16	0.67
33-48	38.5	0	6.4	1	28.5	0	73.2	0	1	0	0	0	0	0	1	0.04
33-53	5.4	1	10.2	0	7.1	1	4.8	3	5	3	3	3	3	12	17	0.71
43-46	1.7	3	4.2	3	1.5	3	1.7	3	12	3	3	3	3	12	24	1.00
43-48	39.9	0	14.7	0	13.2	0	66.0	0	0	0	0	0	3	3	3	0.13
43-53	6.7	1	1.9	3	8.2	1	2.4	3	8	3	3	3	0	9	17	0.71
46-48	41.6	0	10.5	0	14.8	0	64.3	0	0	0	0	0	3	3	3	0.13
46-53	8.4	1	6.1	1	6.7	1	4.1	3	6	3	3	3	0	9	15	0.63
48-53	33.1	0	16.6	0	21.5	0	68.4	0	0	0	0	0	0	0	0	0.00

Appendix C. Point Count / Petrography Correlation Summary.

¹ Δ is the percent difference in the modal percentages for the mineral being compared.

Appendix D – Geochemistry Correlation Data

		Trace Elements												TOTALS								
		Zr		Nd		Gd		Yb		Y		Nb		Ta		Rb		Sr		Ba		
Pair	I	I'	Rank	I	Rank	I	Rank	I	Rank	RAW	SCALED											
4-16	53.3	54.1	1	53.3	1	54.1	1	53.3	1	53.3	1	53.3	1	53.3	1	105.9	1	221.5	0	512.7	0	0.26
8-13	305.1	305.1	0	305.1	0	305.2	0	305.1	0	305.2	0	305.2	0	305.1	0	324.5	0	327.2	0	320.2	0	0.00
8-28	349.4	349.4	0	349.4	0	349.4	0	349.4	0	349.4	0	349.4	0	349.4	0	367.6	0	354.7	0	1048.5	0	0.00
8-35	503.4	503.9	0	503.4	0	504.5	0	503.4	0	504.5	0	503.4	0	503.7	0	671.8	0	510.3	0	1245.8	0	0.00
12-19	241.2	241.8	0	241.2	0	241.7	0	241.2	0	241.7	0	241.2	0	241.2	0	244.1	0	242.4	0	1733.4	0	0.00
13-19	122.5	124.0	0	122.6	0	125.2	0	122.6	0	125.2	0	122.6	0	122.5	0	132.6	0	179.6	1	123.0	1	0.07
13-28	44.3	44.6	1	44.4	1	44.4	1	44.4	1	44.4	1	44.8	1	44.3	1	44.5	1	185.2	0	1086.9	0	0.26
13-35	198.3	199.6	0	198.3	0	199.8	0	198.3	0	199.8	0	198.5	0	199.1	0	388.7	0	282.9	0	1252.8	0	0.00
19-28	166.8	167.4	0	166.8	0	166.8	0	166.8	0	166.8	0	166.9	0	166.8	0	175.5	0	173.7	1	1088.6	0	0.04
19-35	320.8	323.5	0	320.9	0	324.7	0	320.9	0	324.7	0	320.9	0	321.3	0	501.2	0	328.5	0	1267.9	0	0.00
22-37	25.2	25.3	1	25.4	1	25.7	1	25.7	1	30.8	1	27.1	1	25.2	1	100.2	1	341.6	0	784.6	0	0.26
22-42	89.5	90.5	0	89.5	0	89.5	0	89.5	0	89.8	0	89.5	0	89.5	0	144.8	0	308.9	0	322.8	0	0.00
28-35	154.0	156.5	0	154.1	0	154.1	0	154.1	0	162.0	0	154.0	0	154.9	0	364.6	0	155.6	1	215.7	1	0.07
33-43	53.4	57.7	1	53.5	1	53.4	1	53.4	1	55.0	1	53.5	1	53.4	1	120.1	1	55.2	1	162.6	1	0.33
33-46	8.8	11.0	3	8.9	3	8.8	3	8.8	3	10.0	3	8.9	3	8.8	3	26.8	3	41.0	3	130.8	1	0.93
33-48	38.0	44.6	1	38.1	1	38.1	1	38.0	1	39.1	1	38.0	1	38.0	1	64.8	1	140.7	1	96.5	1	0.33
33-53	1.2	12.7	3	2.3	3	1.2	3	1.2	3	6.0	3	1.7	3	1.2	3	3.5	3	4.4	3	98.6	1	0.93
43-46	62.3	64.1	0	62.3	0	62.3	0	62.3	0	62.8	0	62.3	0	62.3	0	146.8	0	67.6	1	66.4	1	0.07
43-48	15.4	15.5	1	15.4	1	15.4	1	15.4	1	15.9	1	15.6	1	15.4	1	57.2	1	150.1	1	66.6	1	0.33
43-53	54.6	55.4	1	54.6	1	54.6	1	54.6	1	55.1	1	54.7	1	54.6	1	123.6	1	57.5	1	77.5	1	0.33
46-48	46.8	49.7	1	46.9	1	46.8	1	46.8	1	47.1	1	46.9	1	46.8	1	90.8	1	181.6	0	62.7	3	0.37
46-53	7.7	9.8	3	7.7	3	7.7	3	7.7	3	7.7	3	7.7	3	7.7	3	23.3	3	44.9	3	32.8	3	1.00
48-53	39.2	40.6	1	39.2	1	39.2	1	39.2	1	39.3	1	39.2	1	39.2	1	68.2	1	137.0	1	40.4	3	0.41

Appendix D. Trace Element Correlation Summary.

I' is the length of line between two data points representing the sameness of the sample pairs. See text (section 4.3.4) for explanation. Note that the Zr I' value was constant for all tests and was not assigned a ranking.